DYNAMIC ANALYSIS OF SUBSTRUCTURES WITH ACCOUNT OF ALTERED RESTRAINT WHEN TESTED IN ISOLATION

By

RAMIN AMID, B.Eng., M.A.Sc.

A thesis

Submitted to the school of Graduate Studies

In Partial Fulfillment of the Requirements

For the Degree of

Doctor of Philosophy

McMaster University

DOCTOR OF PHILOSOPHY (2009) **McMaster University**

(Mechanical Engineering) **Hamilton, Ontario**

TITLE: **Dynamic Analysis of Substructures with Account of Altered Restraint when Tested in Isolation**

AUTHOR: **Ramin Amid**

B.Eng., Technical University of Istanbul, Istanbul, Turkey

B.Eng., Ryerson University, Toronto, Ontario, Canada

M.A.Sc. Ryerson University, Toronto, Ontario, Canada

SUPERVISORS: **Dr. D. Metzger**

Dr. K. Behdinan

NUMBER OF PAGES: xxviii, 257

Abstract

The objective of this research is to simulate the response of an isolated substructure such that the response of the substructure in isolation would be the same as the substructure within the structure. Generally, the behaviour of an isolated subsystem (substructure) subjected to dynamic loading is different than the behaviour of the same substructure within a system (structure). This is primarily caused by the boundary conditions that are imposed on the substructure from the surrounding subsystem in the entire structure.

A new systematic approach (methodology) is developed for performing impact analysis on the isolated substructure. The developed technique is fundamentally based on enforcing the mode shapes around the boundary of the substructure in the full structure to be similar to the mode shapes of the isolated substructure. This is achieved by providing a consistent adjustment to the loading conditions (impact velocity and mass) to account for the loss of restraint at the interface with the full structure. Another important aspect of this research is experimental validation of proposed method. This method allows the experimental testing of an isolated substructure since the testing is performed by impacting the isolated substructure with an appropriate mass and velocity.

In the finite element analysis, the structure is analyzed, and then the isolated substructure simulation is performed using the developed technique. The results obtained from the numerical simulations, for both the substructure *in situ* and the substructure in isolation, are compared and found to be in good agreement. For instance, the effective

plastic strains, kinetic and internal energies for the substructure within the structure and the substructure in isolation range from 7% to 12% discrepancies between two analyses.

The numerical simulations of a full structure are verified by performing a series of experimental impact tests on the full structure. Finally, the experimental applicability of the technique is studied and its results are validated with FE simulation of substructure in isolation. This problem of experimentally testing an isolated substructure had previously not been addressed. The comparisons of FE simulation and experimental testing are made based on the deformed geometries, out-of-plane deflections and accelerometer readings. For example, the out-of-plane deformations from the FE analysis and the experimental test were determined to be within 7% to 9%. The experimental validation and numerical simulations indicates the technique is reliable, repeatable and can predict dynamic response of the substructures when tested in isolation.

Acknowledgements

I would like to take this opportunity to express my deepest gratitude and special thanks to my supervisors, Dr. Metzger and Dr. Behdinan, for all their guidance, tremendous support and encouragement throughout my research.

Furthermore, I wish to express my sincere thanks to my supervisory committee members, Dr. Dokainish, Dr. Stolle, and Dr. Jain, for their support and valuable comments during my work, and helping me throughout the project. Also, I would like to thank the Mechanical Engineering department at McMaster University for their financial support during my attendance, and letting me to be a part of their community.

I am indebted to Dr. Ghaemi for his support, comments, and patience during this work and would like to thank him for his help throughout my research.

Last but not least, I like to dedicate this work to my family. They have supported me and have been a constant source of encouragement. They have given me strength and have empowered me at a time that I had no strength to go on.

This work was partially funded by Material Manufacturing of Ontario (MMO) through collaboration with McMaster University, Ryerson University and Freedom Motor LTD.

Table of Contents

List of Figures

List of Tables

Chapter 1
Statement of the Research and Objectives

1.1 Introduction

Crashworthiness design is of special interest to the automotive industry for enhancing passenger safety and reducing manufacturing cost. An evaluation of any design change involving vehicle structure requires simulation of the system, which is a highly nonlinear transient dynamic problem. The redesign process can be quite tedious and time-consuming when full-scale finite element models are used. In most cases of design for crashworthiness, the subsystem behaviour is strongly coupled to that of the overall system in such a way that even small changes to the subsystem can strongly affect the interactions between the system and subsystem. Since it is too expensive to physically fabricate and test all conceivable design alternatives early in the design stage, analysts use numerical techniques to predict approximate crash characteristics of a proposed design. Consequently, vehicle crash predictions are usually obtained by considering the vehicle as a collection of subsystems that interact with one another and are expected to influence the crash performance of the vehicle as a whole.

When performing a dynamic analysis of a structure, the primary interest is to determine how the structure will respond over time to a given set of conditions (loads, motion, impact with another structure, etc.). Typically, dynamic finite element (FE) codes

compute the parameters of interest by looking at the structure at different points in time and by providing an output that indicates how the structure changes as time progresses.

Numerical methods for simulation of automotive crash events have been developed for the last twenty years and many FE programs are now commercially available. These programs have greatly enhanced the art of simulation of various automotive crash events, such as frontal crash, side impact, rear crash, and offset crash.

Generally, in FE applications of subcomponent simulation, the acceleration, velocity and displacement as a function of time at the boundary of the subcomponent in full-scale simulation is transferred onto the subcomponent in isolation. In doing so, the physical boundary conditions are discarded and the velocity and displacement profile is forced upon the subcomponent. These methods, even though they produce accurate results, are only applicable within FE methods and do not lend themselves to physical testing. In addition, the final approval of any design relies on experimental crash testing of the designed components. In other words, the simulation of the crashworthiness of structures should be followed by experimental verification.

If any modification is made to the subsystem of the FE model, the entire model should be reanalyzed. In addition, any modification to a subsystem (substructure) of the original design required series of experimental testing of the entire car. A new design has to satisfy and meet government rules and regulations thus, warranting experimental testing of the entire system. This process is very expensive and time consuming. It is understood that various substructures within the entire system interact and impose constraints on each other. These boundary conditions cannot be determined in advance

when a system (structure) is subjected to impact loading. The objective of this work is to develop a technique that allows for impact analysis of a substructure in isolation. The existing experimental techniques in substructural testing only look at the energy absorption and deformation of substructure as an independent component. Our proposed technique looks at the energy absorption and deformation of substructure under study as a unit that the surrounding substructures influence its energy absorption and deformation modes. In other words, it includes the boundary conditions of the surrounding subsystems in the entire structure.

In a particular application involving a substructure system, the main activity is to modify the design of a vehicle in order to provide accessibility to wheelchair occupants. The modifications include lowering the center portion of the floor from the rear door to the rear of the front seat and installation of the access ramp. Figure 1.1 is presented only for the purpose of illustrating the problem statement. In Figure 1.1, the full structure is divided into the component and the subcomponent. The component represents the remaining vehicle structure and the subcomponent represents modified substructure. In this case, the modifications were made only to the subcomponent, and therefore the entire assembly needs to be reanalyzed. Here, we are not only interested in obtaining the dynamic response in terms of modifications, but also how to implement boundary conditions consistently, such that the over all change corresponding to the dynamic response would be minimal.

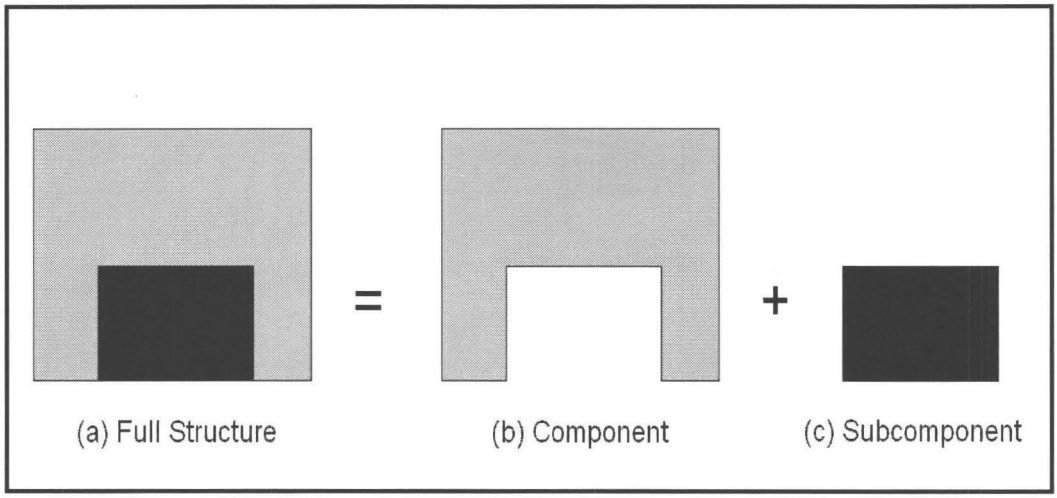

Figure 1.1: Schematic of the component and the subcomponent

In addition, in terms of the modifications to the subcomponent, the overall dynamic response of the system is intended to remain unchanged. Therefore, the dynamic response of the modified and unmodified subcomponents must be the same. In other words, all the assessments can be evaluated at subcomponent level only, as long as the overall dynamic response remains unchanged. This situation is shown in Figure 1.2.

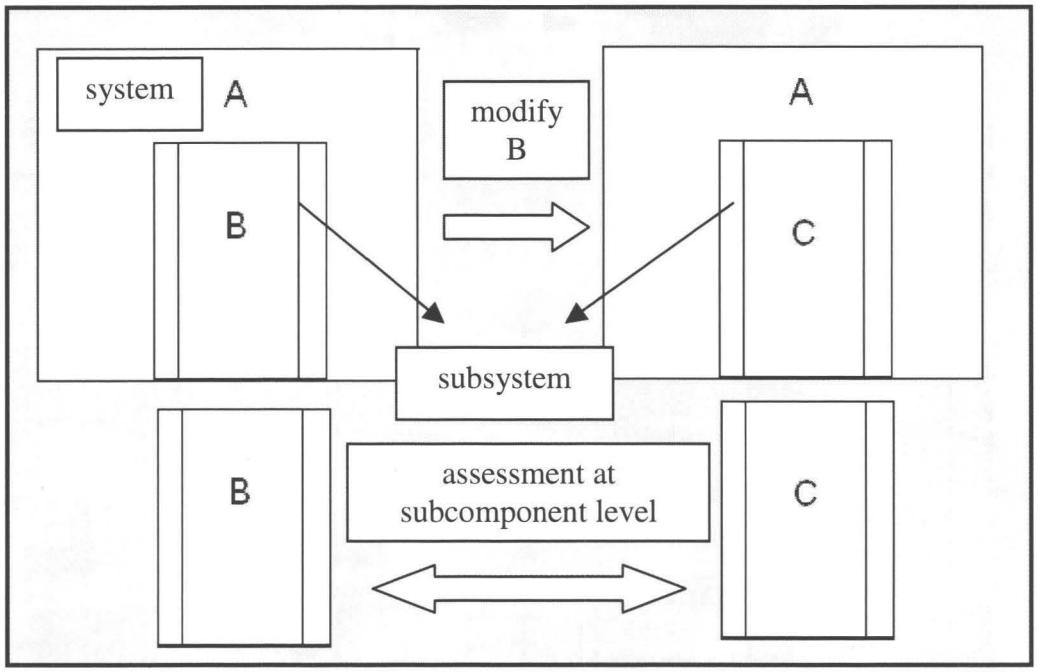

Figure 1.2: Schematic of the system and subsystem

Consider the structure that represents the approximate finite element model of the mini-van (as shown in Figure 1.3) entire vehicle, and the substructure that represents modified substructure. Here, the main objective is to determine the mass and velocity of impact such that the dynamic response of the modified substructure in isolation is similar to the impact response of the substructure within the mini-van. Figure 1.3 depicts rear impact analysis, where the vehicle was rigidly fixed and a moving rigid wall with prescribed velocity and mass impacts the vehicle.

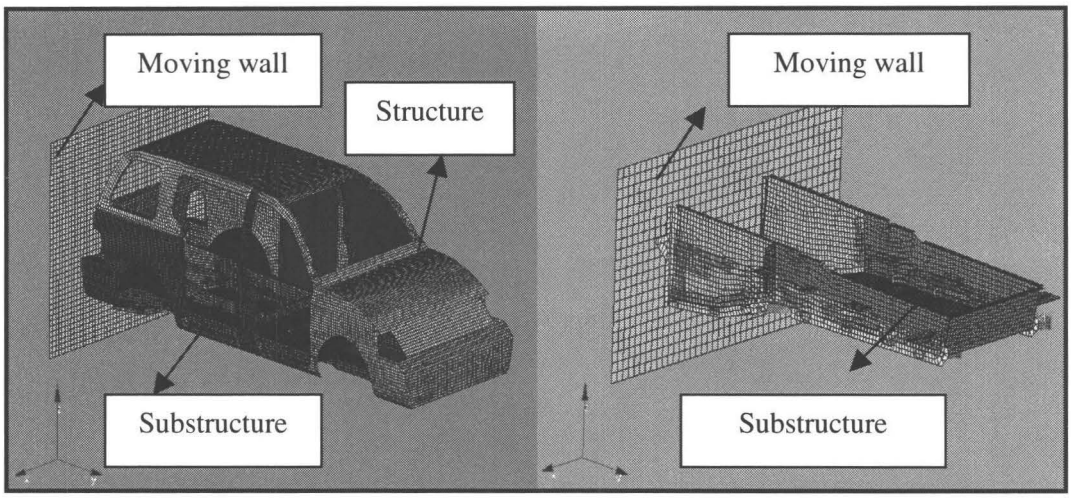

Figure 1.3: Schematic of the structure and its substructure

The subsystem response is influenced whenever the subsystem is subjected to dynamic loadings by its surrounding component. In addition, the substructure response to the dynamic loading would be different in isolation due to the influence of the free boundary around the substructure.

Practically, actual loads on the isolated substructure cannot be applied directly, since the dynamic loads on the interface are not known in advance. As a result dynamic loading needs to be adjusted to account for free boundary whenever the substructure is tested in isolation. Therefore, knowing the velocity and mass of the wall enables one to perform impact analysis on the isolated substructures, such that the isolated response would agree with *in situ* response when the entire structure is tested. Figure 1.4 depicts the simple illustration of the structure and its substructure.

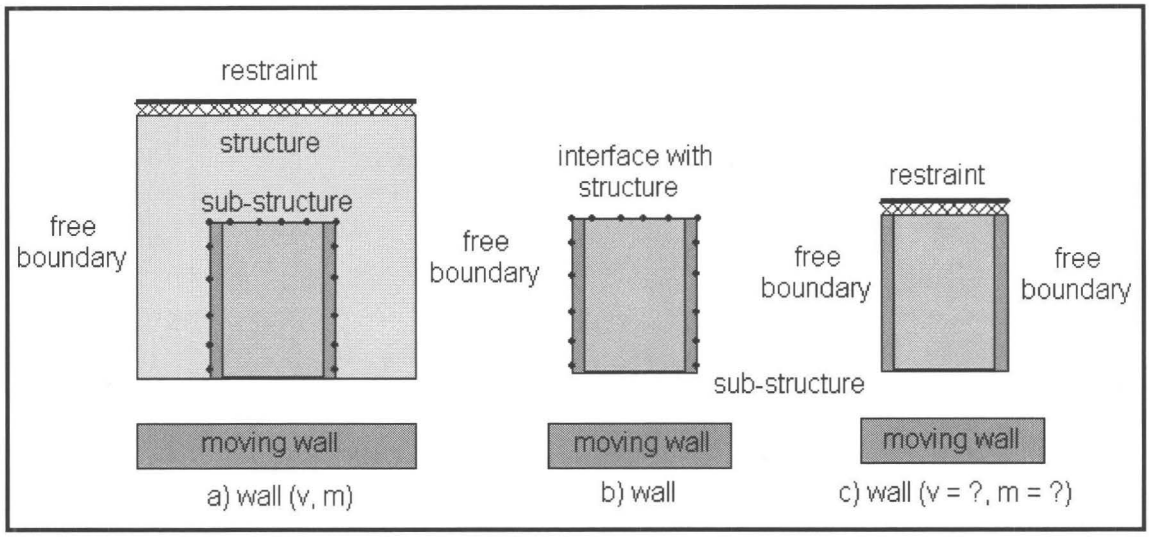

Figure 1.4: Schematic of the structure and the substructure

In order to overcome difficulties associated with testing the subcomponents in isolation, a systematic approach is developed. The technique is inspired partially by the model order reduction technique, but is applied to subcomponent analysis in isolation. The proposed technique not only can be applied to FE analysis but also can be applied to experimental testing. It is important to mention that experimental testing is a requirement of all crashworthiness application. The novelty of this method, in comparison to other methods, is that the impact analysis on the substructure in isolation is performed, by impacting the substructure in isolation with appropriate mass and velocity.

To perform substructure impact analysis in isolation, the baseline performance of the substructure in full structure must first be determined. Thus, the full model must first be analysed under the desired loading condition. The proposed method must achieve similar deformation around the boundary of the substructure when tested in isolation as that of the full model. It is well known that any changes to a subsystem of a system will

change the impact characteristics of the system as a whole. In order to minimize the changes caused by altering any subsystem in the full system, the deformations around the boundary of the subsystem in isolation should agree with the corresponding deformations in the full system. Therefore, the deformation around the substructure boundary in full model testing should be mapped onto the substructure when tested in isolation. This ensures the net effect of any changes made to the substructure will result in minimum change to the overall dynamic response the full structure.

The similarity of the boundary deformation is achieved by considering transient acceleration-time-history, mode shapes and internal energy of the substructure in the full model. The main mode shapes determined from the spectrum of the full model response can be matched with the relevant mode shapes for the isolated substructure. In addition, from transient analysis, the acceleration responses of boundary nodes were extracted under impact of the full model. This is particularly important since the most dominant modes of vibration and their respective mode shapes need to be determined. It is proposed here that if the substructure in isolation is excited at those determined dominant frequencies, the mode shape of the selected nodes and thereby the deformation of the selected nodes will be similar to those of the substructure in the full structure. Note that the FE analysis of the full model is an integral part of the proposed method as the energy transfer to the subcomponent was determined from FE analysis of the full model.

Four main steps in achieving this goal are:

- Develop the methodology for performing impact analysis on isolated substructures
- Apply the correct boundary conditions and developed parametric equations for impacting wall properties
- Perform numerical dynamic simulations on substructures in isolation
- Verify the developed technique and its application in an experimental setting

As a first step, the FE application of the proposed technique of substructural testing was studied. Consequently, to validate the proposed results, the experimental verification of the structure was carried out. Finally, the experimental application of the proposed methodology was examined. The proposed methodology reduces the cost both in manufacturing and time for performing impact analysis on isolated substructures.

1.2 Organization of Thesis

The subsequent chapters are organized as follows:

Chapter 1 - Statement of the Research and Objectives

Chapter 2 - Literature Review

Chapter 3 - Finite Element Analysis of Structural Components

Chapter 4 - Proposed Methodology

Chapter 5 - Experimental Apparatus and Testing Procedures

Chapter 6 - Comparison of Results and Discussion

Chapter 7 - Conclusions and Contributions

Chapter 2
Literature Review

2.1 Introduction

The term "Crashworthiness", first used in the aerospace industry in the early 1950's, provided a measure of the ability of a structure and any of its components to protect the occupants in survivable crashes. Similarly, in the automotive industry, crashworthiness refers to a measure of the vehicle's structural ability to plastically deform and yet maintain a sufficient survival space for its occupants in crashes involving reasonable deceleration loads. Crashworthiness is evaluated by a combination of tests and analytical methods. This section provides an overview of the structural crashworthiness and analytical techniques that have been used to perform crashworthiness analysis.

2.2 History of Crashworthiness Analysis

Analytical simulation of vehicle crashworthiness has evolved over the past 30 years. Three types of models are used to simulate vehicle structures: namely, Lumped Parameter (LP) models, Hybrid models, and Finite Element (FE) models. The FE models can also be divided into two groups: heuristic beam models, and continuum mechanics-based models, which use beam, shell and solid elements. The progression of these models over the years followed a pattern of increasing geometric detail since it was realized that

a simple analytical model of the crash event does not ensure accurate prediction for all possible impact conditions. The history of structural crashworthiness can be best characterized by two periods of historical developments: an early period, which starts from 1970 and ends about 1985, and a second period, which starts from mid 1980's with the introduction of supercomputers and vectorized explicit finite element codes.

2.2.1 Early Development of Analytical Techniques

The first period was essentially a period of trial; a time of attempting to develop some understanding of an extremely complex structural mechanics problem. A variety of numerical techniques were applied to simulate the deformations, including folding and buckling of vehicle structures during the decisive first 50 to 100 ms of a crash test. Approximate solutions were obtained by spring-mass modeling of the vehicle (Rapin, 1970; and Kamal, 1970), an approach originated in the aerospace industry. Alternative solutions using beam element models in conjunction with nonlinear joint formulation were obtained that proved to be very successful (McIvor, 1973; Chang, 1977; Wang and Merdith, 1983); however, this method requires a high degree of skill and experience from the analyst.

There were also attempts to obtain solutions based on first principles by modelling the car body as a continuum. This automated the task of attributing discretized stiffness values to the structural components. Some of this work was based on quasi-static beam element formulation (Mahmood and Paluzeny, 1986), implicit FE techniques (Gamon, 1978; Pifko and Winter, 1981; Argyris et al., 1986), finite difference methods

(Ni, 1981), implicit/explicit FE formulation (Haug et al., 1983), and explicit FE time integration (Belytschko and Hsieh, 1974).

It appears that the first crash model (Winter et al., 1981) simulated a head-on collision of a vehicle front structure with a rigid wall using the computer code DYCAST with an implicit solver (Pifko and Winter, 1981). In this model, the left half of the vehicle was represented by 504 membrane triangular, beam, bar, and spring elements. Haug et al., (1983) discussed the development of implicit-explicit time integration FE PAM-CRASH code and applied it to analyze the response of an A-pillar and to the right front quarter of a unit-body passenger vehicle structure. The quasi-static analysis was accomplished by an iterative incremental force/displacement analysis.

The theoretical background for implicit FE formulation and an associated code for crash analysis were presented in 1986 (Argyris et al., 1986). The developed code was applied to calculate the impact response of a vehicle front structure when it impacted a rigid barrier from an initial velocity of 13.4 m/s. The solution accounted for material strain hardening and rate effects, and provided structural deformations. Other than the three examples mentioned above, the application of implicit FE solvers to crash analysis did not proceed beyond that point. This was due to its inability to account for contact and folding of thin sheet metal structures and due to excessive demands on computer hardware storage and speed.

Some of these developments already contain the essential features that make up the core of any crash analysis software today. They combine time integration with shell elements, node-to-segment contact force transmissions, and plane stress elasto-plasticy.

Since these are still the basic algorithms used in today's analysis environment, it is not surprising that, as early as 1973, good analytical results were obtained on vehicle substructures.

The continuum approach, however, remained mainly limited to research since the goal of full-vehicle simulation could not be achieved with sufficient accuracy due to the limited number of shell elements that could be handeled by state-of-the-art computers before the mid 1980's. The resulting coarse meshes did not allow a representation of the global buckling modes in a full-vehicle model. Due to the high degree of interaction between different components of an automobile structure, it is necessary to consider the full vehicle in a single model to predict the energy absorption of the individual parts during a crash. The inability to fulfill this requirement brought the continuum approach, and thus the finite element approach, to automotive crash simulations to a standstill in the late 1970's and early 1980's.

2.2.2 Later Development of Analytical Techniques

The second period of development began in 1985 and continues to the present. It can be characterized as a period of rapid growth in both explicit finite element technology developments and application to progressively more complex vehicle structures. The breakthrough of finite element methods in the structural crashworthiness field and their consequent implementation in the design process of vehicles happened in the mid 1980's (Hieronimus and Nalepa, 1986; Gonard et al., 1986; DuBois and Chedmail, 1987).

During these years, vectorized supercomputers were introduced to the industry, allowing explicit finite element technology to establish itself as the leading numerical technique for crashworthiness calculations of vehicle structures. During this period, the analytical tools (FE) evolved out of being only a research tool and find its way into becoming an essential part of the vehicle design process.

Similar developments occurred almost simultaneously in the United States (Benson et al., 1986) and Europe (Nilsson, 1989). In 1985, ESI (Engineering System International) Group (Haug et al., 1986) published the first paper about application of explicit FE technology to crashworthiness of actual vehicle structures. The ESI Group modeled the front vehicle structure of a VW-POLO's impact into a rigid barrier from an initial velocity of 13.4 m/s. The analysis provided vehicle kinematics and barrier force-time pulse data. Subsequent to this simulation, automotive manufacturers have attempted many crashworthiness calculations. Other European car companies also started working along the same lines (Chedmail et al., 1986), contributing to the remarkable initial success of this methodology.

In the early 1980's, numerical simulation was almost exclusively a research activity involving very few engineers, and hardly industrial in nature. Since 1986, the development of simulation technology for crashworthiness has become more industrial rather than technological in nature (Nalepa, 1990; Zaouk et al., 1998). Thus, it is instructive to compare the role of numerical simulation of crashworthiness in automotive industry today to what it was in the mid 1980's. These simulations focused on frontal car-to-barrier crashes.

Today, vehicle manufacturers are faced with numerous restraints dictated by the different governments, in-house safety criteria, and consumer-driven requirements that must be met before a new car is introduced to the world market. Corresponding to a variety of collision scenarios, 15 to 20 full-scale vehicle tests may be performed on a specific prototype. In addition to frontal impact performance, the industry must consider U.S. side impact, rear impact, and rollover protection requirements (Chirwa, 1996; Kirkpatric et al., 1999).

With the availability of lower cost supercomputers based on symmetric multi-processor (SMP) and massively parallel processor (MPP) technologies, simulations of the aforementioned impact cases can be made more elaborate and efficient. As these computational advancements continue, simulations of larger and more detailed models could run in a comparable time to the smaller and less detailed models of the past. These vehicle models become useful for a wider range of impact conditions. Additionally, they must be sufficiently validated for the entire range of scenarios (Zaouk et al., 1996).

Numerical simulations have taken up a substantial part of the increased workload of crashworthiness engineers. The potential of the simulations, due to the constant development of hardware and software as well as the accumulated experience of a rapidly growing number of analysts, has evolved quickly enabling analysis groups to become fully integrated in the vehicle design cycle. These simulations complement a testing facility by preventing unnecessary work (additional experimental testing) from being performed. This in turn allows analysts to assess new designs and suggest modifications for improvement (Xue and Schmid, 2004). The strength of simulations lies in being able

to rapidly perform important parametric studies that allow for quick elimination of prototype designs which have a high probability of not satisfying testing criteria (Thacker et al., 1998; Kan et al., 1999).

2.2.3 Overview of FE Technology in Crashworthiness Analysis

The evolution of computational methods for crashworthiness and related fields are linked with the a) decreasing cost of computational resources and b) with improvements in computational methodologies. The latter include multi-time step integration (subcycling), further improvements in elements, adaptive meshes, and the exploitation of parallel computers (Belytschko, 1992).

Recent advances in computer software and hardware have made possible analysis of complex nonlinear transient dynamic events that were nearly impossible just a few years ago. In addition to the improvement in processing time, the cost of computer hardware has decreased an order of magnitude in just the last few years (Fasanella, and Jackson, 2002).

The increasingly rapid evolution of this field is a consequence of two factors:

a. The development of more powerful, theoretically sound algorithms for the simulation of nonlinear structural dynamics problems with severe deformations and other nonlinearities.
b. The rapid growth in the speed of computers and the consequent decrease in the cost of computational resources.

Computer programs for crashworthiness analysis were first developed in the late 1960's. Generally, a vehicle was modeled with five to fifty nodes and very simple elements were used. A noteworthy development in this direction was the development of a hybrid experimental simulation technique (Kamal, 1970). The properties of the elements were obtained using experimental testing of the components, and computer models were used to predict the performance of the complete vehicle for various speeds of impact. However, models of this type cannot be considered first-principles models, and are only suitable for the specific crash environment for which they were designed.

The next generation of crashworthiness codes tended to be first-principles codes, in that their elements embodied the mechanics of large deformation processes, though these were usually limited to beams (Thompson, 1972; Shieh, 1972; Young, 1972; and Melosh, 1972). One of their major shortcomings was their reliance on implicit time integration, which they undoubtedly adopted because of the prevalence of these techniques in general purpose finite element programs of the time. The use of implicit time integration made these computer programs very time-consuming, even for comparatively small models. Furthermore, these implicit techniques have a lack of robustness for highly nonlinear processes; they might fail to converge to a solution during a given time step.

In 1973, the National Highway Transportation and Safety Administration (NHTSA) began a program for the development of computer methods for crash simulation that would enable occupant safety to be established by means of simulation. The effort focused mainly on the adoption of the program WHAMS, which had been

developed for reactor safety studies (Belytschko and Marchertas, 1974). This computer program had originated in the field of weapons effects, where severe nonlinearities and large deformations are common place. Consequently, it used explicit time integration methods. This entailed the use of very small time steps in order to maintain numerical stability but provided a program with a robustness, which made the completion of simulations a simple task. The program, which evolved from these efforts, was called WRECKER (Belytschko et al., 1975; Welch et al., 1975) and its successors were used for a long time at various car manufacturing companies.

A parallel effort was the development of DYCAST at Grumman Aerospace Corporation. This program contained both implicit and explicit integrators; although the emphasis was on the latter. The Grumman team developed considerable experience in the simulation of frontal impact, and it simulated frontal crashes for a prototype of the de-Lorean, the 1984 Chevrolet Corvette (Winter et al., 1984), and the Dodge Caravan (Regan and Winter, 1986). Although these are not entirely first-principles models, in that they could not replicate sheet metal crushing with fidelity, comparison with tests show surprisingly good accuracy with errors in crush distances of only five percent (Regan and Winter, 1986).

The principal development during this time was the development of a new four-node quadrilateral element for thin shells, which required only one point quadrature per element (Belytschko et al., 1984). At the same time, the DYNA-3D program was developed which used explicit time integration and was completely vectorized to take advantage of the Cray computer architecture (Hallquist, 1983). It included both the shell

element (Hughes and Liu, 1981) and quadrilateral element (Belytschko et al., 1984); the latter being significantly faster. Benson, et al., (1986) reported that DYNA-3D calculations have been made with 20,000 shell elements and 120,000 degrees of freedom and required only two hours of simulation; whereas, an implicit calculation with only 2000 elements required over eight hours of simulation. The refinement of models that can be achieved with such tools, indicate that such models are much closer to the goal of achieving first-principle simulations of a vehicle crash than the models of the 1970's (Hallquist and Benson, 1986). Yet, important factors such as the suspension, engine block, and transmission were absent.

The analysis of interacting bodies, which includes the effects of both material nonlinearity and large deformations, has also received considerable attention during these years and has lead to the development of robust and efficient contact-impact algorithms (Lee and Kwak, 1984; Oden and Pires, 1984; Hallquist et al., 1985). Many improvements to this type of analysis have been made, and it is possible to effectively address a class of nonlinear systems and develop stable and accurate methods, which may be applied to general classes of problems.

Because of the lack of robustness of implicit time integration procedures for the complex phenomena that occur in car crashes, most of the currently used programs for car-crash simulation use explicit time integration. The drawback of this method is that a small time step must be used in order to meet the conditional stability. Thus, the presence of a few small elements in the mesh requires the entire mesh to be integrated with a very small time step. This problem was addressed using multi-time step integration where

different time steps can be used for different parts of the mesh (Belytschko, 1980; and Belytschko et al., 1985). In these methods, only the subdomains that contain the smallest elements are integrated with the smallest time step and a much larger time step can be used for the remainder of the mesh. Procedures have also been developed for the automatic selection of time steps so that the advantages of vectorization are not compromised and the overall stability of the process is ensured.

In particular, a general stability study was conducted using energy methods (Gravouil, and Combescure, 2001 and Combescure, and Gravouil, 2002). Actually, this method can be interpreted as a multi-time-scale method at the interfaces between subdomains (Gravouil, and Combescure, 2000). Furthermore, authors proposed an algorithm for implicit dynamics coupled with a multi-space-scaled method for some of the subdomains (Gravouil, and Combescure, 2003). In other terms, the goal was to arrive at a general algorithm for structural dynamics, which would effectively take into account the specific space and time-scale properties. These preliminary algorithmic choices were made with the intention of extending the method to non-linear problems.

2.2.4 Crashworthiness Experimental Testing

In spite of the tremendous progress achieved in crashworthiness simulations of vehicle structures from components to full-scale vehicles using the latest techniques in computational mechanics and supercomputers, final assessment still relies on laboratory tests. There are three categories of tests: component tests, sled tests, and full-scale barrier impacts. It is well documented that the complexity of the test and associated variables

increase from component to full-scale tests. This may cause a decline in test repeatability; this is a reality that may not become apparent from mathematical models.

Motor-vehicle structural models can be separated into three groups: generic components such as S-rails and rectangular tubes, actual isolated components such as upper rails, lower rails and hoods, etc., and subassemblies representing parts of the front structure. These components are typically tested in both quasi-static and dynamic modes to identify their crush performance. In dynamic testing, a drop-silo or sled is used. In drop-silo testing, the component is fixed to the ground on a load cell and loading is typically applied from the gravitational fall of a rigid mass onto the free end of the components.

In sled testing of components, the component is mounted horizontally onto the sled that is launched to impact a rigid or deformable surface with the component making first contact. The component test determines the dynamic response to loading of an isolated component. These component tests are crucial in identifying the crash mode and energy absorption capacity. Understanding their performance is also essential to the development of prototype substructures and mathematical models (Khalil and Vander Lugt, 1989; Jones, 1989; Sheh and Khalil, 1991).

The primary objective of a sled test is the evaluation of the occupant restraint. This is accomplished by high-speed photography of the dummy kinematics (Hoffman et al., 1990; and Khalil et al., 1995). In a sled test, a vehicle buck, representing the passenger compartment with all or some of its interior components, and restraint systems is used. Mechanical surrogates of humans (dummies) or cadaver subjects are seated in the

buck to simulate a driver and/or passenger and subjected to dynamic loads, similar to a vehicle deceleration-time pulse, to evaluate the occupant response in a frontal impact. The dummy's kinematics-deformation, velocity, acceleration, and associated forces and moments are measured to help determine the impact severity and the effectiveness of restraint systems in reducing loads transferred to the occupant.

For more complicated analysis of occupant and vehicle structural responses, mathematical models using either rigid-body-based program (MADYMO, 2004), or deformable-body-based non-linear FE codes such as (LS-DYNA, 1998; PAM-CRASH, 2001) are currently used among auto manufacturers in design of advanced / smart restraint systems for impact safety protection of occupants. In both the multi-body and FE simulations, the restrained occupants can contact the vehicle interior. To capture the motion of the occupant relative to the belt, FE seat belts are used. Contacts between the dummy models and the vehicle interior are defined by using multi-body-multi-body contacts and multi-body-FE contacts in MADYMO (Mathematic Dynamic Model) environment. Parameters for the appropriate contacts between the vehicle interior and dummy were extracted from MADYMO examples (Renfroe, and Partain, 2000).

Recently, a computer-based-simulation of the rollover crash using the MADYMO simulation tool was developed (Jiang, and Sturgess, 2007). The study was focused on investigating the vehicle dynamics and occupants kinematics during a front-crash-induced during the rollover. Simulation results from both the FE model and the rigid body model were validated and evaluated with a series of experimental testing, and good agreements were obtained crash.

To study the driver kinematics, an occupant compartment of a midsize sports utility vehicle (SUV) using MADYMO was created (Bedewi, et al., 2003). In this study the compartment model underwent a rollover motion, and it was concluded that the occupant kinematics is greatly affected by vehicle pre-roll and roll kinematics and, in driver-side leading rolls, the head velocity relative to the vehicle interior is significant. Hu and co-workers (Hu, et al., 2007; Neal-Sturgess, et al., 2007) also conducted rollover simulations with a variety of restraint methods, including seat-belts and/or an inflatable tubular structure. The effect of seat belts on occupant kinematics in rollover events was assessed, and the kinematics and injury risks of two kinds of occupant models were compared and evaluated. The importance of restraints in reducing occupant injuries in rollover was highlighted.

The typical full-scale barrier test involves collision of a guided vehicle, propelled into a rigid flat barrier, at a predetermined initial velocity and angle. A fully instrumented vehicle, with numerous load cells, accelerometers and instrumented dummy in the driver and passenger seats, are typically utilized in the tests. The barrier face is instrumented with several load cells to monitor the impact force-time history.

In addition to frontal crash tests, other tests have been developed to simulate side impact with a deformable barrier (Cheng, et al., 2001), rear impact (Zaouk et al., 2000), and roof crush models, respectively (Horstemeyer et al., 2007). Also car-to-car crash models have been simulated (Thomson et al., 2007). Other frontal impact models include oblique (+/- 30 degree) impacts with a rigid barrier, offset impact models with rigid or

deformable barriers with 40 to 50 percent overlap, vehicle-to-vehicle impact with full or partial overlap, and central or off-center impacts with a rigid pole (Cheng et al., 2001).

Such tests are not only time consuming, but also expensive, particularly at the early stages in vehicle development, where only prototypes are available. Government safety standards are set for passenger and commercial vehicles. Data available to the government in determining safety, specifically vehicle crashworthiness is obtained from physical crash tests. However, because the cost of a single crash test is approximately $25,000 (excluding the cost of the vehicle), comprehensive crash testing for every car manufactured would be extremely expensive (Zaouk, et al., 2000).

Typically, a barrier test uses a complete vehicle where safety engineers run this barrier test to ensure vehicle structural integrity and compliance with government-mandated regulations. In addition, full-scale tests are conducted on the vehicle's rear structure, either by a deformable barrier or by a bullet car to assess the integrity of the fuel tanks (Sheh et al., 1992; Calso et al., 1993; Kohlhoff et al., 1994; and Lin et al., 1995).

2.2.5 State of the Art in Crashworthiness Analysis

Today, explicit crash simulation codes are an essential part of virtual product development in the automotive industry. Crashworthiness analysis with explicit FE programs, such as LS-DYNA, has reached a very mature state. As a result, the number of real physical tests, in the automotive industry has been reduced considerably. Though the element formulation in the explicit programs has been mainly dictated by efficiency, the

quality of the results of today's standard crashworthiness analyses is very high and the demands, for further enhancements to the programs concerning the range of applications, are still increasing. The contribution (Schweizerhof, 2001) is focusing on element formulation, contact algorithms and modeling aspects. Current models in crashworthiness analysis contain well beyond 500,000 elements that may be a mix of shell elements, beam elements, 3-D solid elements, and many connection elements such as springs and dampers with nonlinear properties.

The element formulation was initially focused on reduced integrated elements with hourglass control (Belytschko and Tsay, 1983) even though the limits concerning kinematics have been known. However, the overall efficiency of these elements allowed analysis of models with difficult, yet realistic geometries. An additional advantage is that the Jacobian at the center (integration point) of the element almost never becomes indefinite, even for very large element distortions, so large deformation analyses have been possible even with fairly coarse meshes. After revisions of the original stiffness hourglass control concerning rigid body rotations, the Belytschko-Tsay shell element is still the tool for any larger analysis. The deformations in the so-called hourglass kinematics are controlled by computing the hourglass energy for each element. As a result, any undesired kinematics can be found easily. For such regions (hourglass kinematics, or undesired kinematics), fully integrated shell elements with assumed shear strain distribution can produce reliable results (Schweizerhof et al., 1999). This is contrary to the element formulation used by Bathe within implicit techniques for crash and impact analysis, (Bathe, 1998).

A large variety of material models covering elastic-plastic, viscoplastic, viscoelastic, composite, damage, failure, and nonlinear elastic with many variations can be chosen from the material library in LS-DYNA for the structural elements used in present vehicles. New material models can be developed and incorporated with ease.

Contact is the second dominating aspect in crashworthiness analysis as it is very important to capture the correct geometry during the structural collapse. These developments were focused on the following:

- The search for nodes in local proximity of contact
- The determination of forces on nodes in contact

In general, contact algorithms have two distinguishable parts, namely, search part and contact part respectively. Fully automatic searches, with fairly little computational cost, are available such that unclear situations at corners and edges are almost never encountered in fine models with the very small time steps used in explicit time integration. Detailed local searches and the storage of some localization properties for each contact segment also lead to accurate and fairly efficient algorithms concerning computational overhead and memory requirements. The addition of alternative algorithms, such as the Pinball algorithm (Belytschko and Yeh, 1993), further improves the efficiency of the search and the robustness in some situations, in particular, in combinations with the standard search algorithms.

The treatment of sliding and impact along interfaces has always been an important capability in the DYNA3D codes. Three distinct methods for handling this, which have been implemented, are referred to as the kinematic constraint method, the penalty method

and the distributed parameter method. Contact options in LS-DYNA treat interaction between different parts in a model. When different parts are interacting, forces appear in the contact interface. There are numbers of different contact options in LS-DYNA and the majority of them are based on the penalty method. The penalty method consists of placing springs between all penetrating parts and the contact surface. In this method the spring stiffness is determined by the size of the contact segment and its material properties. On the other hand, soft-constraint-based approach calculates the stiffness of the linear contact springs based on the nodal masses that come into contact and the global time step size. The resulting contact stiffness is independent of the material constants and is well suited for treating contact between bodies of dissimilar materials. The stiffness is found by taking the nodal mass divided by the square of the time step size with a scale factor to ensure stability (Bala, 2001).

Today, automatic contact definitions are commonly used. Accurate modeling of contact interfaces between bodies is crucial to the prediction capability of the finite element simulations. In this approach, the slave and master surfaces are generated internally within LS-DYNA from the geometry of the associated part given for each surface. For automotive crash models, it is quite common to include the entire vehicle in one single surface contact definition where all nodes and elements within the interface interact (Benson and Hallquist, 1990; Hallquist, 1990). Since, in crash analysis, the deformations can be very large and predetermination of where and how contact will take place may be difficult (Bala, 2001).

Over the decades, enormous progress has been achieved in both, the crash simulation methods and the CAE (computer aided engineering) programs used. Due to the high efficiency levels of the current computers and the use of available hardware, such methods are being applied on a widespread basis today (Schelkle et al., 2004). This applies to the whole range of options from the coupled / parallel sequential simulation of manufacturing processes to the cross-functional simulation, including efficient management systems designed to handle the entire CAE process (Koko, 2002).

In the early phases of automotive engineering, the development activities are mostly handled in a sequential manner (Schelkle, and Elsenhans, 2002). That is where the newly conceived CAD/CAE methods come in quite handy: they allow component geometries to be prepared on the basis of topologies and parameters and subsequent modifications to be implemented quite rapidly. This approach allows the inherent design potential to be fully opened up and thus the defined targets to be reached in the most optimum way. However, this requires combining parametric concept geometry with mathematical optimization method. Nevertheless, their wide-spread and consistent introduction into conceptual design is yet to come.

Improving the accuracy of virtual prototypes helps to shorten product development times and reduces the number of physical prototypes required. One way is to include the effects of forming in the material properties. The process of forming the component changes the properties of the material being used. This is generally ignored in the design and validation process of automotive structures even though the changes in material strength and thickness may be substantial. However, although the forming

effects on the performance of individual components have been reported in the literature (Fang et al., 1999; Hora et al., 2000; Dagson, 2001; Lanzerath et al., 2001), there are few papers reporting the consequence of including formed properties in full vehicle models (Dutton et al., 2001; Chen et al., 2002).

Including formed properties in vehicle body structure can have a considerable influence on collapse modes of these components and, importantly, a significant influence on the energy absorbed by surrounding components. Recently, the inclusion of formed properties applied to the development of advanced high strength steels, which leads to the development of the advanced material modeling techniques are used in crashworthiness analysis (Cafolla et al., 2004).

Recent development in computer hardware technology and software advancement has made it possible to develop large and detailed finite element models, which include vehicle structures, interior, seats, airbags, and hybrid III dummies, for crashworthiness evaluation. Today, computer simulation using finite element methods is a routine practice for engineers in design analysis, vehicle structural crashworthiness, and occupant protection assessments (Monclus-Gonzalez et al., 2000; Kan, et al., 2001; Pyttel et al., 2007).

2.3 Model Order Reduction Techniques

In the analysis of large structures, the substructural analysis frequently arises due to the repetition of identical assemblages (substructures) within a structure. A small reduction in the problem size can have a large effect on the storage and time requirements

of the problem. Traditional forms of substructuring, for static problems, employ static condensation to remove the degrees of freedom on the interior of the substructure.

In 1965, Guyan and Irons first proposed the condensation technique or simply static condensation for the elimination of unwanted degrees of freedom (Guyan, 1965; and Iron, 1965). Since its initial proposal, this technique has been widely used in many static and dynamic problems. However, because the inertia effects are ignored in this condensation, the accuracy of the resulting reduced model is generally very low for dynamic problems. To alleviate the limitations, the inertia effects could be partially or fully included in the condensation matrix. The corresponding condensation approaches are generally called dynamic condensation.

The performance of dynamic condensation is fully dependent upon the dynamic condensation matrix. There are three types of dynamic condensations:

- Single-mode-dependent dynamic condensation
- Multimode-dependent dynamic condensation
- Response-dependent dynamic condensation

Usually, the general eigenproblem of a full model, referred to as the full eigenproblem, is given by

$$(K - \lambda M)\varphi = 0 \tag{2.1}$$

where λ and φ are the eigenvalue and corresponding eigenvector of the full model, and K and M are stiffness and mass matrices respectively. The total degrees of freedom of the full model are divided into two categories: a) the master degrees of freedom and b)

the slave degrees of freedom. With this arrangement equation (2.1) may be rewritten in a partitioned form as

$$\left(\begin{bmatrix} K_{mm} & K_{ms} \\ K_{sm} & K_{ss} \end{bmatrix} - \lambda \begin{bmatrix} M_{mm} & M_{ms} \\ M_{sm} & M_{ss} \end{bmatrix}\right)\begin{Bmatrix} \varphi_m \\ \varphi_s \end{Bmatrix} = \begin{Bmatrix} 0 \\ 0 \end{Bmatrix} \tag{2.2}$$

where the subscripts m and s indicate the parameters corresponding to the masters and slaves respectively. A simple multiplication of the matrix on the left-hand side of equation (2.2) expands this equation into two equations, namely

$$(K_{mm} - \lambda M_{mm})\varphi_m + (K_{ms} - \lambda M_{ms})\varphi_s = 0 \tag{2.3}$$

$$(K_{sm} - \lambda M_{sm})\varphi_m + (K_{ss} - \lambda M_{ss})\varphi_s = 0 \tag{2.4}$$

The relation of the eigenvector between the masters and slaves can be obtained from equation (2.4) as

$$\varphi_s = R(\lambda)\varphi_m \tag{2.5}$$

where $R(\lambda) \in \Re^{s \times m}$ is called the condensation matrix and is defined as

$$R(\lambda) = -(K_{ss} - \lambda M_{ss})^{-1}(K_{sm} - \lambda M_{sm}) \tag{2.6}$$

Although the expression for the computation of the condensation matrix is given explicitly in equation (2.6), it is a nonlinear function of the unknown eigenvalue λ. Letting $\lambda = 0$ in equation (2.6), leads to the Guyan condensation matrix.

2.3.1 Single-Mode-Dependent Dynamic Condensation

The single-mode-dependent dynamic condensation matrix is defined as the relationship of an eigenvector between the master and the slave degrees of freedom.

$$\varphi_s = R(\lambda)\varphi_m \tag{2.10}$$

where, φ_m and φ_s are the subvectors of the eigenvector at the master and slave degrees of freedom, respectively and R is the dynamic condensation matrix (Guyan, 1965). The dynamic condensation matrix, R, is given explicitly in equation (2.6). The eigenvector of the full model can be expressed in terms of the eigenvector at the masters as

$$\varphi = T_G \varphi_m \tag{2.7}$$

where, T_G is the coordinate transformation matrix or global mapping matrix, $T_G \in \Re^{n \times m}$. T_G relates the responses at all degrees of freedom to those at the masters and is defined as

$$T_G = \begin{bmatrix} I \\ R_G \end{bmatrix} \tag{2.8}$$

where, I is an $m \times m$ identity matrix, and $R_G \in \Re^{s \times m}$ is called the condensation matrix and is defined as

$$R_G = -K_{ss}^{-1} K_{sm} \tag{2.9}$$

The dynamic condensation matrix depends on the mode. Different modes may have different dynamic condensation matrix and, as a result, a different reduced model. The reduced model is frequency-dependent and, as a result, a special eigenvalue solver is generally required.

2.3.2 Multi-Mode-Dependent Dynamic Condensation

The multimode-dependent dynamic condensation matrix, R, is defined to relate, the multi-eigenvectors, p, between the master and slave degrees of freedom (Kammer, 1987; and O'Callahan et al., 1989), that is,

$$\Phi_{sp} = R\Phi_{mp} \tag{2.11}$$

where, R is the dynamic condensation matrix, Φ_{sp} is the submatrix of the selected eigenvectors at slave and Φ_{mp} is the submatrix of the selected eigenvectors at master, respectively. Using this definition, the dynamic condensation matrix can be directly obtained if these eigenvectors of the full model are available, that is,

$$R = \Phi_{sp}\Phi_{mp}^{+} \tag{2.12}$$

where, Φ_{mp}^{+} is the generalized inverse of matrix Φ_{mp} and is defined as

$$\Phi_{mp}^{+} = (\Phi_{mp}^{T}\Phi_{mp})^{-1}\Phi_{mp}^{T} \tag{2.13}$$

2.3.3 Response-Dependent Dynamic Condensation

The response-dependent dynamic condensation matrix is used to define the relationship of responses between the master and slave degrees of freedom (Qu, 1998), that is,

$$X_s(t) = RX_m(t) \tag{2.14}$$

where, X_m and X_s are the response vectors at the master and slave degrees of freedom, respectively. In this procedure, the system response is simulated using any accurate time

integration scheme. The displacement response vector, at all degrees of freedom, is then sampled at a series of different times during the simulation. The dynamic condensation matrix is then computed from these sampled response vectors. Since the reduced model has m degrees of freedom, the equation represents the relationship of responses contributed by m modes. As a result, this relation is approximate even when the reduced model is exact.

Based on the type of information required to compute the dynamic condensation matrix, the dynamic condensation methods can be categorized as:

- Physical-type dynamic condensation
- Modal-type dynamic condensation
- Hybrid-type dynamic condensation

2.3.4 Physical-Type Dynamic Condensation

In the physical-type dynamic condensation methods, only the system matrices, stiffness and mass matrices, for example, of the full model are directly required in computation. If the modal parameters, particularly the mode shapes of full model, are included in the dynamic condensation matrix, the method is called modal-type dynamic condensation. In hybrid-type dynamic condensation approaches, both the physical parameters and the mode shapes of the full model or slave model are used (Craig and Bampton, 1968; Leung, 1978; and Paz, 1984).

A model reduction technique is usually introduced to reduce the size of the full model and leads to a reduced order model. The dynamic equilibrium condition in

structural dynamic analysis is generally written as a set of linear second-order differential equations

$$M\ddot{X}(t)+C\dot{X}(t)+KX(t)=F(t) \tag{2.15}$$

where M, C and $K \in \Re^{n\times n}$ are the mass, damping and stiffness matrices of the full order model, respectively. In addition, $\ddot{X}, \dot{X}$, and $X \in \Re^{n}$ are the acceleration, velocity and displacement response vectors, respectively, of the full model under the external loads. It is assumed that the total degrees of freedom (n) of the full model are divided into the masters (m) and slaves (s) degrees of freedom. With this division, equation (2.15) can be rewritten in a partitioned form as

$$\begin{bmatrix} M_{mm} & M_{ms} \\ M_{sm} & M_{ss} \end{bmatrix}\begin{Bmatrix} \ddot{X}_m \\ \ddot{X}_s \end{Bmatrix}+\begin{bmatrix} C_{mm} & C_{ms} \\ C_{sm} & C_{ss} \end{bmatrix}\begin{Bmatrix} \dot{X}_m \\ \dot{X}_s \end{Bmatrix}+\begin{bmatrix} K_{mm} & K_{ms} \\ K_{sm} & K_{ss} \end{bmatrix}\begin{Bmatrix} X_m \\ X_s \end{Bmatrix}=\begin{Bmatrix} F_m(t) \\ F_s(t) \end{Bmatrix} \tag{2.16}$$

where

$M_{mm}, C_{mm}, K_{mm} \in \Re^{m\times m}$; $M_{ms}, C_{ms}, K_{ms} \in \Re^{m\times s}$; $M_{sm}, C_{sm}, K_{sm} \in \Re^{s\times m}$ $M_{ss}, C_{ss}, K_{ss} \in \Re^{s\times s}$

; $\ddot{X}_m, \dot{X}_m, X_m, F_m \in \Re^{m\times m}$; and $\ddot{X}_s, \dot{X}_s, X_s, F_s \in \Re^{s\times s}$.

In equation (2.16), M_{mm}, C_{mm}, and K_{mm} are the mass, damping and stiffness matrices of the reduced model, respectively. Many model reduction schemes involve the form of coordinate transformation in the following form:

$$X(t)=TZ(t) \tag{2.17}$$

where, $T \in \Re^{n\times m}$ is the coordinate transformation matrix and $Z \in \Re^{m}$ is the reduced order coordinates. The transformation matrix, T, is generally time-invariant. As a result, the differentiation of Eq. (2.17) with respect to time becomes

$$\dot{X}(t) = T\dot{Z}(t) \tag{2.18}$$

$$\ddot{X}(t) = T\ddot{Z}(t) \tag{2.19}$$

Introducing Eq. (2.17) through (2.19) into Eq. (2.15) and premultiplying both sides by the transpose of transformation matrix T leads to

$$M_R\ddot{Z}(t) + C_R\dot{Z}(t) + K_R Z(t) = F_R(t) \tag{2.20}$$

where M_R, C_R and $K_R \in \Re^{m\times m}$ are the mass, damping and stiffness matrices, respectively, of the reduced model, and F_R is the equivalent force vector acting on the reduced model. They are defined as:

$$M_R = T^T MT \tag{2.20a}$$

$$C_R = T^T CT \tag{2.20b}$$

$$K_R = T^T KT \tag{2.20c}$$

$$F_R = T^T F \tag{2.20d}$$

Equations (2.20) are the reduced dynamic equations of equilibrium. Although the size of the reduce model is much smaller than the full model, the dynamic characteristic of the full model, within the interested frequency range, may be retained in the reduced model.

In the physical coordinate model reduction, the reduced model is obtained by removing part of the physical coordinates of the full model. Thus, the coordinates of the reduced model actually belong to a subset of a full model. This is the most straightforward model reduction among the three categories. The physical coordinate reduction is usually called dynamic condensation and its coordinate transformation matrix takes the form

$$T = \begin{bmatrix} I \\ R \end{bmatrix} \tag{2.21}$$

where I is an identity matrix of order m and, R, is the dynamic condensation matrix (Ramsden and Stoker, 1969; Levy, 1971).

2.3.5 Modal-Type Dynamic Condensation

All the coordinates that are not physical coordinates are generally referred to as generalized coordinates. The modal coordinate and the Ritz coordinate are two types of frequently used generalized coordinates. Modal coordinate reduction is one of the classical methods of the generalized coordinate reduction (Wilson et al., 1982; Nour-Omid and Clough, 1984; Akgun, 1993; Qu, 2001;). The dynamic response of an n degree-of-freedom model in the physical space X can be expressed in terms of the modal coordinates in modal space q_m such that

$$X = \phi_m q_m \tag{2.22}$$

In equation (2.22), $\phi_m \in \Re^{n \times m}$ is the eigenvector matrix corresponding to the full model. Each column of the matrix is an eigenvector or mode shape. Depending on the frequency spectral of exciting forces, the (m) modes maybe taken from the lowest frequency range or any interested frequency range or any interested modes of the full model. Substituting equation (2.22) into equation (2.15) and premultiplying it by the transpose of the eigenvector matrix gives:

$$M_r \ddot{q}_m + C_r \dot{q}_m + K_r q_m = F_r \tag{2.23}$$

where M_r, C_r and K_r are the modal mass matrix, modal damping matrix, and modal stiffness matrix respectively.

2.3.6 Hybrid-Type Dynamic Condensation

Component mode synthesis (CMS) is one of the most popular hybrid coordinate reduction schemes in which the reduced model consists of some physical coordinates and some modal coordinates. The coordinate transformation has the following form

$$T_{CMS} = \begin{bmatrix} \phi_N & R_G \\ 0 & I \end{bmatrix} \tag{2.24}$$

CMS is a method of dynamic analysis for structures having a large number of degrees of freedom. These structures often require lengthy computation times and large computer memory resources. In CMS, a structure is divided into independent components in which the degrees of freedom are defined by a set of generalized coordinates defined by displacement shapes. The displacement shapes are used to transform the component property matrices and any applied external loads to a reduced system of coordinates. Any obtained results are back transformed to the original component coordinate systems.

Generally, component mode synthesis can be categorized into three methods:

- Fixed-Interface method
- Free-Interface method
- Hybrid method

Depending upon the mode shapes used to define substructure coordinates, they are obtained with masters fixed, free or a combination thereof (Hurty, 1965; Goldman,

1969; MacNeal, 1971; Dowel, 1972; Rubin, 1975; and Craig, 1981). The component mode synthesis has the following advantages:

- The computational effort and computer storage can be saved significantly
- The CMS technique makes it possible that different components of a structural system may be analyzed by different groups, at different places, and at different times
- The structural dynamic modification and optimization become easier
- The technique allows a hybrid modelling scheme to be implemented

One feature of component mode synthesis is that partial modal coordinates are used, in place of the physical coordinates, to represent the substructures. These modal coordinates must be transformed to physical coordinates in order to assemble the substructure matrices into global matrices by means of equilibrium and compatibility conditions. The physical-type dynamic condensation is generally more computationally efficient than the other two. This type of approach maybe implemented into the eigenvalue analysis of a large-size model. However, the accuracy or convergence rate depends on what and how many degrees of freedom are selected as the master degrees of freedom. Although the accuracy of the reduced model obtained from iterative dynamic condensation approaches is not dependent on the selection, the proper selection of master degrees of freedom does accelerate the convergence (Friswell et al., 1995).

The reduced model resulting from the modal-type dynamic condensation preserves all the modes. These modes may be at any frequency range of the full model or totally arbitrary. Because this reduction is exact, the selection of master degrees of

freedom does not affect the accuracy of the reduced model provided that the selected modes are observable at the master degrees of freedom. Generally, the number of the selected modes is smaller than that of the master degrees of freedom (Gu and Hulbert, 2000).

The disadvantages that limit the usage of this method are as follows:

- The eigenvectors of the full model should be available before the reduction is performed. This is computationally expensive.
- When the number of selected modes (p) is equal to the number of master degrees of freedom (m) and these modes are all observable, the reduced system matrices have good properties. However, this will be a very heavy burden to obtain that number of modes of a full model because the number is generally large.
- When the number of the selected modes is less than the number of master degrees of freedom, the reduced system matrices defined by SEREP (system equivalent reduction expansion process) are rank deficient and the order ($m - p$) modes of the reduced model are undetermined. This leads to difficulties in further dynamic analysis since the reduced model usually contains m modes and the accuracy of the ($m - p$) higher modes are low (Berkkan and Dokainish, 1990).

The hybrid dynamic condensation technique is supposed to overcome some of the shortcomings of physical-type and modal-type dynamic condensation. However, most hybrid dynamic condensation approaches, available in the literature, do not have good performance. For structural systems that have a large number of degrees of freedom or have components designed by different groups or organizations, the Craig-Bampton

(Craig and Bampton, 1968) method has been proven to be accurate, efficient, and economical. However, in the modal testing, the accelerometers cannot be mounted on these modal coordinates. Therefore, there is a need to develop a transformation matrix that could convert the modal coordinates back to the physical coordinates (Yee, 1990). As a result, the reduced model has only physical coordinates.

2.3.7 Application of Substructuring in Crashworthiness Analysis

The design of automotive structure is generally driven by the use of best practices, and the actual crash performance is known only after completing the detailed design. Different modeling techniques with varying degree of details are available in the literature for the analysis of automotive crash behaviour (Markiewicz et al., 2001; Pipkorn, 2002). These modeling techniques were developed to drastically reduce the size of FE model and the CPU computing time, while preserving a sufficient degree of accuracy for an efficient selection between different designs. The reduced-order model is computationally efficient due to the computational time and cost. However, the reduced model no longer contains all the information due to the elimination of degrees of freedom. Also, the dynamic response corresponding to the mechanical properties of the reduced model is altered.

In addition to the above approaches, other techniques were also developed mostly to guide designers in the early stages when a decision has to be made from fairly large number of ideas (Kim, et al., 1997; Moumni, and Axisa, 2004; Deb, and Ali, 2004; Kim,

et al., 2007; Marur, and Srinivas, 2008). These techniques were mainly used to improve design modifications, although, each proposed technique has a different objective. Design-oriented simulation techniques for predicting crash behaviour were also used for complementing experimental testing. This is performed prior to the testing of the entire vehicle structures. In preliminary design cycles, where design modifications often takes place, the aforementioned methods could save cost and time, prior to the experimental verification of the proposed design. However, these techniques lack experimental application, when this component is tested in isolation. This is mainly due to the different boundary conditions, loading conditions, and various interactions between different structural component/s. In most cases, the model parameters are adjusted to match corresponding experimental results. This contradicts the actual purpose of the simulation, which is to predict the experimental results (Mkrtchyan et al., 2008).

2.4 Research Justification

In the automotive industry, the manufacturers have to comply with strict regulations concerning crashworthiness of their vehicles. This motivates a large amount of effort devoted to perform numerical simulations and laboratory crash tests that aim at gathering knowledge for further improvements in vehicles. Due to the complexity of the structures involved, a large number of degrees of freedom (DOF) are necessary for developing the FE models used in crashworthiness applications. The dynamic equations produced by such models are integrated using appropriate time stepping techniques.

In general, computations are based on three-dimensional finite element models. As a consequence, the time resolution of the simulation is not controlled by the physics of the problem but by the size of the smallest element of the mesh. Therefore, it is generally agreed that if such highly refined and costly models are of major interest to qualify an advanced design, they still are inconvenient for performing the parametric studies needed to guide the choice between various designs.

Inconvenience arises as the consequence of at least two major points, which are briefly summarized as follows. First, a single simulation of a given model requires a large computer and considerable CPU time, providing a large amount of data, which then have to be further, processed in a selective way. Second, the finite element model cannot be easily modified to allow changes in the design of some components, except if substructuring techniques are used, which is scarcely the case in automotive industry (Moumni, and Axisa, 2004). In addition, the current understanding of the impact properties of systems that consist of energy-absorbing materials and structures, as well as the influence of interactions between the constituent structures, is also limited (Mkrtchyan et al., 2008).

Despite the great progress in substructuring using the finite element method, there is still a need to develop the methodology that enables one to overcome some of the issues that are inherent with the experimental testing of substructures in isolation. In this work, a new technique is proposed a technique that not only can be implemented into the FE method but also can be applied to experimental testing.

Various types of experimental tests regarding component(s) can determine the dynamic response to loading of an isolated subcomponent. However, the results obtained in subcomponent testing are not indicative of their response when they are in full model (see sections 2.2.4 and 2.3.7 for references). Therefore, there is a need to develop an experimental technique to study the substructure response in isolation. This work aims to address this issue and outlines the technique that allows for substructural testing experimentally. This method will eliminate the need for full scale testing when the mechanical behaviour of a substructure within the full system is of interest.

Finite element analysis and experimental testing as currently being performed can only provide information on system and its subsystem in terms of energy absorption and deformation modes. However, if any changes needed to be done, whether to improve the existing design or to meet the mandatory requirements, the entire system has to go through numerous testing (finite element analysis and experimental testing). In addition, the existing literature surveys have not addressed this problem yet. The existing techniques, which although have proven to be successful in many areas, have shortcomings when dealing with modifications to the subsystems. This study was motivated to perform (numerical and experimental) analyses on subsystems with the inclusion of the influence of the surrounding subsystems to the subsystem of interest. In other words, this new technique allows the numerical and experimental crash testing of subsystem in isolation such that the subsystem of interest behaves as if it is testing in the entire system.

Chapter 3

Finite Element Analysis of Structural Components

3.1 Introduction

In large complex engineering systems, often only a subsystem or a small part of the system design needs to be modified to adapt or improve performance in some way. For example, to improve frontal crash safety in an automobile, an engineer might focus design changes on only the vehicle's lower compartment rails and the bumper. In most cases of design for crashworthiness, the subsystem behaviour is strongly coupled to that of the overall system in such a way that even small changes to the subsystem can strongly effect the interactions between the system and the subsystem.

This study was initiated by Freedom Motor LTD to perform analysis on redesigned vehicle's floor of minivans for wheelchair accessibility. In order to perform the task, the original floor of minivan is removed and replaced by a wheelchair ramp and accessories. These types of structural change warrant the need for dynamic testing of the modified vehicle. This work involves a study of the subsystem's dynamic response (in this case modified floor), and its overall effects on the system (in this case vehicle) response. Figure 3.1 depicts the mini-van (approximate FE model) of the Dodge Caravan.

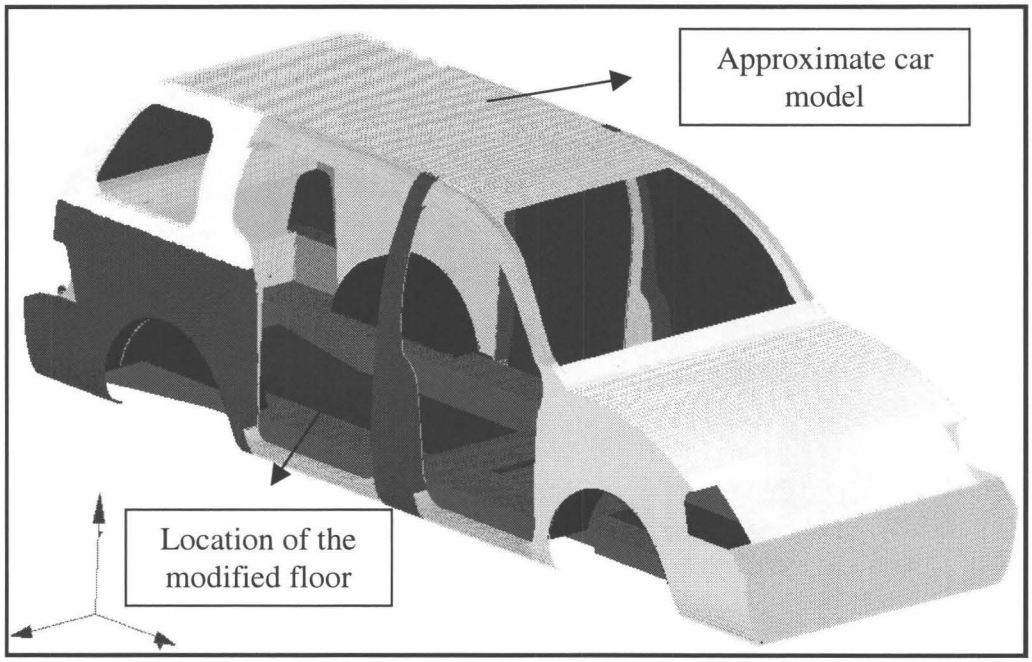

Figure 3.1: Approximate FE model of the mini-van (Dodge Caravan)

In this particular application, the main activity is to modify the design of a vehicle in order to provide accessibility to wheelchair occupants. These modifications are generally applied to two types of mini-vans (Dodge Grand Caravan and Ford Free Star passenger minivan) from leading vehicle manufacturers. The modifications include lowering the centre portion of the floor from the rear door to the rear of the front seat, installation of an access ramp, and securing the wheelchair and its occupant to the vehicle. Since relatively low volumes of production (mini-vans) involve this modification, it is preferable to use stock materials and fittings wherever possible in the design.

Because of the advances made in numerical techniques, analysts have turned to numerical simulation to predict the approximate crash characteristics of a design.

However, any changes to a subsystem warrant the simulation of the entire model all over again. This is computationally and financially expensive. Consequently, vehicle crash predictions are usually obtained by considering the vehicle as a collection or system of interfacing components and subsystems that interact with one another. This involves judgement in isolating regions where crush or energy absorption is anticipated to be significant and is expected to influence the crash performance of the vehicle as a whole.

This chapter is divided into two main sections and each section introduces different finite element models. The first finite element analysis was performed to examine the crashworthiness of the wheelchair accessible floor. The FE results could not be verified experimentally since the existing numerical technique (explicit code using LS-DYNA) only applies to a subcomponent (one component of the entire structure). In other words, the experimental application would have been only possible through experimental testing of the entire car.

The second finite element analysis was performed on the simplified version of the floor. This model was considered for experimental testing but the numerical techniques for testing the isolated subcomponent (using explicit code LS-DYNA) is not applicable to the physical world. In other words, the interface nodes and the corresponding constraints on the single isolated component can not be determined, when single isolated component is tested experimentally. Therefore, the experimental application of the single isolated component can not be achieved. In addition to the aforementioned limitations, the single isolated component needs to be altered using additional components to correspond to the

loss of constraints at attached locations. Thus, a third finite element component was modeled in lieu of developing a technique that makes experimental application possible.

The finite element analysis for each FE model was performed in two stages: full-model simulation and sub-model simulation. At each stage, the subcomponent response was determined from a full-model analysis and then compared to the subcomponent response in a sub-model analysis. In the first two sections, the LS-DYNA subcomponent testing capability is used to determine the subcomponent performance in isolation. The development of the new methodology for performing impact analyses on a structural component that lends itself to experimental testing that is explained in Chapter 4.

3.2 Finite Element Analysis of the Wheelchair Flooring Design

3.2.1 Subcomponent Model Construction

The objective of this finite element analysis was to determine the response e.g., (displacements, velocities and accelerations) around the boundary of the subcomponent so that these boundary conditions could be applied to the subcomponent in isolation. In other words, if a design change is required for the subcomponent (the wheelchair accessible floor), the entire floor need not be tested and only the redesigned subcomponent needs to be analyzed.

Generally, detailed information with respect to motor vehicles is not available in the public domain since the design details of a particular car are proprietary information.

As a result, reverse engineering was used to develop an FE model that would represent an actual car. The model development required both vehicle tear-down and digitization and model generation. The objective of the tear-down and digitization is to characterize the geometry of the structural components that have a significant effect on the crashworthiness of the vehicle (Kirkpatrick, 2000). In this work, the geometry of the vehicle exterior and floor was digitized, using a portable 3D coordinate measurement instrument. A large portion of the vehicle components was not accessible for digitization in their original position, and this limited the digitization of the entire vehicle.

At first, the solid model of a Chrysler mini-van (2006 Dodge Grand Caravan) was constructed from CAD data (an approximate model). The vehicle was modified to make the car wheelchair accessible. The commercial finite element program HYPER-MESH (a FE pre-processor) was used to construct a pre-analysis model of the redesigned floor (hereafter referred to as a substructure). The model was meshed using 4-noded Belytschko-Tsay shell elements, with three integration points through thickness (Belytschko et al., 1984). The entire structure was comprised of 40 components and 31229 shell elements. The connections between various parts were made using rigid elements, which constrained the displacements and rotations in all directions at the connection nodes, to simulate the original fastening configuration.

In the rear impact analysis, the vehicle was initially at rest and a rigid wall moving with a prescribed velocity was made to impact the vehicle. Figure 3.2 depicts the mini-van and the redesigned floor. This figure is presented for illustrative purposes and only shows the wheelchair accessible floor within the mini-van.

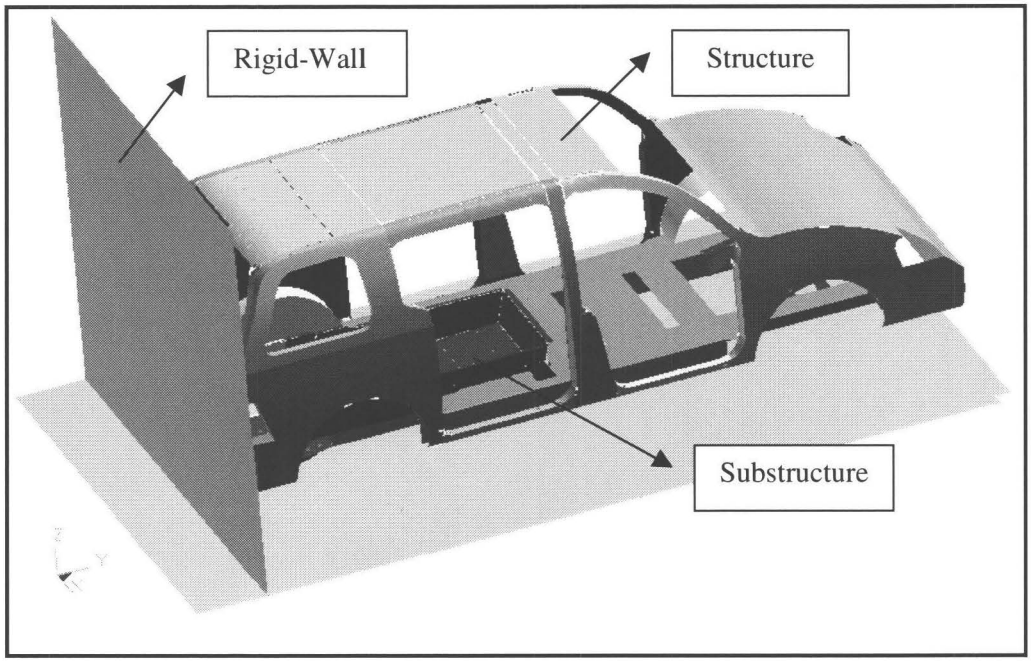

Figure 3.2: Schematic of the car body and modified substructure

Because of limited information regarding CAD data, kinematics of the floor, material properties, and lack of the data with respect to other components of the mini van (as shown in Figure 3.2), analysis was performed only on the floor substructure. Initially, the substructure (floor) was removed from the vehicle and analysis was performed on the substructure in isolation. The substructure model was comprised of different components that are connected to each other to achieve its functional form. That is, for the purpose of exploring methods, the floor substructure is redefined to be the main structure, and subcomponent of the floor (in this case the right side rail) is taken as substructure. In the following, the analysis is focused on studying this structure (as shown in Figure 3.3) and its subcomponents.

In the preliminary work, the FE analysis was performed on the redesigned floor to determine the response of the substructure in full impact analysis (as shown in Figure 3.2). The structure comprised of 11 components, namely, right-rail, left-rail, front-floor, rear-floor, and seven square reinforcing bars. The right-rail (refer to Figure 3.2) for subsequent analysis was arbitrarily selected as a subcomponent, which was considered to be analyzed in isolation.

These analyses were performed in two stages as follows:

1) Full model simulation
2) Isolated model simulation

From full model analysis in stage 1, the nodal displacements corresponding to all the nodes around the boundary of right-rail (subcomponent and the boundary nodes as shown in Figure 3.3) were extracted. In stage 2, these nodal displacements as a function of time were used as prescribed boundary values to perform analysis on the right-rail in isolation. Note that the displacement as a function of time cannot be physically applied in an experimental set up. This is the shortcoming that will be addressed by a technique that is presented in Chapter four.

The entire structure was made from structural steel AISI 1010 and appropriate material properties were incorporated into the finite element model. The elasto-plastic behaviour was modeled using MAT-24 (Hallquist, 2003). This material model has the following properties; mass density ρ = 7830 [kg/m^3], Young's modulus E= 207 [GPa], Poisson's ratio ν = 0.3, and Yield stress σ_Y = 173.28 [MPa]. The FE model was meshed using 4-noded quad (Belytschko-Tsay shell element) with three integration points

through thickness and 3-noded triangle shell elements, (Maker, and Zhu, 2000). The element formulation # 2 was used with shear factor of 0.833. The hourglass option was invoked to account for hourglass viscosity type in control energy option card.

Figure 3.3 depicts the FE model of the redesigned minivan floors (previously named substructure as shown in Figure 3.2).

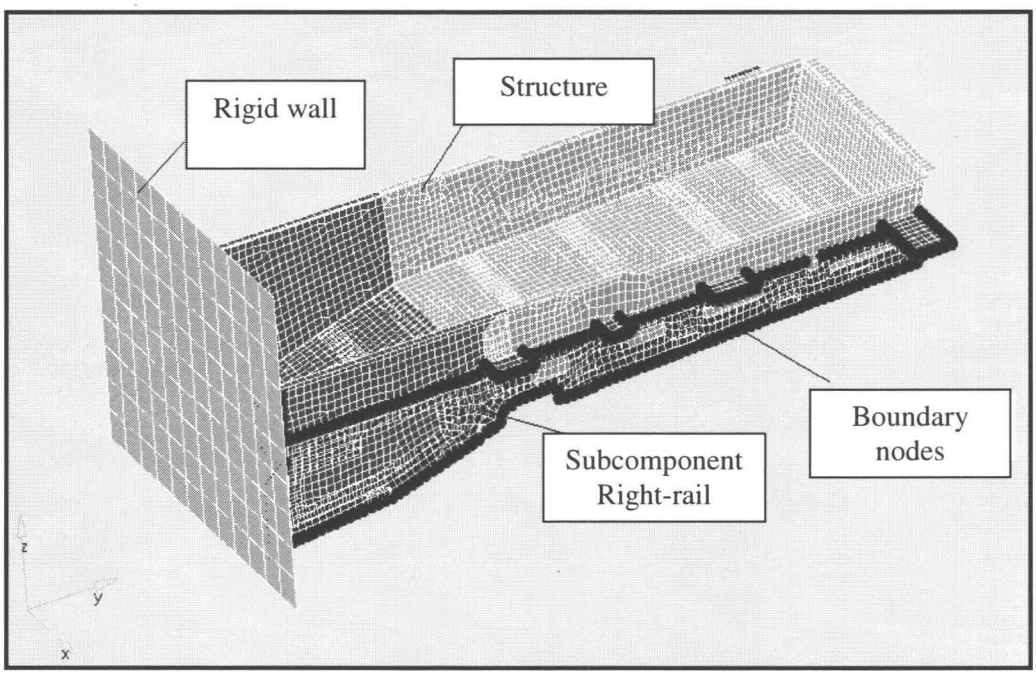

Figure 3.3: Schematic of the structure and boundary nodes around the substructure

3.2.2 FE Analysis of the Modified Floor

As indicated, previously these types of analyses are performed in two stages and are regularly performed on subcomponent(s) in isolation; however, the rigid wall is not taken into account when performing subcomponent analysis in isolation. The accuracy can be greatly improved upon selecting sufficient number of nodes around the boundary

of the isolated subcomponent. Here, all the nodes around the boundary of the isolated subcomponent were taken into account.

In this analysis two contact types were used namely, Automatic Single Surface and Automatic Surface to Surface. The Automatic Single Surface contact was used for each component of the structure to avoid penetration of components into each other. This contact definition requires the thickness of the shell elements to be taken into account. The Automatic Surface-to-Surface contact option was used to define contact regions for impact. The contact nodes on the slave side are first checked for penetration through the master surface and then the master nodes are checked for penetration through the slave surface. In this analysis the default contact parameters were used.

After performing impact analyses on the redesigned mini-van floor (Figure 3.3), the right-rail was isolated to perform subsequent subcomponent analysis. The main objective was to simulate the exact deformation for the isolated part (right-rail) using all the nodes around the boundary of the right-rail such that the selected component deformed in a similar fashion for both cases. To achieve this, around the boundary of the right-rail, a set of nodes was defined that contained the time history of the nodal displacements and nodal velocities. Since the boundary conditions on the isolated part were exactly the same in terms of nodal displacements, all aspects of FE analysis were in excellent agreement with each other.

As indicated before, these types of analyses are often performed in large finite element applications where the response of isolated parts or subcomponents is of the primary interest. The computational time of the full-model impact analysis was 6.48 min,

and computational time of the sub-model analysis was 23 sec. As can be seen from these results, the computational time was reduced significantly for the sub-model analysis compared to the full model analysis. The total computational time relates to three main factors as follows:

- Number of elements in the mesh
- Time step size
- Contact.

The number of elements in the full model FE analysis was 10701 and in the sub model analysis was 826. This is one of the major factors that caused the run time to be reduced by almost 17 times for the sub model analysis. Another factor was the size of the shell element in both the full and sub model simulations that controlled the analysis time step size. The time step size for the full model and sub model analyses were determined to be 4.13e-07 sec., and 1.71e-06 sec., respectively. The third factor was the contact, which reduced the computational time by almost 25%. However, the sub model simulation was performed without using any surface contact, since the deformations mapped from the full model onto the sub model.

All of the aforementioned factors collectively reduced the CPU time for the sub model simulation. Also, the quick determination of the response led to faster decision-making when design modifications were considered for evaluating the new design. In this analysis, all the nodes were selected around the boundary of the isolated subcomponent, and components of the nodal displacement and velocities were the same. This resulted in identical resultant displacements and resultant velocities for both FE models.

These types of analyses can be applied to subcomponents without any limitation in terms of the shape of the geometry. In this method, much the same way as other methods, the second stage of the analysis is completely dependent on the first stage analysis. Although the geometry of this model corresponds to an actual application, the physical size makes experimental comparison difficult and costly. Therefore detailed quantitative results are not pursued any further for this model.

One major shortcoming of this method of subcomponent (right-rail in isolation) analysis, however, is the fact that a subcomponent (right-rail) can be analyzed in isolation and a collection of components that form a substructure cannot be analyzed. Additionally, the wall effect is not considered in sub-model analysis. The second stage analysis is totally depend on the nodal boundary values, which form the boundary of the isolated subcomponent, and therefore limits itself only to the nodes that values are known in advance. The applied technique is only valid within FE analysis, and cannot be performed experimentally. As a result, experimental testing of an isolated subcomponent needs a different approach.

3.3 Finite Element Analysis of Modified Design

3.3.1 Model Formulation

Because of manufacturing cost and time associated with preparing experimental test specimens, the previous structure (as shown in Figure 3.3) was replaced with a

simplified version consisting of one floor, two rails, and three reinforcing bars. The components of the modified structure were assembled and connected to each other using plug-welds. The structure was made from mild structural steel (AISI 1010) and their appropriate material properties were incorporated into the FE analysis. The structure consists of three stiffening bar, two rails, and one floor and their corresponding dimensions are 596.03 by 76.20 by 6.35 mm, and 1219.18 by 48.42 by 3.55 mm, and 1219.19 by 609.60 by 3.17 mm respectively. Figure 3.4 depicts the schematic of the new design with its components.

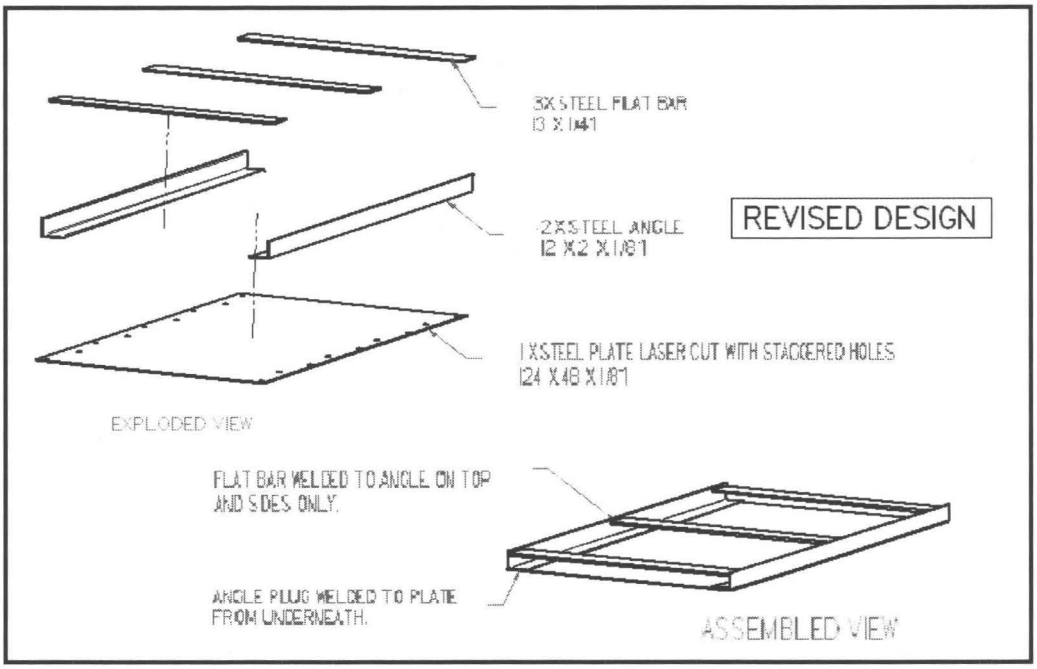

Figure 3.4: Schematic of the modified structure and its components

The finite element model was constructed from CAD data using the commercial software pre-processor (HYPER-MESH) and the FE model was exported into processor (non-linear explicit code LS-DYNA) to perform impact analysis. The elasto-plastic

behaviour was modeled using (Material type 24 in LS-DYNA) from the material library. This material model was used for the structural components, with the following nominal values: mass density ρ = 7830 [kg/m^3], Young's modulus E= 207 [GPa], Poisson's ratio ν = 0.3, and Yield stress σ_Y = 173.28 [MPa].

The data for the true-stress versus plastic-strain test were used for mild steel and incorporated into the material models for structure. Figure 3.5 depicts the stress-strain relationship for this material. These stress-strain points were obtained from available material data, and used with material type MAT-24 (Sadagopan, 2003). These types of simplification for material properties and behaviour made the analysis computationally efficient. The strain rate effect was not considered for this analysis (Sadagopan, 2003).

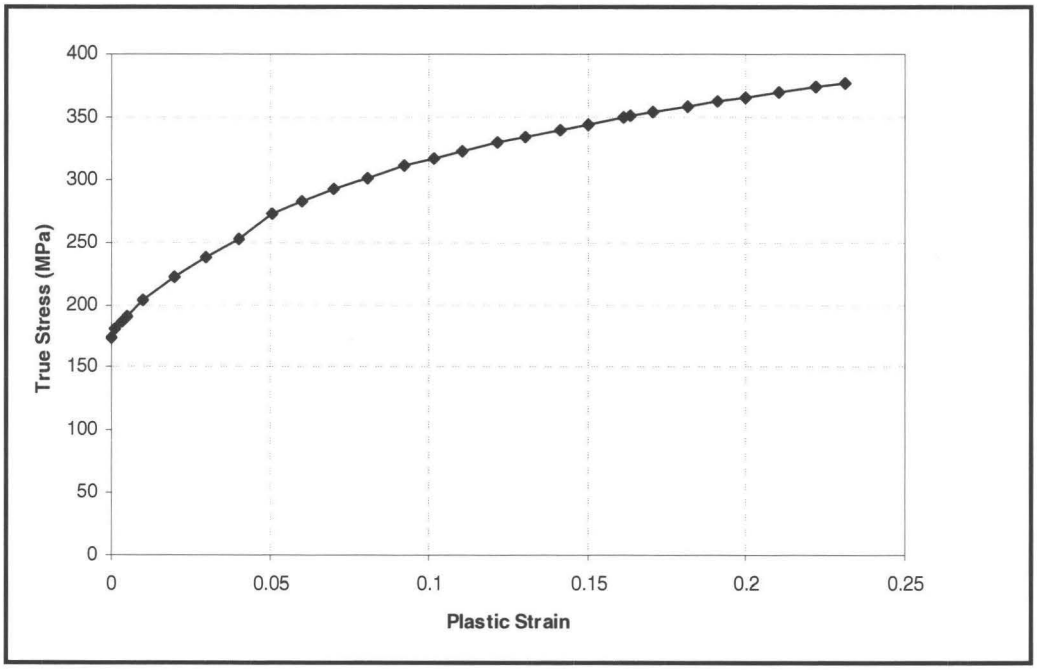

Figure 3.5: Effective stress vs. plastic strain curve for structural components

The model was meshed using 4-noded quad shell elements (Belytschko-Tsay shell element), with three integration points through thickness. Element formulation option was activated with the viscosity type hourglass control option. The element formulation [ELFORM] was # 2, with shear factor [SHRF] 0.833. The hourglass modes were determined by activation of [HGEN], in control energy command.

The FE model consists of 5758 nodes, and 5312 elements respectively. The Element formulation [ELFORM], and shear factor [SHRF] were the same for all the parts. The termination time was set to 0.1 sec., and the time step for performing analysis was determined to be 1.22127E-06 sec. The time step is determined automatically by the software based on the size of the smallest shell element in the mesh. The control time step card was also activated, and default values for initial time step size [DTINIT], and scale factor for computed time step [TSSFAC] were used. In this analysis, a total of 84 rigid elements were used to connect various components to each other to represent weld connections; connections were made every 304.8 mm. Figure 3.6 depicts the finite element model, its components, and the rigid wall.

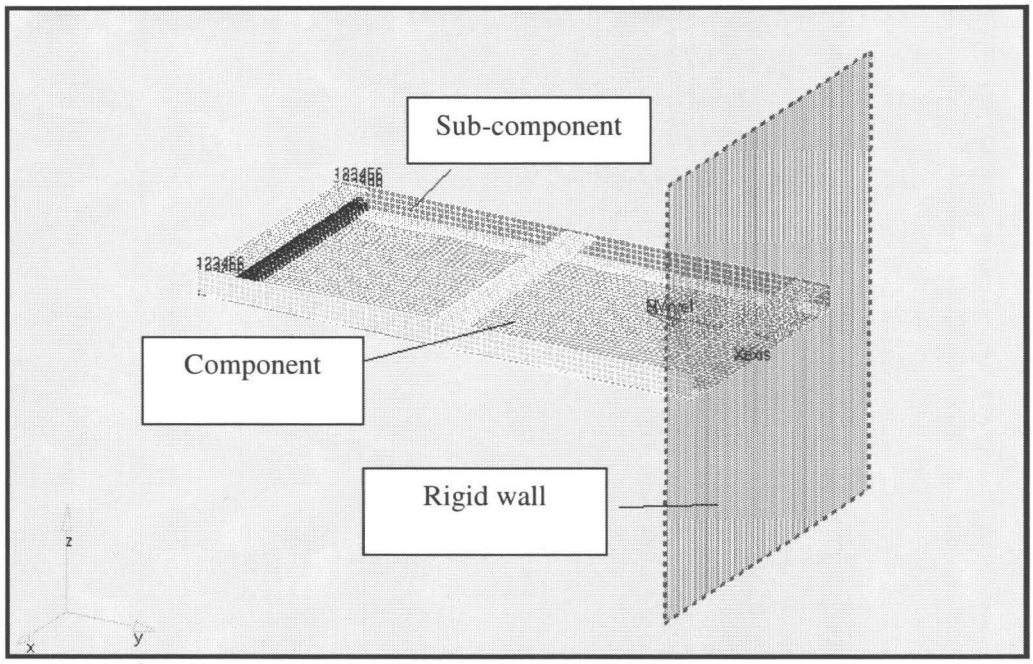

Figure 3.6: Schematic of the FE model and its components

The following units were used in the analysis: length [mm], time [s], mass [tonne (=1000 kg)], force [N], stress [MPa], energy [N-mm], density [tonne/mm^3], and Young's modulus [GPa].

3.3.2 Contact Surface Modelling

Rigid wall definitions have been divided into two separate sections, namely, Planar, and Geometric. In this analysis, a Rigid Wall Planar Moving card was used that represents the simplest contact problem. As shown in Figure 3.5, the boundary of the wall is flat and is defined by an outward normal unit vector with its origin at a corner point on the wall.

Since the outward normal vector defines the wall, the wall automatically takes the role of master and the remaining structure becomes slave to the rigid wall. In other words

the slave and master definitions for contact are different. Additionally, this wall can possess mass and an initial velocity. The outward normal vector is defined by assigning values to the x, y, and z component for the head and tail of the normal vector, which is directed toward the structure. Also in this analysis a contact interface, the Automatic Single Surface option was used. This contact option was selected to simulate a probable self-contact between interacting parts within the structure. This contact option takes into account the thickness of the shell elements and eliminates penetrations between the various elements within the structure.

3.3.3 Interface Definitions

Interface definitions are used in this analysis to define surfaces, nodal lines, and nodal points for which the displacement and velocity time histories are saved. This data may then be used in a subsequent analysis as an interface ID in the Interface Linking Edge as the master edge for a series of nodes. This capability is especially useful for studying the detailed response of a small member in a large structure.

For the first analysis, the members of interest only need to be discretized such that the displacements and velocities on its boundaries are reasonably accurate. After the first analysis is complete, the member can be finely discretized in the region bounded by the interfaces. Finally, the second analysis is performed to obtain highly detailed information in the local region of interest. The first analysis starts with specifying the name for the interface segment file in the (explicit finite element software LS-DYNA) execution line

upon performing subsequent analysis on isolated subcomponent using additional command line.

3.3.4 Comparison of Results

In the full model analysis, the structure was fixed at one end and then impacted on by the rigid wall with a mass of 74 [kg] moving at a speed of 10.5 [m/s], which translates, to 4.1 [kJ] of energy. The objective was to define the set of data that contains the displacement time history for the user defined nodes that could simulate the response such that the isolated component(s) behave in a similar manner. The subcomponent analysis was performed, using isolated subcomponent with only end nodes being constrained (geometric boundary conditions). The wall was not included into second stage (subcomponent in isolation), and only the predefined binary file was copied from first analysis in to the second analysis prior to performing the isolated FE model. This predefined binary file controls the motion during second analysis.

As expected, the stress and plastic strain were very high at the impacting front and reduce gradually along the structure. A set of interface nodes was defined along the boundaries of each rail, which was used to perform subsequent analysis on the subcomponent in isolation. Figures 3.7 and 3.8 depict the effective plastic strain and resultant momentum for the purpose of comparing them for two stages of the analysis.

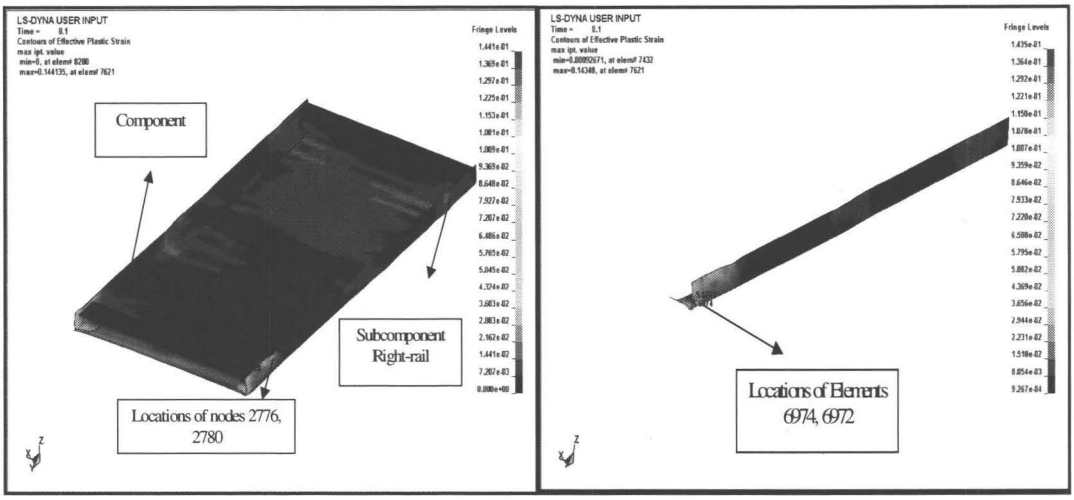

Figure 3.7: Contour plots of the effective plastic-strain a) entire FE model b) isolated right rail along with the locations of selected nodes and elements on the FE model

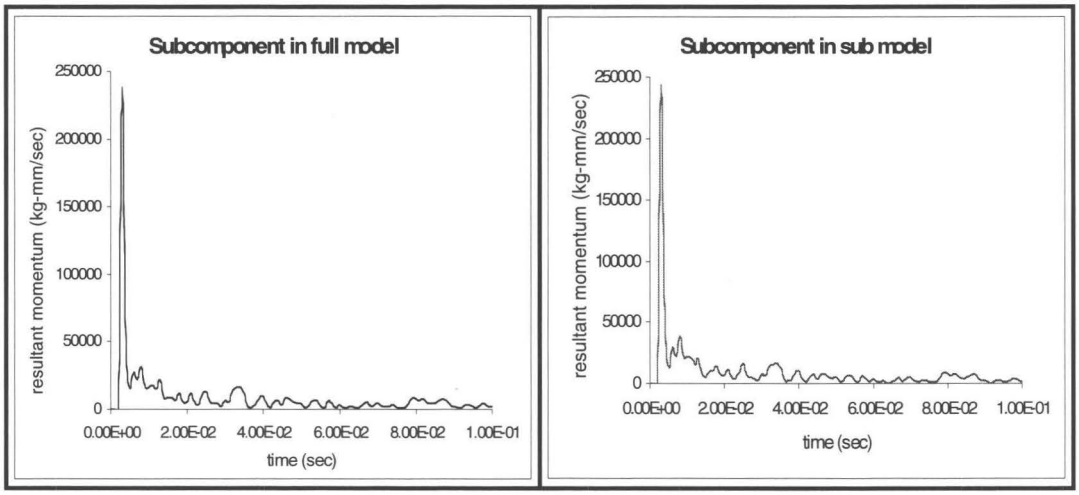

Figure 3.8: Contour plots of the resultant momentum a) subcomponent in full model b) subcomponent in isolation

It was noticed from these results that the maximum deformations are located at the same places for both analyses. This indicates interface nodes result in a similar response for both cases as a result, deformations on both model are in very good agreement with each other. The detailed analysis between a full model and a sub model

was performed on a nodal and an elemental basis to investigate various similarities and differences between the two models.

In these analyses, only 47 nodes were selected from the boundary of isolated subcomponent, unlike the previous analysis, where all the nodes around the isolated part were taken for performing sub model analysis. The isolated subcomponent consists of 747 nodes and 656 elements respectively. This selection was based on obtaining accurate results (full model versus sub model), since less number of nodes would not suffice, for sub model analysis. Therefore, the criteria for selecting sufficient number of nodes must be considered prior to the performing sub model analysis. In addition, these nodes were selected where the constraints applied (rigid connections), due to connection with other part, and also along the boundary of isolated subcomponent, so as to be able to capture exact deformations during impact analysis.

The locations of these nodes and elements are shown in Figure 3.7. These detailed analyses include a comparison of resultant displacements and resultant velocities for preselected nodes, and a comparison of effective stresses and effective plastic strains for preselected elements from the full model and sub model FE simulations. Figures 3.9, 3.10, 3.11, and 3.12 depict these comparisons for selected nodes and elements that were shown in Figure 3.7.

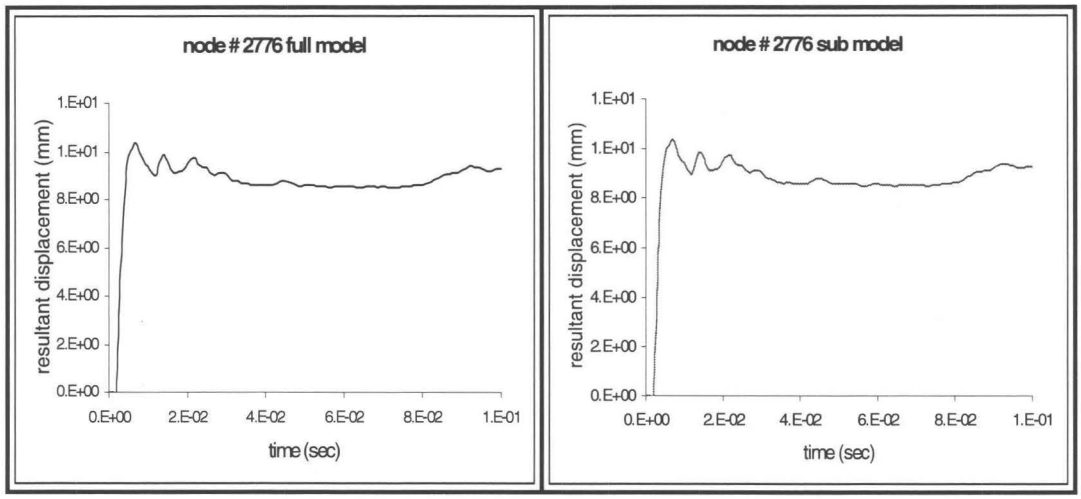

Figure 3.9: Plots of resultant displacement for node # 2776 for the a) the full model b) the sub model

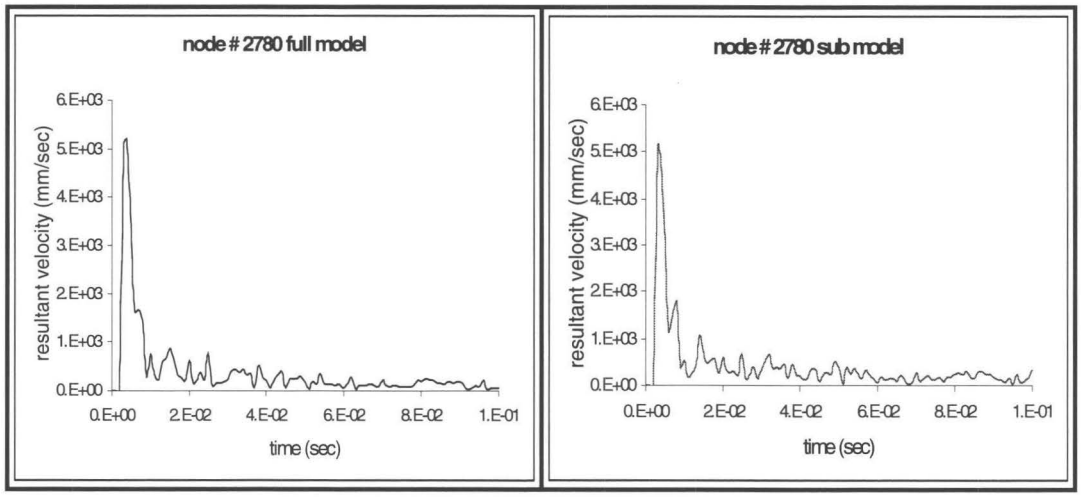

Figure 3.10: Plots of resultant velocity for node # 2780 a) the full model b) the sub model

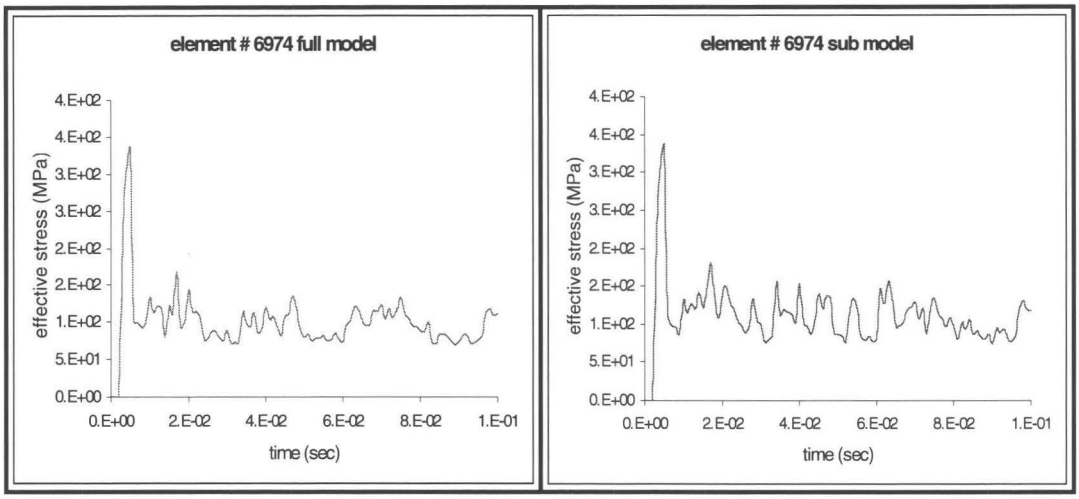

Figure 3.11: Contour plots of effective (v-m) stress [MPa] for element # 6974 a) the full model b) the sub model

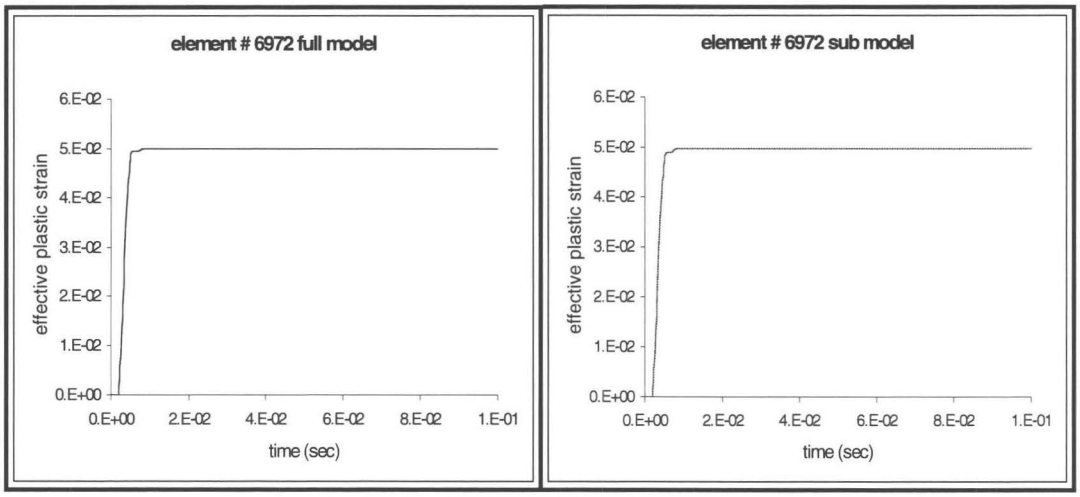

Figure 3.12: Contour plot of effective plastic strain for element # 6972 a) the full model b) the sub model

These Figures (3.9 through 3.12) show good agreement between the full model and isolated model simulations. The discrepancy in this work is defined as the percent difference between full model results and sub model results using the following expression: next section

$$\%Error = \left| \frac{FullModel - IsolatedModel}{FullModel} \right| \times 100$$

In both analyses, the response in terms of resultant displacement and resultant velocity were the same for selected nodes. Furthermore, the resultant plastic strain for selected elements was also in excellent agreement. The results were obtained at the end of the simulation time to allow the settlement (damping) of stresses. The results obtained from these analyses are listed in Table 3.1.

Table 3.1: Comparison of FE results for a subcomponent in full model and isolated model simulations

	Subcomponent in full model	Subcomponent in isolation
Plastic strain [mm/mm]	1.441e-01	1.435e+01
Resultant displacement [mm]	1.92e+01	1.92e+01
Resultant velocity [mm/sec]	1.633e+02	4.795e+02
Internal energy [N-mm]	5.73e+05	5.85e+05
Kinetic energy [N-mm]	2.58e+04	2.73e+04
Resultant Momentum [kg-mm/sec]	2.44e+05	2.38e+05
Analysis time [min]	59	4

Given the fact that these analyses provided excellent agreement between numerical results, the main question was analysis time. In both analyses, the termination time was set to 0.1 seconds and run times were compared for each case. The computational time of the full-model impact analysis was 59 min, and computational

time of the sub-model analysis was 4 min. Therefore, the run time for the sub-model analysis was almost $1/15^{th}$ of the run time for performing the full-model analysis.

As indicated previously, these analyses were performed in two stages namely, stage 1, and stage 2 respectively. Using the predefined interface boundary set from stage 1, the analysis was performed on this isolated part and the results were compared to each other. The objective was to define a set of boundary nodes such that the selected nodes within the defined set could produce the same response in terms of deformation for the isolated part in the sub-model analysis.

Particular attention was paid to defining the nodes around the periphery of the weld sections where different parts were connected to each other. These analyses as indicated previously were performed, using 47 nodes, since less number of nodes would not be sufficient to accurately obtain the subcomponent (right-rail) response. This selection was evaluated based on the nodal displacement time histories obtained from full model simulation from the right-rail. The time displacement histories were then used in isolated right-rail to perform second stage analysis. Therefore, the criteria for selecting sufficient number of nodes are vital and must be carefully considered prior to the performing sub model analysis.

The major difference between this analysis and the previous one was defining the nodes, mostly, around the connecting spot welds, which was later used for subsequent analysis on the subcomponent in isolation. Figure 3.13 depicts the FE model and the location of the interface nodes.

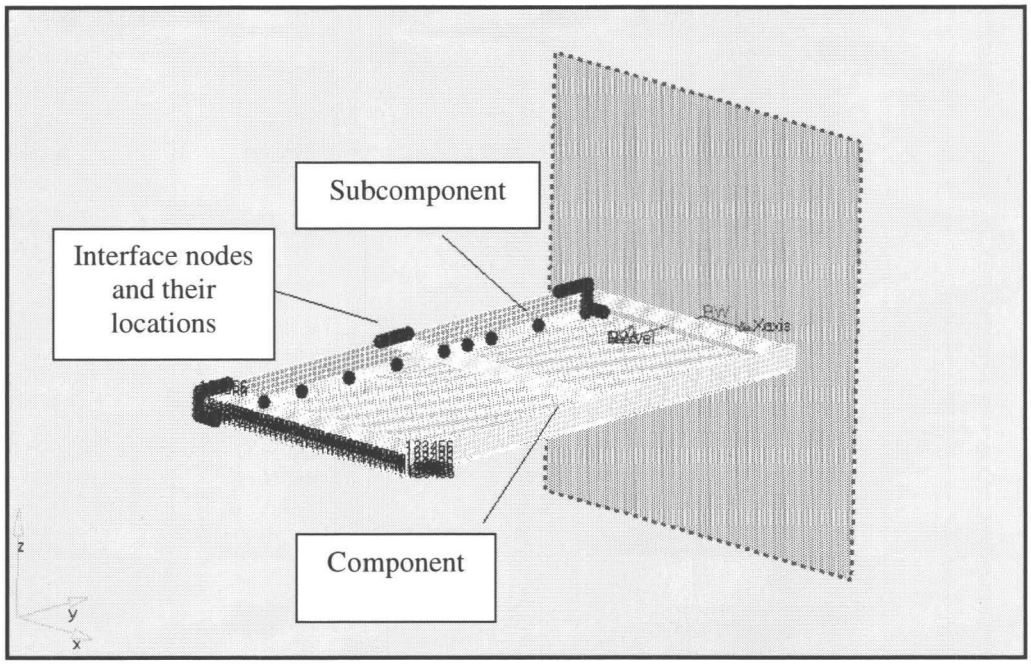

Figure 3.13: FE model of the modified design and locations of interface nodes

In this analysis, a database was created in the first run (stage 1) that recorded the motion of the interfaces. In later calculations, the isolated component was reanalyzed with the motion of their boundaries specified by the database created in stage 1. In stage 2, the interface linking edge option card was used to perform impact analysis on the isolated subcomponent.

Subsequent analyses can also be performed upon additional refinement to the FE mesh (right-rail) for locations of particular interest. Therefore, with only reanalyzing the isolated subcomponent with arbitrarily mesh sizes, the additional design modifications can also be performed if needed. The results were obtained at the end of the simulation time (0.1 sec), to allow the stresses to get settled due to the oscillation.

The reduction in computational time was almost 92%; this is a significant reduction in CPU time as well as cost for performing such analyses. The value corresponding to the resultant displacement was the same for both FE models. Also, the location of the maximum effective plastic strain was the same for both FE models.

The total energy, which is the combination of the internal energy and kinetic energy, were also in very good agreement with each other. Further analyses on the nodal and element base were also performed for the purpose of comparing similarities and differences between the two stages of these analyses. These comparisons included, determining the effective stresses, effective plastic strains, and resultant displacements on the isolated left-rail and comparing these parameters for the subcomponent in a full-model and the subcomponent in a sub-model. Additional figures are provided in Appendix D (see figures D.28 through D32), comparing other instances of time between full model and sub model responses. Figures 3.14, and 3.15 depict these results.

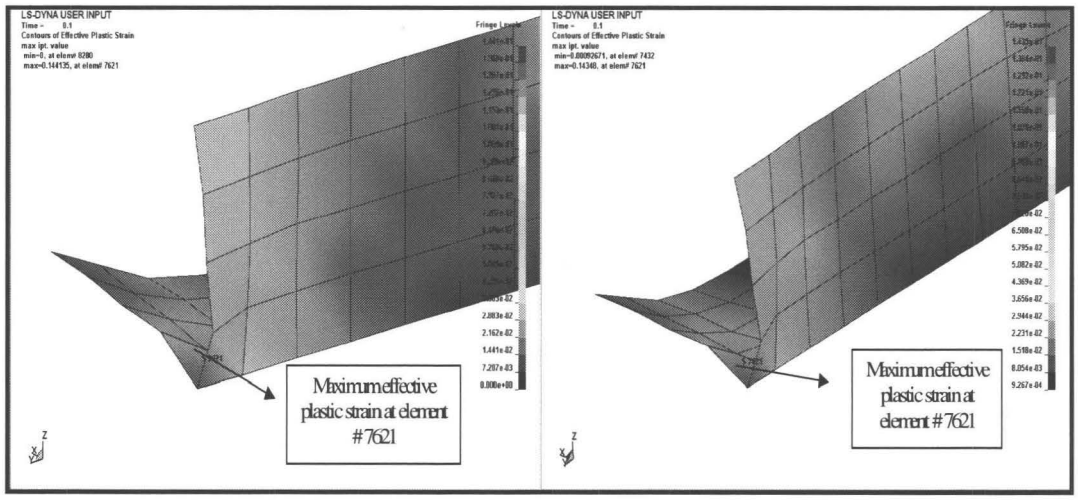

Figure 3.14: Contour plots of effective plastic strain on the left-rail and the location of the maximum plastic strain a) full model b) sub model

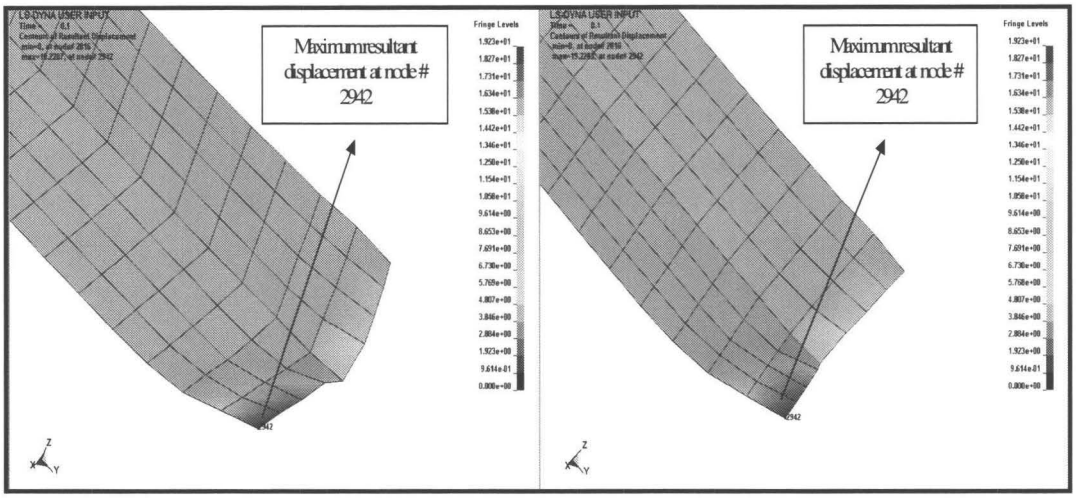

Figure 3.15: Contour plot of resultant displacements [mm] on the left-rail and the location of the maximum resultant displacement a) full model b) sub model

As can be seen from these figures, the maximum effective plastic strain corresponded to the same element, 7621, on both models. The maximum value of the resultant displacement, also, corresponded to the same node, 2942, on both models. The values corresponding to the effective stress changed from an element point of view, and corresponded to element 7623 on the full model and element 6986 on the sub-model. However, the distribution of the von-Mises stresses was in very good agreement for both stages.

The discrepancies can be related to the number of selected nodes, which did not include all of the nodes around the boundary, which corresponded to the FE model of the left-rail. In order to obtain comparable results, one should make a dataset from all the nodes around the boundary of a subcomponent.

However, the objective was to obtain reasonable accuracy between two FE models with the minimum number of predefined nodes. The selection of these nodes would provide excellent agreement with respect to various parameters that were considered for these analyses. The deviations in two variables, namely effective stress, and resultant velocities, can be related to the interaction of other subcomponents with the isolated rail, and localization of stress concentration at the weld connections. The resultant displacements were in excellent agreements, however the resultant velocities deviated by the large amount. This can be related to the differentiation of the time history of the nodal displacement values that in return causes the large amount of deviation in resultant velocities. Once again, this method can only be applied to a subcomponent, and not to a substructure, with appreciable accuracy. The results from the two analyses and the errors are listed in Table 3.2.

Table 3.2: Error analyses on the left-rail of the modified design determined by full model and sub model FE simulations

Full model vs. Isolated model	Percentage of discrepancies%
Effective Plastic Strain	0.42%
Material Internal Energy	1.98%
Material Total Energy	2.17%
Resultant Momentum	2.46%

The discrepancies (errors) corresponding to the resultant velocity were very large when considering the entire isolated component. However, on some nodes, these

discrepancies were small and varied only from 1 to 6 percent between two analyses. These discrepancies can be related to the two main factors, stress wave propagations and prescribed boundary nodes conditions, respectively. The full model deformations caused by stress waves propagations, whereas in isolated simulation only prescribed nodal displacements causes the deformations. In addition, performing the derivatives on the time history causes the velocity profile to deviate. Therefore, the time velocity history would be different, due to the numerical errors that are inherent upon taking derivatives.

The resultant displacements from two models were the same since the time history of the nodal displacements were used as nodal boundary values for the predetermined nodes. In the second stage, the rigid wall did not exist and therefore results were obtained on the basis of the nodal boundary values that corresponded to the values of the predetermined interface nodes. Although these types of analyses are often performed in large engineering systems, their objective is to study the response of a particular component within the entire system and compare their response in terms of modifications to the design. As a result, these analyses on isolated subcomponents lack experimental application that is a mandatory requirement for crashworthiness of a design. Performing experimental testing on a single component is a challenging task and the results are often not indicative of the response of the component *in situ*.

Chapter 4

Proposed Methodology and its Application

4.1 Introduction

This section reports on the development of the methodology for performing impact analysis on a substructure in isolation. The purpose of this work is to establish test procedures to perform dynamic testing on a substructure in isolation.

It is well known that the mechanical behaviour of a substructure subjected to impact loading is different in isolation than the same substructure *in situ* (Goodman et al., 2007). The objective of this research is to perform substructural testing in isolation that results in similar mechanical performance of the substructural testing *in situ.* This is achieved by imposing appropriate deformations from the full-model analysis onto the sub-model, and determining the energy transferred to the substructure using the FE results. Furthermore, a parametric equation is defined to determine the velocity required for impact testing on subcomponent in isolation.

Performing dynamic analyses on the entire vehicle is very costly and time consuming and requires a lot of detailed information (CAD data, and mechanical properties) related to the various parts and components. These informations are not available to the public domain. In section 3.2, the car and modified assembly were named structure (mini-van), substructure (floor) and subcomponent (right-rail). Here, for

simplicity, the simple structural components are named structure, which represents the car, and substructure, which represents the floor in the car.

The main objective of this work is, therefore, to apply correct boundary conditions on substructures in isolation under impact loadings. This work is performed in two steps: analytical and experimental. Each of these steps is an integral part of the proposed scheme. The analytical part of the methodology is used to perform FE analyses on the structure and the substructure in isolation and the results are compared to each other. The experimental impact testing is also performed on the structure and the substructure in isolation and results from impact testing are compared with numerical results.

4.2 Sequence of Methodology

It was explained that model order reduction does not lend itself to substructural analysis of complex structures and explicit FE techniques can only be applied to single components. Thus, development of a new technique for substructural testing is warranted. The proposed technique adopted the participation factor concept from model order reduction methods and energy transfer in the explicit method used by LS-DYNA. It is argued that one should excite the substructure in isolation such that the mode shape is similar to the mode shape of the substructure *in situ*. Therefore, the velocity of impact that produces a similar mode shape for each node can be determined from the fundamental frequencies of excitation from each selected node. This technique enables

one to perform evaluation of the substructures in isolation in both a FE simulation and an experimental setting.

A methodology was developed to perform FEA on a substructure in isolation. The proposed methodology takes into account the effect of boundary conditions around the substructure imposed by surrounding systems of the entire structure. Therefore, the subsystem under study will behave as if it was studied *in situ.* The developed methodology is obtained using the following steps:

- Performing FE analysis on the entire structure
- Determining the energy transferred to the substructure from full-model analysis
- Performing modal analyses on the full structure and determining the participation factors and modal displacements from preselected nodes
- Determining fundamental frequencies using FFT for preselected nodes in full-model analysis
- Performing modal analysis on the substructure in isolation
- Determining frequencies corresponding to these nodal displacements from modal analysis for substructure in isolation
- Mapping deformations from full-model analysis onto sub-model analysis using similar nodal displacements
- Using proposed parametric equation for determining required speed
- Performing FE impact analysis on a substructure in isolation using appropriate mass and velocity

These steps are pictorially represented in the flowchart shown in Figure 4.1.

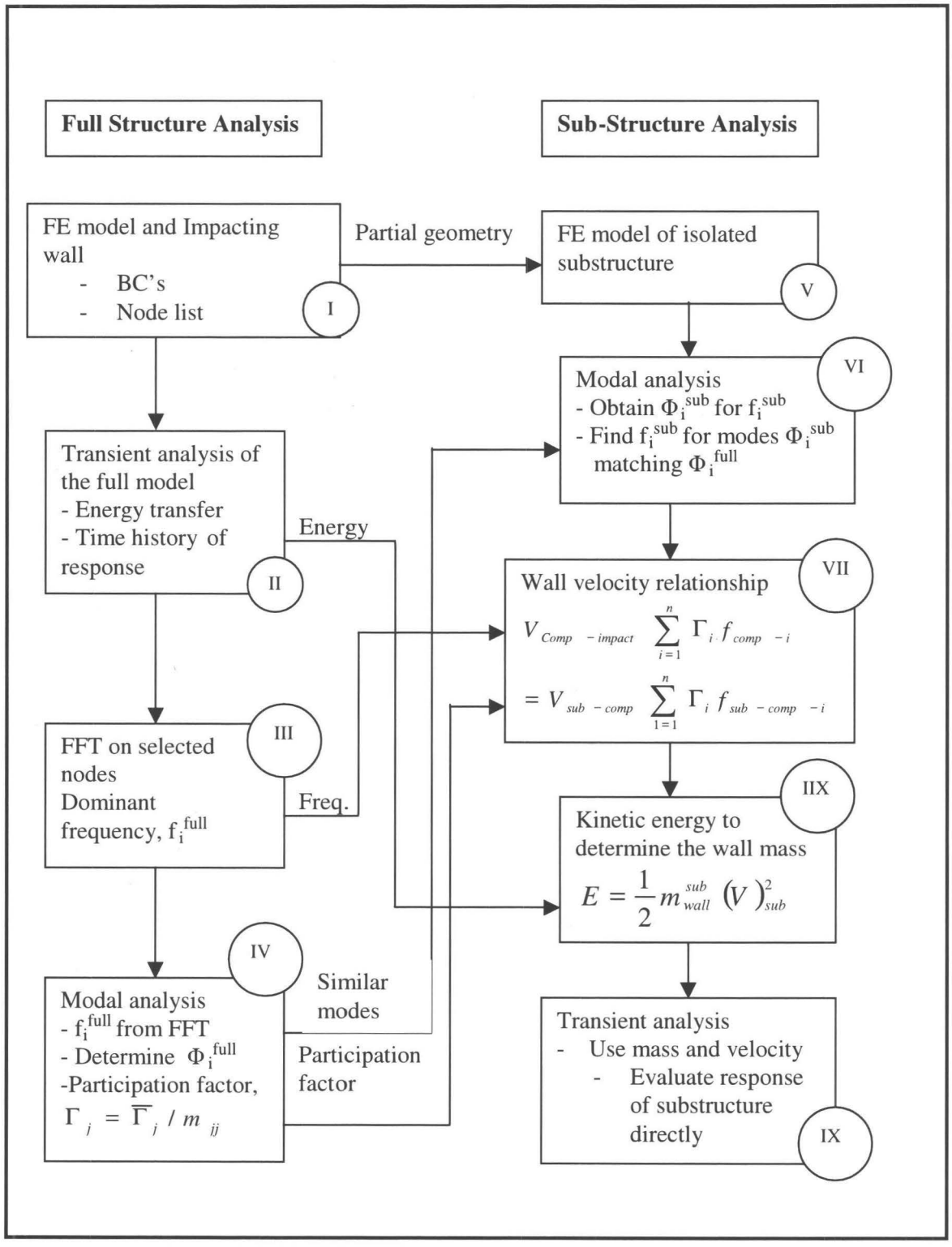

Figure 4.1: Flowchart of the methodology

In the Figure 4.1, each block is numbered for simplicity and arrows connecting the blocks indicate the sequence of the proposed method. The first block represents the FE model of the structure and impacting wall for performing dynamic analysis. After impact simulation, the results from the full model FE analysis are carefully studied (block I). The energy (internal) transferred to the substructure, is determined from full model analysis, block II. In addition, the time history of the pre-defined nodes corresponding to the displacements, velocities, and accelerations are determined. The internal energy transferred to the substructure (from block II), is then equated to the wall energy required for isolated analysis, block VIII.

4.3 Application of the Methodology

In this work the technique is applied to determine the dynamic response of a substructure when analyzed in isolation. To do so, a relatively simple structure with a segment of the structure defined as the substructure is modeled. A total of 66 nodes are selected on the boundary of substructure from full model analysis, prior to the performing substructure analysis in isolation. These nodes were distanced every 4 elements around the boundary, and away from the welded locations. After performing FFT on 66 preselected nodes, it was noticed that many of the nodes' fundamental frequencies were similar. As a result, the number of nodes was reduced from 66 to 15.

The most dominant frequencies corresponding to 15 nodes, were calculated by performing FFT on FE data, block III. The participation factors for 15 nodes were calculated using modal analysis block IV. These participation factors were also used in

block VI. Furthermore, similar modes (displacement vectors) in block IV were matched with similar modes (displacement vectors) in block VI. The fundamental frequencies determined in block II along with participation factors calculated in block IV were transferred to the block VII. These information were used in the left hand side of the parametric equation in block VII.

The Modal analysis was performed on the isolated substructure (partial geometry) and nodal displacements were extracted. Similar nodal displacements (modal vectors) were matched (substructure in full model vs. substructure in isolation) and corresponding fundamental frequencies were determined for the isolated substructure, block VI.

The same participation factor of each fundamental frequency determined in full structure analysis was used for the corresponding nodes and its frequency on subcomponent, from block IV to block VI. This information was then transferred to the right hand side of the parametric equation, block VII. Therefore, using proposed parametric equation, the only unknown that is the velocity for isolated test was determined. Finally, knowing the energy transferred to substructure, block VIII, and impacting velocity of subcomponent, block VII, the mass required for the impacting wall was calculated. The substructure in isolation was then impacted with calculated mass and adjusted velocity in block IX.

4.3.1 Mesh Sensitivity Analysis

In any FE analysis, to obtain a reliable result, the finite element results should be independent of the mesh size (keeping element formulation type, contact type, material

properties, and boundary conditions constant). Therefore, the FE models of a structure suitable for impact testing (Figure 4.2) were descritized with various mesh sizes. Figure 4.2 depicts the simple structural component.

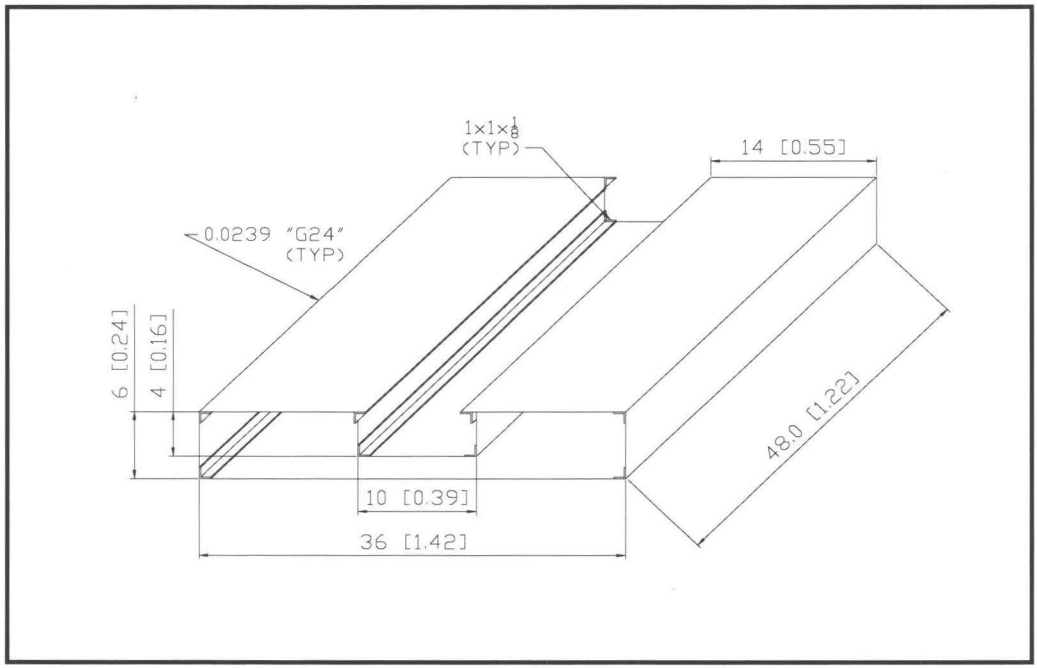

Figure 4.2: Schematic diagram of the simplified structure and its components

The structural components are made from structural steel (AISI 1010 and AISI 1020) and their appropriate material properties were incorporated into the FE model. The corresponding dimensions for the structure, and for the substructure are shown in Figure 3.20. The L-angles are made from AISI 1020, and their corresponding dimensions are 25.4 by 25.4 by 3.17 mm. All the remaining structural components are made from structural steel (AISI 1010).

The analysis started with the coarse mesh, which, consisted of 1891 nodes and 1468 elements. Subsequently, eight additional analyses were performed with progressive refinement of the first model. Note that the locations of constrained corresponding to the physical weld connections were kept the same for all analyses. Figure 4.3 depicts the effective plastic strain result obtained from FE convergence analysis. The maximum plastic strain at the termination time for this analysis was determined to be 2.086e-02 [mm/mm].

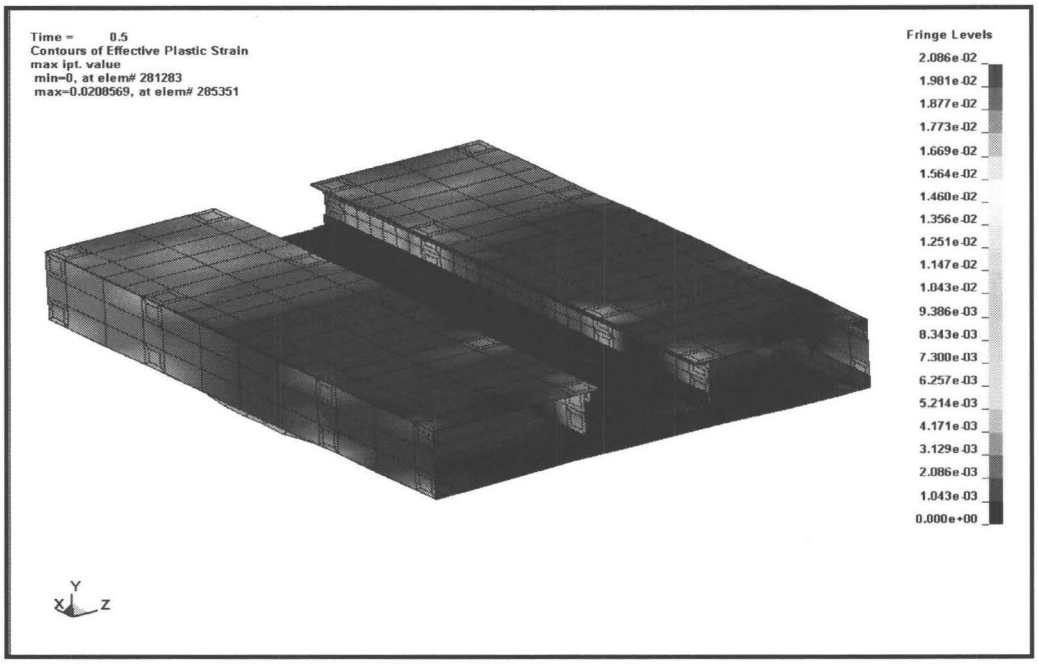

Figure 4.3: The effective plastic strain resulted from 1st sensitivity analysis

The next analysis was performed on yet another geometrically identical model with finer mesh compared to the second mesh. The result from this analysis is shown in Figure 4.4. The second analysis was performed with model that consists of 2448 nodes

and 1916 elements. The maximum plastic strain stabilizes for this analysis at 1.999e-02 [mm/mm].

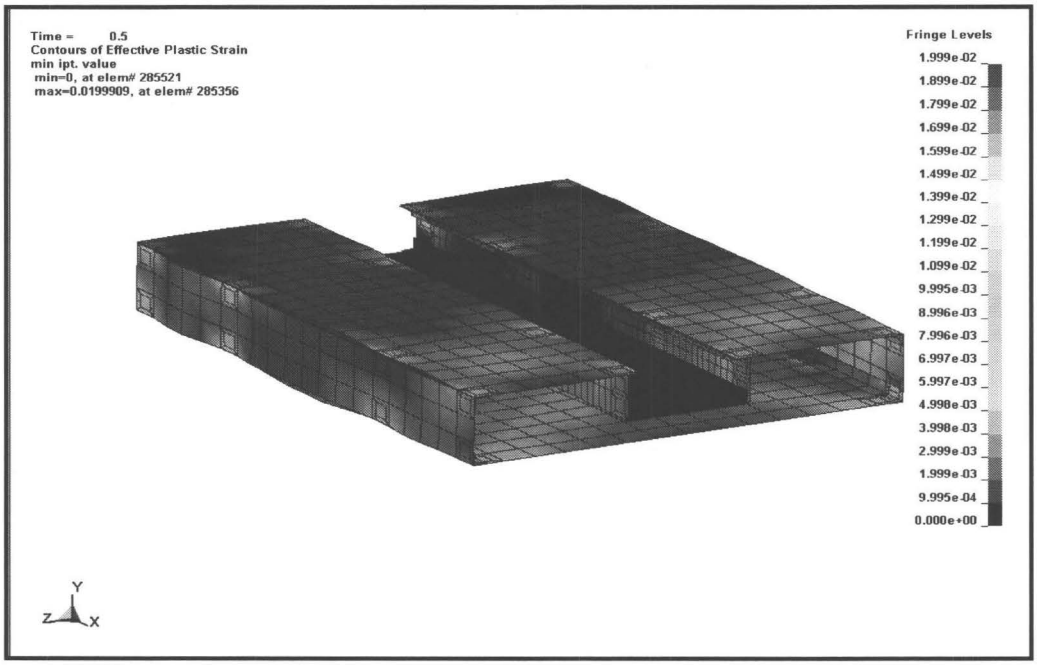

Figure 4.4: The effective plastic strain resulted from 2nd sensitivity analysis

One more FE simulations were performed on model, which consisted of 3508 nodes and 2736 elements respectively. The result from the last convergence analysis is shown in Figure 4.5. The maximum plastic strain stabilizes for this analysis to be 1.971e-02 [mm/mm] respectively.

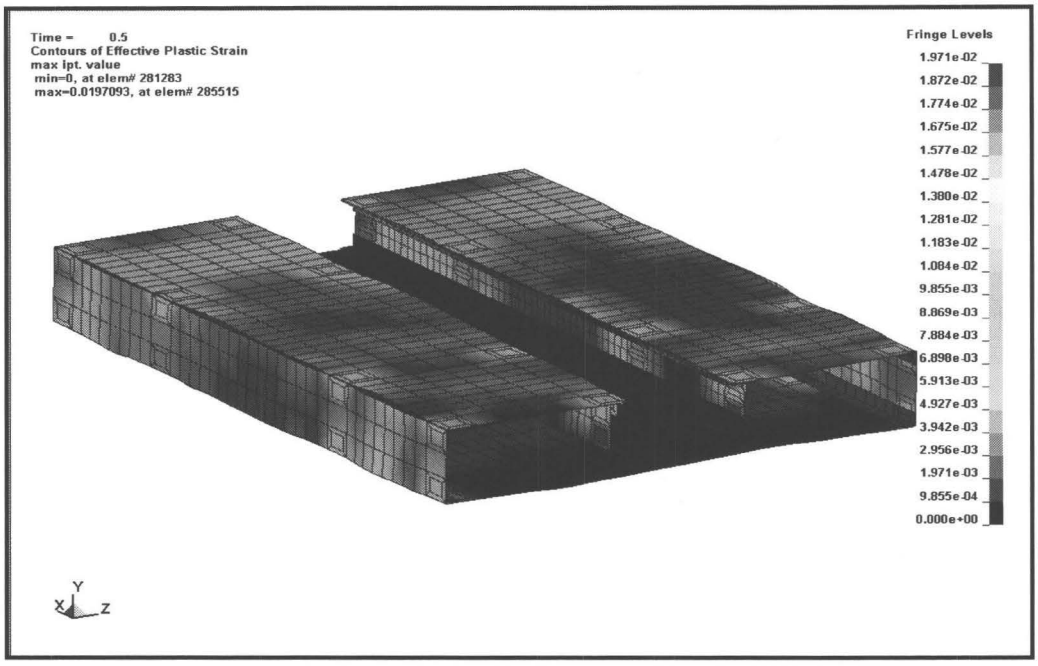

Figure 4.5: The effective plastic strain resulted from 3rd sensitivity analysis

It was determined from these analyses that value of the maximum effective plastic strains does not change with additional mesh refinement significantly. Upon additional mesh refinement, it was revealed that the differences between maximum values of effective plastic strain are less than 0.6%. The maximum effective plastic strains are listed in Table 4.1.

Table 4.1: Comparison of effective plastic strains for sensitivity analyses

Sensitivity analysis #	Nodes/elements	Effective plastic strain
1st FE analysis	1891/1468	2.086e-02
2nd FE analysis	2448/1916	1.999e-02
3rd FE analysis	3058/2500	1.971e-02

Figure 4.6 depicts the nodal locations around the boundary of the substructure. This was performed for identical nodes on each of the aforementioned nine models with refined mesh. In addition, 5 nodes were selected from predetermine nodes on the full-scale model and dominant frequency of these nodes were calculated using FFT performed on the acceleration/time data.

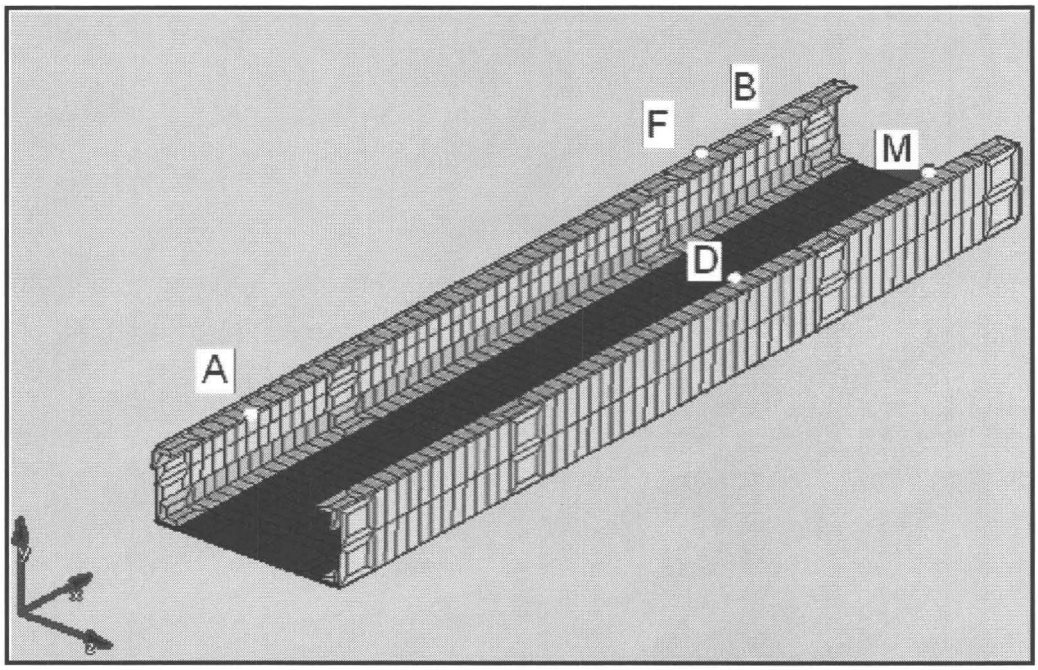

Figure 4.6: Locations of the selected nodes for sensitivity analyses

The resultant dominant frequencies of each FE model are listed in Table 4.2 (the nodal locations are shown in Figure 4.6). The aforementioned sensitivity analyses were performed on these nodes (as shown in Figure 4.6) with the same physical locations on each FE models. These two criteria (effective plastic strain and the dominant frequencies)

were used to determine the optimum mesh size, Based on these analyses the model with 2717 nodes and 2100 elements was chosen for this study.

Table 4.2: Comparison of dominant frequencies for sensitivity analyses

Mesh sensitivity	Nodes	Frequency (Hz)
1st FE analysis	A, B, D, F, M	604, 786, 1176, 1798, 2246
2nd FE analysis	A, B, D, F, M	633, 841, 1237, 1864, 2330
3rd FE analysis	A, B, D, F, M	639, 857, 1263, 1879, 2344
Final FE model	A, B, D, F, M	636, 851, 1259, 1871, 2338

As Figures 4.7, 4.8, and 4.9 indicate, the fundamental mode shapes do not change significantly after the characteristic mesh size of 12 mm. This shows that further refinement of the mesh does not add significant accuracy to the results. Thus, the added accuracy after the characteristic mesh size of 12 mm does not justify the computational time and expense. Therefore, this is considered as mesh independent model (refer to the FE analysis that was used in this study). This mesh size (2717 nodes and 2100 elements) is used from this point forward for all FE analyses.

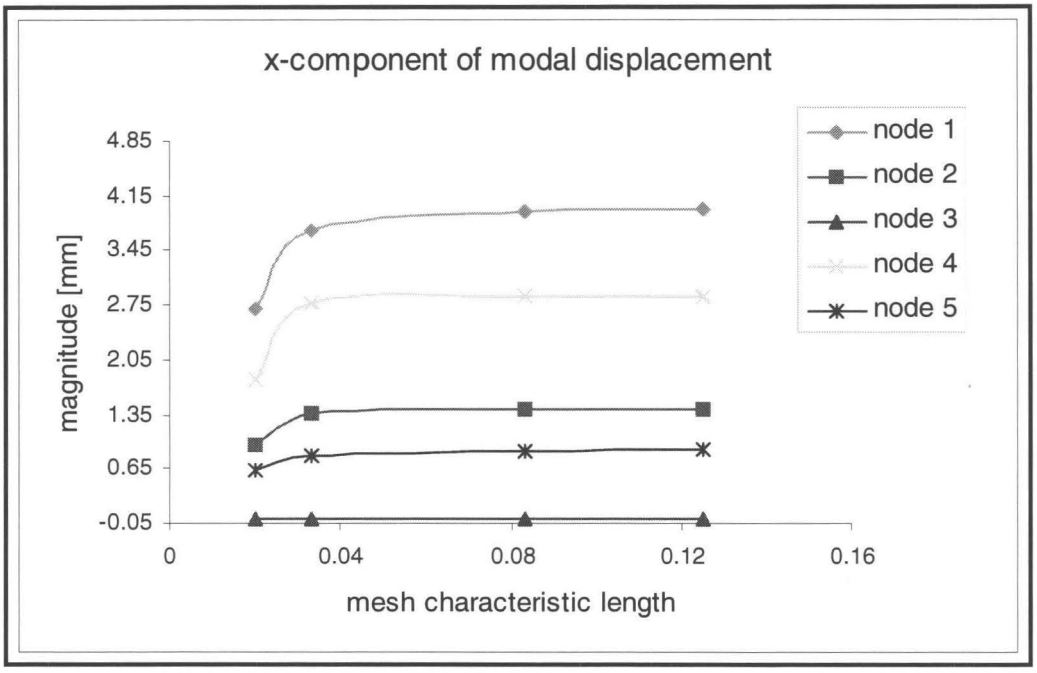

Figure 4.7: X- component of selected nodes resulted from convergence analyses

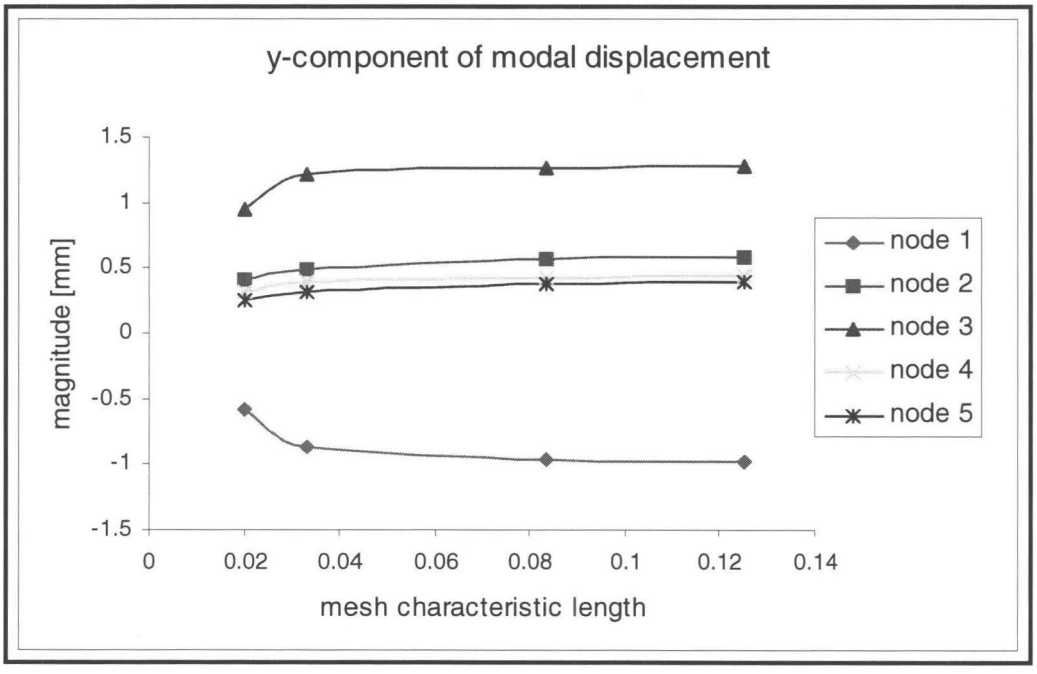

Figure 4.8: Y- component of selected nodes resulted from convergence analyses

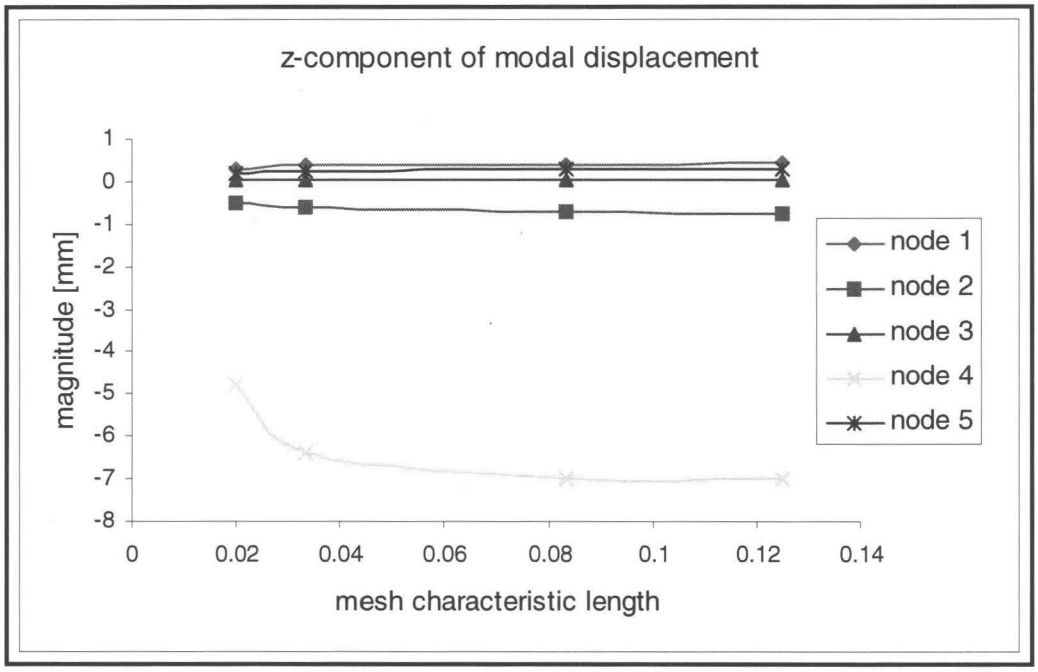

Figure 4.9: Z- component of selected nodes resulted from convergence analyses

4.3.2 Time Domain Analyses

At first, a simple structural component (referred to as the structure) was designed and manufactured. Then the FE model of this structure was constructed from CAD data and FE analyses were performed on this model. The commercial FE program HYPER-MESH (an FE pre-processor) was used to construct a pre-analysis model (as shown in Figure 4.2). The model was meshed using 4-noded Belytschko-Tsay shell elements, with three integration points through thickness. Element formulation #16 was used with activating option (ELFORM) for the shell elements, which corresponds to the fully integrated element formulation with four quadrature points (no hourglass modes). Using

fully integrated elements is computationally expensive compared to the one quadrature point, but there is no hourglass effect to influence the solution.

The entire structure comprised of 2717 nodes, and 2100 shell elements. The connections between various parts were made using 128 rigid elements, which constrained the displacements and rotations in all directions at the connection nodes, to simulate the original fastening configuration. Once the discretized model of the simple structure was constructed, the FE model was exported into the non-linear explicit code (LS-DYNA) to perform impact analysis.

Quad elements (4-noded Belytschko-Tsay shell) were used for the entire FE model. Figure 4.10 depicts the FE model. Welds were represented using rigid-elements connecting the opposing elements' corner nodes. This technique eliminated relative motion (translation and rotation) between connected nodes.

On the physical model, the weld points corresponded to the square areas that represented weld connections. Therefore, the FE mesh was refined around the boundary of the weld on the FE model, such that the refined mesh represented weld areas. The location of the weld points and the spacing between the weld connections on both FE models were chosen to replicate the physical models. In the full model analysis, the structure was fixed at one end and then impacted by the rigid wall with an arbitrarily chosen mass of 72 [kg] moving at a speed of 10.5 [m/s] on the opposite end.

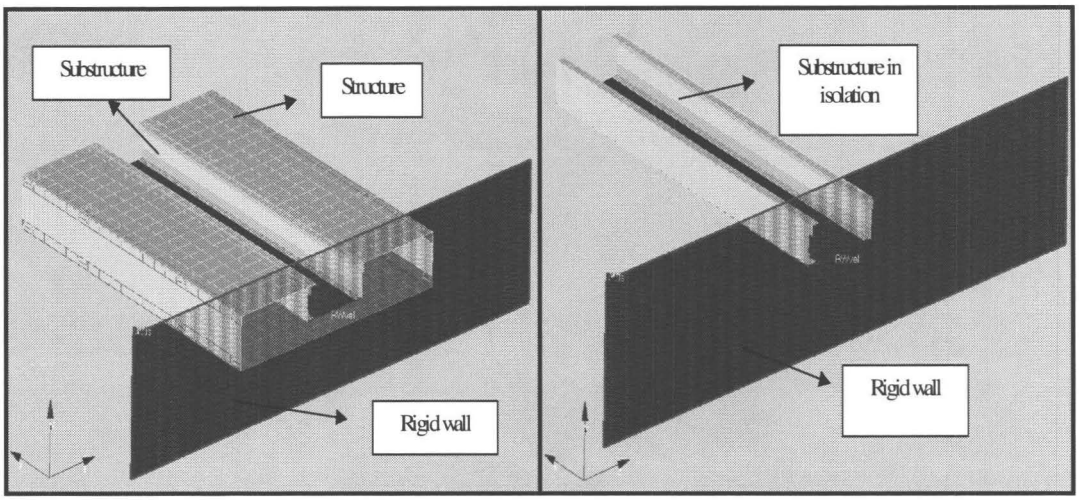

Figure 4.10: Finite Element models of the structure, substructure and rigid-wall

4.3.3 Contact Surface Modelling

To simulate the impact analysis accurately, the contact between the rigid wall and the component becomes of great importance. Various contact configurations exist in LS-DYNA (For example, automatic single surface). However, much like automatic single surface contact, these contact surfaces failed in the analyses due to edge-to-edge penetration that caused elements along the sharp edges to penetrate into each other. Most contact types do not check for edge-to-edge penetrations as the search entails only nodal penetration through the segment. This may be adequate in many cases; however, in some unique shell contact conditions such as this analysis, the treatment of edge-to-edge contact becomes very important.

Generally, edge-to-edge contact is divided into two main categories that exclude or include interior edges. An exterior edge is defined as belonging to only a single element or segment. An interior edge is shared by two or more elements, or segments.

The first type by default, considers only exterior edges in its edge-to-edge treatment. The entire length of each exterior edge, as opposed to only the nodes along the edge, is checked for contact. The option card Contact Automatic General Interior was used in these analyses, which is associated with a penalty cost that includes interior edges for edge-to-edge contact and works for both solid and shell elements. This is a single surface contact, which only the slave side defines as the contact. This contact checks for nodal penetration through the three closest segments.

The three-segment check is more expensive but may be more robust for contact in corners. Another important way in which this contact differs from single surface is the way in which the shell edge contact is handled. These contacts check for penetration along the entire length of the free (unshared) shell edges. By adding the interior option, edges of the interior shells are also taken into account. In this analysis, the contact between the structure and wall was defined using a rigid wall planar finite moving option card.

The control contact option was activated using these cards with their default values:

- Scale factor for sliding interface penalty [SLSFAC]
- Scale factor for rigid wall penalties [RWPNAL]
- Initial penetration check [ISLCHK]
- Shell thickness consideration [SHLTHK]
- Penalty stiffness value option [PENOPT]
- Shell thickness change consideration [THKCHG]

- Reorientation of contact interface segment [ORIEN]
- Mass treatment of eroded nodes [ENMASS]
- Maximum penetration check multiplier [XPENE]
- Initial penetration by tracking the initial penetration [IGNORE]
- Time step size for eroding contact [ECDT]
- Projection of slave nodes to master surface [TIEDPRJ].

In addition, coefficients of friction for static [SFRIC] and dynamic [DFRIC], along with exponential decay coefficient [DC], and coefficient for viscous friction [VC] were included into the analysis. For this purpose, additional cards using optional card # 4, were added to the contact option. These parameters are defined by their default values, and are listed as follows: [IGNORE], [FRCENG], [SKIPRWG], [OUTSEG], [SPOTSTP], and [SPOTDEL]. The aforementioned options were used in Control Contact option card to perform analyses in this study. The termination time was set to 0.5 sec., and the time step for performing analysis was determined to be 1.35732E-06 [sec.]. The control time step card was also activated, and default values for initial time step size [DTINIT], and scale factor for computed time step [TSSFAC] were used.

The total energy dissipated was found by taking the difference between the total kinetic energy of all the nodal points slaved to the rigid wall, before and after impact with the wall. The coefficient of the coulomb friction was set to 0.125, for this analysis. This value is typically in sheet metal forming problems and chosen by the analyst. Generally, sheet steel on sheet steel is anywhere from 0.1 to 0.15, (for most metal to metal contact,

Dutton, 2005; Du et al., 2007) to give frictional resistance to the tangential motion of any boundary node while it is in contact with the rigid boundary.

For structural components made from mild steel 1010, the material model MAT-24 was used with a Yield stress σ_Y = 272.5 [MPa], and the values for the true stress and the corresponding plastic strain were updated locally at every time step and used for the next time step (as shown in Figure 4.11). For structural components made from mild steel 1020, the material model MAT-24 is used with a yield strength of 350 [MPa]. In this material model, the plastic region was modeled using eight points, which corresponds to the values of true stress vs. plastic strain (Douthit, and Van Tyne, 2005; Dietenberger et al., 2005).

This material properties used for the structural components, had nominal values of mass density ρ = 7830 [kg/m^3], Young's modulus E= 200 [GPa], and Poisson's ratio ν = 0.3. The strain rate effect was also included in this material model using piecewise-linear plasticity with Cowper-Symonds. The corresponding Cowper-Symonds parameters (c = 40, p = 5) for mild steel were included in the MAT-24 material model (Simunovic et al., 2003; Dietenberger et al., 2005; Wierzbicki and Akerstrom, 1997; Douthit, and Van Tyne, 2005).

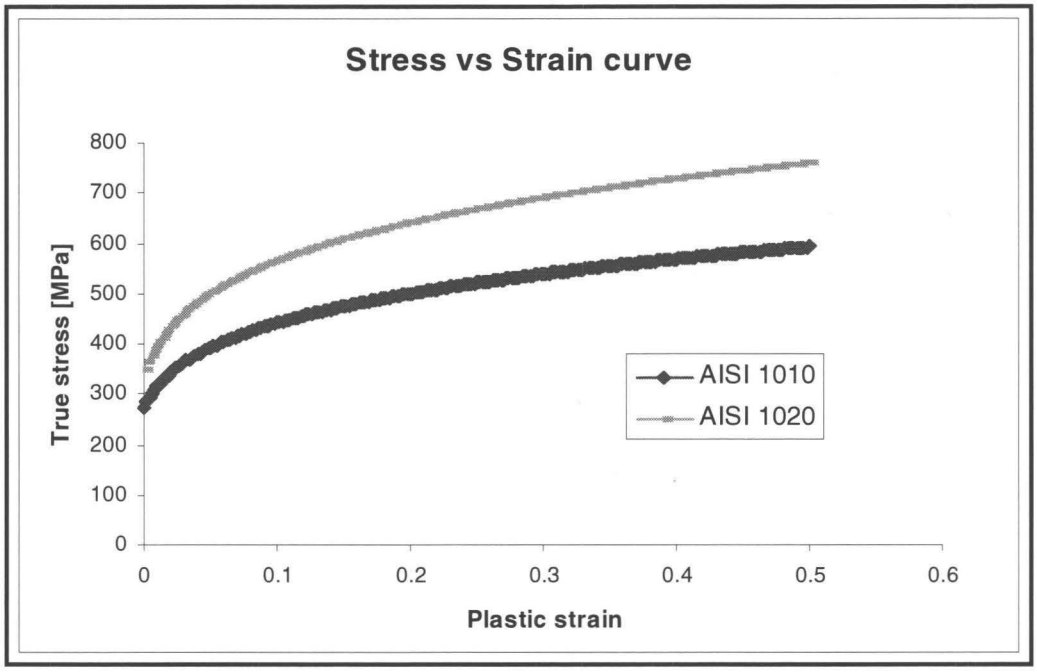

Figure 4.11: Plot of true-stress vs. plastic-strain corresponding to structural steel 1010, and 1020

4.3.4 Frequency Domain Analyses

After performing FE analysis on the entire structure, 66 nodes were selected around the boundary of the substructure. These nodes were distanced every 4 elements, and away from weld locations. The time history of the z-component of acceleration corresponding to these 66 nodes was extracted from the full-model FE analysis, and then converted to the frequency data using Fast Fourier Transform (FFT) analysis. The objective was to determine the dominant frequency of the selected nodes, and determine the contribution of these frequencies and modes of deformation with respect to the excitation of the system (refer to Appendix D, Figure D.1 for node locations)

Matlab software (Matlab version 7, 2005) was used to perform FFT analysis based on the time history of acceleration data for selected nodes. The FFT analysis revealed that physically close nodes had very close fundamental frequencies. Therefore, one participation factor was considered for the nodes with similar fundamental frequencies. This indicated that 66 nodes were not needed and a reduced number of nodes could suffice. In other words, the objective was to determine the most dominant frequency and the corresponding dominant mode, which had the most significant effect and therefore controlled the response of that particular node.

Generally, the contribution of the most dominant mode is between 80% and 85%; whereas, the contributions of other nodes are between 10% and 15% at the most (Humar, 1990; Craig, 1995; Bhatt, 2002; Chopra, 2007). A complete list of selected nodes resulting from transient analyses of acceleration data and their corresponding frequencies are given in Appendix A. Figures 4.12 and 4.13 depict the typical time history and their corresponding frequency response data.

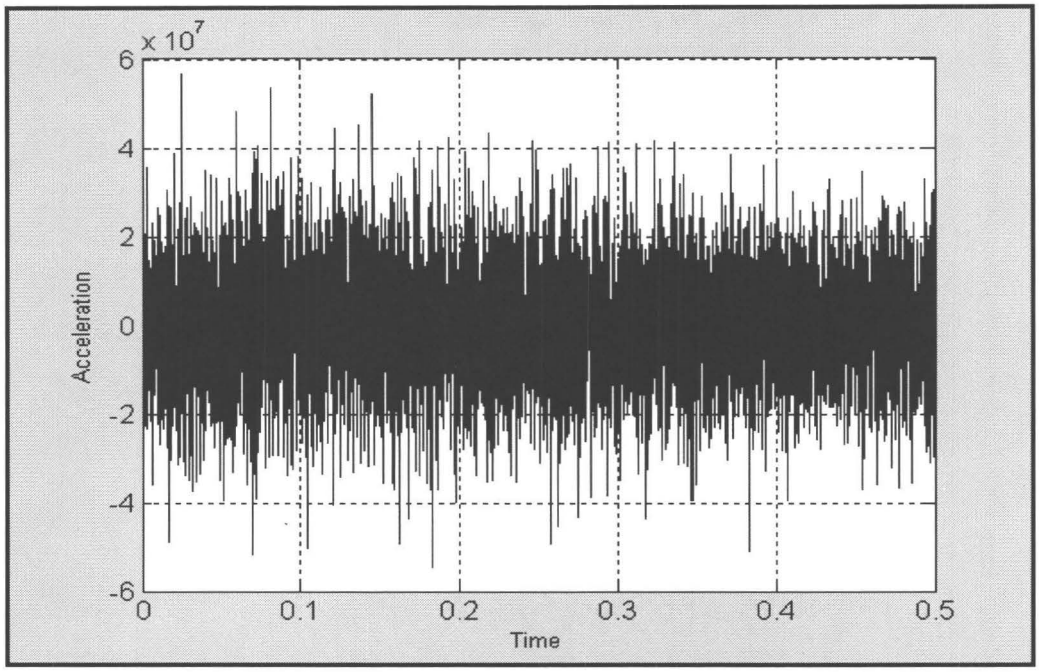

Figure 4.12: A typical plot of acceleration vs. time determined by transient analysis

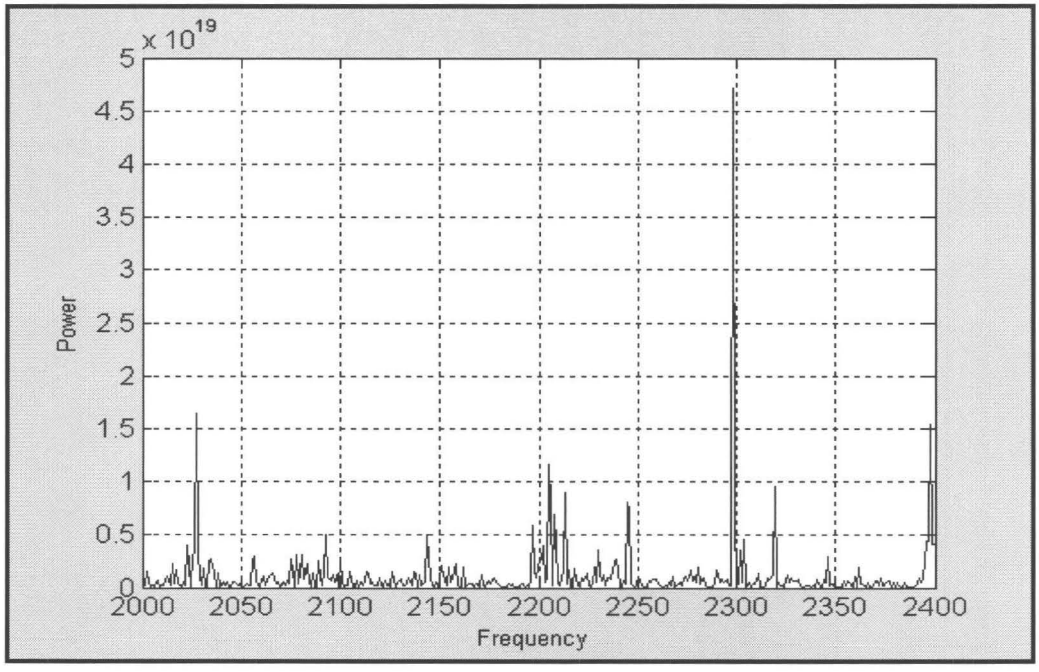

Figure 4.13: A typical plot of corresponding frequency vs. time determined by performing FFT analysis

The displacement history from the FE analysis was also extracted for selected nodes. The displacements for selected nodes and their resultants were calculated using the x, y, and z components of displacement from the FE analysis results. From modal analysis, nodal displacements for the same selected nodes were extracted and compared to those obtained from the FE results. From these comparisons, it was then decided that only 15 nodes were needed (refer to Appendix A). Figure 4.14 depicts the locations of the selected nodes on the FE model. After FFT analysis, it was found that nodes physically close to each other have approximately same fundamental frequencies. Thus, it was concluded that 15 nodes were sufficient for the purpose of this investigation. Generally if more accurate results are needed, a larger number of nodes can be used to extract fundamental frequencies.

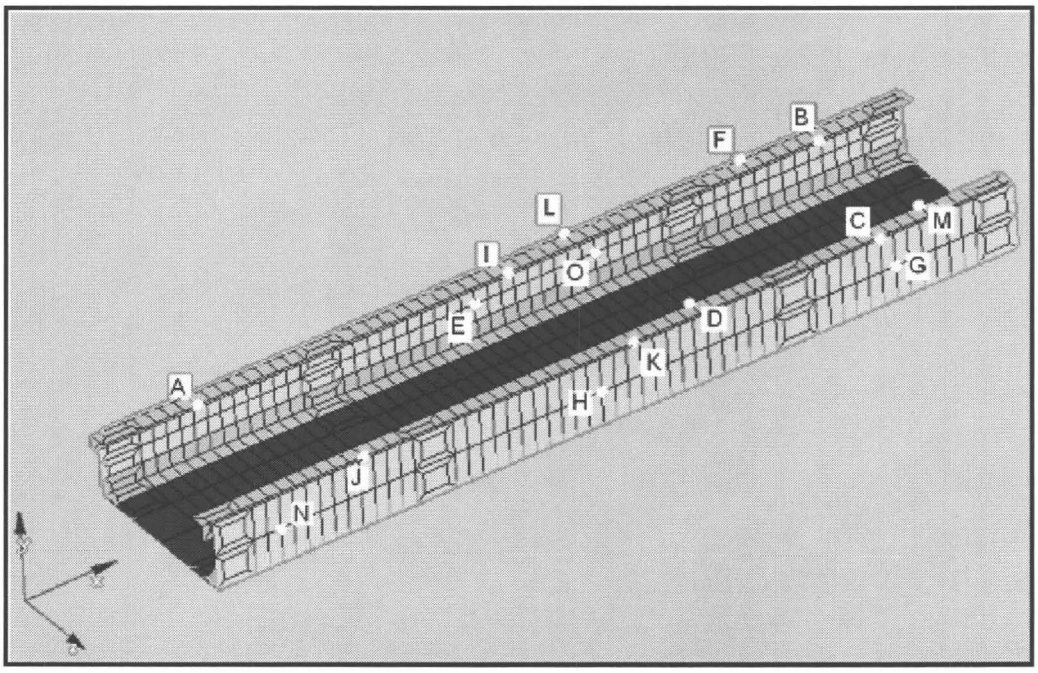

Figure 4.14: Locations of preselected nodes on the FE model

Tables 4.3 and 4.4 list the typical nodal displacement vectors and their resultants obtained from the full model and sub model modal analyses, respectively. Nodal displacement vectors were obtained from the full model modal analysis, and modal analysis was performed on an isolated substructure. The unknowns in modal analysis become the weights (amplitudes) of each mode. If a complete set of modes is used, i.e. the number of modes is equal to the number of degrees of freedom in the model, the method is exact and can be considered as a transformation into a set of generalized coordinates. Typically however, only a small number on modes are used, so the method becomes approximate and substantial computational savings can be realized (Craig and Bampton, 1968; Leung, 1978; Paz, 1984; and Qu, 2001).

The objective of modal analysis was to determine the similar displacement vectors between full model and sub model. This is done by activating Control Implicit General, Control Implicit Eigenvalue, Control Implicit Modes, and Control Implicit Solver cards, and defining the nodes for which their mode shapes needs to be determined. The complete lists of the nodal displacements are given in Appendix B. These similar vectors are listed in the following Table 4.3 and Table 4.4.

Table 4.3: Nodal displacement values and their respective resultant magnitude determined by full model analysis

Nodes	X-displacement [mm]	Y-displacement [mm]	Z-displacement [mm]	Magnitude [mm]
A	3.58	-0.87	0.38	3.70
B	0.99	0.60	-0.71	1.36
C	1.30	0.47	-0.62	1.51
D	2.20	0.43	3.35	4.03
E	0.02	-0.12	-0.20	0.23

Table 4.4: Corresponding nodal displacement values and their resultant magnitude determined by sub model analysis

Nodes	X-displacement [mm]	Y-displacement [mm]	Z-displacement [mm]	Magnitude [mm]
A	3.94	-0.96	0.42	4.08
B	1.11	0.66	-0.78	1.51
C	1.42	0.57	-0.70	1.68
D	2.45	0.50	3.67	4.44
E	0.02	-0.13	-0.22	0.26

The displacement vectors were matched using the following equation:

$$\cos\theta = \frac{u.v}{\|u\|.\|v\|} \tag{3.1}$$

In equation 3.1, the angle θ is the angle between two equivalent vectors, namely, u and v. The components of the vector u in Cartesian coordinate systems are u_1, u_2, u_3, and the components of the vector v in Cartesian coordinate system are v_1, v_2, v_3. Their resultant magnitudes are calculated using equations (3.2), and (3.3).

$$\|u\| = (u_1^2 + u_2^2 + u_3^2)^{1/2} \tag{3.2}$$

$$\|v\| = (v_1^2 + v_2^2 + v_3^2)^{1/2} \tag{3.3}$$

The dot product of the two vectors is given by:

$$(u.v) = (u_1 v_1 + u_1 v_2 + u_3 v_3) \tag{3.4}$$

For the equivalent vectors, the angle θ has to be zero or at least very small. In this work, small angles were considered (0 to 0.008 radian) for the similar displacement magnitudes using equations (3.1) through (3.4). Table 4.5 tabulates the typical resultant displacement magnitudes. The complete list of resultant magnitudes are given in Appendix B.

Table 4.5: Comparison of the typical resultant displacement magnitudes determined by full model and sub model modal analyses

Nodes	Full model analysis	Sub model analysis
A	3.70	4.08
B	1.36	1.51
C	1.51	1.68
D	4.03	4.44
E	0.23	0.26

4.3.5 Determination of Participation Factors

Participation factors provide a method for judging the significance of the vibration modes that are used for performing these analyses (Humar, 1990; Bhatt, 2002). The diagonal mass matrix was formulated using the connectivity table from the full model analysis. The corresponding mode shapes were determined from the full model Eigen analysis for the preselected 15 nodes, and the participation factors corresponding to these preselected nodes were calculated. The modal participation factor was calculated using the following equation:

$$\Gamma_j = \frac{\overline{\Gamma}_j}{m_{jj}} \tag{3.5}$$

In equation (3.5), Γ_j is defined as the modal participation factor corresponding to the j^{th} mode. Also in equation (3.5), $\overline{\Gamma}_j$ and m_{jj} are defined as excitation factor and

generalized mass corresponding to the jth mode, respectively. The system's excitation factor and generalized mass matrix are defined as:

$$\overline{\Gamma}_j = \phi_j^T MI \tag{3.6}$$

$$m_{jj} = \phi_j{}^T M\phi_j \tag{3.7}$$

In equations (3.6) and (3.7), ϕ_j^T is the transpose of the jth mode, M is the diagonal mass matrix, ϕ_j is the corresponding jth mode and I is the unit vector.

After determining the displacement of selected nodes from the full model Eigen analysis, the magnitudes for these displacement components were calculated to form the modal vectors for selected nodes. Once these vibrating modes were determined, equation (3.5) was used and the participation factors for each node were determined.

After determination of the participation factors, the resultant displacements for the selected nodes from the substructure in the full model were enforced onto the corresponding nodes of the substructure in isolation. This is called mapping the deformations. Here, it is argued that each selected node should deform in a similar fashion as that of the full model. In order to achieve this objective, the participation factor for each dominant frequency for each selected node was considered to be the same for both the substructure *in situ* and the substructure in isolation. The participation factors were determined from the full model modal analysis. Table 4.6 lists typical results for the structure and the substructure in isolation. The lists of complete participation factors, and corresponding frequencies are given in Appendix B.

Table 4.6: Normalized participation factors and their respective frequencies determined by full model FE simulation and sub model modal analyses

Nodes	Participation factors	Frequencies of system (Hz.)	Frequencies of subsystem (Hz.)
A	0.072	636	881
B	0.068	704	1084
C	0.093	851	1302
D	0.095	966	1462
E	0.054	1032	1588

In the following a parametric equation is proposed that gives the velocity required to perform analysis on a substructure in isolation. The equation uses the same participation factors but with different frequencies. One frequency corresponds to the substructure in the full model analysis and the other to the substructure in isolation. The required velocity to perform sub model analysis is determined using the following parametric equation:

$$V_{Comp\ -impact} \sum_{i=1}^{n} \Gamma_i f_{comp\ -i} = V_{sub\ -comp} \sum_{1=1}^{n} \Gamma_i f_{sub\ -comp\ -i} \qquad (3.8)$$

where Γ_i is the participation factor, f is the corresponding frequency for substructure, and i is the number of nodes around the boundary of substructure.

The number of terms in equations (3.8) depends on the number of selected nodes. The participation factor for the selected nodes in the full model and in isolation is taken to be the same. Thus, the required impact velocity for the subcomponent testing can be

determined. Note that the FE analysis of the full model is an integral part of the proposed method as the energy transfer to the subcomponent is determined from the FE analysis of the full model. Therefore, knowing the impact energy and velocity, the impactor mass can easily be calculated using kinetic energy equation

$$E = \frac{1}{2} m V^2 \tag{3.9}$$

Upon balancing the energy transferred from the full model analysis, the internal energy was extracted and its value was equated to the value of the kinetic energy of the moving wall. From equation (3.8), the velocity is determined to be 7.1 m/s. Knowing the kinetic energy of the wall from equation (3.9) and its velocity from equation (3.8), the mass of the wall is determined to be 27.5 [kg].

In these analyses, the existence of the rigid wall is crucial for performing experimental impact testing on the substructure in isolation. For example, if one needs to analyze a subsystem of a system, one no longer needs to analyze the entire system as long as one knows how to implement the correct boundary conditions around the subsystem in isolation. These boundary conditions include nodal displacement (mode shapes), internal energy (energy causing permanent deformation), participation factor and the fundamental frequencies of excitation. Figures 4.15 through 4.22 depict these results. These comparisons included, determining the effective stress, effective plastic strain, internal energy, and resultant displacement for the substructure in a full model and the substructure in isolation.

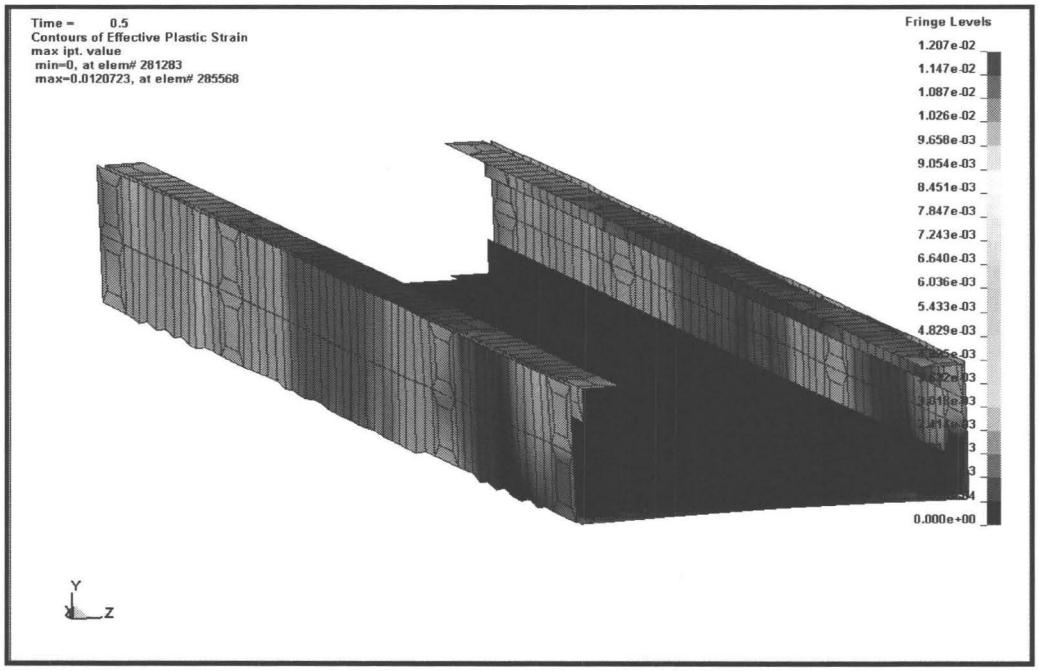

Figure 4.15: Contour plot of effective plastic strain determined by the full model FE simulation

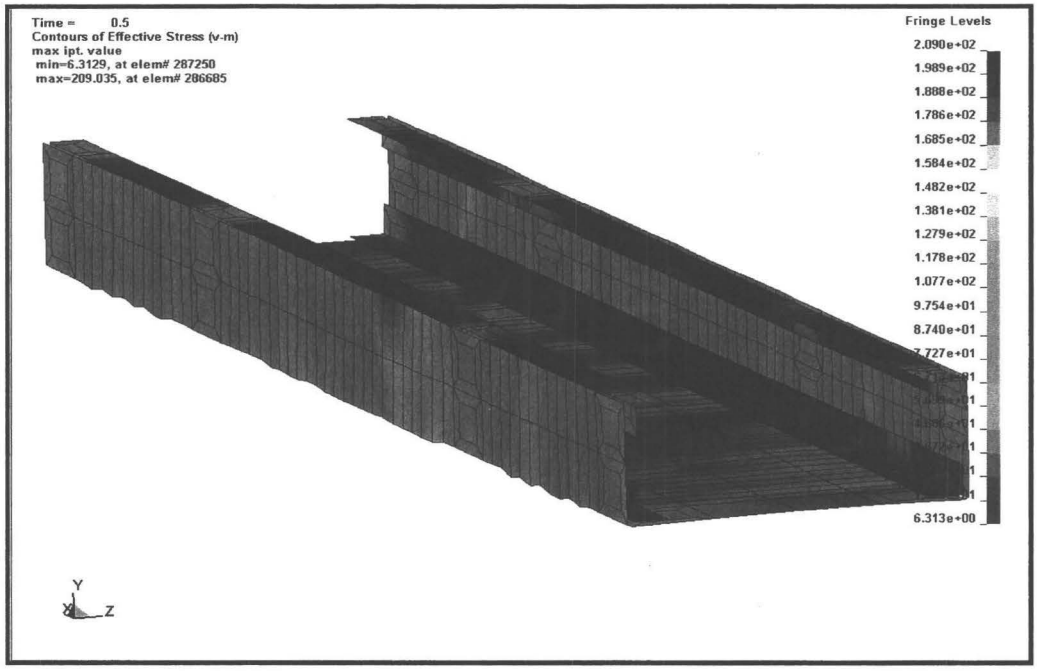

Figure 4.17: Contour plot of effective stress [MPa] determined by the full model FE simulation

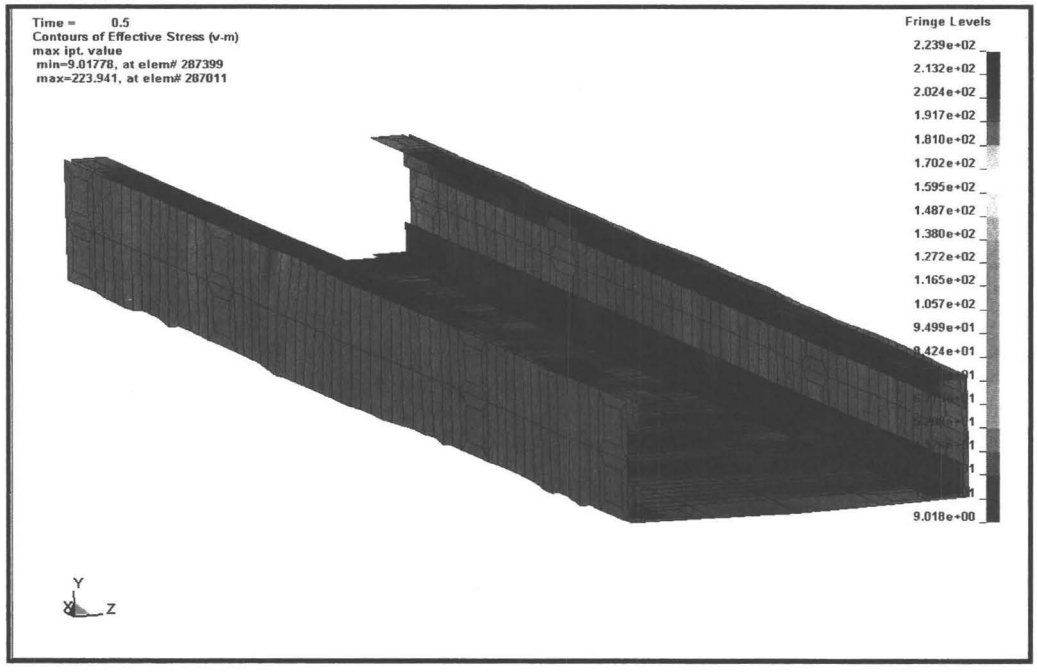

Figure 4.18: Contour plot of effective stress [MPa] determined by the isolated model FE simulation

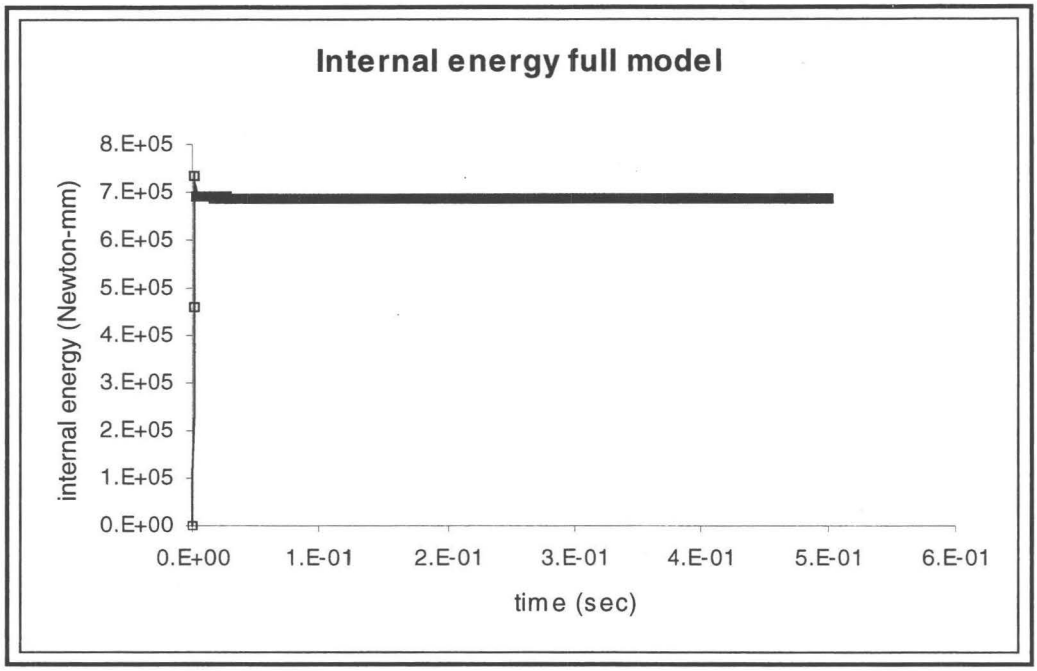

Figure 4.19: Plot of material internal energy determined by the full model FE simulation

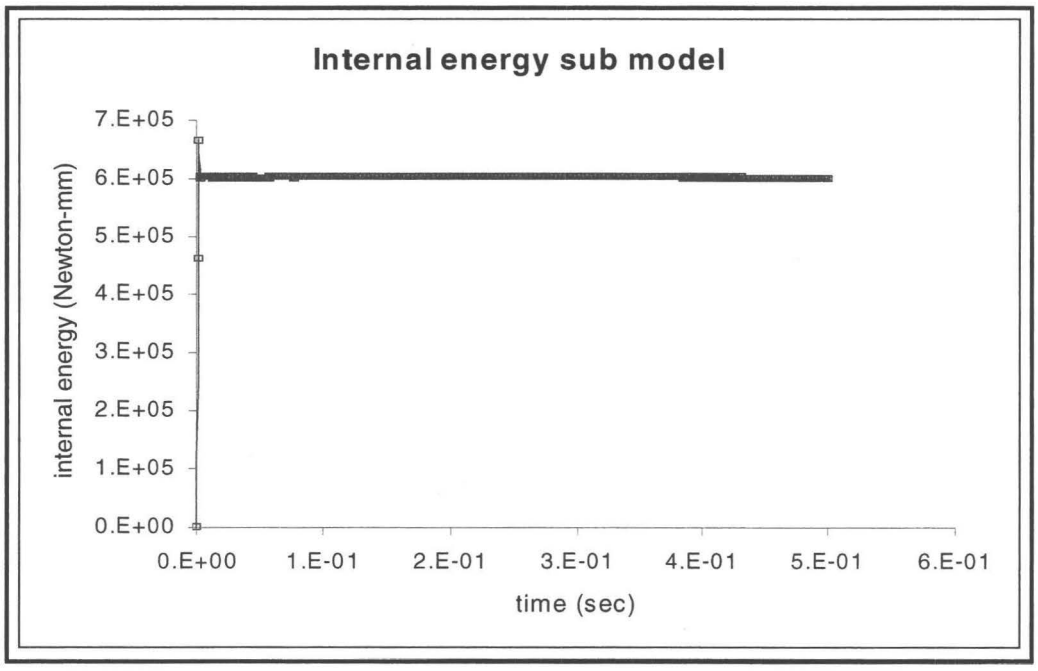

Figure 4.20: Plot of material internal energy determined by the isolated model FE simulation

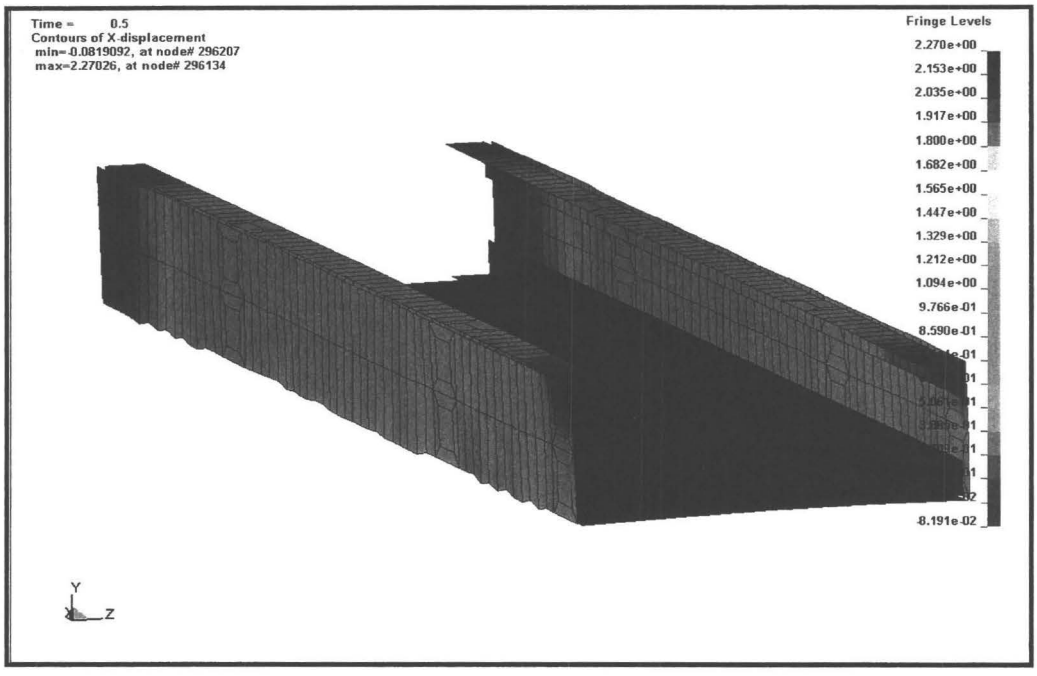

Figure 4.21: Contour plot of x-displacement [mm] determined by the full model FE simulation

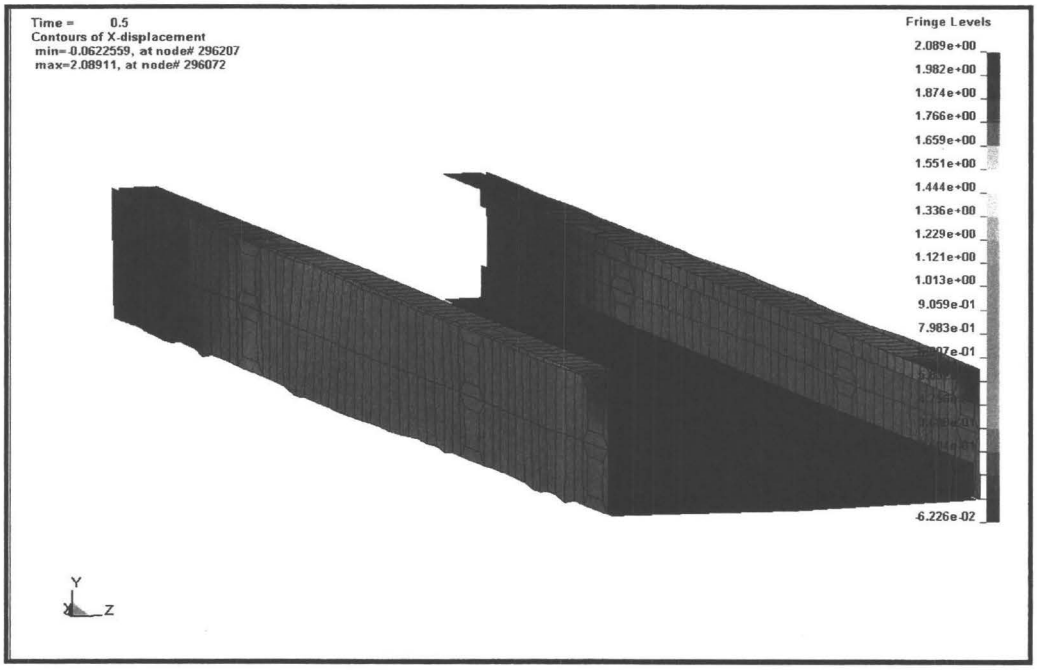

Figure 4.22: Contour plot of x-displacement [mm] determined by the isolated model FE simulation

Table 4.7 compares the various results obtained from these analyses and lists the results. All the comparisons are based on the entire substructure and are global.

Table 4.7: Comparison of the results for a substructure

	Substructure in full model	Substructure in isolation
Effective plastic strain [mm/mm]	1.207e-02	1.186e-02
Internal energy [N-mm]	6.96e+05	6.10e+05
Resultant displacement [mm]	5.12e+00	5.88e+00
Kinetic energy [N-mm]	2.94e+03	2.62e+03
Resultant momentum [kg-mm/s]	6.13e+05	5.87e+05
Computational time	10.12 hr.	4.27 hr.

The full model consisted of 2717 nodes and 2100 elements, and the sub model consisted of 1411 nodes and 1024 elements. The run time was reduced from 10 hours for the full model to 4.5 hours for the sub model. In other words, the computational time reduced by almost 57.8%. The time step for performing the analyses was controlled by shell elements # 289911 and # 285646 for the full model and sub model respectively, which are the smallest sized elements. The time steps for the full model and the sub model simulations were determined to be 1.36e-06 sec., and 1.46e-06 sec., respectively. The maximum effective plastic strain for both models was determined to be 0.01207 [mm/mm] and 0.01186 [mm/mm], which corresponds to the same element in both FE models.

For the purpose of substructural analysis, an identical FE model of the substructure was created. For consistency and to reduce error introduced by the FE analysis, identical mesh size and material properties were used for the substructure. Additionally, the same boundary conditions and contact conditions between the rigid-wall and the isolated substructure were used. Subsequent to the above comparisons, detailed analyses were performed on the node and element basis. Figure 4.23 depicts the locations of certain selected nodes and elements. These detailed analyses were performed on a few randomly selected nodes and elements along the boundary of the substructure.

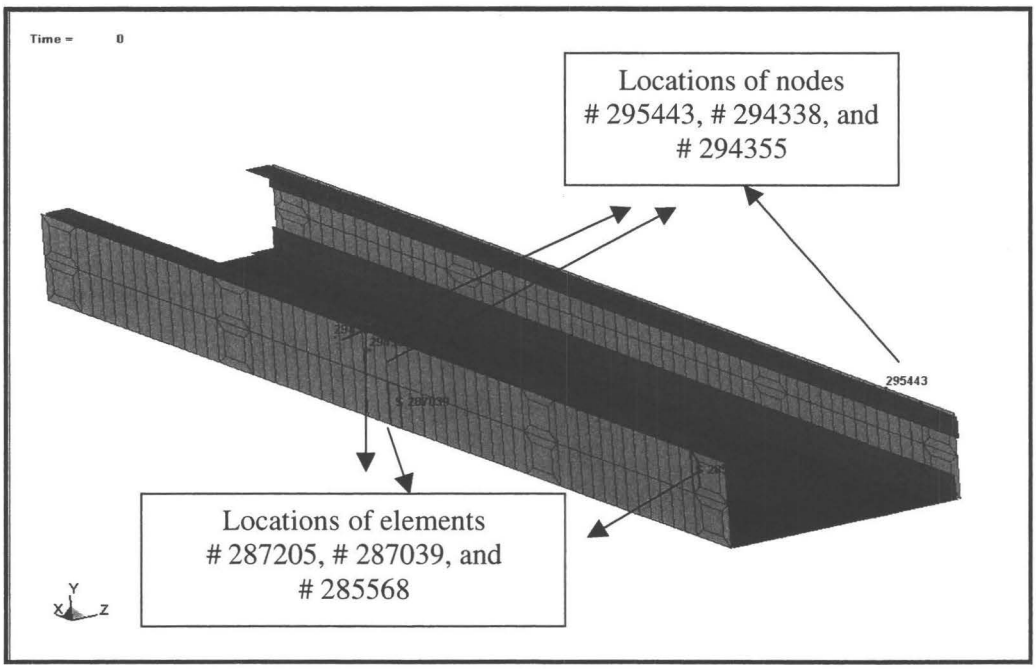

Figure 4.23: Locations of randomly selected nodes and elements for detailed analyses, along the boundary of substructure

These detailed analyses include the comparison of resultant displacements, resultant velocities, and effective plastic strains for preselected elements between the full

model and the sub model. Figures 4.24 through 4.29 depict some of these results. The results from these analyses were compared for the substructure in a full model and the substructure in isolation (additional comparisons are shown in Appendix D).

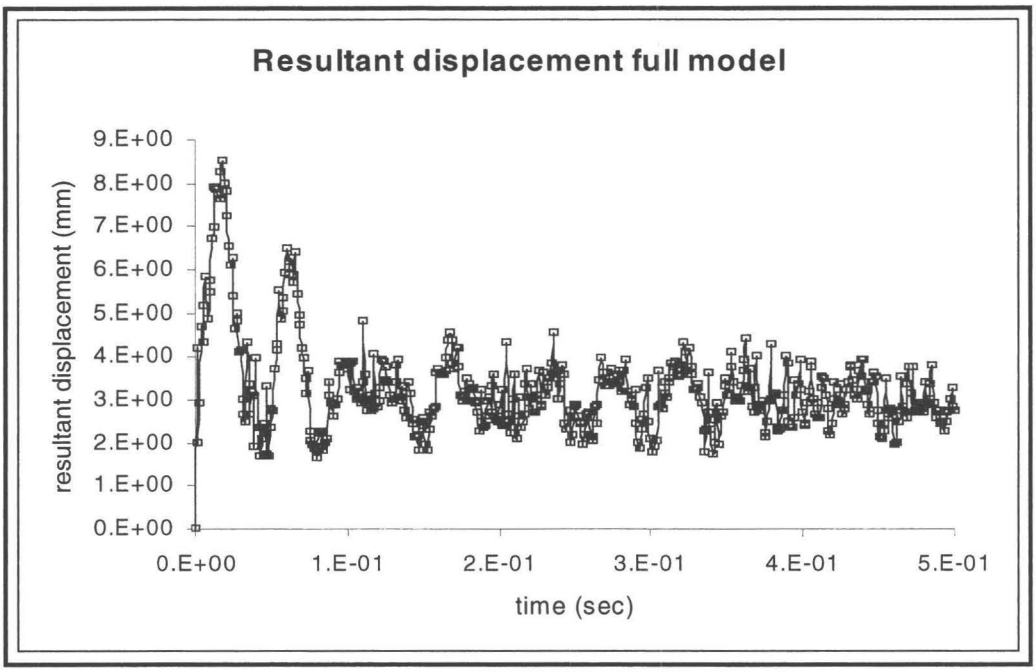

Figure 4.24: Plot of resultant displacements for node # 295443 determined by the full model FE simulation

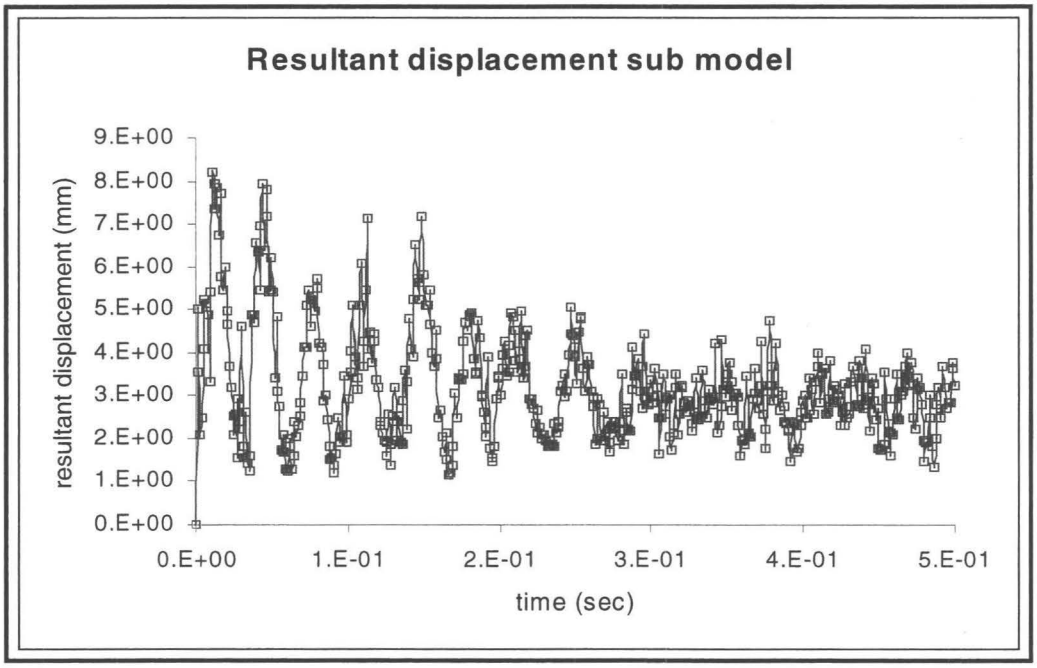

Figure 4.25: Plot of resultant displacements for node # 295443 determined by the isolated model FE simulation

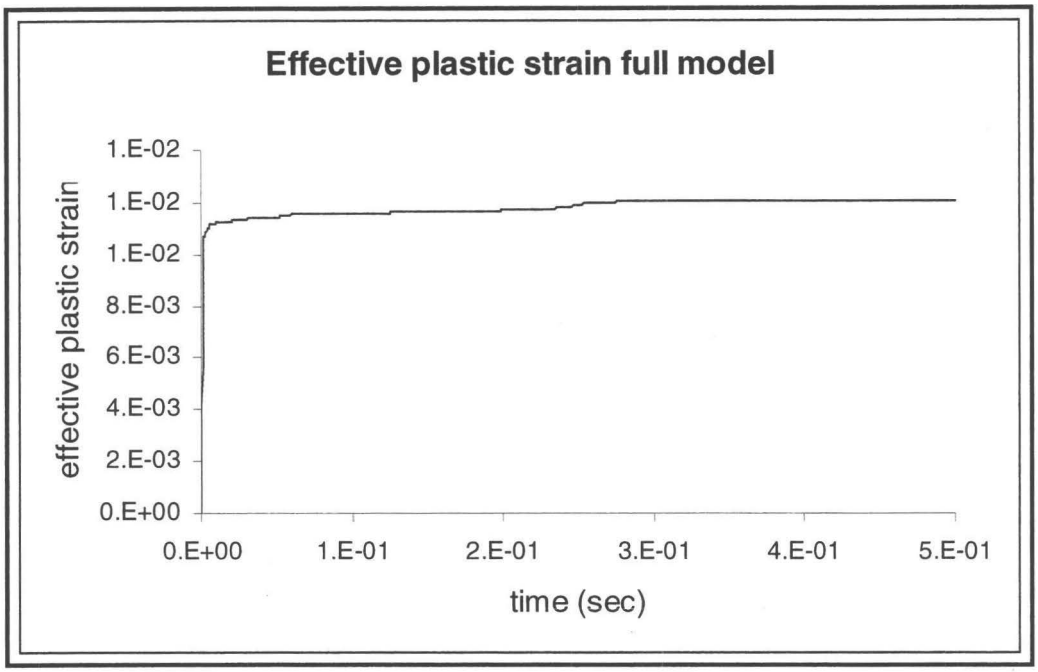

Figure 4.26: Plot of effective plastic strain for element # 285568 determined by the full model FE simulation

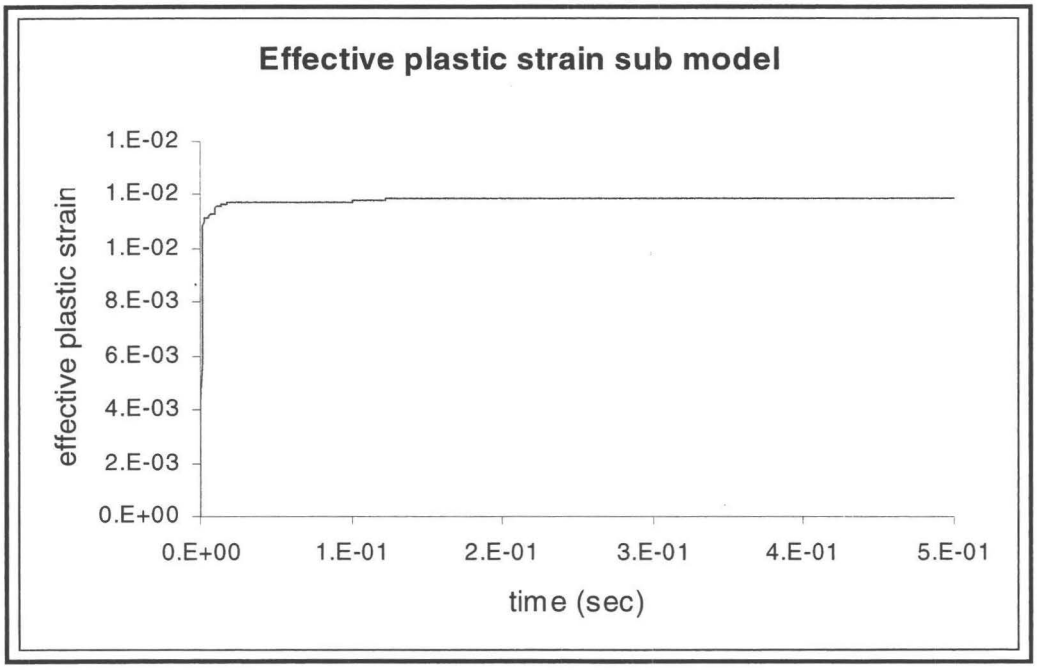

Figure 4.27: Plot of effective plastic strain for element # 285568 determined by the full model FE simulation

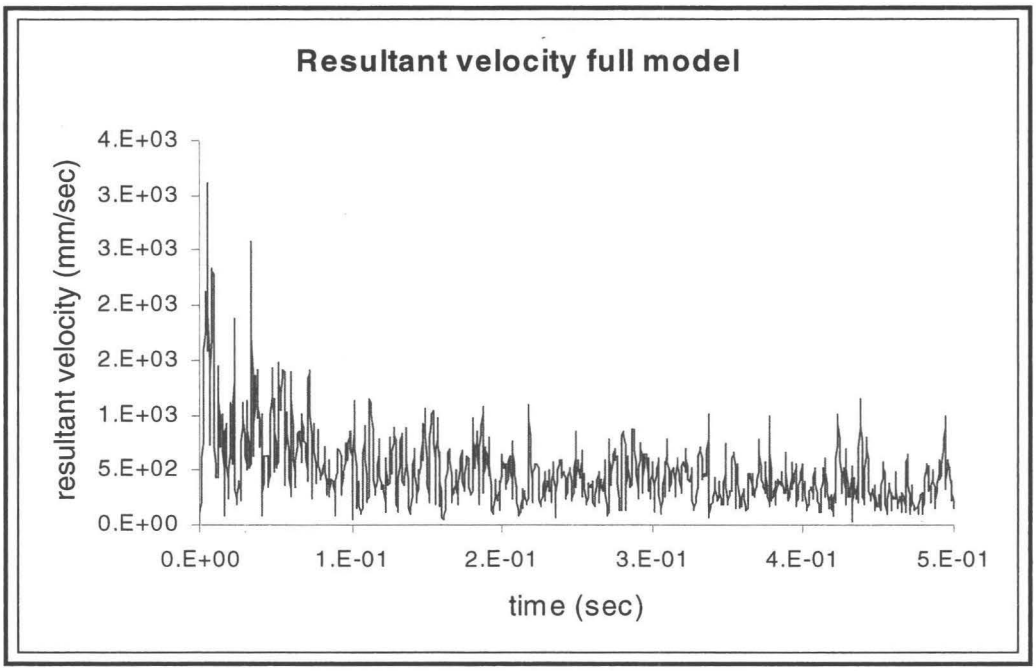

Figure 4.28: Plot of resultant velocity for node 294338 determined by the full model FE simulation

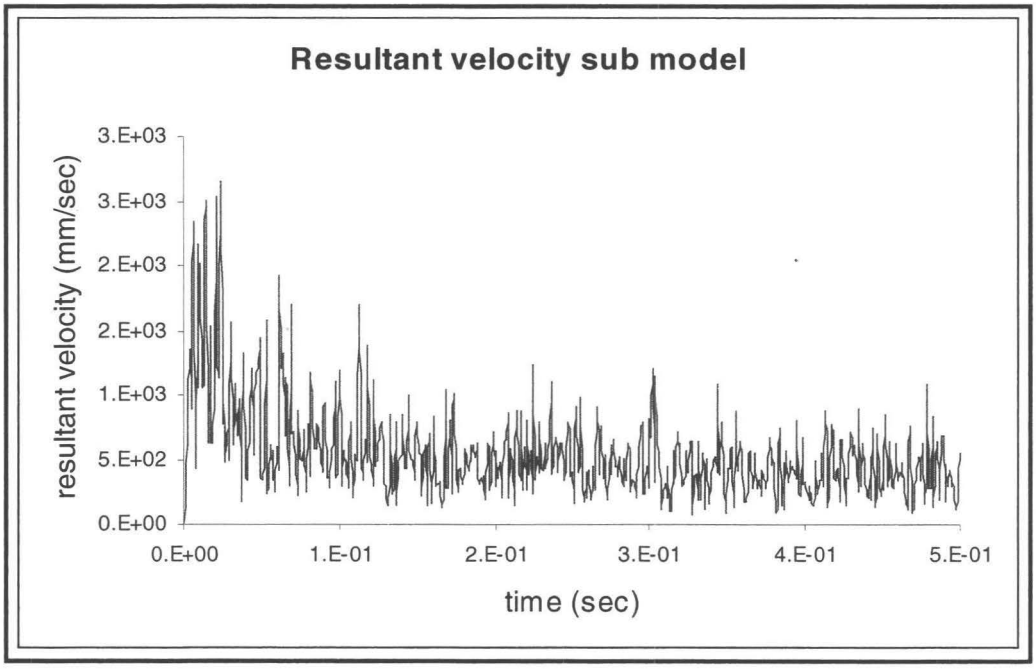

Figure 4.29: Plot of resultant velocity for node 294338 determined by the isolated model FE simulation

The termination time for both analyses was set to 0.5 second for stresses to be settled and then results were compared to each other. The results obtained from these analyses using the proposed methodology were compared at the end of termination time for both the full model and sub model analyses.

4.3.6 Further Comparisons of Structural Component

The FE analyses were performed in two stages. In stage one, the structure was impacted by the rigid wall moving at a prescribed mass and velocity. In stage two, by using the developed methodology, the FE analysis was performed on the substructure in isolation. The main objective was to simulate an isolated substructure such that it behaved in a similar manner as a substructure within a full model. The rigid wall was used for both stages of these analyses and results were compared between a substructure in a full model and a substructure in isolation.

In addition, the deformed configurations obtained from these two analyses were compared with each other. Figures 4.30 and 4.31 depict the deformed configuration of the substructure determined by full model and sub model simulations. In these figures, the x-axis was in the direction of the impact, and the z-axis corresponded to the out-of-plane deformations. The out-of-plane deformations in the middle and front sections were more than rear sections. The front section was the impacting end and the rear section was the fixed end. In addition, the out-of-plane deformations of the right and left sides of the rear section were similar for both numerical models.

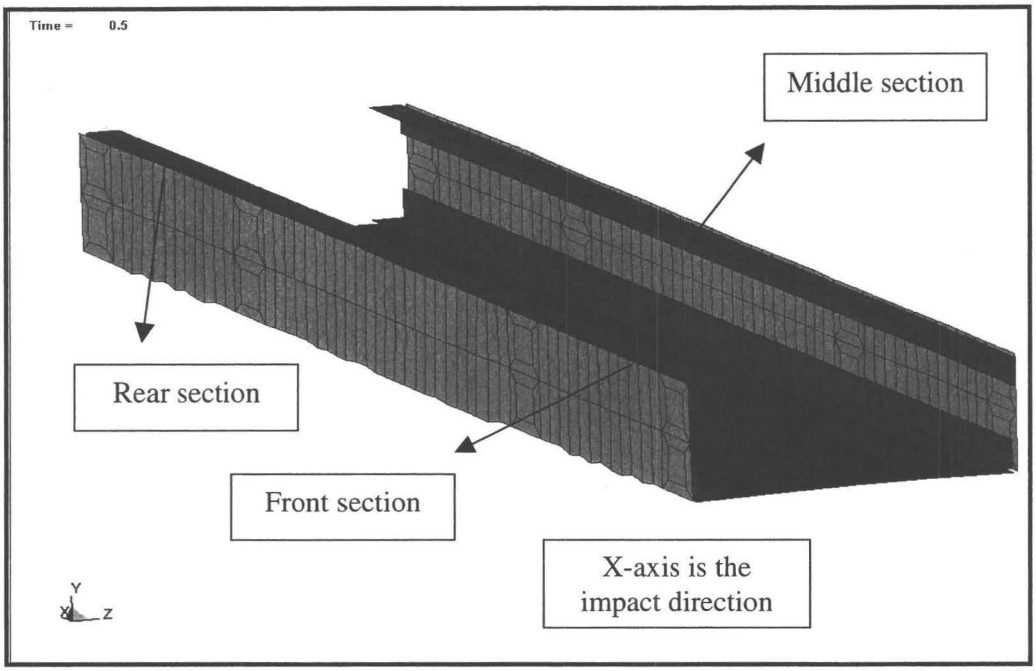

Figure 4.30: Deformed configuration of the substructure determined by the full model FE simulation

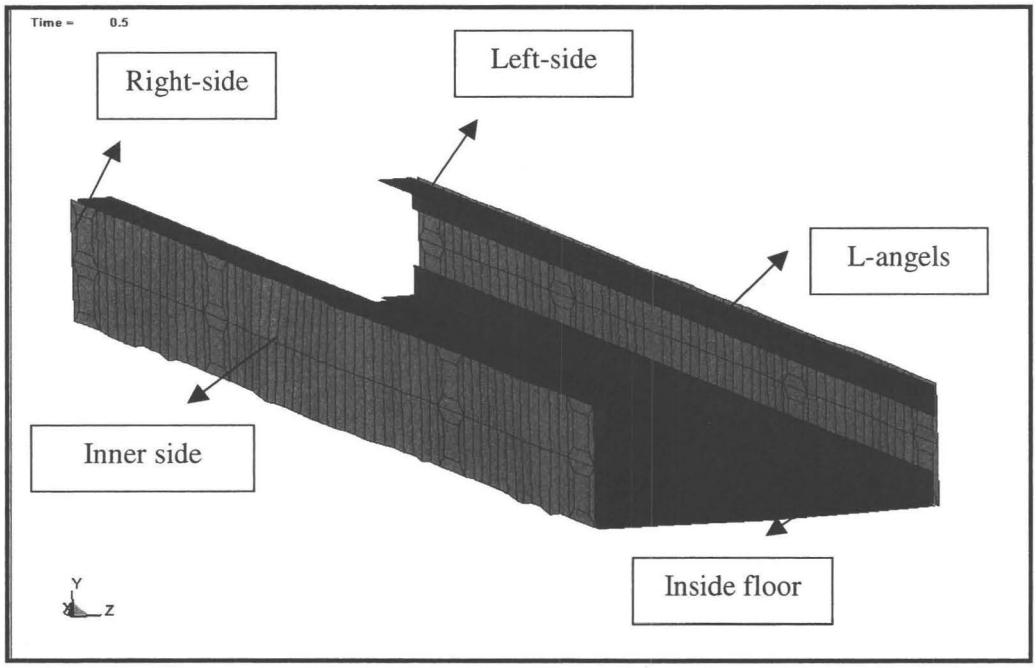

Figure 4.31: Deformed configuration of the substructure determined by the isolated model FE simulation

A series of measurements were also taken along the x-axis that measured the reduction in length along the impact direction (refer to Figure 4.30). Measurements were taken at different sections, namely, the front, middle, and rear sections (as shown in Figure 4.30), of the substructure from both FE simulations. These measurements were taken along the inner-side components on both the left and right sides, which corresponded to the reduction in length along the x-axis (as shown in Figure 5.15). The results obtained from these measurements are listed in Table 4.8.

Table 4.8: Comparison of the measurements along the x-axis determined by the full model and sub model simulations

		Dimensions of substructure in full model [mm]	Dimensions of substructure in isolation [mm]
Front Section	Original Length	241.4	241.4
	Left side	241.045	240.789
	Right side	241.080	240.811
Middle Section	Original Length	482.8	482.8
	Left side	482.256	482.268
	Right side	482.249	482.230
Rear Section	Original Length	241.4	241.4
	Left side	240.697	241.119
	Right side	240.699	241.130

For the front section on the left and the right side of the structure, the error between the two analyses was determined to be approximately 0.11%. In addition, for the middle section on the left and the right sides, the error between the two analyses was determined to be approximately 0.004%. For the rear section, on both the left and right side, the errors were determined to be 0.17% and 0.18%, respectively. Table 4.9 lists

typical measurement data corresponding to the out-of-plane deformations. Complete lists of measurement data are given in Appendix C.

Table 4.9: Comparisons of the out-of-plane deformations determined by the full model and sub model FE simulations

Substructure in full model, Numerical dimensions in [mm]			Substructure in isolation, Numerical dimensions in [mm]		
Front	Middle	Rear	Front	Middle	Rear
9.22	6.49	5.45	9.96	6.85	5.19
10.10	6.10	5.92	10.88	6.95	5.42
10.27	6.23	6.13	11.24	7.21	5.66
10.39	5.94	6.23	11.84	6.81	5.77
10.65	6.91	6.31	12.33	7.52	5.90

The measurements tabulated above were taken from the front section, middle section and rear section along the z-axis, and compare the out-of-plane deformations between a substructure in a full model and a substructure in a sub model. Figure 4.32 depicts a graphic comparison corresponding to out-of-plane measurements. At each section, namely, front, middle and rear, a total of 8 nodes were selected and the corresponding out-of-plane displacements were measured for both substructure. The minimum and maximum discrepancies were determined to be 4.81% and 13.67%, respectively.

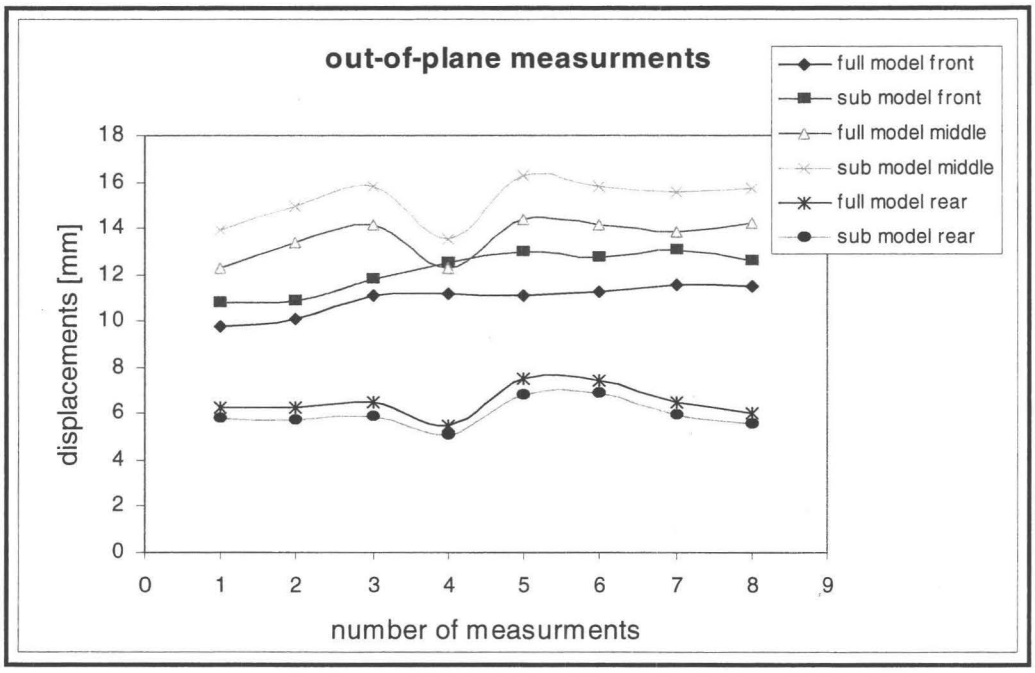

Figure 4.32: Out-of-plane deformations along the z-axis corresponding to the front, middle, and rear sections determined by full model and sub model simulations

The average errors were determined to be 9.18% for front section, 10.41% for the middle section and 7.74% for the rear section (refer to Figures 4.30 and 4.31). The locations of these measurements are provided in Appendix C.

It was observed that out-of-plane displacements corresponding to the isolated substructure, in the front and middle sections, were more than the out-of-plane displacements, corresponding to the same sections, in a substructure in a full model. The out-of-plane displacement of the geometric mid point in the front section of the isolated substructure was measured to be 12.25 mm; and for the same node in the full model, the middle node displacement was measured to be 10.91 mm, which translates to an 11.01% difference. In the geometric mid point of the middle section, the maximum out-of-plane

displacement in full model and sub model analyses were determined to be 10.03 mm and 8.94 mm, respectively, which translates to a 10.84% difference.

The discrepancies in measurements can be related to the excitation frequencies and the free boundaries. However, the deformed configurations were very similar. In the rear section, where the boundary was fixed, the amount of out-of-plane displacements was minimal as compared to the front and middle sections. The same observation was made in the rear section for both FE models. In the rear section, the out-of-plane displacement for the geometric mid point was measured to be 6.74 mm and 6.25 mm in full model and sub model, respectively. That translates to a 7.33% difference. The out-of-plane displacements for the rear section were higher in the full model as compared to the sub model. However, the overall deformed configurations were very similar in both FE models.

Also, a series of additional comparisons were made on the nodal and elemental basis for a few randomly selected nodes and the results were compared between the two FE models (as shown in Figure 4.23). A detailed analysis between the structure and substructure was performed on the nodal and elemental basis to investigate various similarities and differences between the two models. Figures 4.33 – 4.38 depict these comparisons.

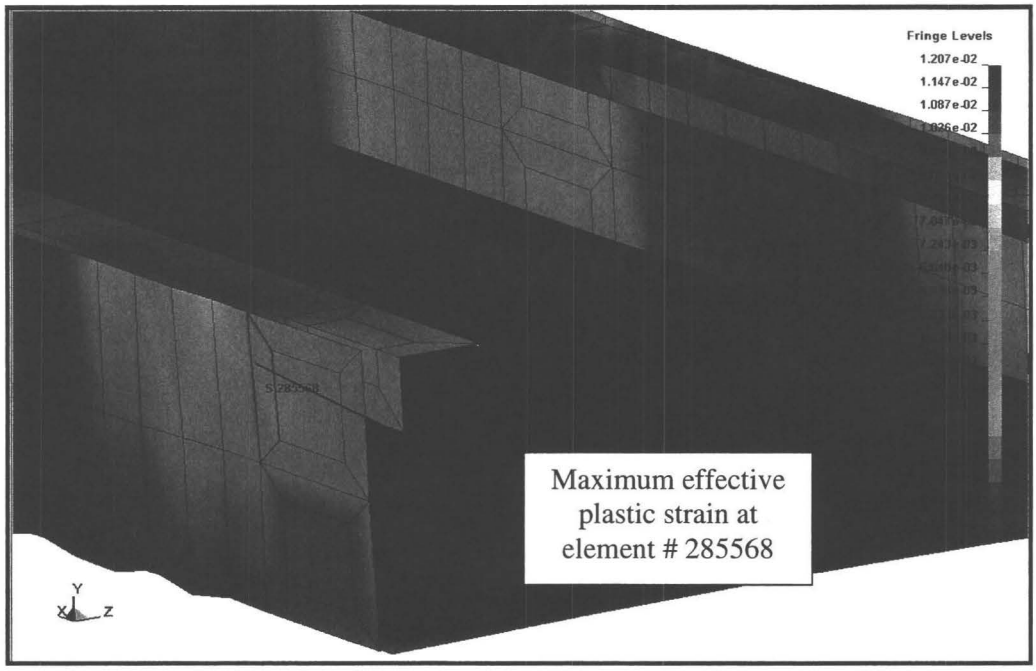

Figure 4.33: Contour plot of the effective plastic strain and the location of the maximum plastic strain determined by full model FE simulation

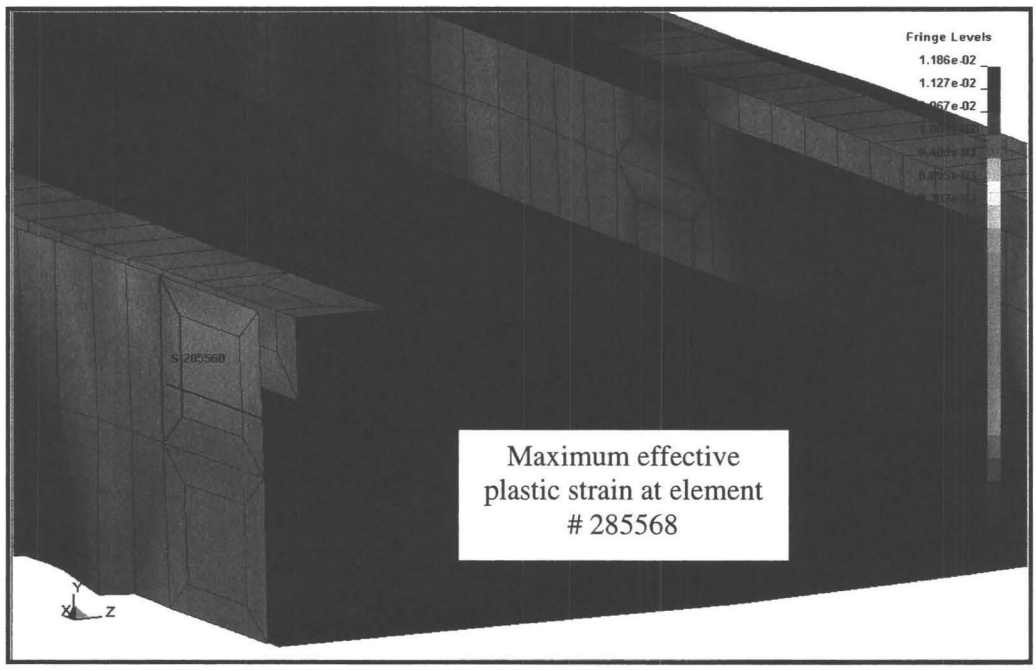

Figure 4.34: Contour plot of the effective plastic strain and the location of the maximum plastic strain determined by isolated model FE simulation

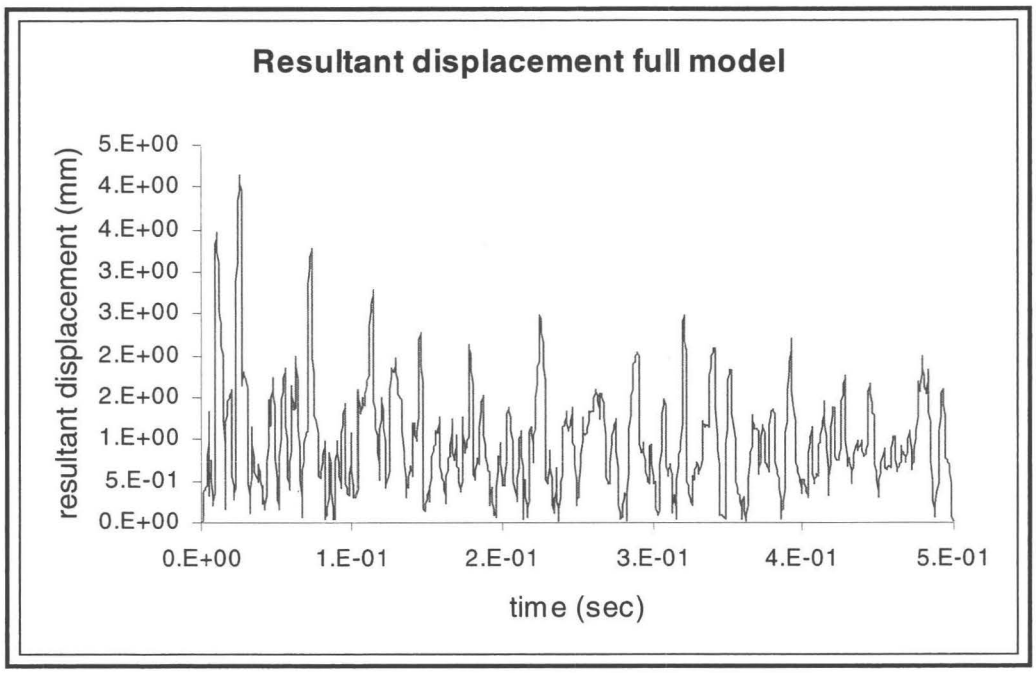

Figure 4.35: Plot of the resultant displacement [mm] for node # 294355 determined by full model FE simulation

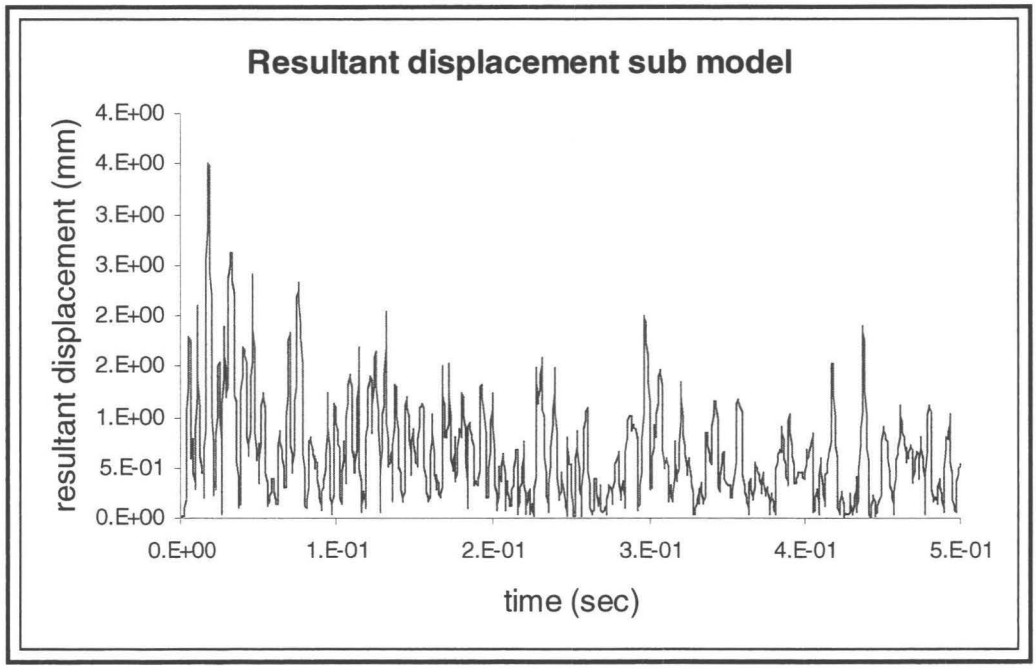

Figure 4.36: Plot of the resultant displacement [mm] for node # 294355 determined by isolated model FE simulation

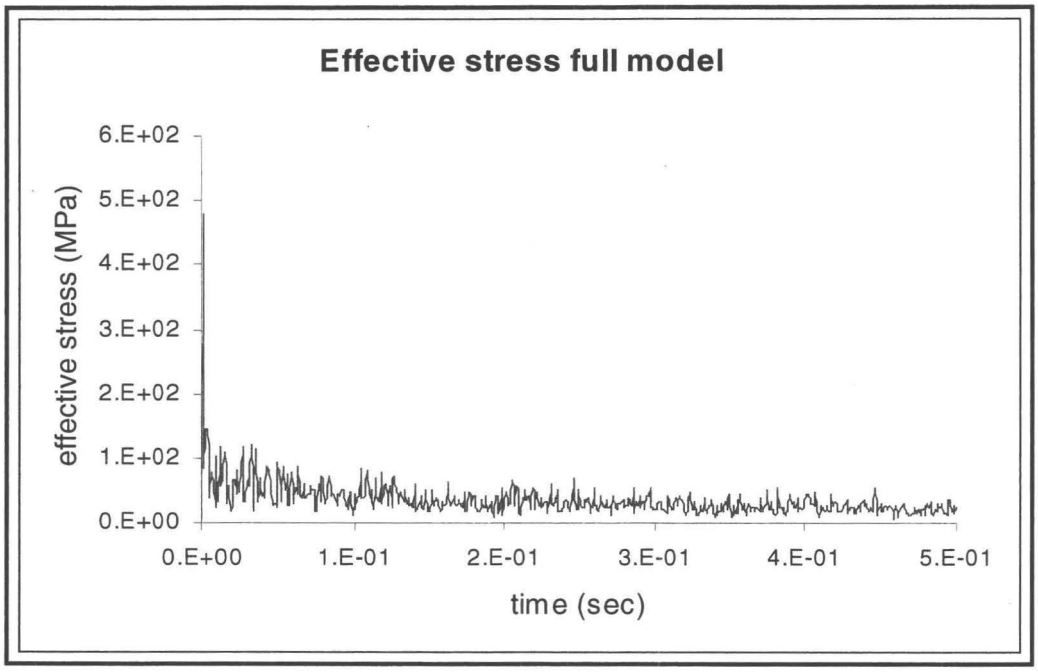

Figure 4.37: Plot of the effective stress (v-Mises) [MPa] for element # 287205 determined by full model FE simulation

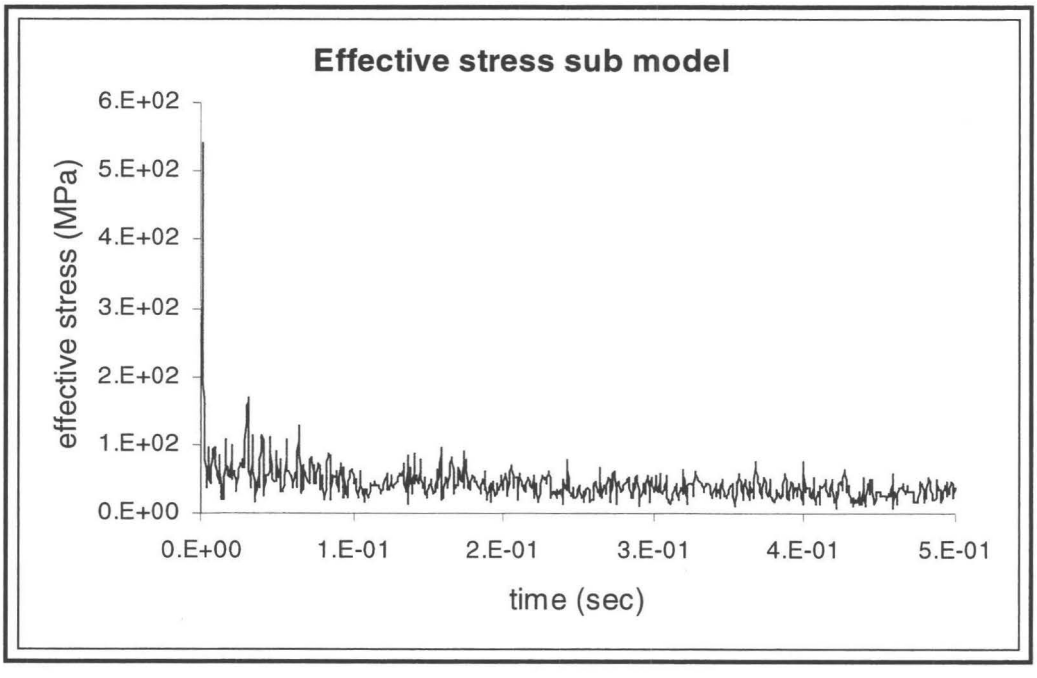

Figure 4.38: Plot of the effective stress (v-Mises) [MPa] for element # 287205 determined by isolated model FE simulation

Table 4.10 compares the calculated errors for stresses, strain, internal energies, and resultant displacements and velocities at the termination time (0.5 sec.) for both stages of the analyses.

Table 4.10: Comparisons of the errors determined by full model and sub model FE simulations

Substructure, Full vs. Isolated	Percentage of Error%
Effective plastic strain	1.74%
Internal energy	12.48%
Kinetic energy	10.61%
Resultant momentum	4.24%
Resultant displacement	12.87%

The discrepancies between the results shown in Table 4.10 can be related to two main factors: 1) energy absorption and 2) matched displacements. The energy transferred from the full model transient analysis was based on the amount of internal energy transferred to the substructure in the full model analysis. Since the internal energy was the main source that caused permanent deformation, the internal energy was used in the calculation of the speed and mass for the substructural testing simulation. Other energy sources, such as stonewall energy, system damping energy, and sliding interface energy were considered to be the source of the variations that caused internal energies to deviate from the full model compared to the sub model. These energies contributed to the slight

deviation of the deformed configuration and the mechanical response of the substructure in isolation.

Table 4.11 lists resultant displacements with their associated discrepancies obtained from comparing these values from the full model onto the sub model. The nodes used for these comparisons are shown in Figure 4.14.

Table 4.11: Error analysis of the resultant displacements determined by full model and sub model modal analyses

Nodes	Resultant displacements full model [mm]	Resultant displacements sub model [mm]	Error% percentage
A	3.70	4.08	9.35%
B	1.36	1.51	10.04%
C	1.51	1.68	10.14%
D	4.03	4.44	9.29%
E	0.23	0.26	10.50%
F	2.31	2.55	9.47%
G	1.14	1.27	9.63%
H	3.50	3.92	10.58%
I	0.35	0.39	10.34%
J	2.48	2.75	9.87%
K	5.86	6.53	10.27%
L	0.95	1.05	9.74%
M	6.85	7.55	9.22%
N	0.90	1.01	10.69%
O	1.53	1.69	9.59%

The other source of error was due to the nodal displacements, corresponding to the mode shapes. The mode shapes were approximated (not exact values) and, have also

contributed to the slight deviation in results as listed in Table 4.11. These nodal displacements were matched to within 9% to 11% error from the full model onto the sub-model. However, in this analysis, unlike the previous FE analyses, the substructure was impacted by the rigid wall, which allowed one to perform impact analysis on an isolated substructure.

It was extremely important to determine the validity of the results in full system FE analysis, as it was the basis for substructural simulation. To validate the FE results, a test article was fabricated and experimentally tested using a component testing apparatus. It is extremely important, as experimental testing is vital for validating the structural component as required by crashworthiness analysis.

In all, the analysis was performed using three different FE models and the results were compared for the full model analysis and the sub model analysis. The latest analyses were performed using a rigid wall for the structure and the substructure in isolation. The introduction of the developed technique in substructural testing was presented using the FE method.

Chapter 5
Experimental Apparatus, Testing Procedures and Results

5.1 Introduction

In general, Experimental testing is performed to validate the results of numerical simulation. Thus, the purpose of the experimental testing was two-fold:

- To provide a benchmark for the validation of the FE results for the full structure testing prior to the application of the developed method
- To study the applicability of the introduced method in experimental settings

To achieve these goals, a component impact testing apparatus was designed and built at Ryerson University. The apparatus was designed and commissioned by Dr. Behdinan (supervisor) and Dr. Ghaemi. A brief overview of the apparatus' functionality and limitations are provided. Please note that detailed information such as the pneumatic circuit, fail-safe circuitry, etc, are proprietary and cannot be disclosed here.

To achieve these goals, a component impact testing apparatus was designed and built. The component testing apparatus can be used to perform dynamic testing on small to medium size components. This chapter is divided into two main sections, namely, a) a description of the experimental apparatus and b) procedures for the experiment to perform impact analyses and experimental results.

5.2 Experimental Apparatus

The testing apparatus was comprised of the following:

- Pressure vessel
- High speed ball valve assembly and pneumatic actuator
- Holding frame for the actuator assembly
- Holding frame for components and test article
- Railing frame and damper
- Impactor
- Series of pressure gauges and limit switches.

The experimental apparatus and its components are explained in detail in Appendix E.

5.2.1 Design Limitations

The largest test article that can be examined by this apparatus is 2.2 m in length and the smallest test article is 1.0 m in length. However, the smallest test article size was not considered to be a limitation as the holding fixture could have provided the means of testing smaller test articles. There were two specific limitations associated with this apparatus, namely, speed and accelerating mass. The supply pressure from the vessel and the impacting properties of the railing system determines the maximum speed. The minimum speed is determined by the break out pressure of the cylinder, which, was determined to be 344 kPa after initial calibration and proof testing of the apparatus.

This apparatus was manufactured such that the maximum speed of 15 m/s was permissible. The pressure capability of the tank and the pneumatic actuator can be used to achieve higher speed, but the system was designed to withstand impact energy achieved by 15 m/s and mass of 100 kg. During the testing and calibration of the apparatus this speed was never achieved, as the main supply pressure was not sufficient to achieve the maximum speed. This was taken into account during the design process and a pressure switch and a valve were incorporated into the intake manifold of the pressure vessel.

The operator could switch the supply pressure from the main line to a nitrogen tank if a higher pressure was desired. The minimum speed was determined to be 5 m/s. This speed corresponded to the minimum pressure required to move the cylinder, which was 345 kPa.

The accelerating mechanism mass is the combined mass of the cylinder ram (extension arm) and the stopping end plate. In the existing design, the mass of the actuator ram and stopping end plate was measured to be 60 kg in total. The accelerating mechanism comes to a complete stop when it contacts the rubber dampers of the railing assembly. Thus, the bounce back energy of the damper that reflects back onto the accelerating mechanism should not exceed its critical energy absorption capacity. It is to be noted that the accelerating mass is not the impacting mass.

5.2.2 High-Speed Camera

To accurately measure the impacting speed just prior to impact, a high-speed camera was incorporated into the system (Troubleshooter HR, High speed Imaging Inc,

Markham, Ontario, Canada). The camera had a maximum capture speed of 16000 frames per second at a resolution of 1280 by 32 pixels. However, the speed and resolution could be changed according to the field of view desired for a specific impact testing. For this experiment, 1000 frames per second at 640 by 480 frame resolution was chosen which resulted in 4.4 seconds of recording time and 4368 frames. The main purpose of the inclusion of the camera was to measure the speed as well as allow for visual inspection of the experiment. In addition, a high-speed, a capture card and software MIDAS 4.0 Express was incorporated.

5.2.3 Pressure-Velocity Correlation

Once the apparatus was completed, a series of tests were performed to determine the velocity at a given pressure. This provided the operator with an excellent estimation of the velocity achieved by the impacting head for a given pressure in the storage tank. High-speed camera described earlier was used to measure the velocity of the impact just before the impact took place. Figure 5.1 depicts the pressure-velocity profile. The pressure-velocity profile was used to determine the required pressure for a desired velocity.

5.3. Experimental Procedures

This section introduces procedures for performing the experimental analyses. The experimental impact testing was performed on two different structural components. The numerical analyses for both structures were discussed in detail in the previous chapter. The impact energy and boundary conditions in the experimental work were identical to those used in the numerical work. Much like the numerical study, the experimental work consisted of two stages: 1) testing the entire component and 2) testing the subcomponent.

5.3.1. Experimental Testing of Modified Design

This section describes the impact testing of the modified design that was mentioned in the previous chapter. The structure was made from structural steel and its components were connected to each other using plug-welds. The structure consisted of one floor, two rails, and three stiffening bars. In order to compare the experimental and numerical results, two accelerometers were connected to the floor and accelerometer data was collected during the experiment. The accelerometers were connected to the floor by means of dental glue on the left rail at two locations sufficiently away from the impact point to avoid damage. The accelerometers had 100 G capacity with 50% over load protection. Therefore, if the impact acceleration exceeded the limits by 50%, the accelerometer would not have been damaged. The accelerometer was capable of reading 980 m/s with 0.01% accuracy. The comparison of acceleration data between the numerical model and experimental test are given in Chapter 6. Figures 5.2 and 5.3 depict

the deformed configuration of the test article (full model) and the subcomponent (left-rail).

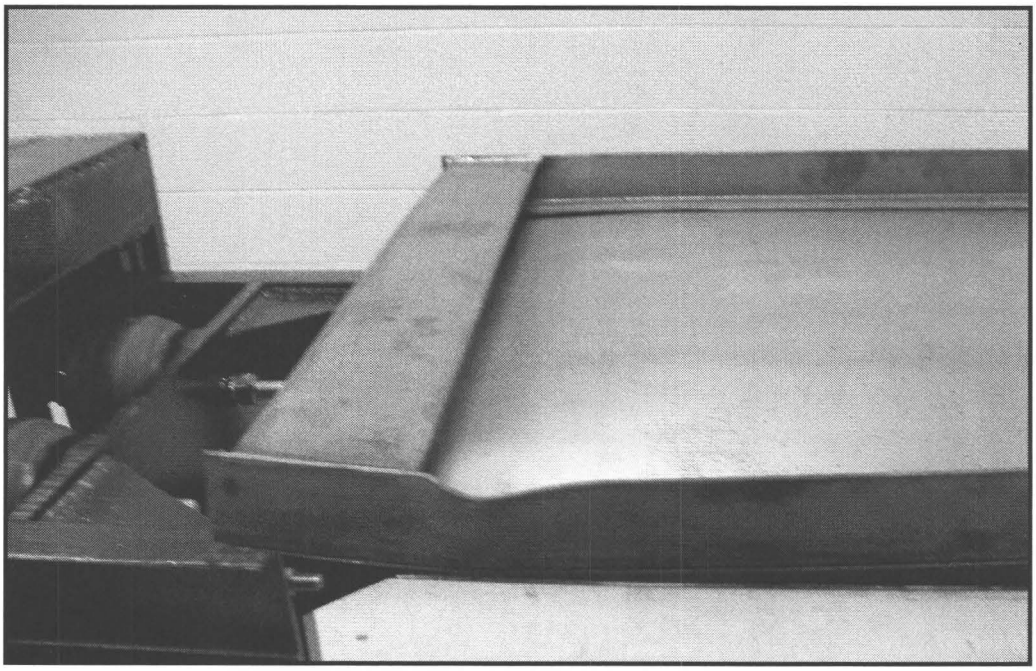

Figure 5.2: Deformed configuration of the test article (modified design)

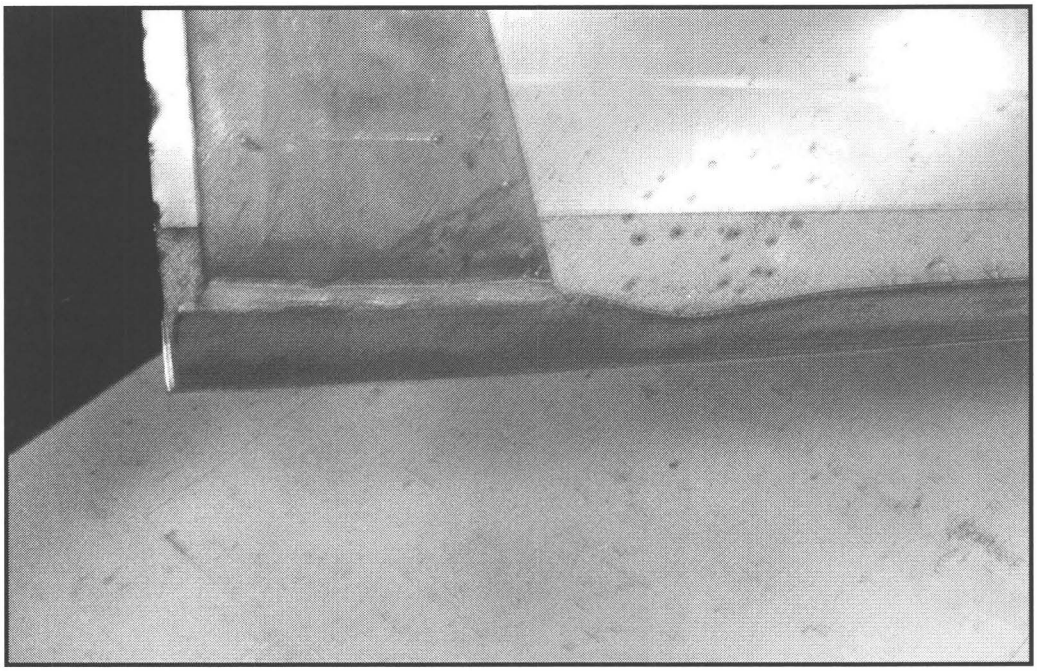

Figure 5.3: Deformation of the left-rail determined by experimental testing

5.3.2. Experimental Testing of Structural Component

This section introduces the experimental work corresponding to the third FE model (as shown in Figure 4.8). The experimental work was performed based on the developed methodology presented in Chapter 4. In this experimental work, accelerometers of ± 1000 G with 1 Hz to 10 kHz of broadband resolution were used to ensure the accelerometers captured the entire history of the impact (Dalimar Instrument, Vaudreuil-Dorion Quebec, Canada). The impact energy and boundary conditions in the experimental work were identical to the numerical work.

5.3.2.1. Experimental Testing

A specialized fixture was designed and manufactured for holding the structure and also for connecting the fixture to the holding frames. The boundary conditions at the end location where the fixture connects the structure to the impact testing apparatus was fixed. As a result, there was no translational and rotational motion at the end where the structure connected to the holding frames. Four accelerometers were used for performing impact analysis on the entire structure.

In order to correlate the experimental results with the analytical results, four nodes from the numerical model were picked that had the same physical location as the accelerometer. In these analyses, 1-D accelerometers were used that measured the acceleration only in the impact direction. Therefore, the z-component of accelerations were used in the FE analyses. Figure 5.4 depicts the location of the accelerometers in the FE model.

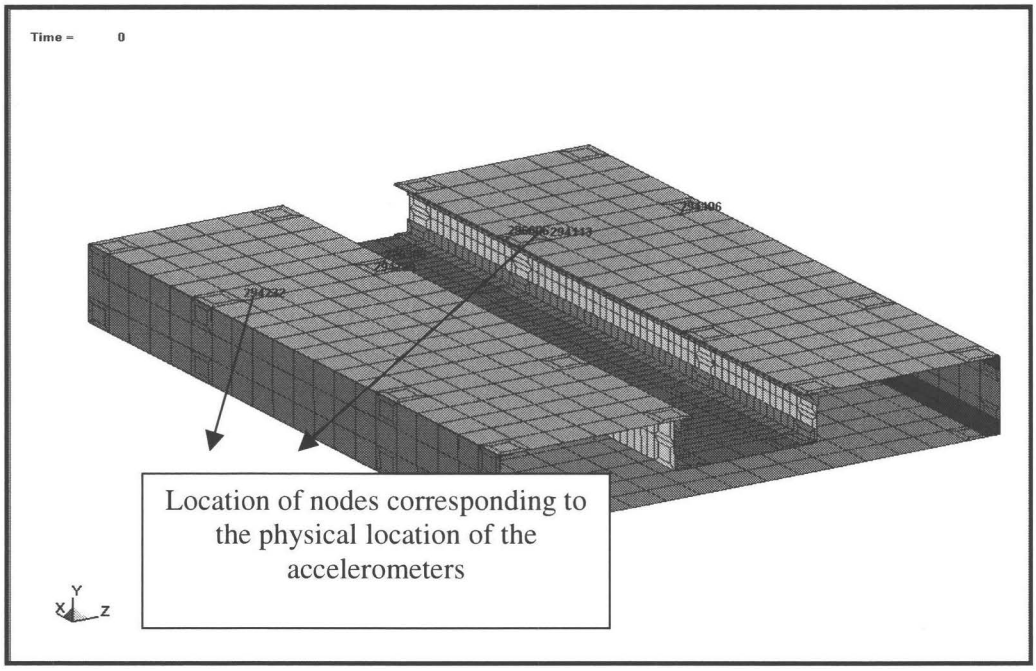

Figure 5.4: Locations of the accelerometers on the full finite element model

In this experimental testing, the structure was fixed and impacted on by the rigid impactor that was moving with a speed of 10.5 m/s and a mass of 72 kg. Figures 5.5 and 5.6 depict the deformation of the structure and substructure within the structure, respectively. As can be seen from (Figures 5.5 and 5.6), the out-of-plane deformations were larger in front and middle sections as compared to the rear sections, which is the fixed end. For clarity, the out-of-plane deformation in the middle, rear and the front section of the structure is shown on Figure 5.5. Similarly, the same locations for out-of-plane deformation for substructure are shown in Figure 5.6.

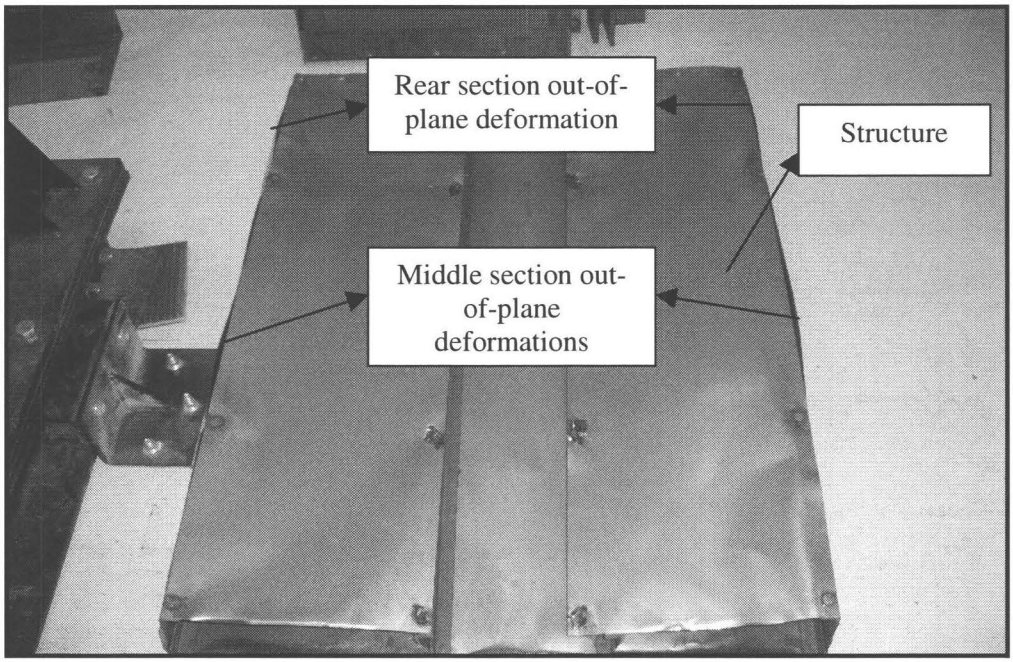

Figure 5.5: Deformed configuration of the entire structure determined by experimental testing

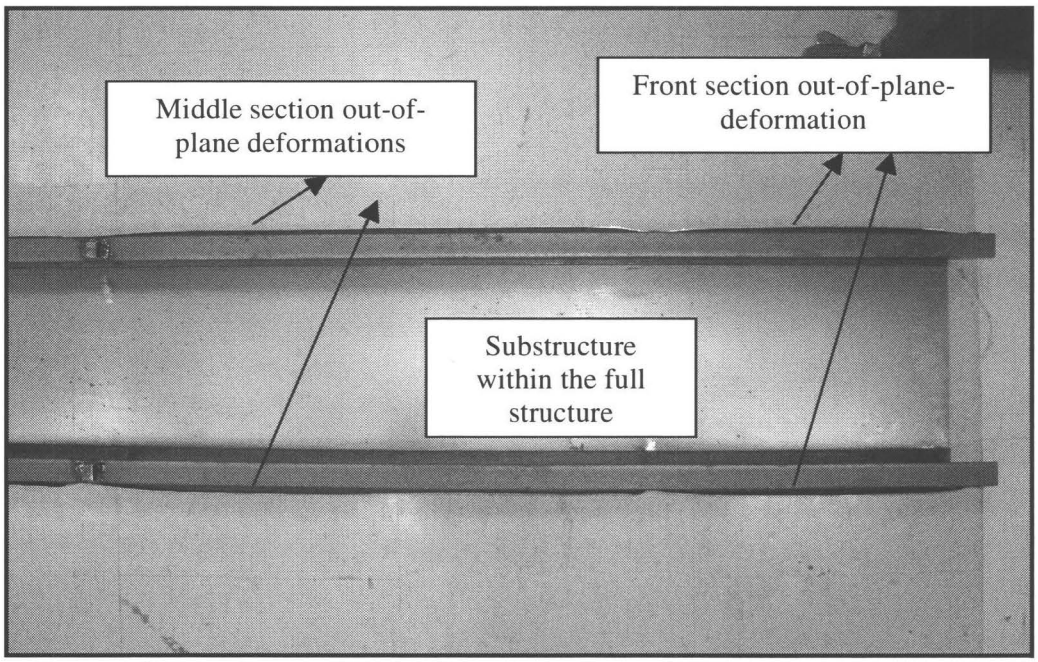

Figure 5.6: Deformed configuration of the substructure in the full model determined by experimental testing

In order to validate the experimental results with the numerical FE results, the acceleration data obtained during testing was converted to frequency data by performing FFT on the time history of accelerometers. The objective was to compare the dominant modes resulting from impact through data collected from accelerometer to see whether these readings corresponded to the same fundamental modes that excite the modeled system. Figures 5.7, 5.8, 5.9 and 5.10 depict accelerometer readings and the dominant frequencies. The dominant frequencies are within 10-12% of those obtained through FE analyses.

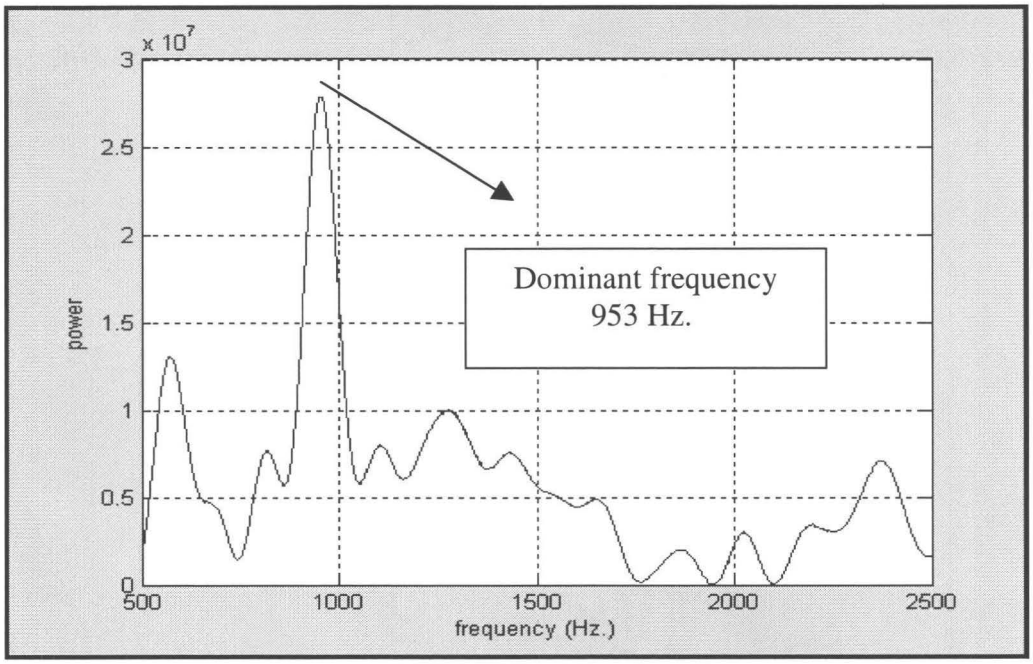

Figure 5.7: Corresponding dominant mode resulting from 1st accelerometer determined by full experimental testing

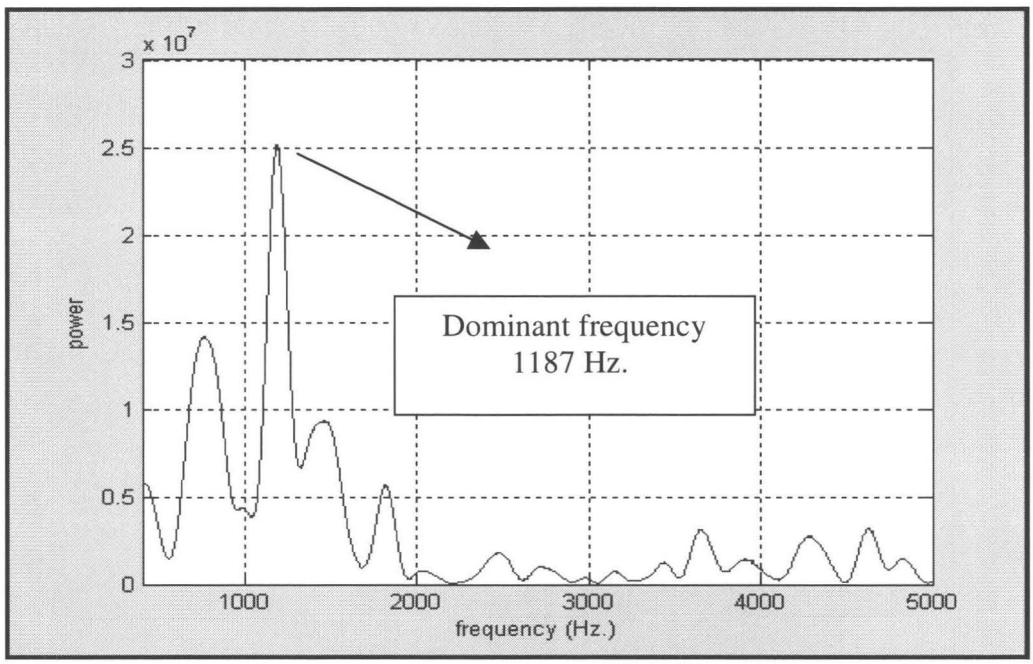

Figure 5.8: Corresponding dominant mode resulting from 2nd accelerometer determined by full experimental testing

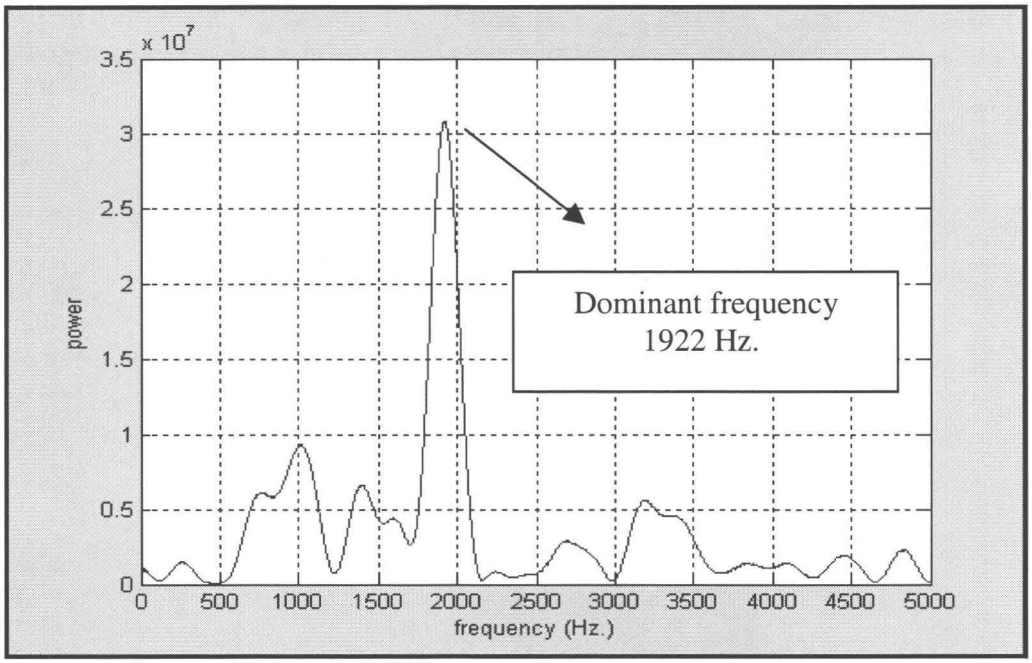

Figure 5.9: Corresponding dominant mode resulting from 3rd accelerometer determined by full experimental testing

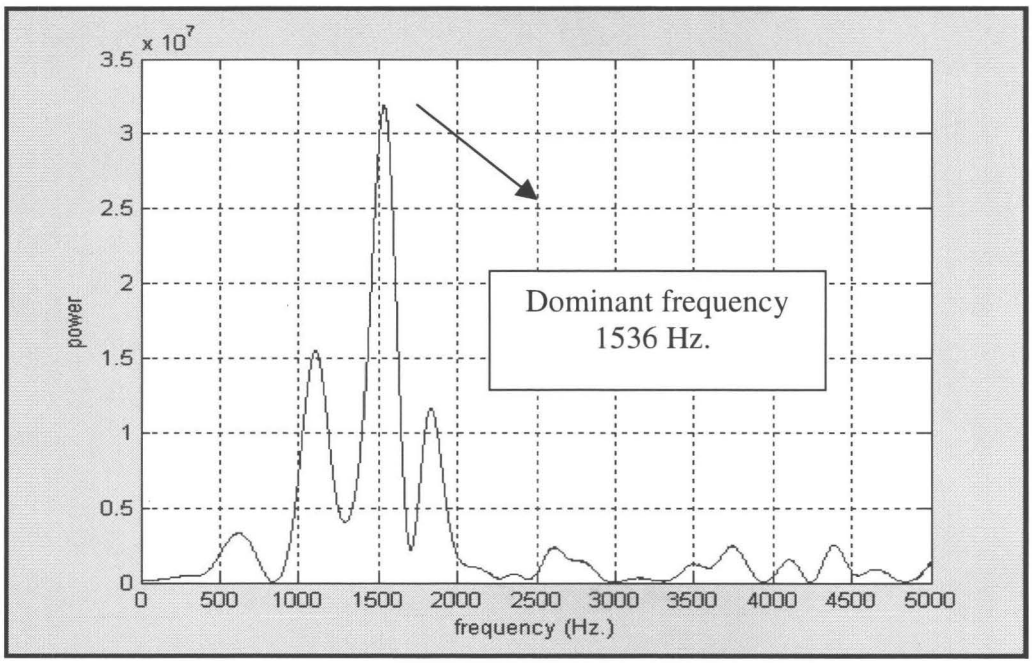

Figure 5.10: Corresponding dominant mode resulting from 4th accelerometer determined by full experimental testing

5.3.2.2. Experimental Testing of the Substructure

The substructure was then mounted to the holding frames using a fixture and experimental testing was performed on this substructure. The properties associated with the impactor were determined from developed methodology. Two accelerometers were used for performing this impact testing. The accelerometers were connected at the top by means of dental glue at two different locations away from the impact location to avoid damage. In these analyses, 1-D accelerometers were used that measure the acceleration in the impact direction only. The locations of the accelerometers on the substructure are shown in Figure 5.11. Similarly, two different nodes were selected on the FE model, which corresponds to the location of these accelerometers.

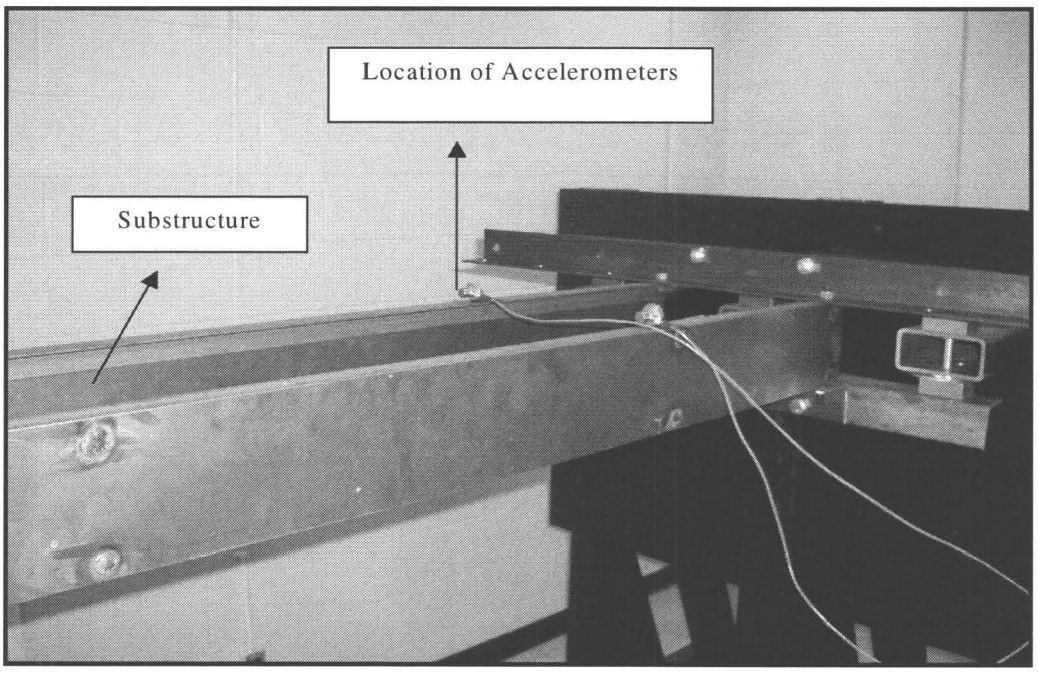

Figure 5.11: Substructure and location of the two accelerometers

In this analysis, the substructure was struck by the rigid impactor of mass 27.5 kg that was moving with a speed of 7.1 m/s. Figure 5.12 depicts the deformed configuration of the isolated substructure resulting from impact testing. As can be seen from Figure 5.12, the out-of-plane deformations were higher in the front and middle sections compared to the rear sections.

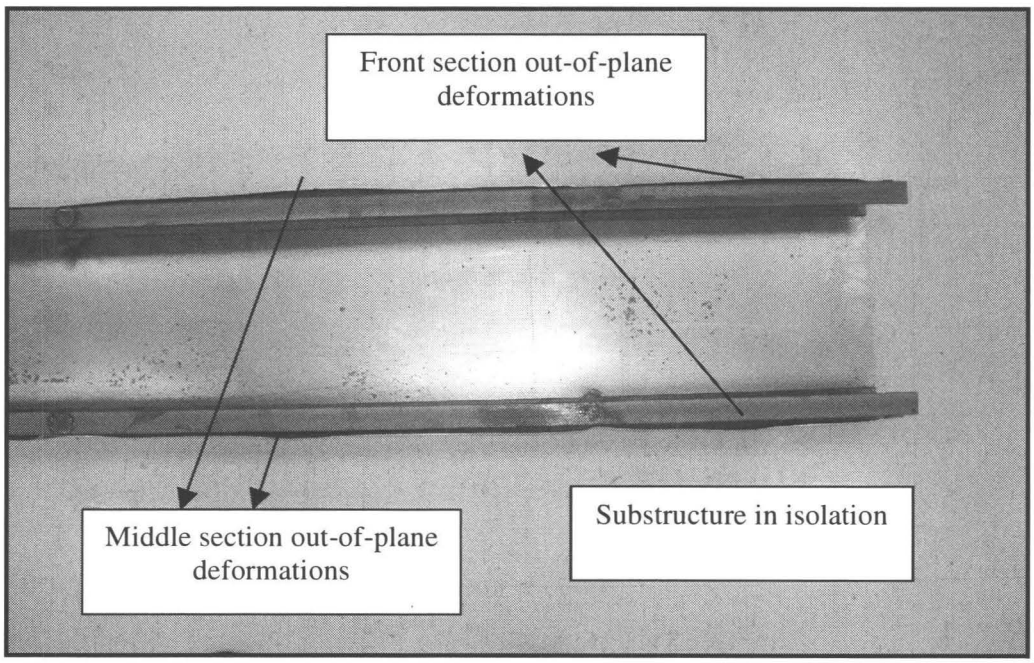

Figure 5.12: Deformed configuration of isolated substructure determined by experimental impact testing

In this experimental testing, the data was recorded during the experimental analysis from accelerometers readings. The data was converted to the frequency domain by performing FFT. Figures 5.13 and 5.14 depict the dominant modes resulting from the

accelerometer readings. The dominant modes resulted from the FFT analyses were compared to the same dominant modes in the FE model of the substructure in isolation.

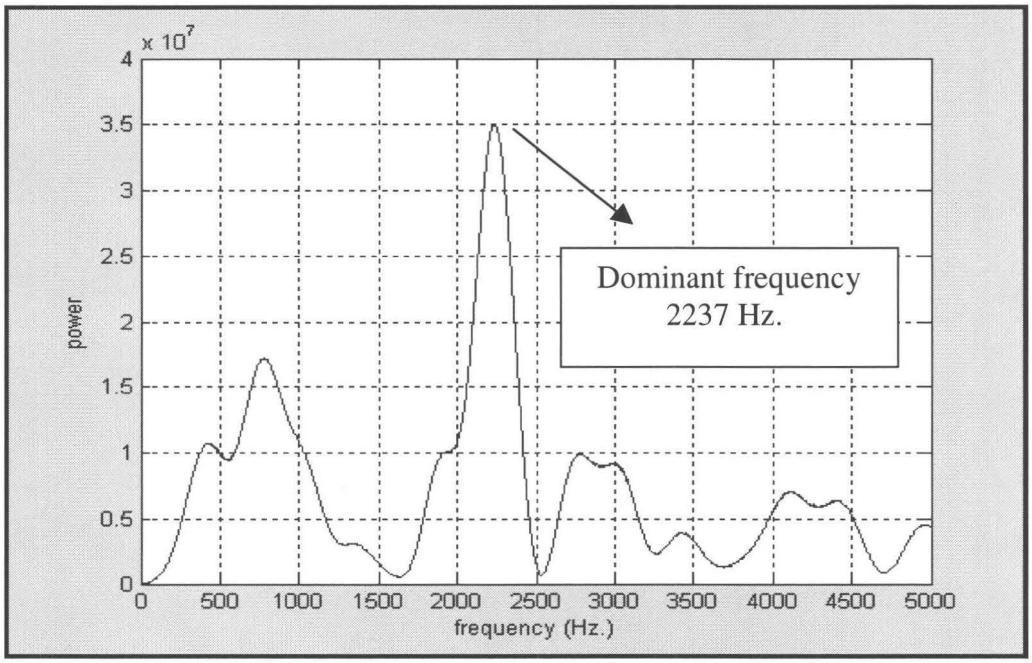

Figure 5.13: Corresponding dominant mode resulting from 1st accelerometer determined by isolated experimental testing

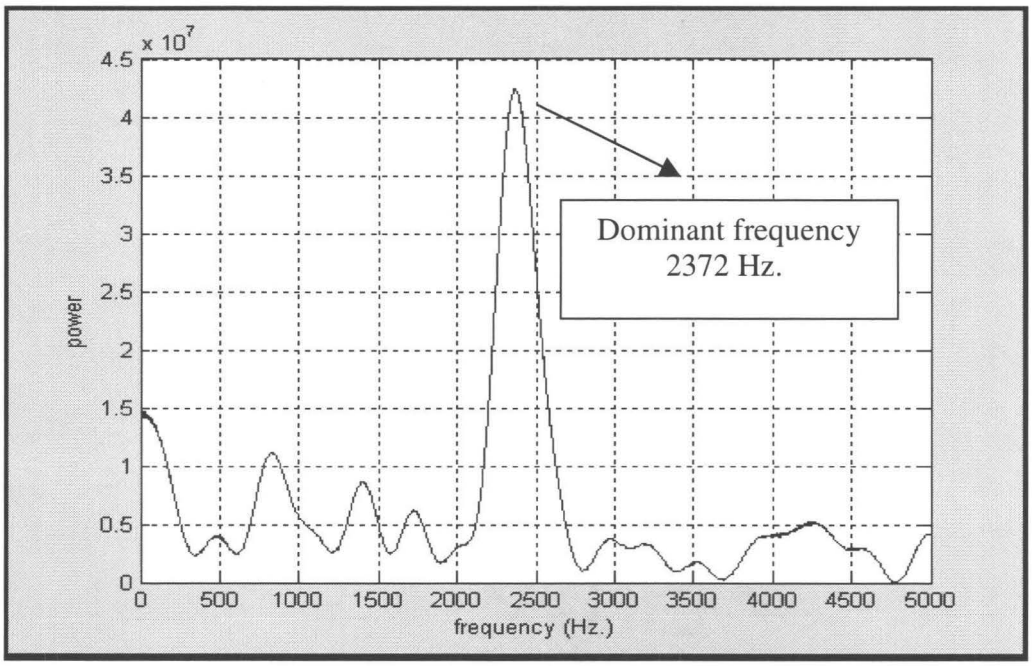

Figure 5.14: Corresponding dominant mode resulting from 2nd accelerometer determined by isolated experimental testing

Fast Fourier Transform analyses (FFT) were performed on the acceleration data corresponding to the full test component and corresponding to the isolated test component. The most dominant frequencies were determined to be higher in the isolated substructure as compared to in the *in situ* substructure. This implies that the frequencies required for excitation of the isolated model are higher than that of the *in situ* test component. Higher frequencies can be related to the overall stiffness of the isolated substructure. Since the stiffness is different for the substructure in isolation than on the substructure in full test article, the dominant frequencies required for excitations are higher in the isolated substructure. In addition, the mechanical properties, associated with stiffness and free boundaries, also caused the isolated test component to excite at higher frequencies compared to the full model test component.

Figure 5.15 depicts the deformed configuration for a substructure in full model and in isolation. In the FE analyses of the structure and the isolated substructure, the rigid-wall impacted the FE models squarely. However, in the experimental tests, this was not the case. Even though the impacting head (rigid-wall) was guided by a railing system, it had a small amount of room to move laterally and impacted the test article obliquely at small angle of $\pm 3^{o}$. This caused a certain level of asymmetric deformation.

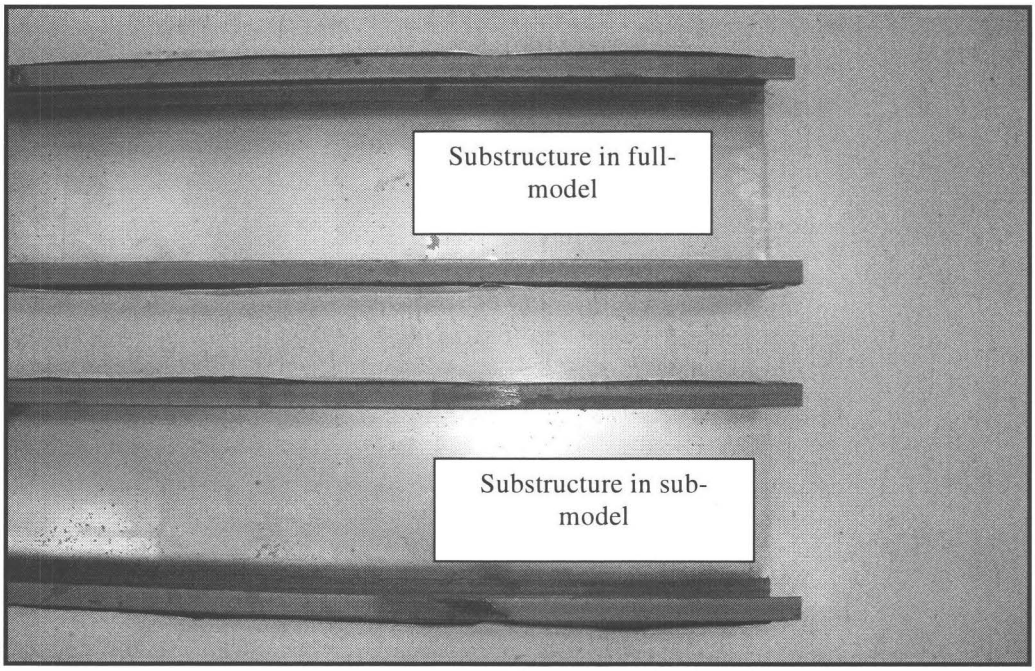

Figure 5.15: Comparison of deformed configurations determined by full and isolated experimental testing

In addition, a series of measurements were obtained which correspond to the out-of-plane deformations at different locations around the boundary of the substructure. These measurements compare the out-of-plane deformations at different points on the experimental specimens.

5.3.2.3 Additional Comparison of Experimental Results

This section compares the experimental findings and discusses the similarities and differences between the full-model test component and the sub-model test component. The comparisons were made based on the measured out-of-plane deformations obtained form experimental testing. The measurements were obtained at various locations

corresponding to the different sections, namely, front, middle and rear, for both isolated and *in situ* test articles.

After performing full impact testing on the structure, weld connections were ground off and the substructure was removed from the rest of the structure. To determine the out-of-plane deformations, a standard digital micrometer was used and measurements were taken from various locations along the periphery of the substructure. The same locations were used for obtaining out-of-plane deformations on both test articles and results were compared to each other. These locations were identical in both the full and isolated models.

The measurements were obtained at five different locations along each section (as shown in Appendix C), and the corresponding discrepancies were calculated for each measurement. The maximum error was determined to be 10.3% and the minimum error was determined to be 7.2% for both stages of the experimental testing. The average errors corresponding to these measurements for the front, middle, and rear sections were determined to be 8.7%, 9.7%, and 7.6%, respectively. This indicates that the imposed technique could be implemented in an experimental setting with a great degree of confidence and that the results of the isolated test were similar to the full model test. Figure 5.16 depicts a graphic comparison of the experimental measurements (the location of these measurements are shown in Appendix C).

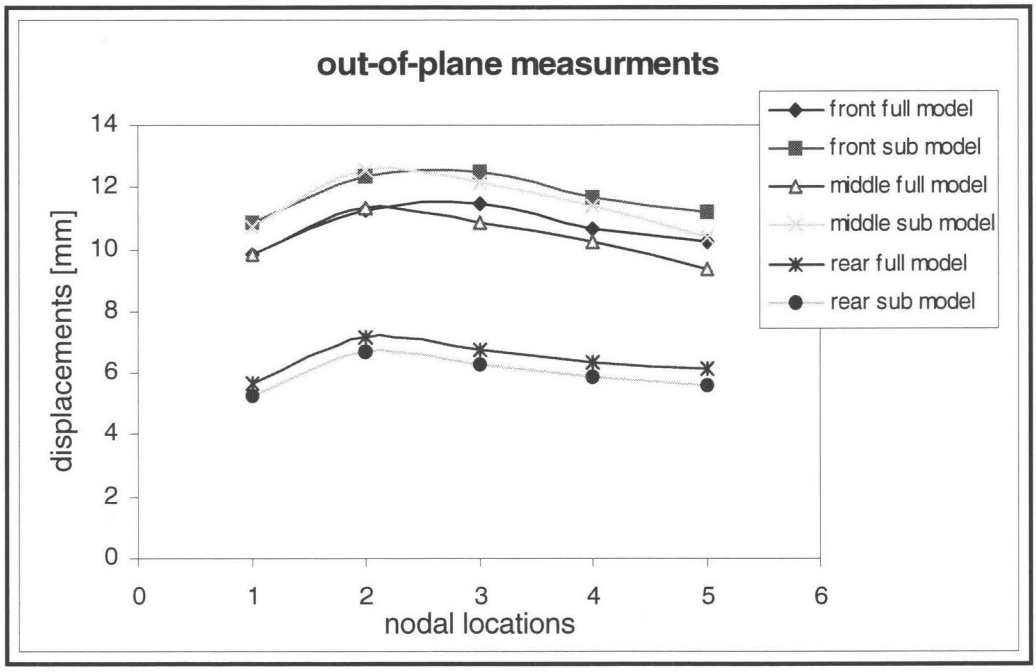

Figure 5.16: Comparison of the out-of-plane measurements [mm], corresponding to the front, middle, and rear sections, determined by full and sub model experimental testing

The measurements show that the out-of-plane deformations of the isolated test article, corresponding to the front and middle sections, were slightly larger than those of the *in situ* test article. These discrepancies can be related to the free boundary around the periphery of isolated substructure. However, the deformed configurations were very similar for both test articles. At the rear sections, where the boundaries were clamped, the out-of-plane deformations were minimal compared to the other sections. Still, the overall deformation patterns corresponding to the deformed configurations were very similar on both test articles.

Up to this point, the experimental impact testing was performed on the full model and the sub model. The substructure out-of-plane deformation in the full model test was 11.27 mm on the left side and 10.62 mm on the right side. This translates to 5.77%

difference in deformation from one side to the other. Equally, in the substructural testing in isolation, the out-of-plane deflection on the right side was measured to be 11.68 mm and a 10.84 mm out-of-plane deformation was measured on the left side. This translates to 7.19% difference in deformation from one side to the other side in the isolated model. It is extremely important to note that these types of discrepancies are encountered in any full scale crash test and cannot be fully eliminated. Nonetheless, the measured out-off-plane deformation was higher in the isolated model than in the *in situ* model.

Chapter 6
Comparison and Discussion of results

6.1 Introduction

It is well known that the response of a subcomponent (substructure) subjected to impact loading in isolation is different than the response of the same subcomponent (substructure) *in situ.* This is primarily caused by the differences in the boundary conditions of a subcomponent (substructure) in isolation and a subcomponent (substructure) *in situ.* This research introduces a novel approach to substructural testing that produces similar results for a substructure in isolation and a substructure *in situ* within FEA. This approach lends itself to experimental testing of substructures.

This work was conducted in two parts: finite element analysis and experimental testing. The purpose of the experimental testing was two folds: to provide a benchmark for the validation of the FE results of full structure testing and to study the application of the proposed method. Generally, when testing impact characteristics of a structure, accelerometers and high-speed cameras are used to obtain the data. Conventional transducers, such as strain gauge, are not suitable for impact data collection. In this work, a conventional technique is followed that uses accelerometers and high-speed cameras to obtain the necessary information.

For the purpose of the substructural analysis, identical physical models and FE models of the substructure were created. In the FE analysis, identical mesh sizes and material properties were used for the substructure *in situ* and in isolation. Additionally, the same boundary conditions and contact conditions were used for the model of the impactor and test article.

This chapter is divided into two main sections, which explain the results in terms of similarities and differences between the two stages of analysis, namely, the full-model and sub-model analyses. The purpose of these comparisons is to assess the response for both the full-model and sub-model analyses, and to be able to produce similar results for isolated substructures. The chapter includes:

- A comparison of the FE results and experimental findings (as shown in Figure 3.4) for the modified design.
- A comparison of the FE results and the experimental testing data (as shown in Figure 4.2), which includes determining the similarities and differences based on proposed methodology between the substructure in full model and substructure in isolation.

In the first section, the FE model of the modified floor is compared with full scale experimental testing of the test component. The first part of this section discusses the similarities and differences between these two full-model analyses. The second section introduces results and comparisons between the FE models and test components for both substructure in full model and substructure in isolation. At the end of each section, the shortcomings are addressed in terms of limitations for performing further analyses.

6.2 Comparison of FE and Experimental Results

This section compares the FE results with experimental findings. The first part of this section discusses the similarities and differences between the two full-model analyses. The second part compares and evaluates the responses from both FE analyses and experimental findings.

6.2.1 Comparison of the Results for the Simplified Structure

In order to compare the experimental and numerical results, two accelerometers were connected to the floor and data was collected during the experiment. The experimental results were correlated with the analytical results by picking two nodes on the numerical model with the same physical location of the accelerometer on the physical model. Figure 6.1 compares typical acceleration data from the numerical analysis and experimental testing. From Figure 6.1, the experimental measurements of acceleration using the accelerometer are in excellent agreement with the numerical findings. In other words, at the onset of impact, the acceleration data recorded in experimental testing is within 10% of the numerical data. This indicates that the numerical results accurately simulate the experimental testing when the entire structure is compared. Figure 6.1, corresponds to the simplified floor (full model testing) indicated in Chapter 3 (refer to Figure 3.4).

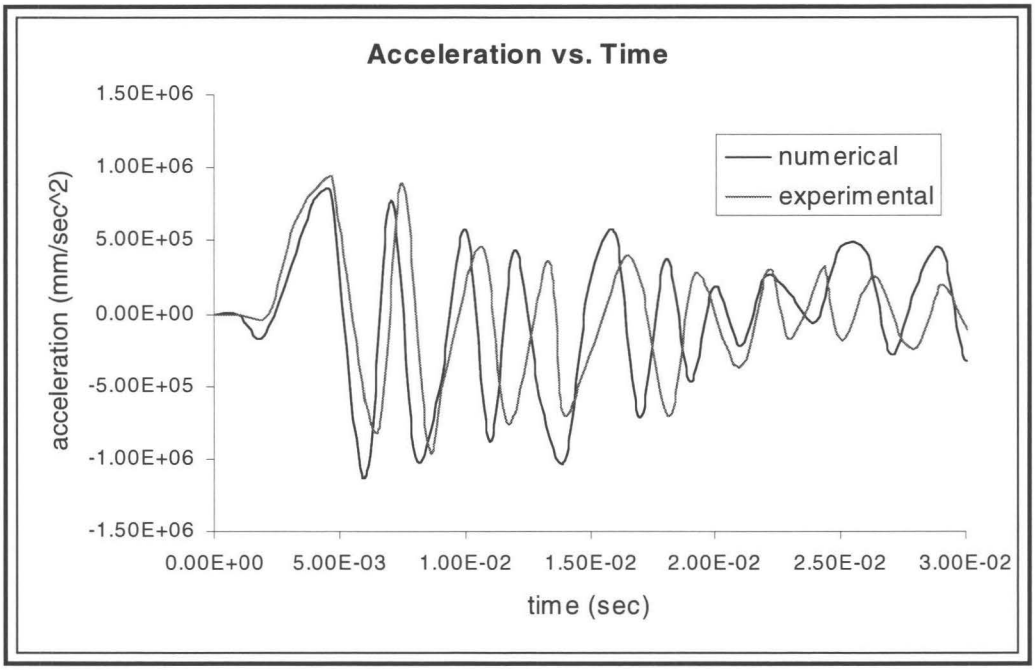

Figure 6.1: Comparison of acceleration data determined by a full model FE simulation and experimental impact testing

Figures 6.2 and 6.3 depict the deformed geometry and compare them to each other. The deformed configurations, obtained from the FE analysis and experimental testing, are in good agreement with each other. The maximum deformation corresponds to the left rail on both the numerical model and the experimental test component. However, when performing experimental testing on a single isolated subcomponent (right rail), this is no longer valid since the free boundary on an isolated single subcomponent (right rail) is different from that of a subcomponent within a full component (modified floor, as shown in Figure 3.4). Also, experimental testing of a single subcomponent can not be achieved without using additional members such as a bar or link.

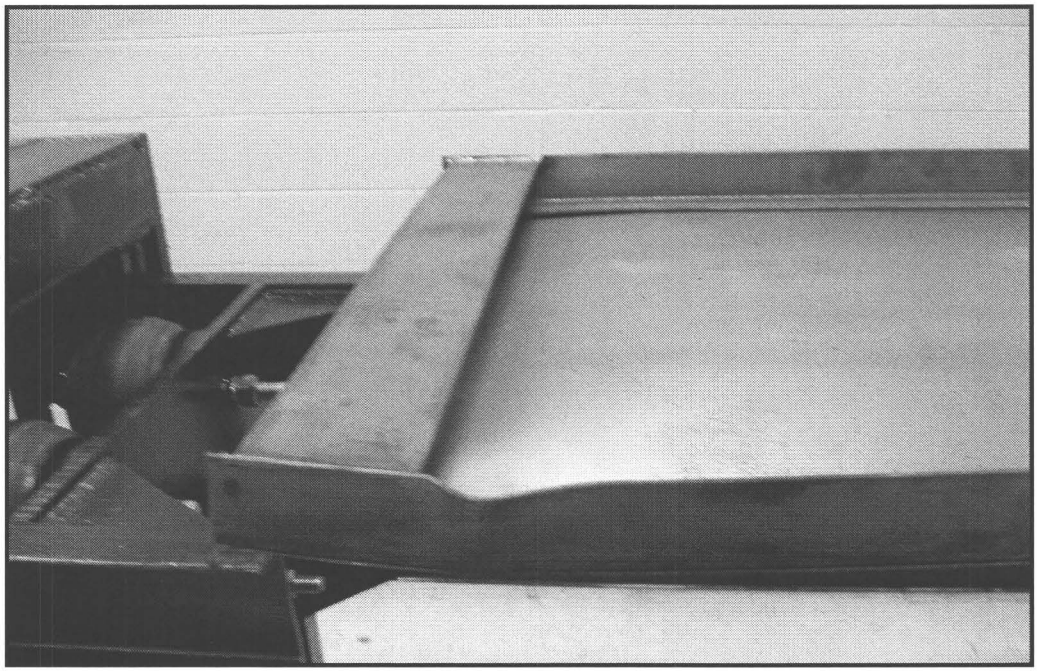

Figure 6.2: Deformation configuration of the modified design determined by experimental impact testing

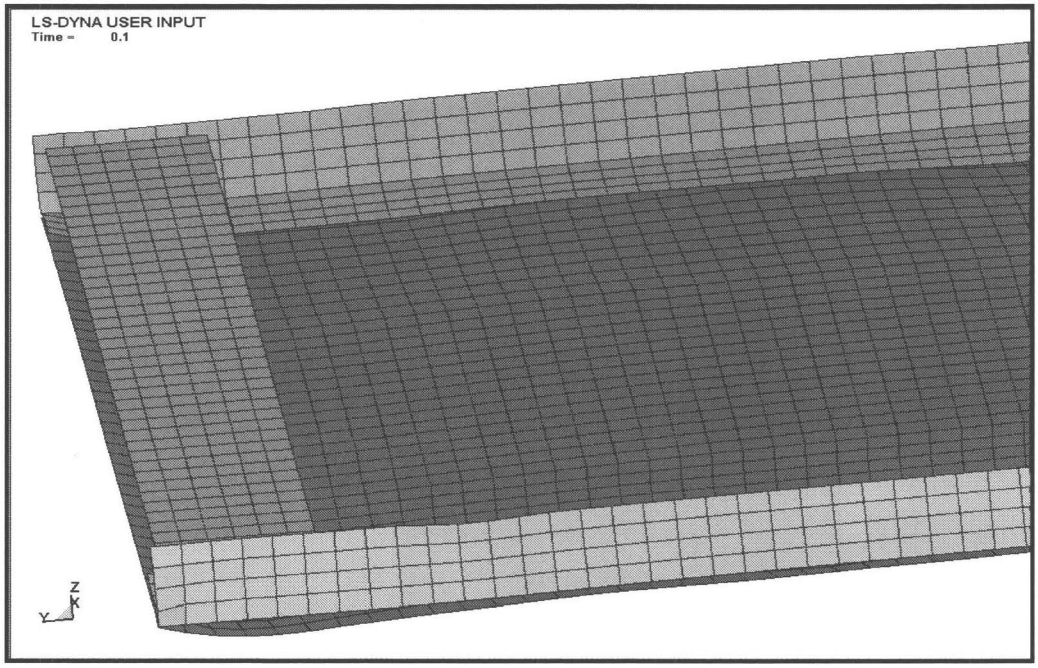

Figure 6.3: Deformation of the modified design determined by numerical FE simulation

6.2.2 Comparison of Results for Structure and Substructure

In this section, the results obtained from the full-model and the sub-model FE analyses are compared with the experimental findings. The measurements corresponding to the out-of-plane deformations on both FE models are compared to the measurements from experimental testing. Also, the corresponding dominant frequencies obtained from the accelerometer readings are compared with the corresponding dominant frequencies in the finite element models. This section is divided into two parts: The first part discusses the similarities and differences between experimental and FE results when using a of full model. The second part discusses the similarities and differences between experimental and FE results when using a sub model.

6.2.2.1 Full Model Comparisons

After performing FE analysis on the full model, the sub-model (substructure) was removed from the full model and measurements were obtained at various nodes, corresponding to the front, middle, and rear section of the substructure, within the structure (refer to Appendix C). Similar procedures were followed in the experimental testing, where the substructure was removed from the structure after impact and measurements were obtained. The locations of the selected nodes on the FE model corresponded to physical locations in the experimental setup. At each section, four nodes were selected and errors were determined for each measurement. The errors resulting from these readings were averaged over a number of measurements and average

discrepancies were determined for each section. Figure 6.4 compares the out-of-plane measurements.

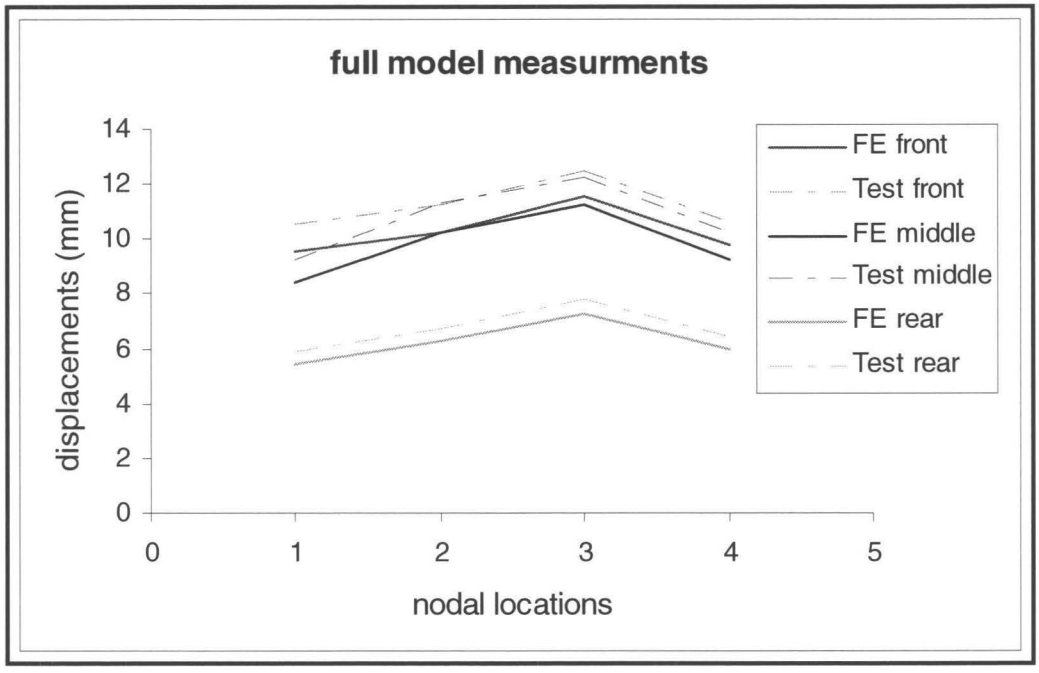

Figure 6.4: Comparison of the out-of-plane measurements for a substructure in a full model determined by numerical simulation and experimental testing

The average errors corresponding to these measurements were calculated and determined to be 8.48%, 9.12%, and 7.41% for the front, middle and rear sections, respectively. After comparing the deformations resulting from these measurements, it was concluded that the deformation corresponding to the experimental impact was higher in the front and middle sections as compared to the deformations in the FE model. Although, the out-of-plane deformation resulting from the experimental testing was higher in the front and middle sections as compared to the numerical model, deformation

patterns were very similar on both the FE model and the test article. This indicates that the FE simulation predicts the physical response of the test component fairly well.

In the experimental impact testing, four accelerometers were used. The location of accelerometers on the test article in the experiment closely matched the position of the nodes in the FE model (as shown in Figure 5.4). 1-D accelerometers were used in this test, which measured acceleration only in the impact direction. The acceleration data was recorded during the experimental work and the dominant modes were determined by performing FFT analysis on the experimental data. The dominant frequencies in the full test article obtained from accelerometer readings were determined to be 953 [Hz], 1187 [Hz], 1922 [Hz], and 1536 [Hz], respectively. Table 6.1 shows a comparison between the experimental and numerical work for full model testing.

Table 6.1: Comparison of fundamental frequencies, corresponding to the full model, determined by FE simulation and experimental testing

Structure Numerical	Structure Experimental	Error percentage%
849 Hz.	953 Hz.	10.91%
1039 Hz.	1187 Hz.	12.47%
1680 Hz.	1922 Hz.	12.59%
1395 Hz.	1536 Hz.	9.18%

The fundamental frequencies resulting from the accelerometer readings are higher than the frequencies determined from FE transient analysis. The discrepancies in

fundamental frequencies can be related to a number of factors including the accuracy and location of the accelerometers, the inexactness of manufacturing, and damping.

The accelerometers used in this experiment had a deviation of less than 2.5% at each frequency tested, i.e. -2% at 1000 [Hz] or -20 [Hz]. In addition, the locations of the nodes on the FE structure were the exact locations; whereas, in the experimental testing the accelerometers correspond to a location in the vicinity of that particular node. The accelerometers used in this study have a 4.5 mm base diameter. Therefore, the physical locations of the accelerometers are slightly different than the corresponding selected nodes of the numerical simulation. Through paying extra attention in the experimental set up, this location discrepancy can only be reduced. The manufacturing of the component was not as precise as the FE model, which would result in a deviation of the simulated and experimental results. Finally, there is a difference in the real damping in the physical structure and that of the damping used in the numerical model. As a result, these factors could cause the differences in the determined dominant frequencies between the experiments and the simulations.

Figures 6.5 through 6.12 show the comparison of numerical and experimental frequency spectrum. The dominant modes measured experimentally and numerically are within 10% to 12% at each location. This signifies the close agreements between experimental and numerical testing.

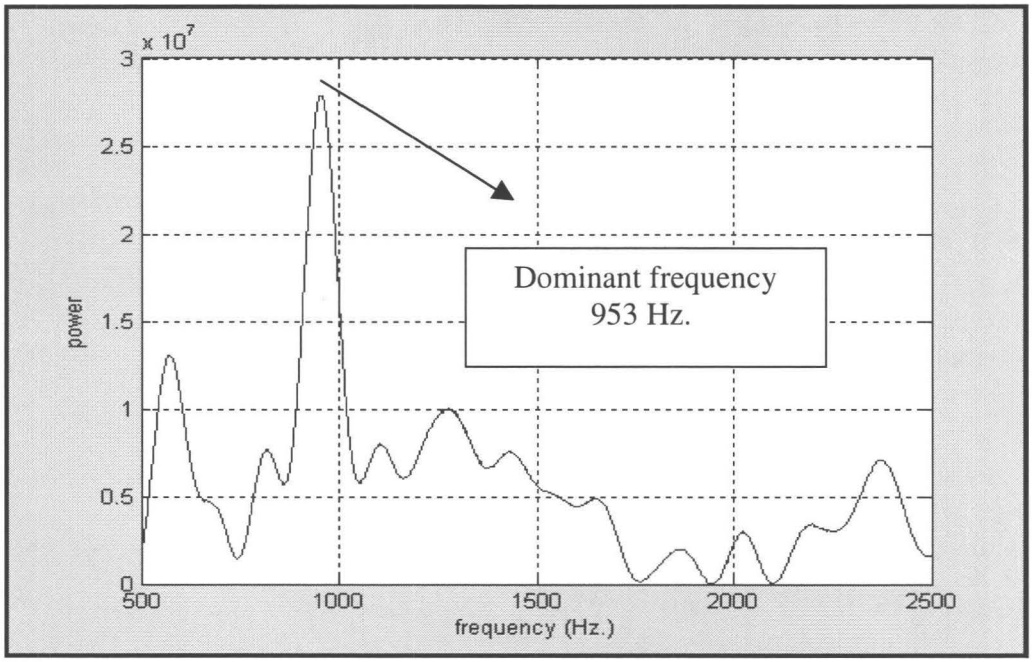

Figure 6.5: Dominant frequency resulting from the 1st accelerometer reading determined by experimental testing

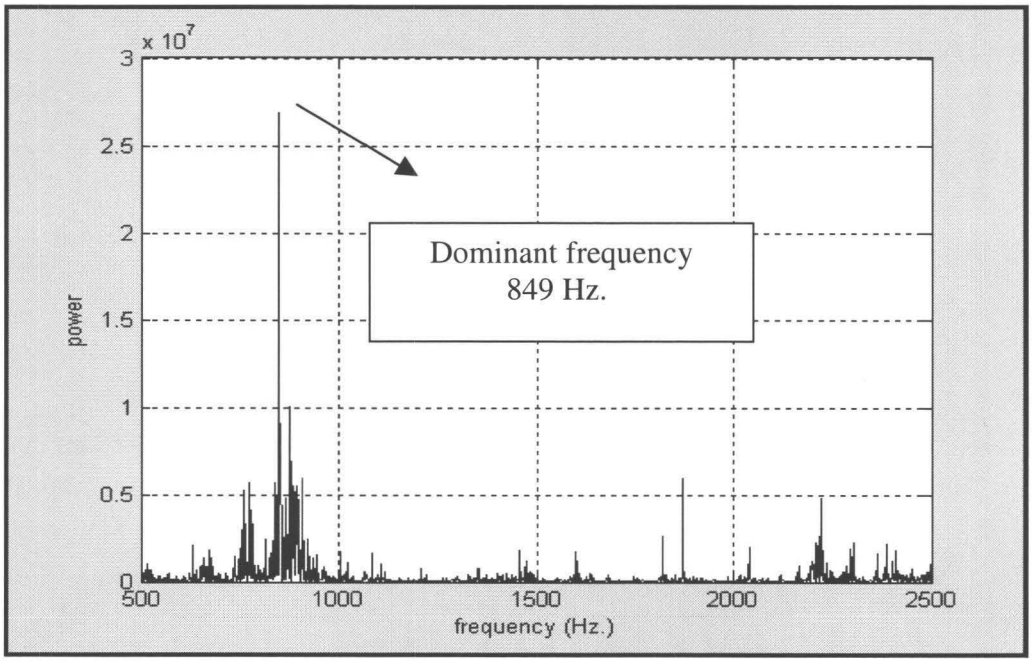

Figure 6.6: Dominant frequency at node # 294239, corresponding to the 1st accelerometer reading, determined by full model numerical simulation

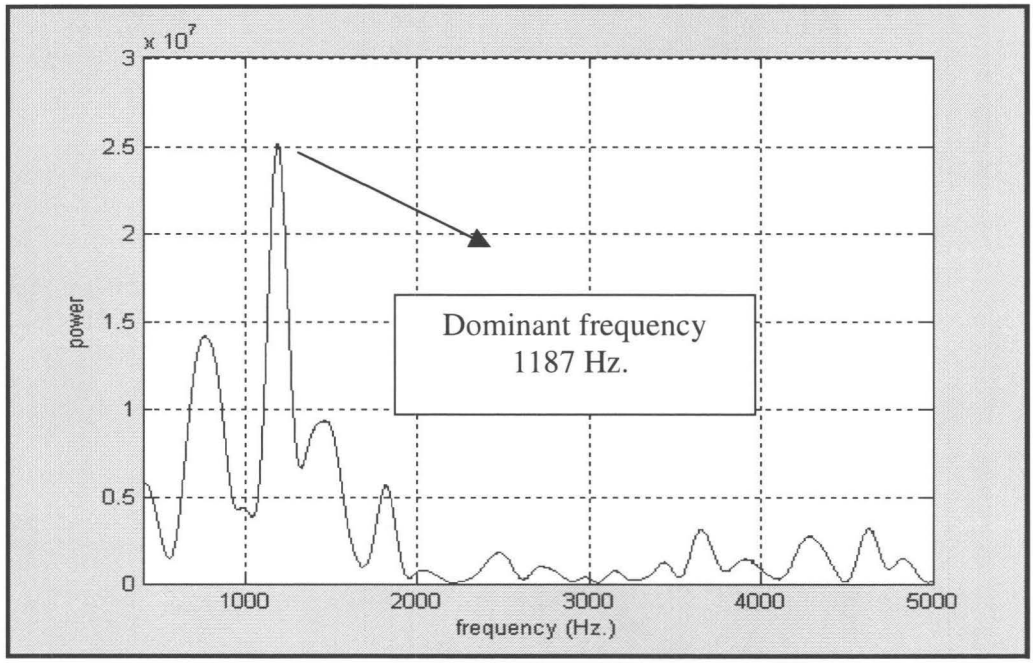

Figure 6.7: Dominant frequency resulting from the 2nd accelerometer reading determined by experimental testing

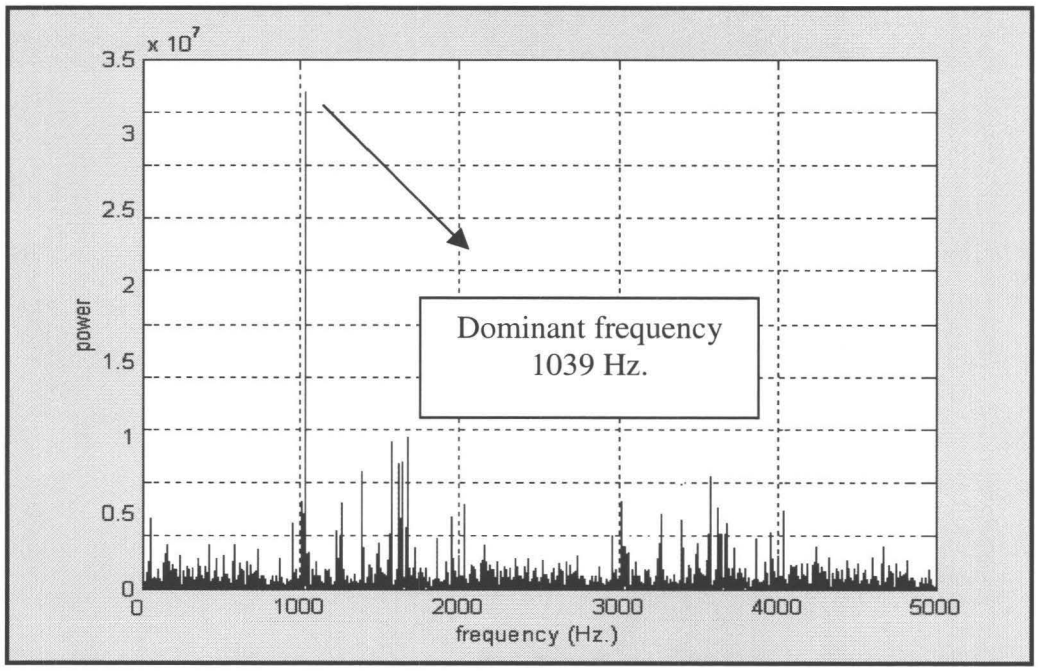

Figure 6.8: Dominant frequency at node # 294106, corresponding to the 2nd accelerometer reading, determined by full model numerical simulation

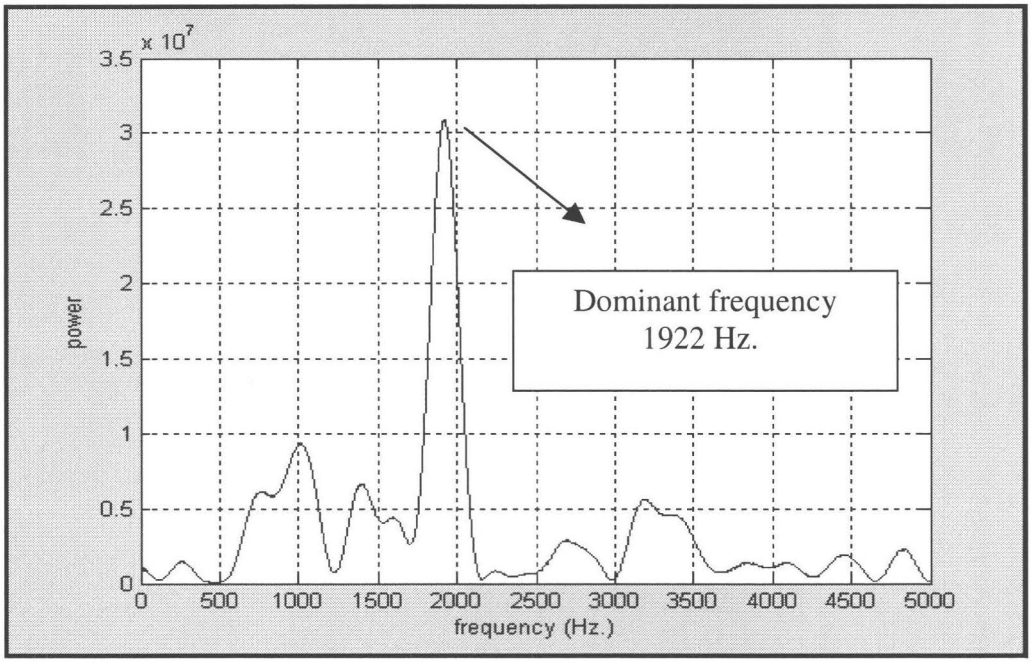

Figure 6.9: Dominant frequency resulting from the 3rd accelerometer reading determined by experimental testing

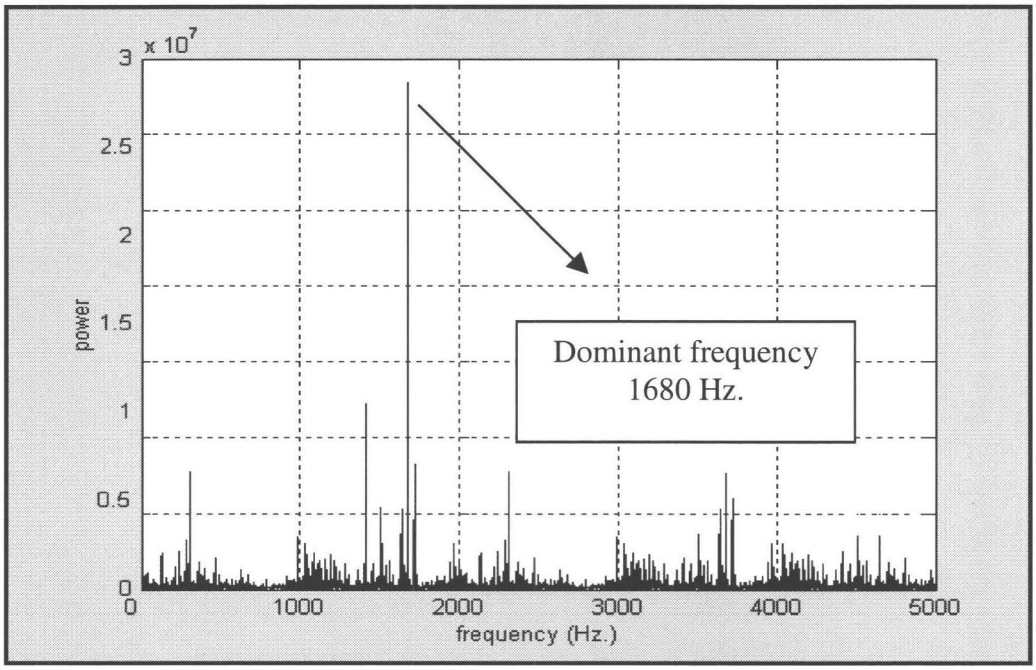

Figure 6.10: Dominant frequency at node # 294232, corresponding to the 3rd accelerometer reading, determined by full model numerical simulation

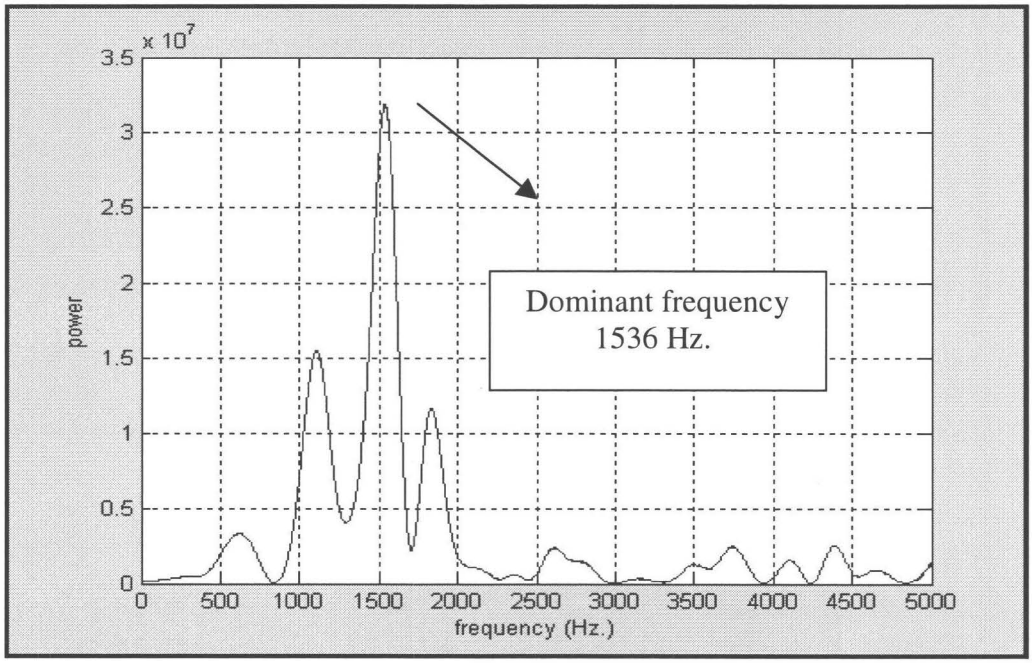

Figure 6.11: Dominant frequency resulting from the 4th accelerometer reading determined by experimental testing

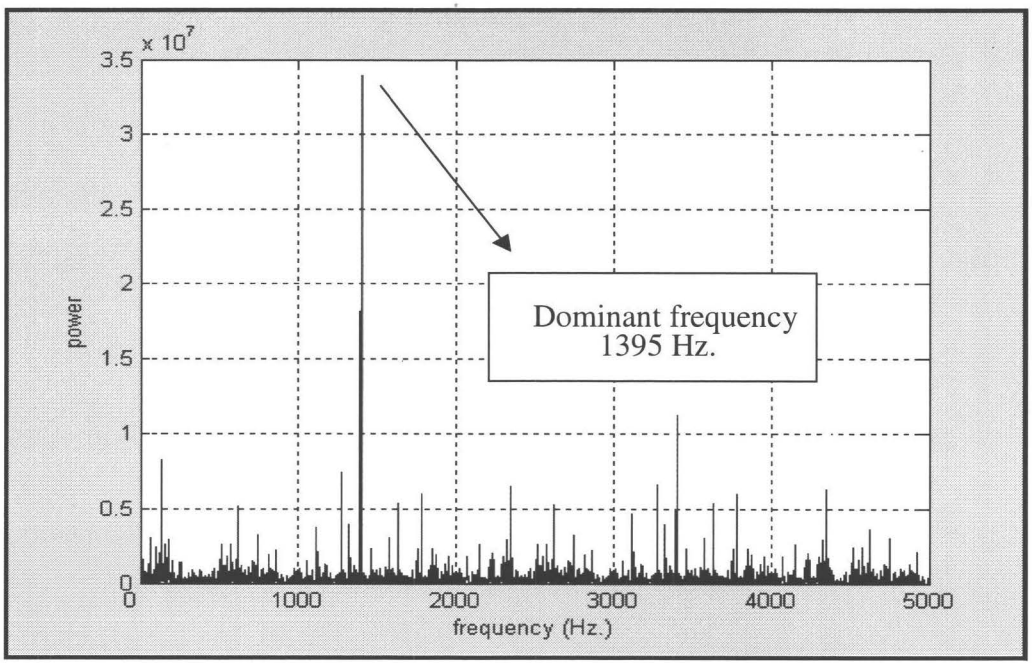

Figure 6.12: Dominant frequency at node # 294113, corresponding to the 4th accelerometer reading, determined by full model numerical simulation

Figures 6.13 and 6.14 depict the deformed configuration of the full structure after performing impact. As can be seen from Figures 6.13 and 6.14, the deformed configuration on both the numerical model and the full test article closely match each other. The out-of-plane displacement of the geometric mid point in the front section of the isolated substructure was measured to be 12.25 mm; and for the same node in the full model, the middle node displacement was measured to be 10.91 mm, which translates to a 11.01% difference. In the geometric mid point of the middle section, the maximum out-of-plane displacement in full model and sub model analyses were determined to be 10.03 mm and 8.94 mm, respectively, which translates to a 10.84% difference.

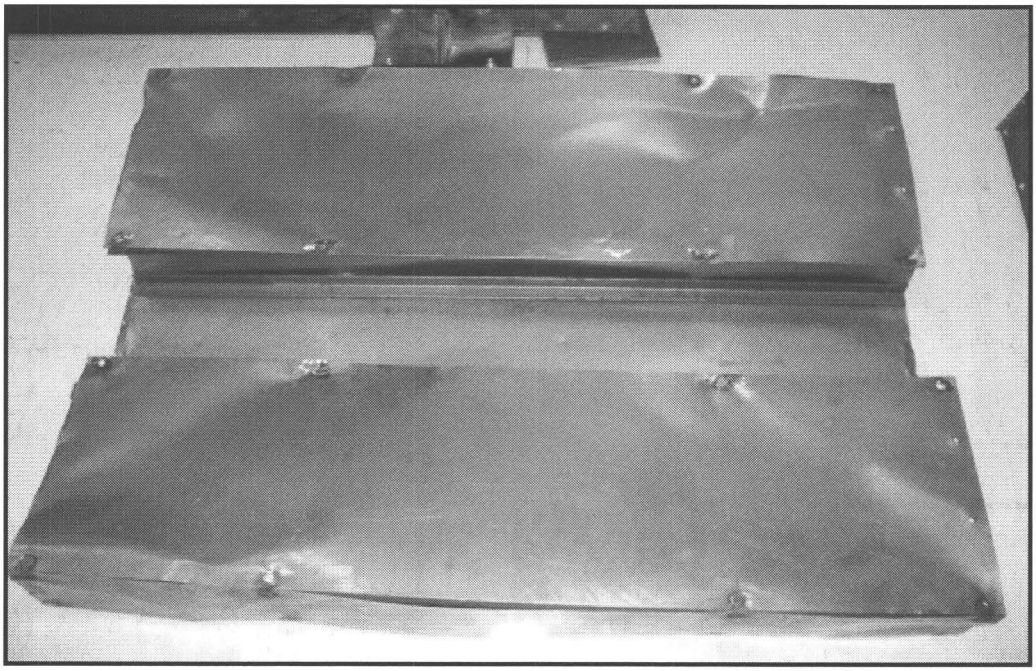

Figure 6.13: Deformed configuration of the full test article determined by experimental testing

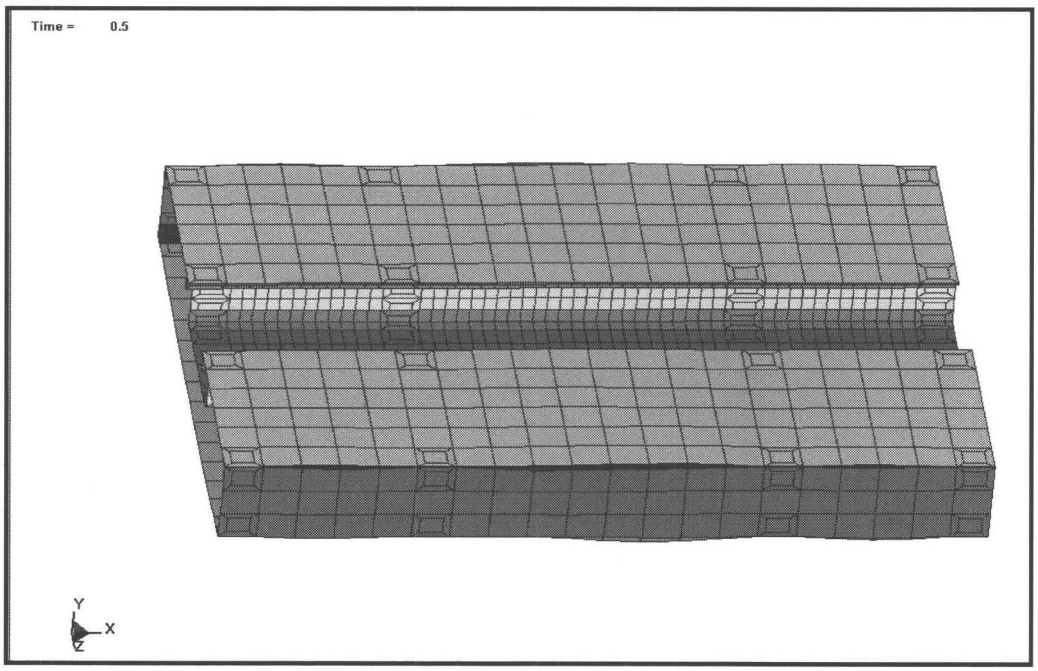

Figure 6.14: Deformed configuration of the full model determined by numerical simulation

Additionally, the deformed configurations were compared, for substructures in a full model, for both finite element analysis and experimental work. As can be seen from Figure 6.15, the out-of-plane deformation on left side, corresponding to the front section, was more than right side; the same also can be seen in the numerical analysis (see Figure 6.16). The difference corresponding to the maximum deformation for the front section was determined to be 9.65%.

From Figure 6.15, the out-of-plane deformation on the right side, corresponding to the middle section, was more than the left side in the experimental test article. The same can also be seen in the numerical model. Figures 6.15 and 6.16 depict the deformed geometry for the test component and the FE model. Although the out-of-plane deformations resulting from experimental testing were higher in the front and middle sections, the deformation patterns corresponding to the out-of-plane measurements were very similar.

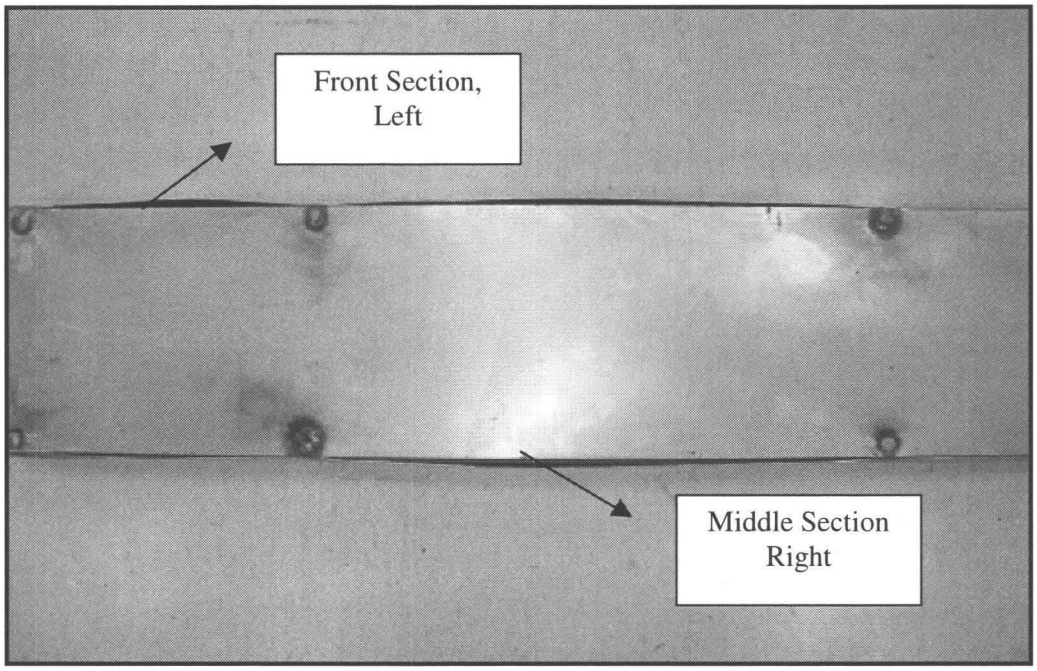

Figure 6.15: Deformed configuration of the substructure within a full structure determined by experimental impact testing

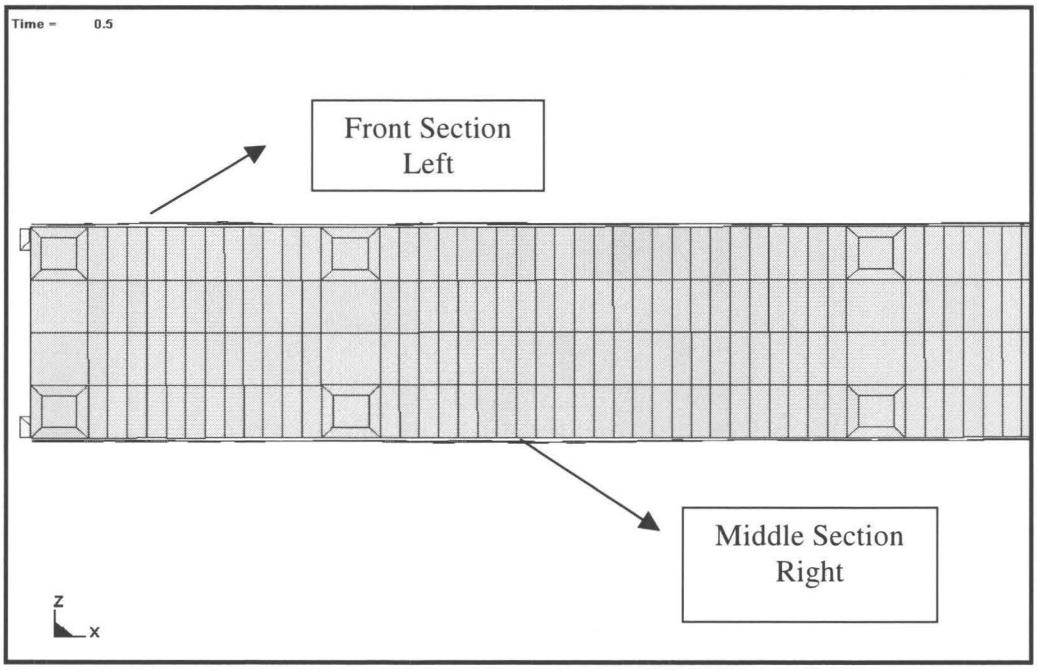

Figure 6.16: Deformed configuration of the substructure within the full structure determined by full model FE simulation

6.2.2.2 Comparison of the results of substructure in Isolation of FE and experimental test

This section compares the sub model results of the experimental work, and the FE simulation. Similar comparisons are made for the isolated substructure between the experiment and numerical simulation as for the full model. The results are compared between the FE simulation and experimental test based on the out-of-plane deformations resulting from the measurements and fundamental frequencies.

A total of two accelerometers were used in the experimental testing of a substructure in isolation. In the FE model, two nodes were selected that corresponded to the physical location of the accelerometers on the test article. After performing FFT on the acceleration data, the most dominant modes were determined from the transient analysis and compared with the most dominant frequencies resulting from experimental findings. The results are listed in Table 6.2.

Table 6.2: Corresponding dominant frequencies for the isolated substructure determined by FE simulation and experimental testing

Substructure, Experimental	Substructure, Numerical	Error Percentage%
2237 Hz.	1949 Hz.	12.87%
2372 Hz.	2119 Hz.	10.67%

The locations of the two selected nodes were given earlier in Figure 5.4, and the physical locations of the accelerometers were given in Figure 5.11. Figures 6.17, 6.18, 6.19 and 6.20 depict these fundamental frequencies and compare them with each other.

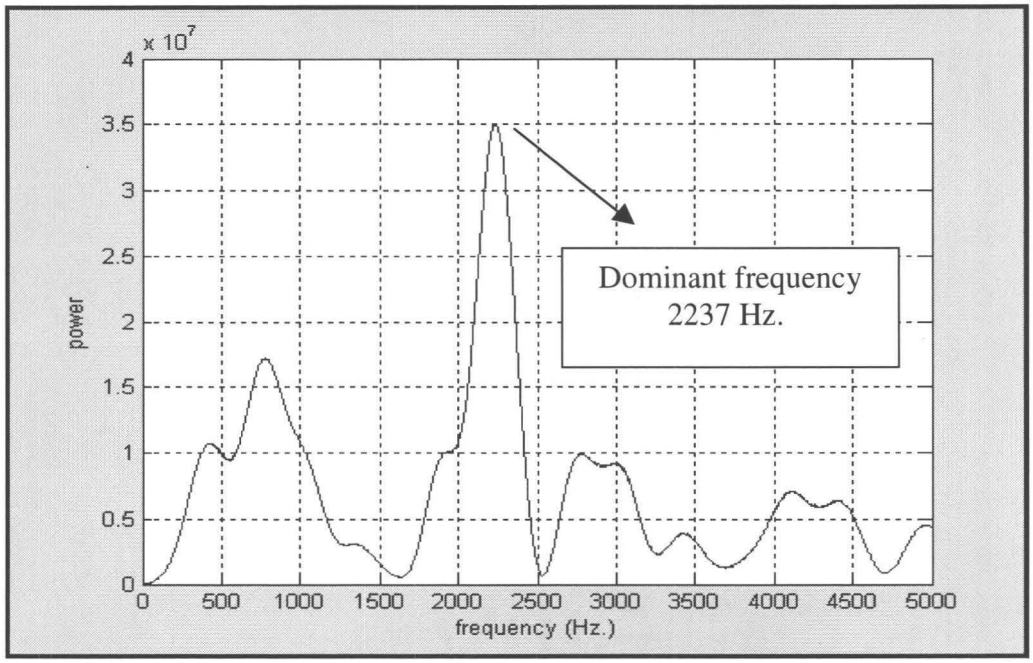

Figure 6.17: Dominant frequency, corresponding to the 1st accelerometer reading, determined by sub scale experimental impact testing

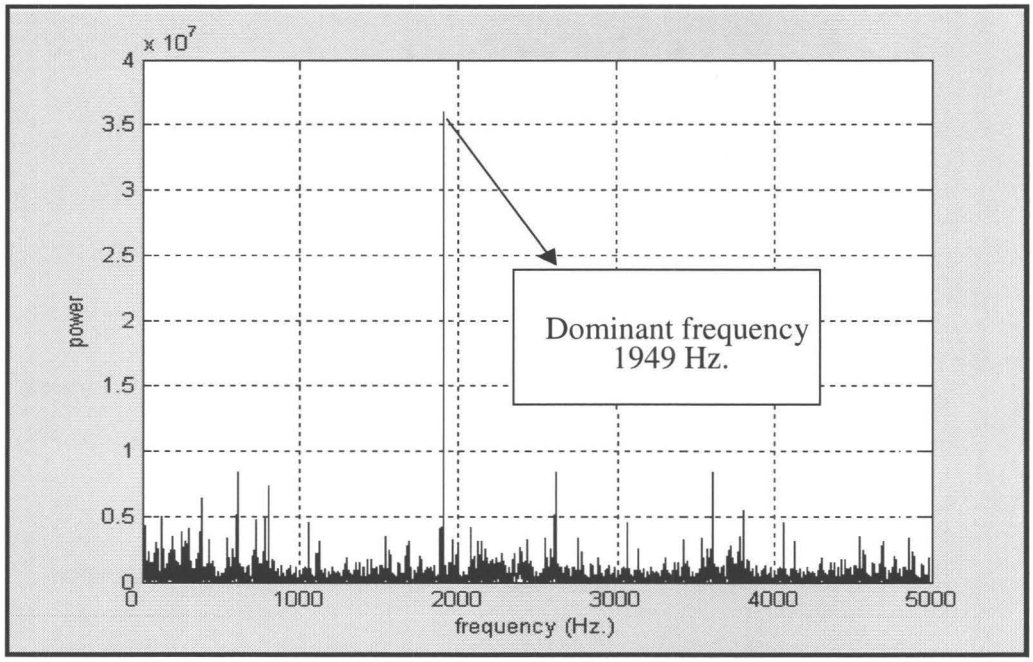

Figure 6.18: Dominant frequency at node # 296386, corresponding to the 1st accelerometer reading, determined by isolated model simulation

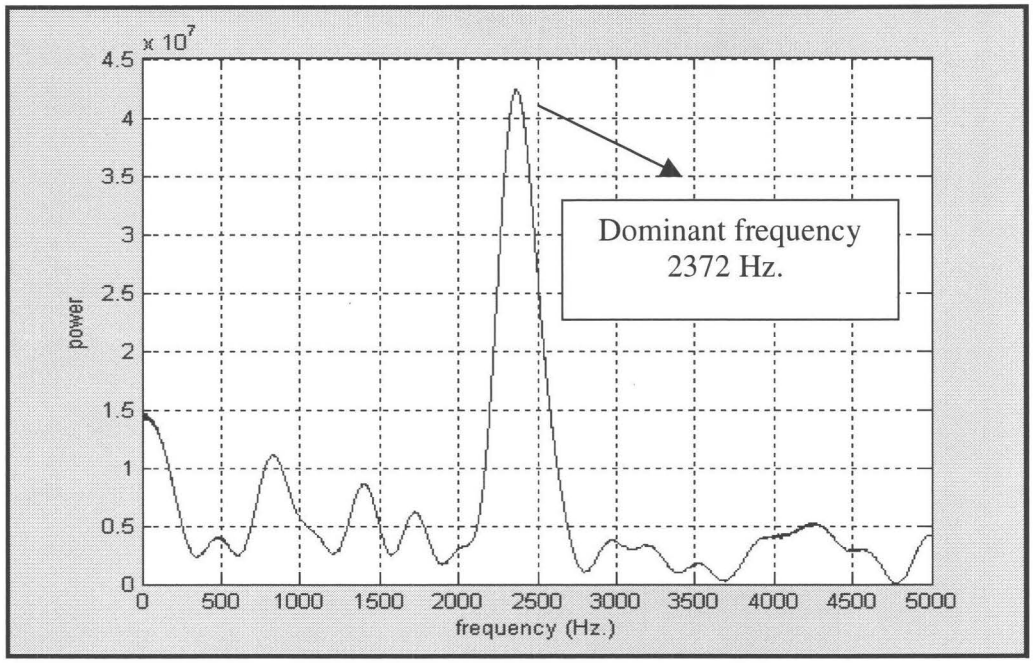

Figure 6.19: Dominant frequency, corresponding to the 2nd accelerometer reading, determined by sub scale experimental impact testing

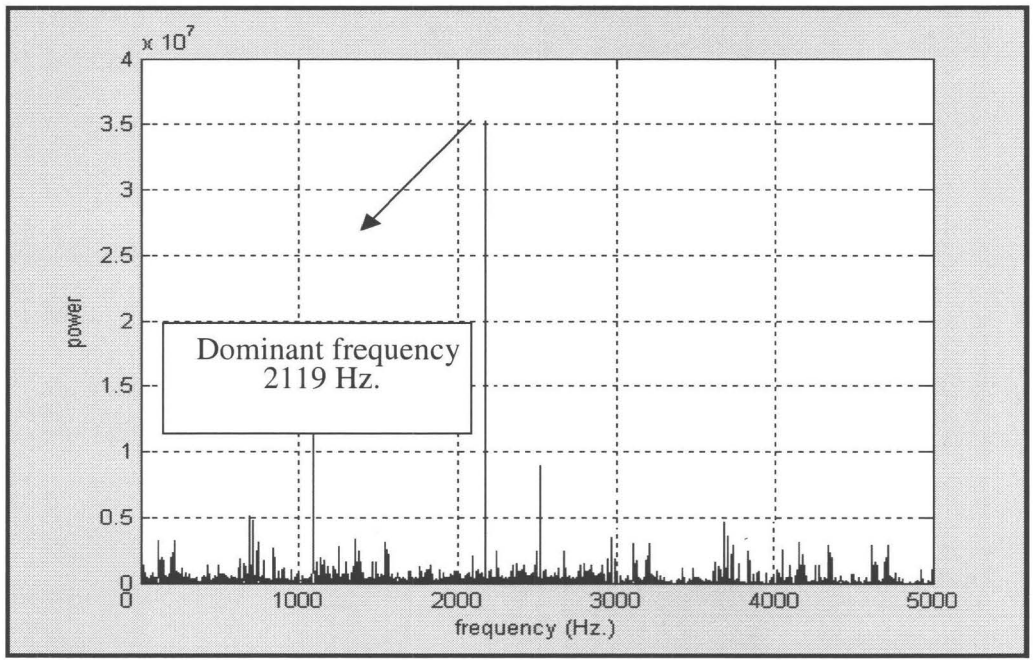

Figure 6.20: Dominant frequency at node # 296606, corresponding to the 2nd accelerometer reading, determined by isolated model simulation

The out-of-plane deformations obtained from the experimental testing of the test component were more than the out-of-plane displacements predicted from the FE simulation. The discrepancies in displacements could be related to the differences in excitation frequencies that were higher in the experimental test component. In other words, the experimental test component excited at higher frequencies. The discrepancies in fundamental frequencies can be related to a number of factors including the accuracy and location of the accelerometers, the inexactness of manufacturing, and damping.

The results obtained from these measurements indicated that the out-of-plane deformations were higher in the front and middle sections on the experimental test article as compared to the FE model. In addition, the fixed boundaries at the end section caused less out-of-plane deformations at the rear sections. The results indicated that the out-of-plane deformations were higher in the test article compared to the numerical model. Figure 6.21 compares the out-of-plane measurements.

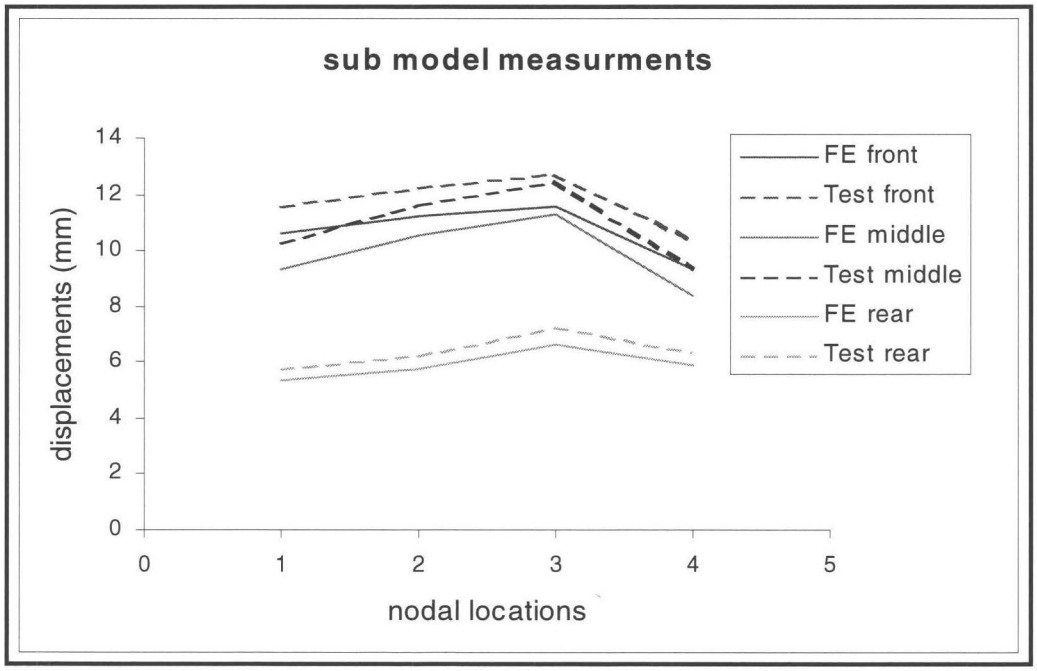

Figure 6.21: Comparison of the out-of-plane measurements for a substructure in a sub model determined by numerical simulation and experimental testing

The average errors corresponding to the measurements in the front section, middle section, and rear section were calculated and determined to be 8.61%, 9.63%, and 7.68%, respectively. The maximum and minimum errors corresponding to these measurements varied between 7.30% and 10.12%. The maximum deflections in the test article and the FE model at the front section were measured to be 12.68 mm and 11.59 mm, respectively. This indicates a difference of 8.62% between numerical and experimental results. Also, in the middle section, the maximum deflections in both the test article and the FE model were determined to be 12.43 mm and 11.28 mm, respectively, which results in a 9.23% difference. In the rear section, the maximum deflections were measured to be 7.21 mm and 6.62 mm that translate to 8.28% difference. Figures 6.22 and 6.23 depict the deformed configurations.

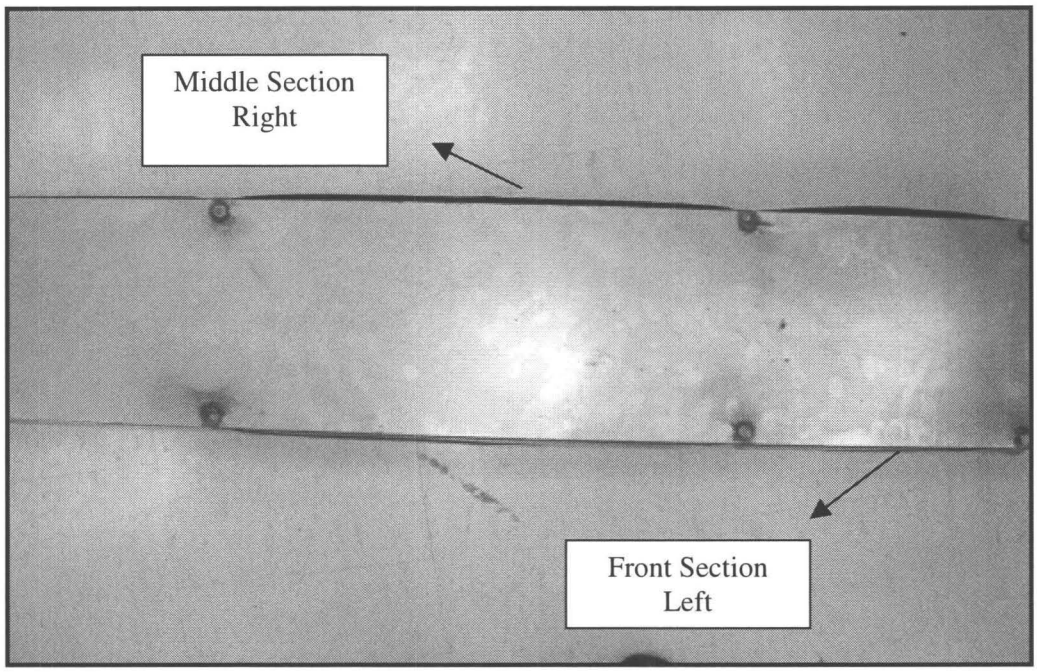

Figure 6.22: Deformed geometry of the isolated substructure determined by experimental testing

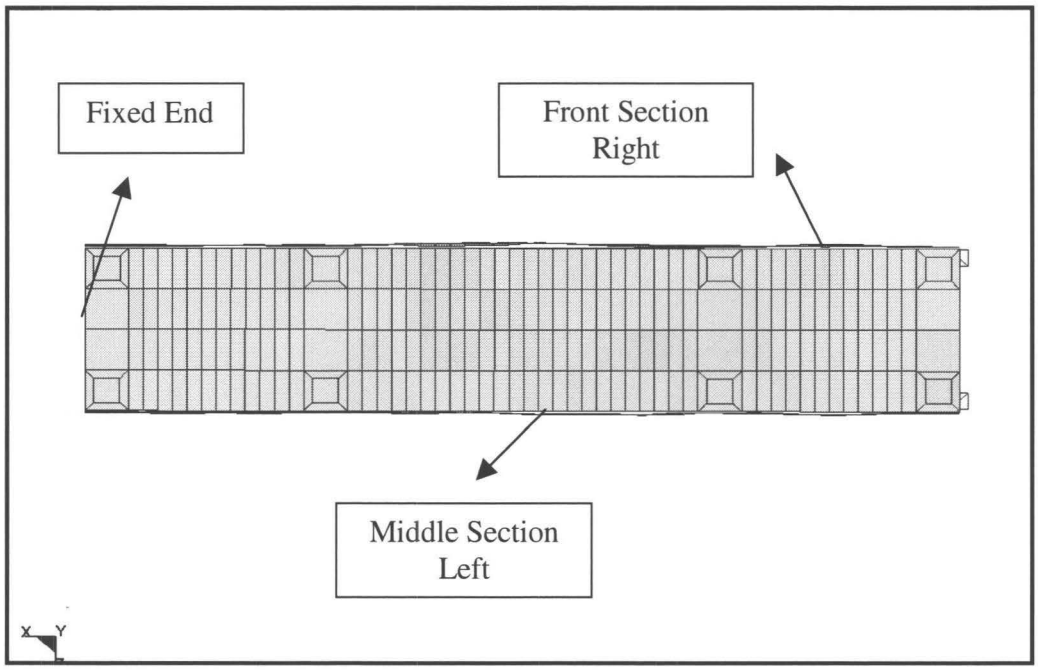

Figure 6.23: Deformed configuration of the isolated substructure determined by numerical simulation

As illustrated in Figures 6.22 and 6.23, the out-of-plane deformations on the right side, corresponding to the front section of both the experimental test article and the numerical model, were slightly higher than the left side. The maximum and minimum errors corresponding to the front section measurements were determined to be 9.48% and 5.89%, respectively. As can be seen from Figure 6.23, the out-of-plane deformation of the middle section on the right side is more than the left side in the numerical simulation. The same can also be observed in the experimental test article.

The out-of-plane deformation from the experimental test was slightly higher in the front and middle sections compared to the numerical model. The measurements indicated that where the boundaries were fixed, the out-of-plane deformations were minimal compared to the front and middle sections. At the rear end, less deformation can be related to the fixed boundaries and constraints that caused the rear section to experience less deformation.

The discrepancies were partly caused by the small free lateral movement of the impacting head. As indicated before, the impacting head was accelerated in a guided manner to reach the required speed. However, the guiding rail provided a small lateral movement that resulted in oblique impact. This is the main reason for the asymmetric deformations in the experimental work that can be experienced in FE simulation. Overall, the deformed configurations were very similar which signifies the validity of the technique.

6.3 Final Remarks

In this work, a methodology was developed, presented and validated for performing impact analysis on an isolated substructure. In the FE analyses, the full structure was analyzed and then the substructure was analyzed in isolation using the proposed method. A parametric equation was introduced that incorporated fundamental frequencies and their corresponding participation factors for determining the substructural impact velocity. A quantitative verification of the proposed method was carried out, based on the FE results, between the full model and the sub model. The verification employed a broad range of comparisons for different variables, namely, energy absorptions, displacements, velocities, and stresses, and effective strains.

In addition, a component testing facility was used for performing experimental testing on fabricated test articles. In the experimental testing, the full structure was tested prior to the application of the proposed method on the substructure in isolation. The experimental results (i.e. fundamental modes and out-of-plane measurements of the deformation) for both test articles were compared.

The purpose of the experimental testing was to provide a benchmark for the validation of the FE results. The results were compared, based on deformed configurations, out-of-plane measurements, and fundamental modes, between the FE analyses and the experimental testing. It was demonstrated that the technique introduced here could be used in FE analysis to predict accurate results for substructural testing. In

addition, it was shown that the method allows for experimental testing that had not previously achieved.

Chapter 7
Conclusions and Contributions

7.1 Conclusions

The mechanical behaviour of a subcomponent of a system under dynamic testing differs from the mechanical response of the same subcomponent tested in isolation. For instance, if the design of the bed of a road vehicle is to be changed, the entire car has to go through rigorous experimental testing to comply with safety regulations. There are two points to be considered in these situations; the new bed has to respond in a similar fashion and the effect of the new designed bed on the overall performance of the car has to be the same as the old design. This makes the notion of redesigning a structure very costly and time consuming.

Here, a technique is introduced that can potentially reduce the cost and time of redesigning and changing an existing structure. The FE simulation and experimental testing of substructure in isolation can be performed through determination of internal energy, mapping the mode shapes and dominant frequencies. In doing so, the developed parametric equation provides the appropriate mass and velocity of impact for impact analysis on the substructure. The validity of the proposed method was examined in FE analysis and experimental testing. In FE analysis, the results of the full-model and isolated model were in very good agreement. For example, the errors corresponding to

the effective plastic strains and the internal and kinetic energies for a substructure in a full-model and a sub-model analysis were determined to be 1.74% and 12.9%, and 10.8% respectively. Equally, the experimental results of the substructure testing showed excellent agreement with the experimental results of the full model testing.

The maximum error corresponding to out-of-plane deformations for test articles in the full model versus a substructure for the front, middle, and rear sections were determined to be 9.07%, 10.27%, and 8.76%, respectively. These results indicate the validity and accuracy of the proposed technique. The novelty of this method, in comparison to other methods, is that the impact analysis on the substructure in isolation is performed by impacting the substructure with an appropriate mass and velocity that produces similar results as that of a substructure in a full model.

This technique is also easily implemented for laboratory experimental testing. From the full model analysis, the maximum errors corresponding to the out-of-plane deformations from the FE analysis and the experimental test corresponding to the front, middle and rear sections were determined to be 9.34%, 9.52%, and 7.79%, respectively. This indicates that the numerical model closely represents the experimental test results. Additionally, the maximum error corresponding to the dominant frequency for the experimental and numerical full model was calculated to be 12.5%.

The maximum out-of-plane deformation in the isolated substructure for the numerical analysis and experimental work corresponding to the front, middle and rear sections were determined to be 9.47%, 10.39%, and 8.28%, respectively. Furthermore, the maximum error for the dominant frequency between the FE analysis and the

experimental test was calculated to be 12.87% for the isolated substructure. These results indicate that the dominant frequencies were well within the acceptable range and the out-of-plane deflections also were well within the acceptable range for substructural testing.

7.2 Contributions

Other finite element packages, such as ANSYS and NASTRAN, perform substructuring on isolated subcomponent. This is achieved by using only interface nodes where the components are connected to each other to form the boundaries of the subcomponent. Although the size of the FE model reduces due to elimination of unwanted degrees of freedom, the properties corresponding to the isolated subcomponent are generally altered due to the elimination of interior nodes. Nonetheless, the aforementioned methods are only applicable in FE analysis and lack experimental verifications.

The main contribution of this work is the development of a new methodology for substructural testing. This method allows the FE simulation and experimental testing of substructure in isolation with the inclusion of boundary condition imposed on substructure by surrounding subsystems. This is achieved by impacting the substructure in isolation with appropriate mass and velocity of impact that are determined based on the internal energy and appropriate mode shapes. The novelty of this method is two-fold:

- The present approach avoids the need to eliminate unwanted degrees of freedom, which in return does not necessitate altering the associated properties within the

FE model. It uses energy transfer and similarity of mode shapes in place of directly mapping the deformations around the sub-model boundary.

- It can be applied to the physical domain and laboratory testing of substructure. This is useful, since government regulations enforce experimental testing of every new developed design for verification of crashworthiness.

7.3 Future Work

In this work, the developed methodology was applied to the structure with one plane of symmetry. Future work could involve extending this method to general geometries with no limitation of symmetry. Also, further investigation is required to implement the developed technique into actual car components, such as the modified floor, which was used by the manufacturer and replaced the original floor in order to provide wheelchair access to the mini van, and to perform crash analysis of more complicated substructural sections.

In addition, the developed method could provide insight to the deformed configuration prior to the testing of the entire vehicle, whenever any modifications takes place within the modified floor. However, the detailed CAD data must be provided prior to implementing the technique. As mentioned previously, the developed method could reduce cost and time for performing impact testing on the isolated substructure (combination of various components that forms the substructure).

References

Akgun, M.A. (1993). A New Family of Mode Superposition Methods for Response Calculations, Journal of Sound and Vibration, Vol.167, No.2, pp.289-302.

Argyris, J., Balmer, H.A., ST.Doltsinis, J. and Kruz, A. (1986). Computer Simulation of Crash Phenomena, International Journal for Numerical Methods in Engineering, 22, pp.497-519.

Bala, S., (2001). Contact Modeling in LS-DYNA, Part 1: Some recommendations, Livermore Software Technology Corporation, Livermore, California.

Bala, S., (2001). Contact modeling in LS-DYNA, Part 3: Modeling Guidelines for Full Vehicle Contact, Livermore Software Technology Corporation, Livermore, California.

Bedewi, P.G., Burel, J., Digges, K., and Tamborra, N., (2003). Modelling Vehicle and Occupant Kinematics in Roll-Over, In Proceedings of the Fifth MADYMO Conference User's Meeting of the Americas, (TNO, Automotive, Delft, Holland).

Belytschko, T., Welch, R.E., and Bruce, R.W. (1975). Sheet Metal Behavior in Crash, In Aircraft Crashworthiness, (Edited by Saczalski, K., et al.), University of Virginia Press, pp.549-560.

Belytschko, T. (1980). Partitioned and Adaptive Algorithms for Explicit Time Integration, In Nonlinear Finite Element Analysis in Structural Mechanics (Edited by Wunderlich, W., stein, E., and Bathe, K.J.), Springer, Berlin, pp.572-584.

Belytschko, T. (1992). On Computational Methods for Crashworthiness, Computers and Structures, Vol.42, No.2, pp.271-279.

Belytschko, T., and Marchertas, A.H. (1974). Nonlinear Finite Element Method for Plates and its Application to Dynamic Response of Reactor Fuel Subassemblies, Trans. ASME, Journal Pressure Vessel Technology, Vol.96, pp.251-257.

Belytschko, T., and Tsay, C.S. (1983). A Stabilization Procedure for the Quadrilateral Plate Element with one-Point Quadrature, International Journal For Numerical Methods in Engineering, Vol. 19, pp.405-419.

Belytschko, T., and Yeh, I.S. (1993). The Splitting Pinball Method for Contact-Impact Problems, Computer Methods in Applied Mechanics and Engineering, Vo.105, pp.375-393.

Belytschko, T., Lin, J.I., and Tsay, C.S. (1984). Explicit Algorithms for the Nonlinear Dynamics of Shells, Computer Methods in Applied Mechanics and Engineering, Vol.42, pp.225-251.

Belytschko, T., Smolinski, P., Liu, W.K. (1985). Stability of Multi-Time Step Partitioned Integrators for First Order Finite Element Systems, Computer Methods in Applied Mechanics and Engineering, Vol.49, pp.281-297.

Belytschko, T.B. and Hsieh, B.J. (1974). Nonlinear Transient Analysis of Shells and Solids of Revolutio by Convected Elements, AIAA Journal, 12, pp.1031-1039.

Benson, D.J., and Hallquist, J.O. (1990). A Single Surface Contact Algorithm for the Postbuckling Analysis of Shell Structures, Computer Methods in Applied Mechanics and Engineering, Vo.78, pp.141-163.

Benson, D.J., Hallquist, J.O., Igaraski, M., Shimomaki, K., and Mizuno, M. (1986). The Application of DYNA3D in Large Scale Crashworthiness Calculations, Lawrence Livermore National Laboratory, Report No.UCRL-94028.

Berkkan, K., and Dokainish, M.A. (1990). Accuracy of Condensed Eigenvalue Solution, AIAA Journal, Vol.28, No.7, pp.1324-1325.

Bhatt, P. (2002). Programming the Dynamic Analysis of Structures, Taylor & Francis Group, Spon Press Publications.

Cafolla, J., Hall, R.W., Norman, D.P., McGregor, I.J. (2004). "Forming to Crash" Simulations in Full Vehicle Models, 4th European LS-DYNA Users Conference, Metal Forming II.

Calso, S., Deb, A., and Saha, NK. (1993). Simulation of Offset In-Line Car to Car Rear Impact, in Symposium on Crashworthiness and Occupant Protection in Transportation, ASME Publisher, pp.149-161.

Chang, D.C. (1977). A Design-Analysis Method for the Front Crush Strength of Body Structures, SAE Paper No.770593.

Chedmail, J.F., DuBois, P., Dagba, B., Haug, E., Picket, A.K., Winkelmuller, G. (1986). Numerical Techniques, Experimental Validation and Industrial Applications of Structural Impact and Crashworthiness Analysis with Supercomputers for the Automotive Industry, International Conference on Supercomputing, Zurich, Switzerland.

Chen, G., Liu, S.D., Knoeer, L., Sato, K., Liu, J. (2002). Residual Forming Effects on Full Vehicle Frontal Impact and Body-in-White Durability Analysis, Society of Automotive Engineers, Inc., Paper No. 202-02M-186.

Cheng, Z.Q., Thacker, J.G., Pilkey, W.D, Hollowell, W.T., Reagan, S.W, and Sieveka, E.M., (2001). Experiences in Reverse-Engineering of a Finite Element Automobile Crash Model, Finite Elements in Analysis and Design, Vol. 37, pp. 843-860.

Chirwa, E.C. (1996). Structural Crashworthiness Simulation of a Rear End Collision of a Small European Car, International Journal of Crashworthiness, Vol. 1, No.1, pp.21-35.

Chopra, A.K. (2007). Dynamics of Structures, Theory and Applications to Earthquake Engineering, Third Addition, Pearson Prentice Hall, Upper Saddle River, NJ 07458.

Combescure, A., and Gravouil, A. (2002). A Numerical Scheme to Couple Subdomains with Different Time Steps for Predominantly Linear Transient Analysis, Computer Methods in Applied Mechanics and Engineering, Vol. 191, pp. 1129-1157.

Craig, R.R., Jr. (1981). Structural Dynamics, John Wiley and Sons, New York.

Craig, R.R., Jr. (1995). Structural Dynamics, An Introduction to Computer Methods, John Wiley and Sons, New York.

Craig, R.R., Jr., and Bampton, M.C. (1968). Coupling of Substructures for Dynamic Analysis, AIAA Journal, Vol.6, No.7, pp.1313-1319.

Dagson, N. (2001). Influence of the Forming Process on the Crash Response of a Roof Rail Component, Master Thesis, Department of Solid Mechanics, Linkoping University.

Deb, A., Ali, T. (2004). A Lumped Parameter-Based Approach for Simulation of Automotive Headform Impact with Countermeasures, International Journal of Impact Engineering, Vol. 30, pp. 521-539.

Dietenberger, M., Buyuk, M., and Kan, Cing-Dao. (2005). Development of High Strain-Rate Dependent Vehicle Model, 4th European LS-SYNA User Conference, Bamberg, Germany.

Douthit, T.J., and Van Tyne, C.J. (2005). The effect of Nitrogen on the Cold Forging Properties of 1020 Steel, Journal of Materials Processing Technology, Vol. 160, pp. 335-347.

Dowel, E.H. (1972). Free Vibrations of an Arbitrary Structure in Terms of Component Modes, Journal of Applied Mechanics, Vol.39, No.3, pp.727-732.

Du, C., Chen, X.M., Lim, T., Xiao, P., and Liu, S.D., (2007). Correlation of FEA Prediction and Experiments on Dual Phase Steel Automotive Rails, Proceedings of 9th International Conference on Numerical Methods in Industrial Forming Processes.

DuBois, P., and Chedmail, J.F. (1987). Numerical Techniques, Experimental Validation, and Industrial Application of Structural Impact and Crashworthiness Analysis with Supercomputers for Automotive Industries, SAE Paper No. 870565.

Dutton, T., Richardson, P., Knight, A., Sturt, R. (2001). The Influence of Residual Effects of Stamping on Crash Results, Third European LS-DYNA Users Conference, Paris.

Dutton, T., (2005). Review of Sheet metal Forming Simulation Progress to Date, Future Developments, 8th International LS-DYNA Users Conference.

Fang, X.F., Kruger, M., Lambert, F., Rubben, K., Mohrbacher, H., Patzold, D., Pflitsch, R., Vandierendonck, D. (1999). Stamping and Welding Experience with Ultra High

Strength Steels for Automotive Body Applications, Society of Automotive Engineers, Inc. Paper No. 1999-01-3194.

Fasanella, E.L, and Jackson, K.E. (2002). Best Practices for Crash Modeling and Simulation, NASA/TM-2002-211944, U.S Army Research Laboratory, Vehicle Technology, Langley Research Center, Hampton, Virginia.

Friswell, M.I., Garvey, S.D., and Penny, J.E.T. (1995). Model Reduction Using Dynamic and Iterative IRS Technique, Journal of Sound and Vibration, Vol.186, No.2, pp.311-323.

Gamon, M.A. (1978). General Aviation Airplane Structural Crashworthiness, User's Manual, Vol.1, Program KRASH theory, FAA Report No. FAA- RD 77-18.

Goldman, R.L. (1969). Vibration Analysis by Dynamic Partitioning, AIAA Journal, Vol.7, pp.1152-1154.

Goodman, E.D., Averill, R.C., and Sidhu, R. (2007). Multi-Level Decomposition for Tractability in Structural Design Optimization, Advances in Intelligent and Distributed Computing, Proceedings of the 1st Symposium on Intelligent and Distributed Computing, Craiova, Romania, October 2007.

Gonard, Germain-Lacour, P., and Azais, F. (1986). Computer aided design analysis of automotive vehicles, International Conference on Supercomputers Applications in the Automotive Industry, 7-9 October, Zurich, Switzerland.

Gravouil, A., and Combescure, A. (2001). Multi-Time-Step Explicit-Implicit Method for Nonlinear Structural Dynamics, International Journal for Numerical Methods in Engineering, Vol. 50, pp. 199-225.

Gravouil, A., and Combescure, A. (2000). A Time-Space Multi-Scale Algorithm for Transient Structural Nonlinear Problems, ICTAM 2000 Congress, Paper 1135, Chicago, Illinois, USA.

Gravouil, A., and Combescure, A. (2003). Multi-Time-Step and Two-Scale Domain Decomposition Method for Non-linear Structural Dynamics, International Journal for Numerical Methods in Engineering, Vol. 58, pp. 1545-1569.

Gu, M.A., and Hulbert, G.M. (2000). A New Load-Dependent Ritz Vector Method for Structural Dynamics Analysis, Quasi-Static Ritz Vectors, Finite Element in Analysis and Design, Vol.36, No. (3-4), pp. 261-278.

Guyan, R.J. (1965). Reduction of Stiffness and Mass Matrices, AIAA Journal, Vol.3, No.2, pp.380.

Hallquist, J.O. (1998). LS-DYNA, User Manual, Livermore Software Technology.

Hallquist, J.O. (1983). Theoretical Manual for DYNA-3D, Report No.UCID-19401, University of California, Lawrence Livermore National Laboratory, Livermore, CA.

Hallquist, J.O. (1990). DYNA3D User's Manual (Nonlinear Dynamic Analysis of Solids in Three Dimensions), Livermore Software Technology Corporations, Report No.1007.

Hallquist, J.O. (2003). LS-DYNA Keyword User's Manual, Version 971, Livermore Software Technology Corporation, Livermore, California.

Hallquist, J.O., and Benson, D.J. (1986). DYNA-3D A Computer Code for Crashworthiness Engineering, Report No.UCRL-95152, Lawrence Livermore National Laboratory, Livermore, CA.

Hallquist, J.O., Goudreau, G.L., and Benson, D.J. (1985). Sliding Interfaces with Contact Impact in Large Scale Lagrangian Computations, Computer Methods in Applied Mechanics and Engineering, Vol.51, pp.107-137.

Haug, E., Arnadeau, F., Dubois, J. and De Rouvray, A. (1983). Static and Dynamic Finite Element Analysis of Structural Crashworthiness in the Automotive and Aerospace Industries, in Structural Crashworthiness, N. Jones and T. Wierzbicki (eds.), Butterworths Publisher, pp.175-218.

Haug, E., Scharnhorst, T., and DuBois, P. (1986). FEM Crash Simulation of Frontal Impact (VW-POLO), translated from German, VDI Report 613, pp.479-505.

Hieronimus, K., Nalepa, E. (1986). Introduction and use of a Supercomputer at Opel E.G., for Crash Simulation, International Conference on Supercomputer Applications in the Automotive Industry, Zurich, Switzerland, pp. 29-42.

Hoffman, R., Ulrich, D., Portard, J.B., Wester, H. (1990). Finite Element Analysis of Occupant Restraint System Interaction with PAM-CRASH, in 34th Stapp Car Crash Proceedings, SAE Publisher, pp.289-300.

Hora, P., Feurer, U., Wahlen, A., Reissner, J. (2000). Methods for Handling of FEM Input and Output Data with the Goal of Higher Computational Reliability, European Congress on Computational Methods in Applied Sciences and Engineering, ECCOMAS-2000, Barcelona.

Horstemeyer, M.F., Siervogel, J., Kwasniewski, L., Wekezer, J., Christiana, B., and Roufa, G., (2007). Material and Structural Crashworthiness of Paratransit Buses, International Journal of Crashworthiness, Vol.12, No.5, pp. 509-520.

Hu, Y., Neal-Sturgees, C.E., Hassan, A.M., and Guo, R., (2007). Modelling the Effects of Seat Belts on Occupant Kinematics and Injury Risk in the Rollover of a Sports Utility Vehicle (SUV), SAE Paper, No. 2007-01-1502.

Hughes, T.J.R., and Liu, W.K. (1981). Nonlinear Finite Element Analysis of Shells, Part-I, Three Dimensional Shells, Computer Methods in Applied Mechanics and Engineering, Vol.26, pp.331-362.

Humar, J.L. (1990). Dynamics of Structures, 1st Edition, Prentice-Hall, Englewood Cliffs, NJ.

Hurty, W.C. (1965). Dynamic Analysis of Structural Systems Using Component Modes, AIAA Journal, Vol.3, No.4, pp.678-685.

Irons, B.M. (1965). Structural Eigenvalue Problems Elimination of Unwanted Variables, AIAA Journal, Vol.3, No.5, pp.961-962.

Jiang, C., and Neal-Sturgess, C.E., (2007). A Study of the Simulation of a Front-Crash-Induced Rollover Crash, Proceedings of the Institution of mechanical Engineers, Part D: Journal of Automobile Engineering, Vol. 221, pp. 1487-1497.

Jones, N. (1989). Structural Impact, Cambridge, Cambridge University Press, pp. 408-415.

Kamal, M.M. (1970). Analysis and Simulation of Vehicle to Barrier Impact, Society of Automotive Engineers, Detroit, MI, SAE Paper No.700414

Kammer, D.C. (1987). Test-Analysis Model Development Using an Exact Modal Reduction, The International Journal of Analytical and Experimental Modal Analysis, Vol.2, No.4, pp.174-179.

Kan, C.D., Tamborra, N., and Fein, O. (1999). Development of Finite Element Model of a Small-Size Vehicle for Crashworthiness Applications, Proceedings of 32nd International Symposium on Automotive Technology and Automation, Vienna, Austria, pp.319-326.

Kan, C.D., Marzougui, D., Bahouth, G.T., Bedewi, N.E. (2001). Crashworthiness Evaluation Using Integrated Vehicle and Occupant Finite Element Models, International Journal of Crashworthiness, Vol. 6, No. 3, pp. 387-398.

Khalil, T.B., and Vander Lugt, D.A. (1989). Identification of Vehicle Front Structure Crashworthiness by Experiments and Finite Elements, In Symposium on Crashworthiness and Occupant Protection in Transportation Systems, ASME, publisher, AMD-Vol.106/ BED-Vol.13, pp.41-53.

Khalil, T.B., Sheh, M.Y., Chalons, P., and DuBois, P.A. (1995). Integrated Vehicle Dummy Airbag Model for Frontal Crash Simulation by FE Analysis, in Symposium on Crashworthiness and Occupant Protection in Transportation Systems, ASME Publisher, pp.355-383.

Kim, B.G., Lee, J., Chung, T.J. (2007). A Structural Analysis of Vehicle Body-in-White using a Substructuring Technique, Proceedings of the Institution of mechanical Engineers, Part D: Journal of Automobile Engineering, Vol. 221, pp. 157-164.

Kim, H.S., Lee, I.H., Park, S.H., Kang, S.Y., and Han, D.C. (1997). Vehicle Frontal Crashworthiness Analysis by Simplified Structure Modelling using Nonlinear Spring and Beam Elements, International Journal of Crashworthiness, Vol. 2, pp. 107-117.

Kirkpatrick, S.W (2000). Development and Validation of High Fidelity Vehicle Crash Simulation Models, SAE Technical Paper, No. 2000-01-0627, SA.E 2000 World Congress, Detroit, Michigan, March 6-9.

Kirkpatrick, S.W., Simons, J.W., and Antoun, T.H. (1999). Development and Validation of High Fidelity Vehicle Crash Simulation Models, International Journal of Crashworthiness, Vol.4, No.4, pp.395-406.

Kohlhoff, S.T., Norbert, J., and Scharnhorst, T. (1994). A Computational Approach to an Investigation of Frontal Car to Car Collision for the Development of Barrier Test, Numerical Analysis in Automobile Engineering, VDI Conference, Wurzburg, Germany, pp.467-484.

Koko, B. (2002). The MSC. Software Simulation Data Management Initiative, Conference Proceedings for the 3rd Worldwide MSC. Software Aerospace Conference & Technology Showcase, April 8th – 10th.

Lanzerath, H., Ghouati, O., Wesemann, J., Schilling, R. (2001). Influence of Manufacturing Processes on the Vehicles in Frontal Crash, Third European LS-DYNA Users Conference, Paris.

Lee, B.C., and Kwak, B.M. (1984). A Computational Method for Elasto-Plastic Contact Problems, Computers and Structures, Vol.18, pp.757-765.

Leung, A.Y.T. (1978). An Accurate Method of Dynamic Condensation in Structural Analysis, International Journal for Numerical Methods in Engineering, Vol.12, No.11, pp.1705-1715.

Levy, R. (1971). Guyan Reduction Solutions Recycled for Improved Accuracy, NASTRAN Users, pp.201-220.

Lin. T.C., Wawa, C., and Khalil, T.B. (1995). Application of a FE Model of the Hybrid III Dummy for Frontal Crash with Air Bag, in Stapp Car Crash Conference Proceedings, SAE Publishers, pp.37-51.

MacNeal, R.H. (1971). A Hybrid Method for Component Mode Synthesis, Computers and Structures, Vol.1, No.4, pp.582-601.

Mathematic Dynamic Model (MADYMO), (2004). User's Manual, Version 6.2, TNO Automotive, Department of Injury Prevention, TNO Road-Vehicle Institute.

Mahmood, H.F. and Paluzeny, A. (1986). Analytical Technique for Simulating Crash Response of Vehicle Structures Composed of Beam Elements, 6th International Conference on Vehicle Structural Mechanics, SAE Publisher.

Maker, B.N. and Zhu, X. (2000). Input Parameters for Metal Forming Simulation Using LS-DYNA, FEA Information International News for the World-Wide Engineering Community, Livermore Software Technology Corporation, April-2000. CA.

Markiewicz, E., Marchand, M., Ducrocq, P., and Drazetic, P. (2001). Evaluation of Different Simplified Crash Model: Application to the Under-Frame of a Railway Driver's Cab, International Journal of Vehicle Design, Vol. 26, pp. 187-203.

Marur, P.R., Srinivas, S. (2008). A Reduced-Order Finite Element Model for the Simulation of Automotive Side Structure Crash Response, International Journal of Crashworthiness, Vol. 13, No. 2, pp. 211-218.

Matlab, (2005). The Language of Technical Computing, Fourier analysis and Fast Fourier Transform (FFT), Version 7, The Math Works, Inc.

McIvor, I.K. (1973). Modeling and Simulation as Applied to Vehicle Structures and Exteriors, Proceedings of Vehicle Safety Research Integration Symposium, DOT-HS-820-306.

Melosh, R.J. (1972). Car-Barrier Impact Response of a Computer Simulated Mustang, Report No.DOT-HS-091-1-125A, Philco-Ford Corporation, Palo Alto, CA.

Mkrtchyan, L., Sahr, C.H., Berger, L., and Maier, M. (2008). Interactions Among Structural Components During Complex Impact Events, International Journal of Crashworthiness, Vol. 13, No. 1, pp. 9-24.

Monclus-Gonzalez, J., Kan, C.D., and Bedewi, N. (2000). Versatility and Limitation of a Fully Detailed Finite Element Model of a 1997 Dodge Grand Caravan for Crashworthiness Applications, 2000 SAE Congress, Detroit, Michigan.

Morvan, H., Tan, K.H., Robache, F., Pacaux, M.P., Drazetiz, P. (2007). Pre-Crash Investigation Using a Driving Simulator and Numerical Analysis to Determine the Influence of the Arms Positions, International Journal of Crashworthiness, Vol. 12, No. 5, pp. 531-539.

Moumni, Z., Axisa, F. (2004). Simplified Modelling of Vehicle Frontal Crashworthiness Using a Modal Approach, International Journal of Crashworthiness, Vol. 9, No. 3, pp. 285-297.

Nalepa, E. (1990). Crashworthiness Simulation of the Opel - Vectra Using the Explicit FE Method, International Journal of Vehicle Design, Vol.11, No. 2, pp. 191-201.

Neal-Sturgess, C.E., and Guo, R., (2007). Modelling the Effects of an Inflatable Tubular Structure (ITS) on Occupant Kinematics and Injury Risk in the Rollover of a Sports Utility Vehicle (SUV), International Journal of Crashworthiness, Vol. 12, No. 4, pp. 355-366.

Ni, C.M. (1981). A General Purpose Technique for Nonlinear Dynamic Response of Integrated Structures, 4th International Conference on Vehicle Structural Mechanics, SAE Publisher.

Nilsson, L. (1989). Computational Crash Analysis at the Saab Car Division, 12th International Technical Conference on Experimental Safety Vehicles, Goteburg, Sweden

Nour-Omid, B., and Clough, R.W. (1984). Dynamic Analysis of Structures Using Lanczos Coordinates, Earthquake Engineering and Structural Dynamics, Vol.12, No.4, pp.565-577.

O'Callahan, JC, Avitabile, P, and Riemer, R. (1989). System Equivalent Reduction Expansion Process (SEREP). Proceedings of the 7th International Modal Analysis Conference (Las Vegas, Nevada), Union College, Schenectady, NY, pp. 29-37.

Oden, J.T., and Pires, E.B. (1984). Algorithms and Numerical Results for Finite Element Approximations of Contact Problems with Non-Classical Friction Laws, Computers and Structures, Vol.19, pp.137-147.

PAM-CRASH, (2001), PAM-CRAH Reference Manual, Version 2001, PAM System International.

Paz, M. (1984). Dynamic Condensation, AIAA Journal, Vol.22, No.5, pp.724-727.

Pifko, A.B.and Winter, R. (1981). Theory and Application of Finite Element Analysis to Structural Crash Simulation, Computers and Structures, Vol.13, pp.277-285.

Pipkorn, B. (2002). A Mathematical Hybrid Model for Evaluating Vehicle Performance in CAR-to-Car Side Impacts, International Journal of Vehicle Design, Vol. 2, pp. 48-69.

Pyttel, T., Floss, A., Thibaud, C., Goertz, C. (2007). Realistic Simulation Models for Airbags and Humans-New Possibilities and Limits of FE Simulation, International Journal of Crashworthiness, Vol. 12, No. 5, pp. 481-492.

Qu, Z.Q. (1998). Structural Dynamic Condensation Techniques, Theory and Applications, PhD Dissertation, state Key Laboratory of Vibration, Shock and Noise, Shanghai Jiao Tong University, Shanghai, China.

Qu, Z.Q. (2001). Accurate Methods for Frequency Responses and Their Sensitivities of Proportionally Damped Systems, Computers and Structures, Vol.79, No.1, pp.87-96.

Ramsden, J.J., and Stoker, J.R. (1969). A Semi Automatic Method for Reducing the Size of Vibration Problems, International Journal for Numerical Methods in Engineering, Vol.1, No.4, pp.333-349.

Rapin, M.P. (1970). Vehicle Structural Crashworthiness, in Proceedings of 1970 International Automobile Safety Conference Compendium, Detroit, Michigan, pp.927-940.

Regan, A.J., and Winter, R. (1986). Nonlinear Finite Element Crash Analysis of Minivan, In Computational Mechanics, Proceedings of the VI International Conference on Computational Mechanics, Springer, Tokyo, PP.223-231.

Renfroe, D.A., and Partain, J.F., (2000). Modelling of Occupant Impacts During Rollover Collisions, SAE Paper No. 2000-01-0854.

Rubin, S. (1975). Improved Component Mode Representation for Structural Dynamic Analysis, AIAA Journal, Vol.13, No.8, pp.995-1006.

Sadagopan, S. (2003). Formability Characterization of a New Generation of High Strength Steels, Final Report, AISI/DOE Technology Roadmap Program, U.S Department of Energy, American Iron and Steel Institute, Pittsburgh, PA 1522.

Schelkle, E, Klamser, H, Porsche, F., (2004). CAE Simulations for Passive Safety Focused on the Porsche Cayenne- The Transition to New Technologies, 4TH European LS-DYNA User Conference, Plenary Session I, D-71287, Research and Development Center Weissach, Germany.

Schelkle, E, Elsenhans, H., (2002). Virtual Vehicle Development in the Concept Stage-Current Status of CAE Outlook on the Future, Conference Proceedings for the 3rd Worldwide MSC.Software Aerospace Conference & Technology Showcase, April 8th - 10th.

Schweizerhof, K. (2001). On the Current State-of-the-Art Crashworthiness Analysis with LS-DYNA, University of Karlsruhe, Institute for Mechanics Publications

Schweizerhof, K., Walz, M., Rust, W., Franz, U., and Kirchner, M. (1999). Quasi-Static Structural Analysis with LS-DYNA, merits and Limits, II. European LS-DYNA User Conference, Proceedings Goeteborg.

Sheh, M.Y., and Khalil, T.B. (1991). The impact Response of a Vehicle Structural Rail by Experiments and Finite Element Analysis, In Symposium on Crashworthiness and

Occupant Protection in Transportation Systems, ASME, publisher, AMD-Vol.126/ BED-Vol.19, pp.195-207.

Sheh, M.Y., Ried, J.D., Lesh, S.M, Cheva, W. (1992). Vehicle Crashworthiness Analysis Using Numerical Methods and Experiments, 8th International Conference on Vehicle Structural Mechanics and CAE, Traverse City, Michigan, SAE Publisher, pp.119-128.

Shieh, R.C. (1972). Basic Research in Crashworthiness II-Precollapse Dynamic Analysis of Plane, Ideal Elasto-Plastic Frame Structures Including the Case of Collision into a Narrow Rigid Pole Obstacle, Cornell Aeronautical Laboratory, Ithaca, CAL Report No.BV-2987-V-3.

Simunovic, S., Fekete, J., and Meulemann, D. (2003). Modeling of Strain Rate Effects in Automotive Impact, SAE Transactions Paper No. 2003-01-1383, Detroit, MI.

Thacker, J.G., Reagan, S.W., Pellettiere, J.A., Pilkey, W.D., Crandall, J.R., and Sieveka, E.M. (1998). Experiences during Development of a Dynamic Crash Response Automobile Model, Finite Element in Analysis and Design, Vol. 30, pp.279-295.

Thompson, J.E. (1972). Control of Structural Collapse in Automotive Side Impact Collisions, Ph.D. Dissertation, University of Detroit, MI.

Thomson, R., Edwards, M., Martin, T., Zweep, Cor V.D., Damm, R., and Della Valle, G., (2007). Car-Car Crash Compatibility: Development of Crash Test Procedures in the VC-Compact Project, International Journal of Crashworthiness, Vol. 12, No. 2, pp. 137-151.

Wang, H.C. and Merdith, D. (1983). The Crush Analysis of Vehicle Structures, International Journal of Impact Engineering, Vol.1, No.3, pp. 199-225.

Welch, R.E., Bruce, R.W., and Belytschko, T. (1975). Finite Element Analysis of Automotive Structures under Crash Loadings, Report No.DOT-HS-105-3-697, IIT Research Institute, Chicago, IL.

Wierzbicki, T., and Akerstrom, T. (1997). Dynamic Crushing of Strain Rate Sensitive Box Columns, SAE Paper No. 770592, Proceedings of 2nd International Conference on Vehicle Structural Mechanics, April 18-20.

Wilson, E.L., Yuan, M.W., and Dickens, J.M. (1982). Dynamic Analysis by Direct Superposition of Ritz Vectors, Earthquake Engineering and Structural Dynamics, Vol.10, pp.813-821.

Winter, R., Crouzet-Pascal, J., and Pifko, A.B. (1984). Front Crash Analysis of Steel Frame Auto Using a Finite Element Computer Code, SAE Paper 840278, VSM Conference, Detroit, MI.

Winter, R., Mantus, M., and Pifko, A.B. (1981). Finite Element Crash Analysis of a Rear Engine Automobile, 4th International Conference on Vehicle Structural Mechanics, SAE Publisher, pp.55-61.

Xue, X and Schmid, F., (2004). Analyses of the Crashworthiness of a Conventionally Designed Rail Vehicle, in Proceedings of International Crashworthiness Conference, San Francisco, CA, 14-16 July.

Yee, V. (1990). Reduction of Component Mode Synthesis Formulated Matrices for Correlation Studies, AIAA Journal, Vol.28, No.6, pp.1142-1143.

Young, J.W. (1972). A Computer Simulation of Nonlinear Transient Response of Structures, Report No.DOT-HS-091-1-125-B, Philco-Ford Corporation, Palo Alto, CA.

Zaouk, A.K., Marzougui, D., and Bedewi, N.E. (1998). Development of a Detailed Vehicle Finite Element Model Part I: Methodology, International Crashworthiness Conference, Dearborn, Michigan, pp.184-195.

Zaouk, A.K., Marzougui, D., and Bedewi, N.E. (2000). Development of a Detailed Vehicle Finite Element Model Part I: Methodology, International Journal of Crashworthiness, Vol. 5, No.1, pp.25-36.

Zaouk, A.K., Marzougui, D., and Bedewi, N.E. (2000). Development of a Detailed Vehicle Finite Element Model Part II: Material Characterization and Component Testing, International Journal of Crashworthiness, Vol. 5, No.1, pp.37-50.

Zaouk, A.K., Bedewi, N.E., Kan, C.D., and Schinke, H. (1996). Evaluation of a Multi-Purpose Pickup Truck Model using Full Scale Crash Data with Application to Highway-Barrier Impacts, Proceedings of the 29th International Symposium on Automotive Technology and Automation, Florence, Italy.

Appendix A

Time Domain and Frequency Domain Analyses

The list of selected nodes from transient analyses regarding acceleration data and their corresponding frequencies are introduced in this section. The locations of the selected nodes were shown in Figure A.1. In this work, the following units were used: for, time [second], acceleration [mm/sec^2], and frequency [Hertz]. All of the analyses were performed using these units. Figures A.2 through A.31 depict the time history of the acceleration data and their respective frequencies.

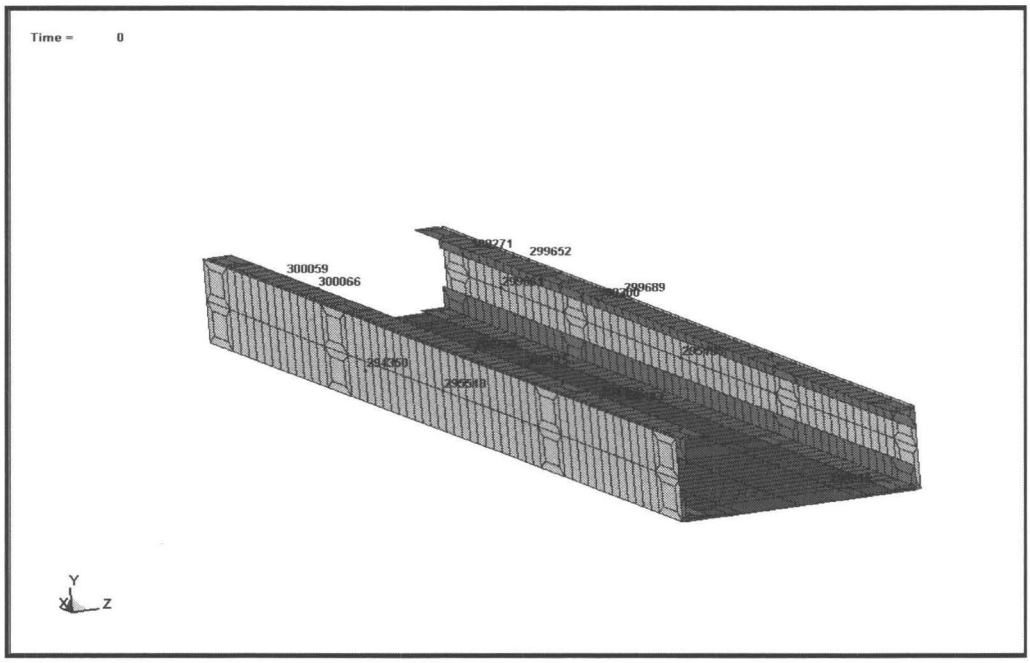

Figure A.1: Locations of preselected nodes on the FE model

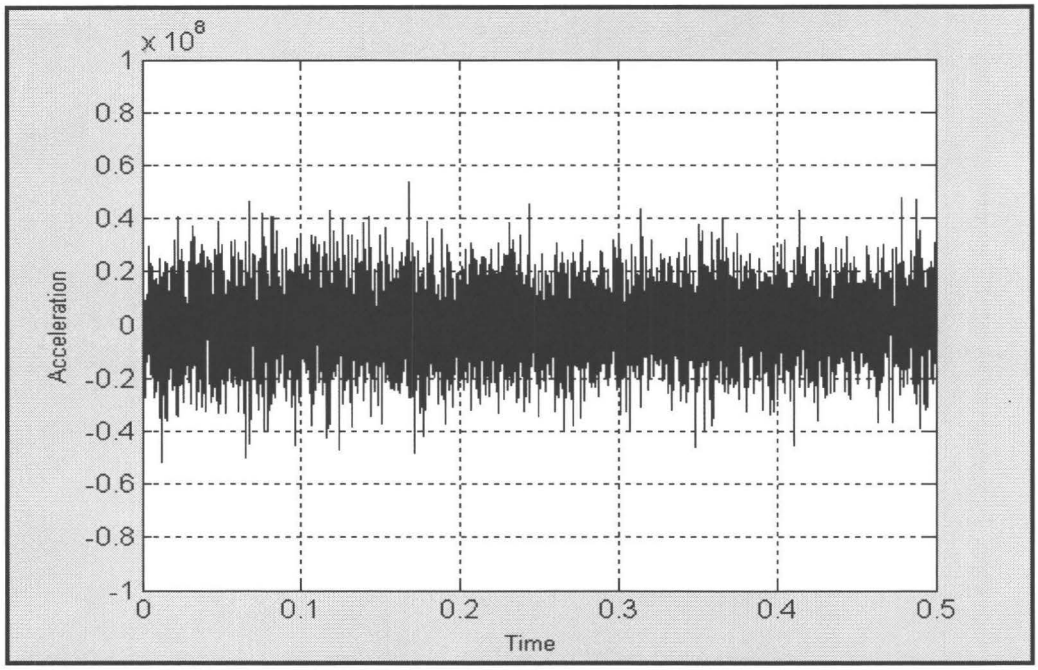

Figure A.2: Plot of the acceleration vs. time for node # 300143 determined by full model simulation

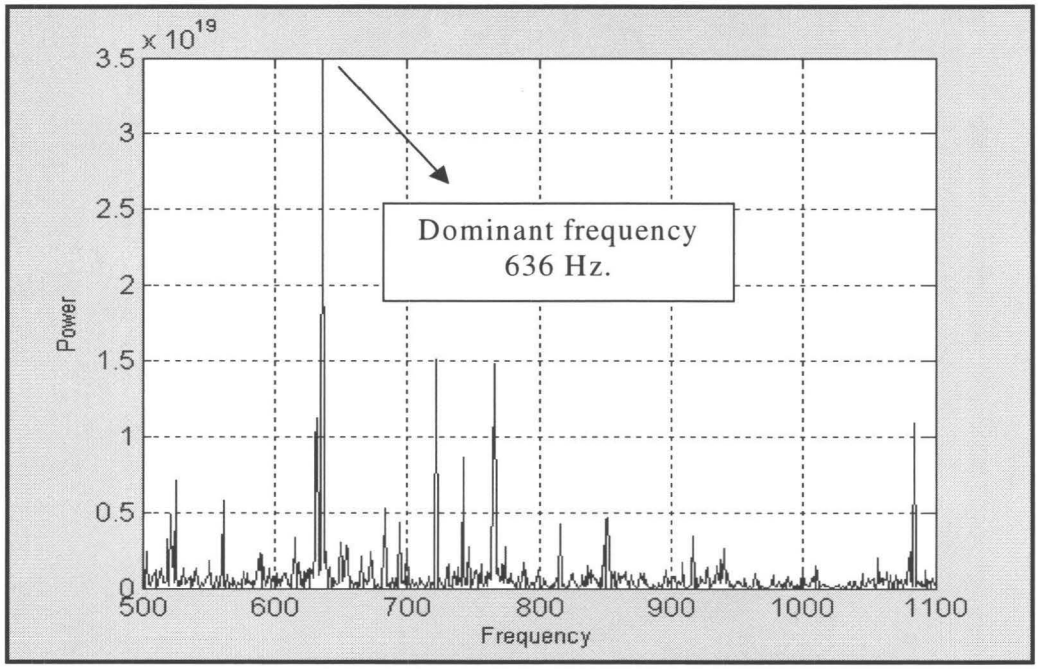

Figure A.3: Plot of the corresponding frequency vs. power for node # 300143 determined by FFT analysis

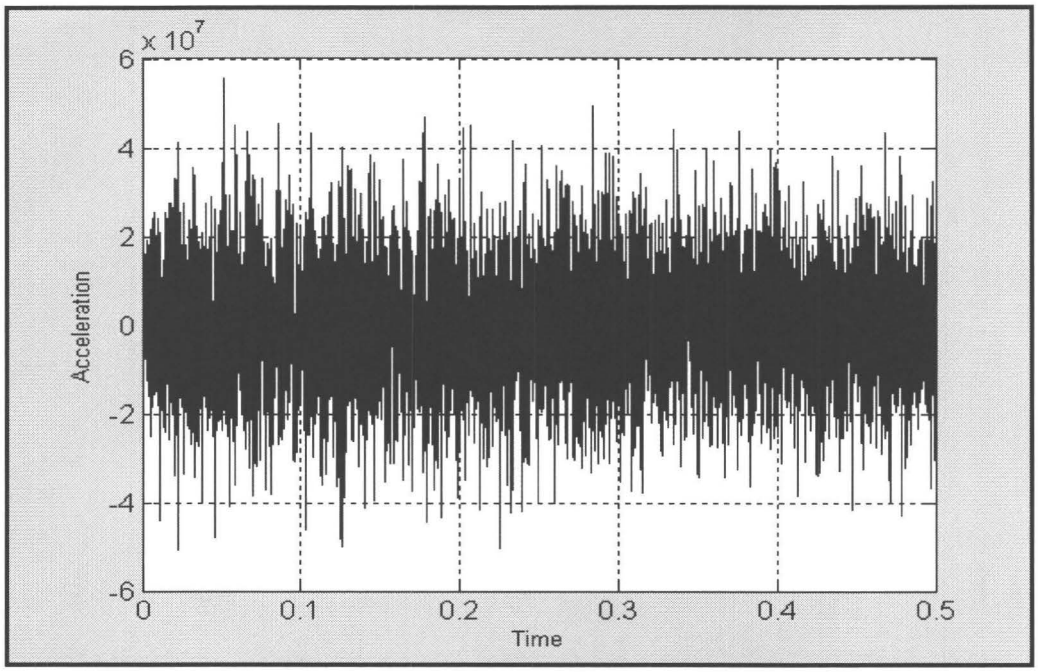

Figure A.4: Plot of the acceleration vs. time for node # 300059 determined by full model simulation

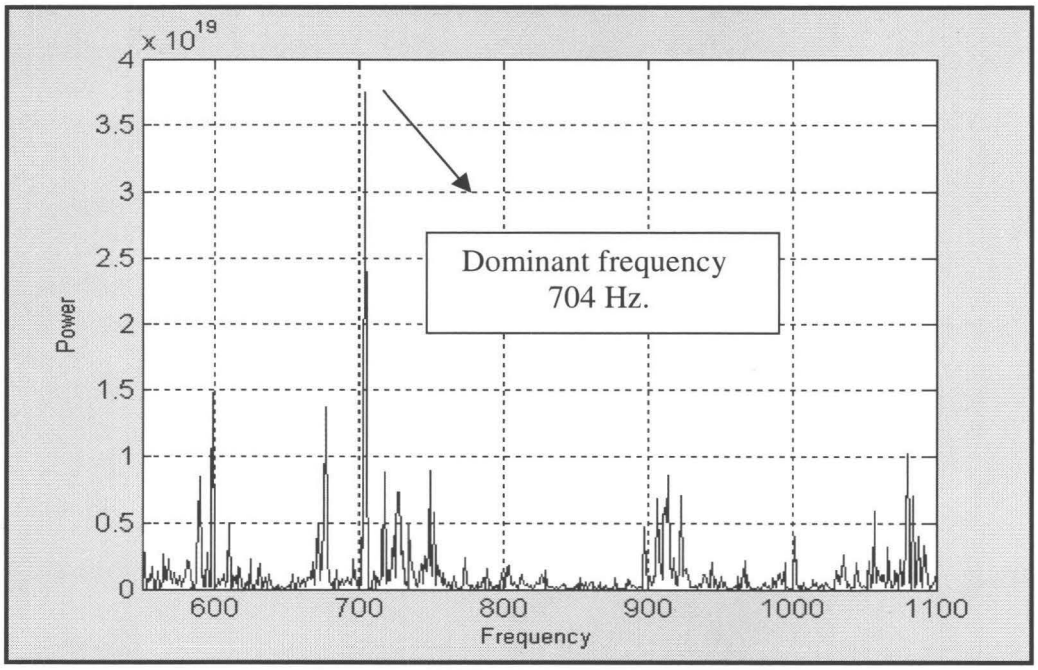

Figure A.5: Plot of the corresponding frequency vs. power for node # 300059 determined by FFT analysis

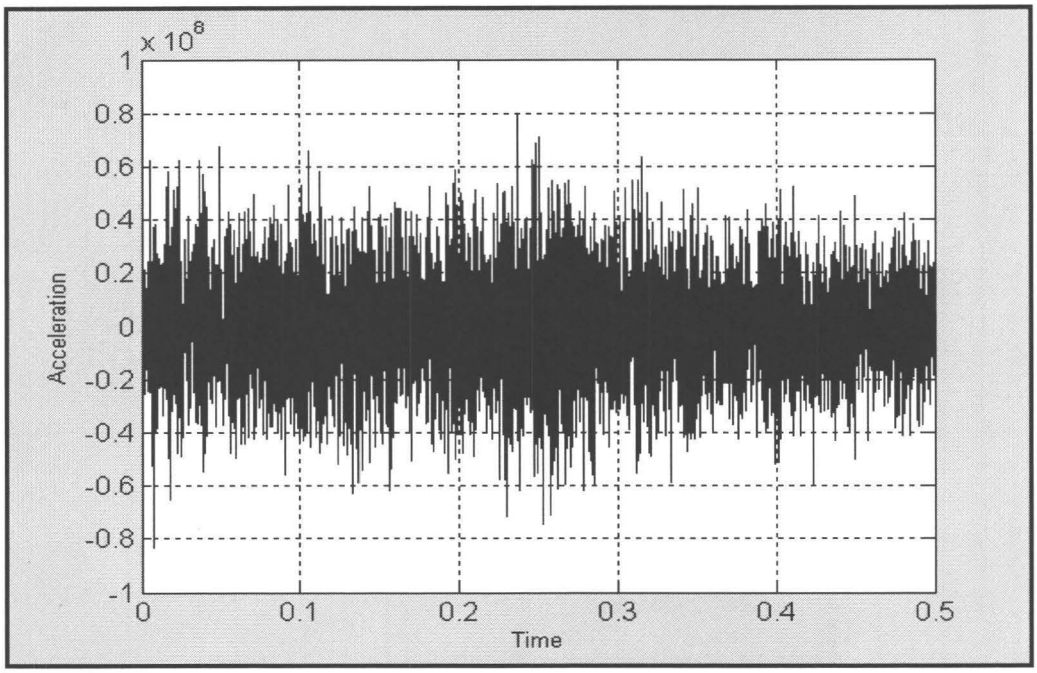

Figure A.6: Plot of the acceleration vs. time for node # 299652 determined by full model simulation

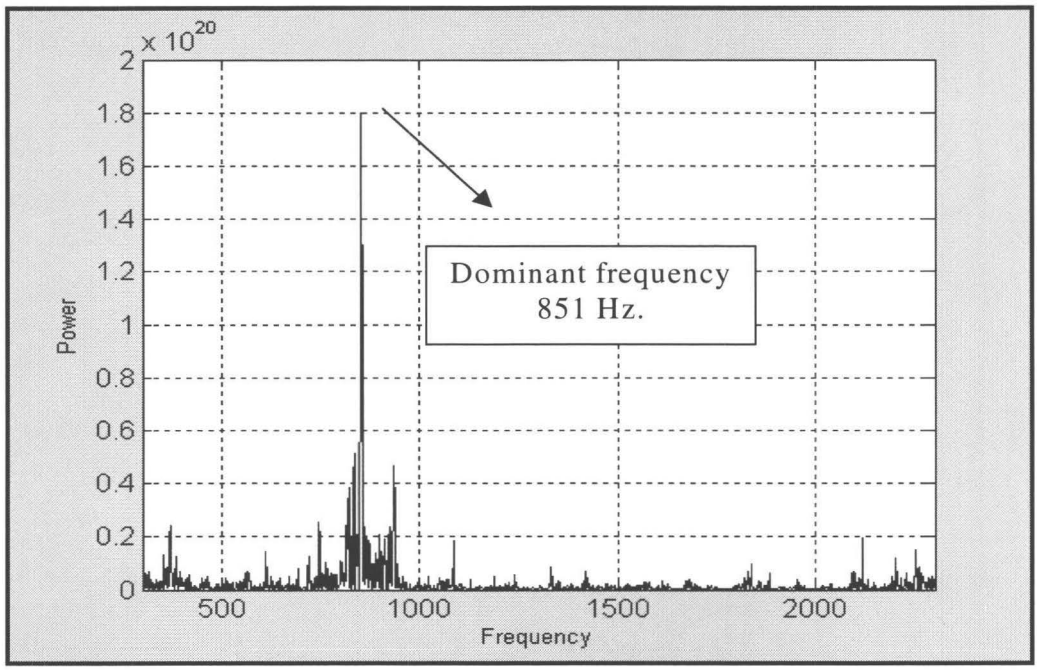

Figure A.7: Plot of the corresponding frequency vs. power for node # 299652 determined by FFT analysis

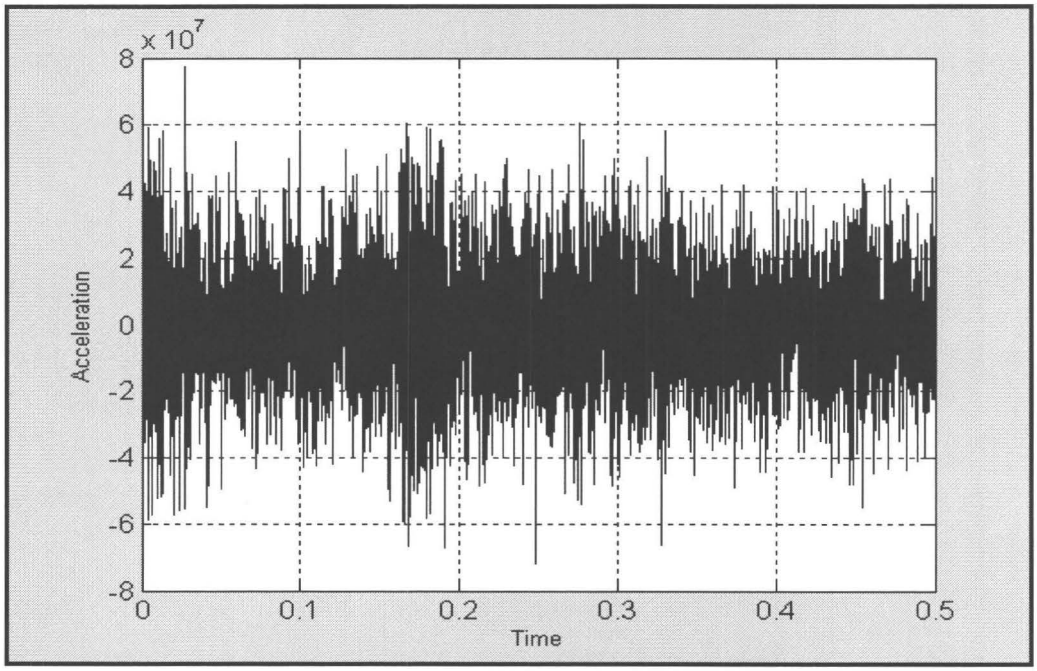

Figure A.8: Plot of the acceleration vs. time for node # 299689 determined by full model simulation

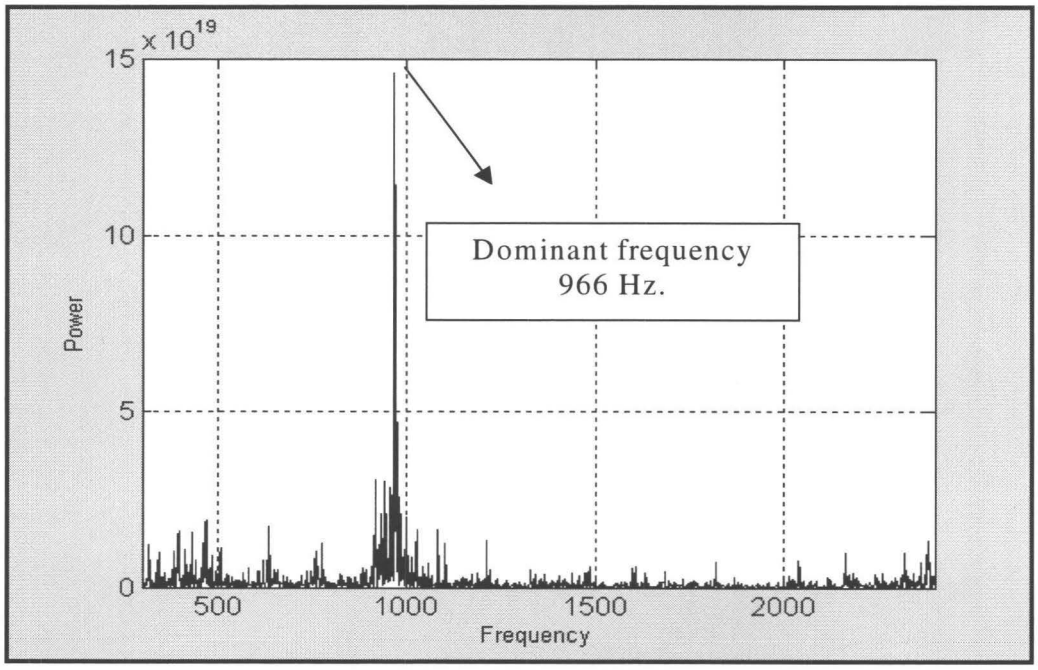

Figure A.9: Plot of the corresponding frequency vs. power for node # 299689 determined by FFT analysis

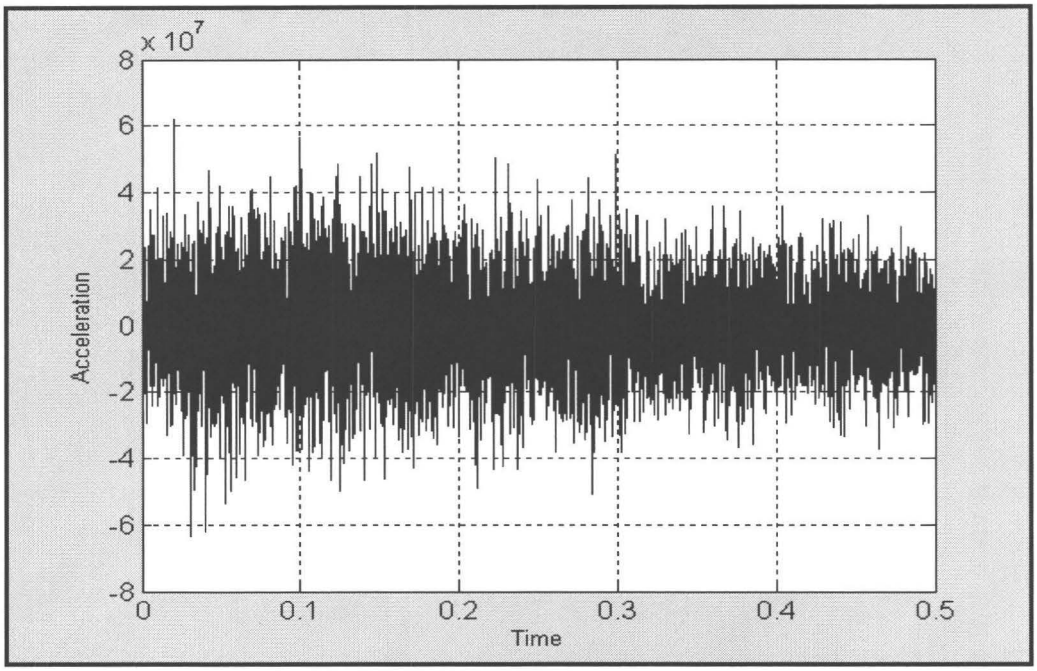

Figure A.10: Plot of the acceleration vs. time for node # 299915 determined by full model simulation

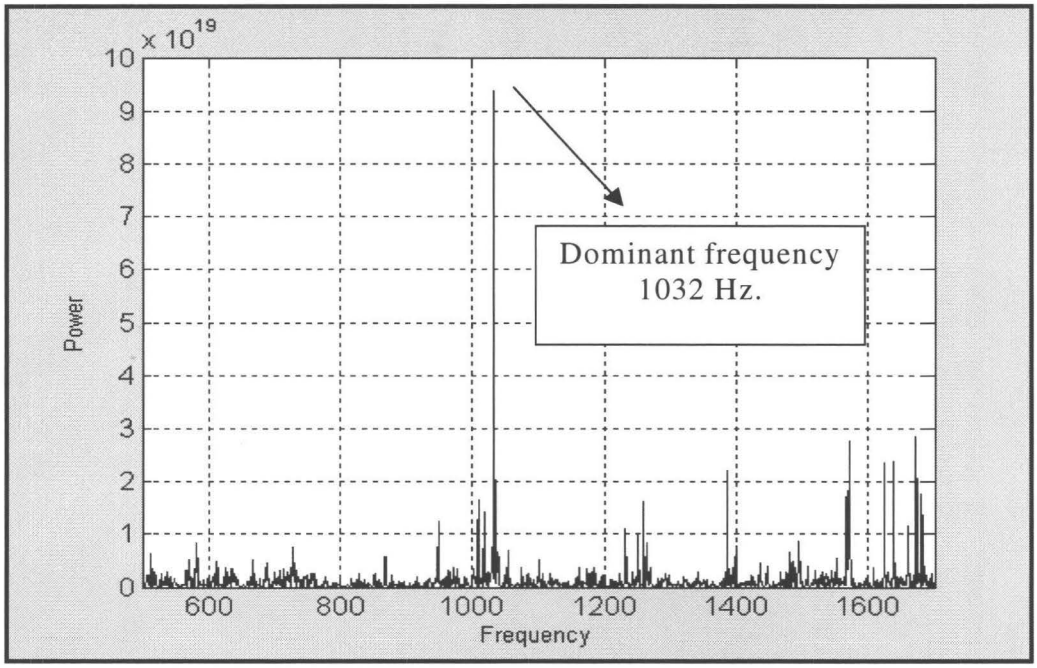

Figure A.11: Plot of the corresponding frequency vs. power for node # 299915 determined by FFT analysis

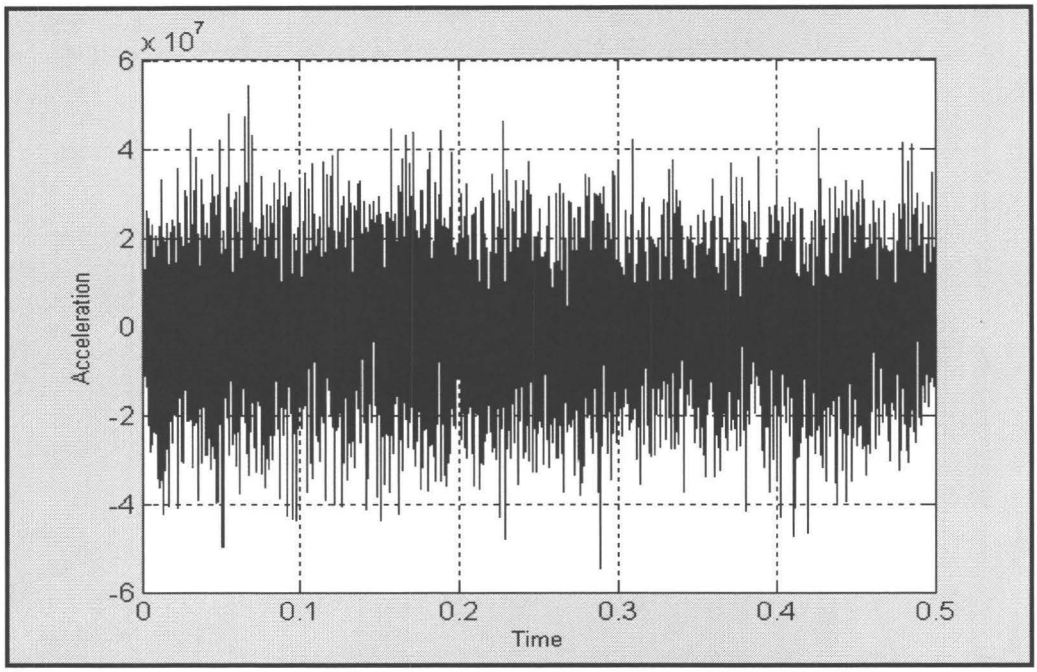

Figure A.12: Plot of the acceleration vs. time for node # 300066 determined by full model simulation

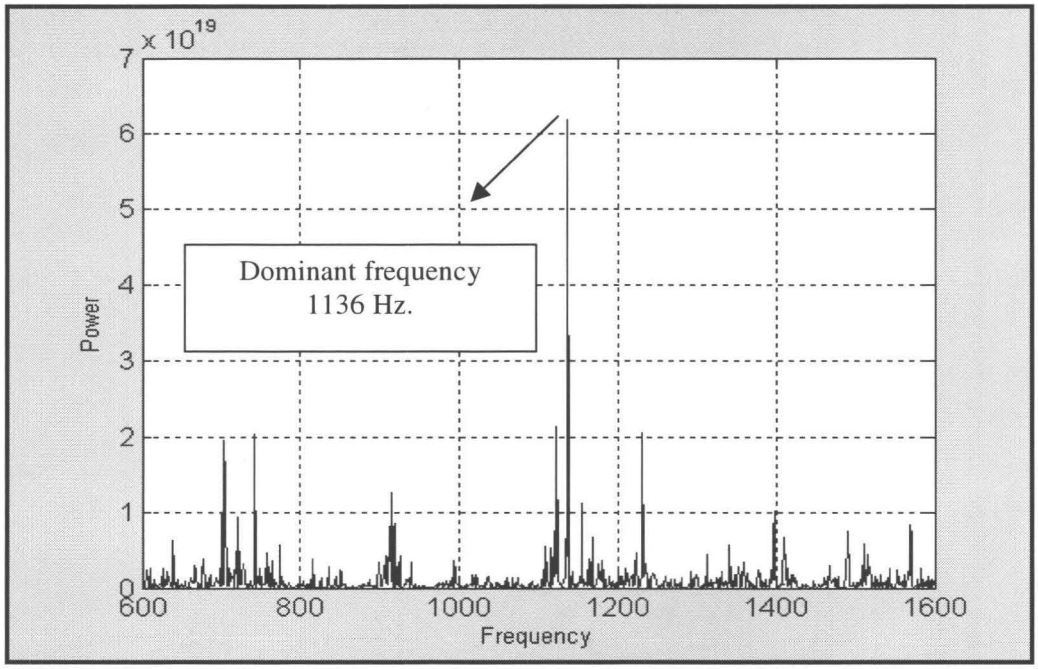

Figure A.13: Plot of the corresponding frequency vs. power for node # 300066 determined by FFT analysis

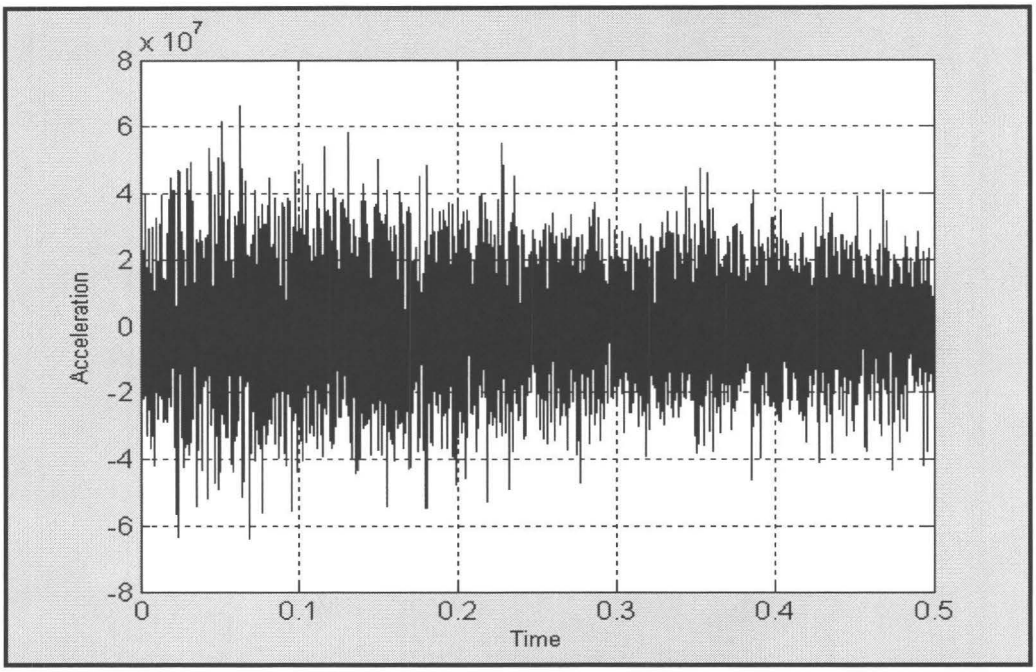

Figure A.14: Plot of the acceleration vs. time for node # 294350 determined by full model simulation

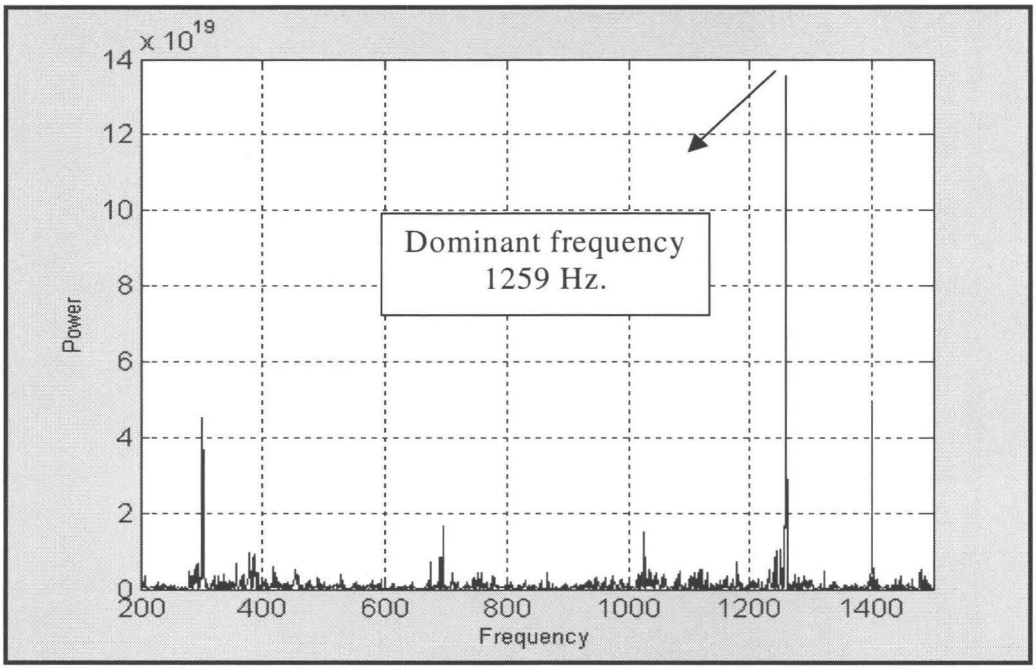

Figure A.15: Plot of the corresponding frequency vs. power for node # 294350 determined by FFT analysis

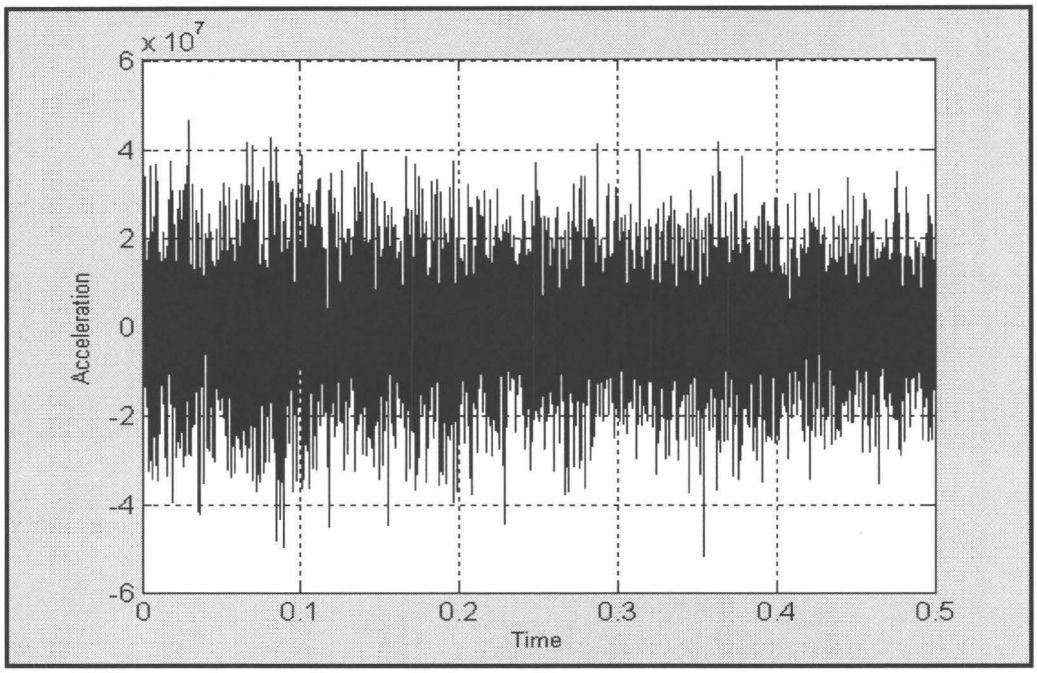

Figure A.16: Plot of the acceleration vs. time for node # 300125 determined by full model simulation

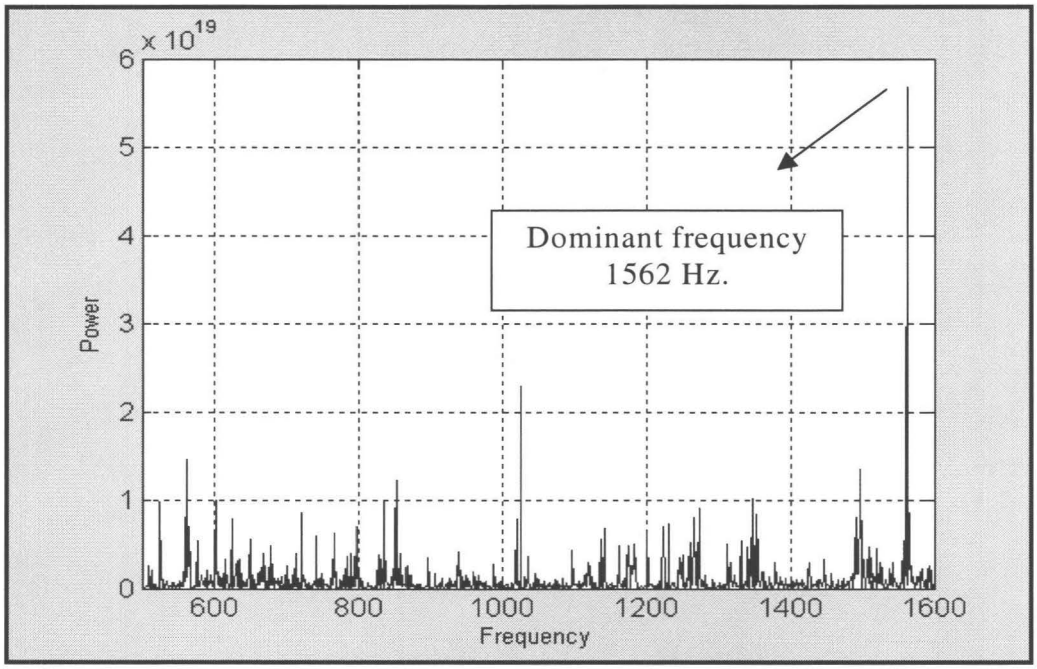

Figure A.17: Plot of the corresponding frequency vs. power for node # 300125 determined by FFT analysis

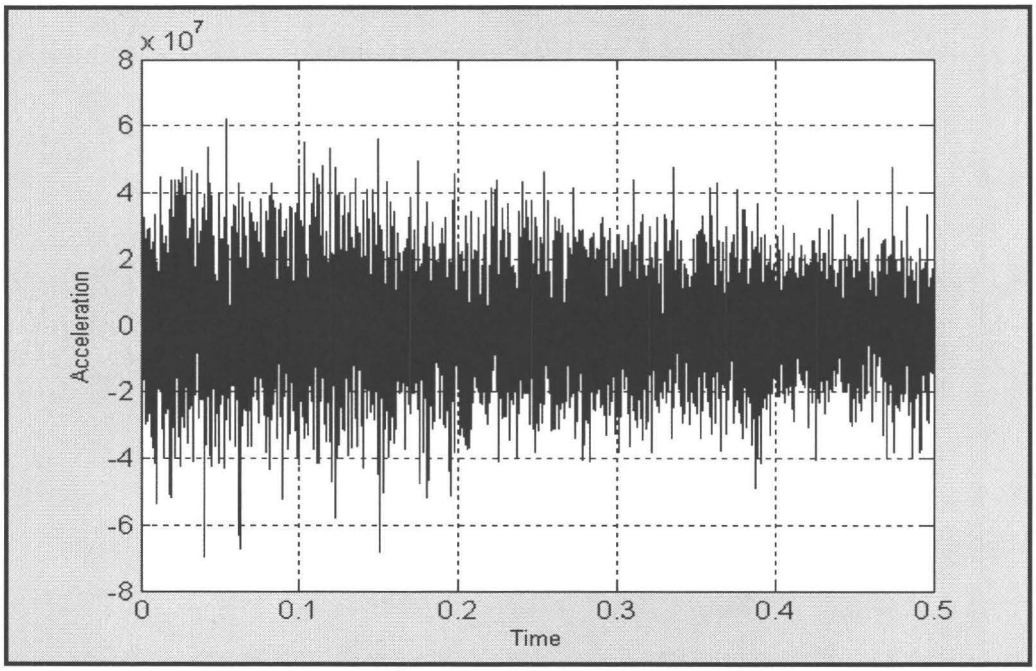

Figure A.18: Plot of the acceleration vs. time for node # 299760 determined by full model simulation

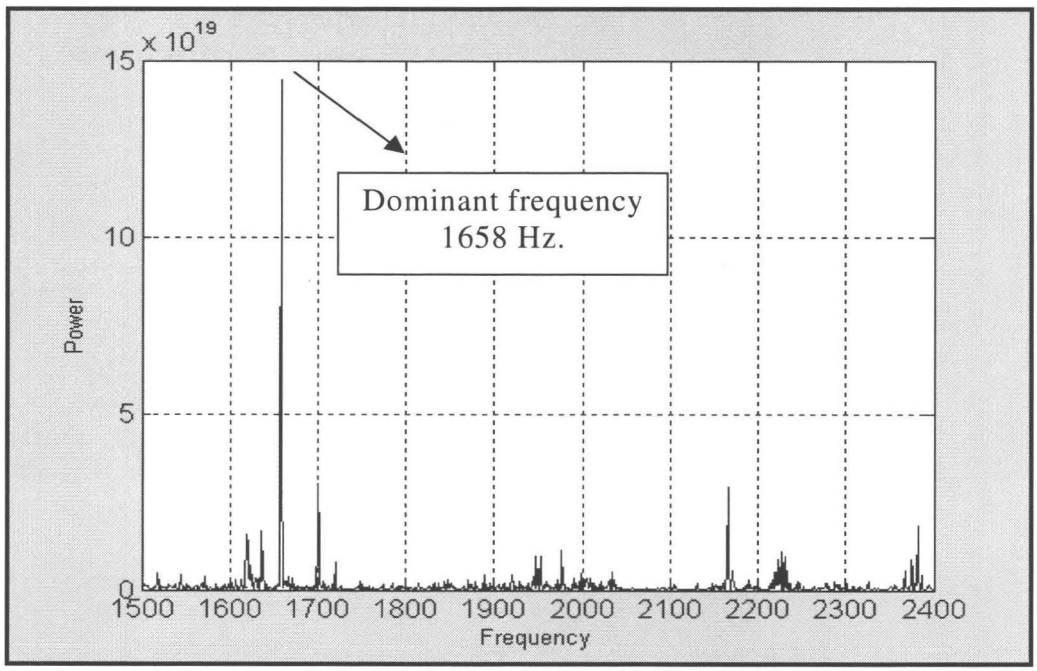

Figure A.19: Plot of the corresponding frequency vs. power for node # 299760 determined by FFT analysis

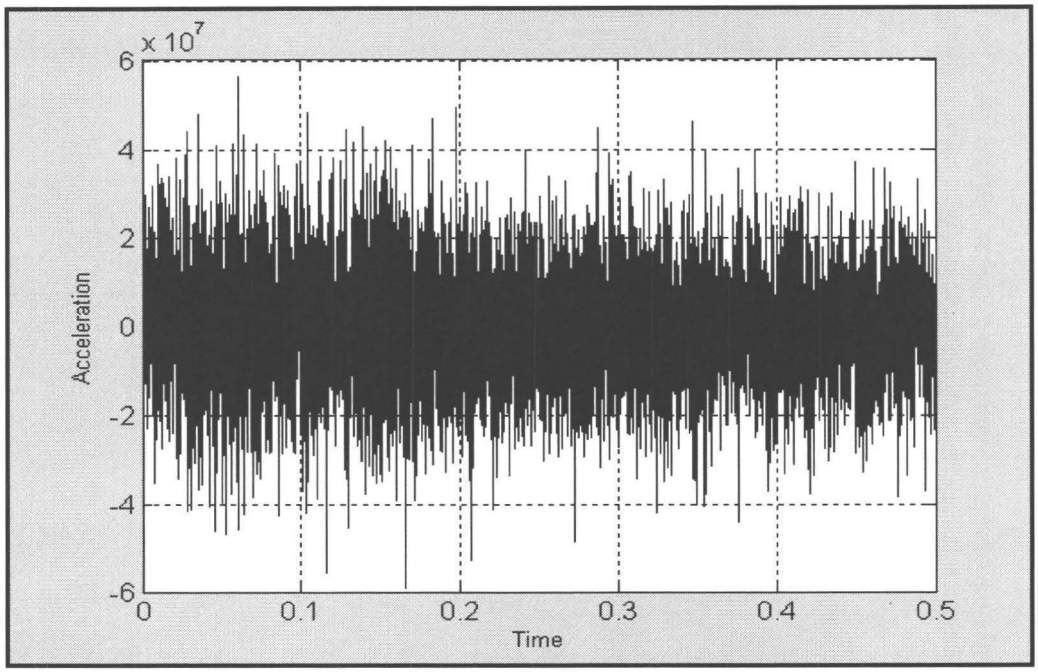

Figure A.20: Plot of the acceleration vs. time for node # 300300 determined by full model simulation

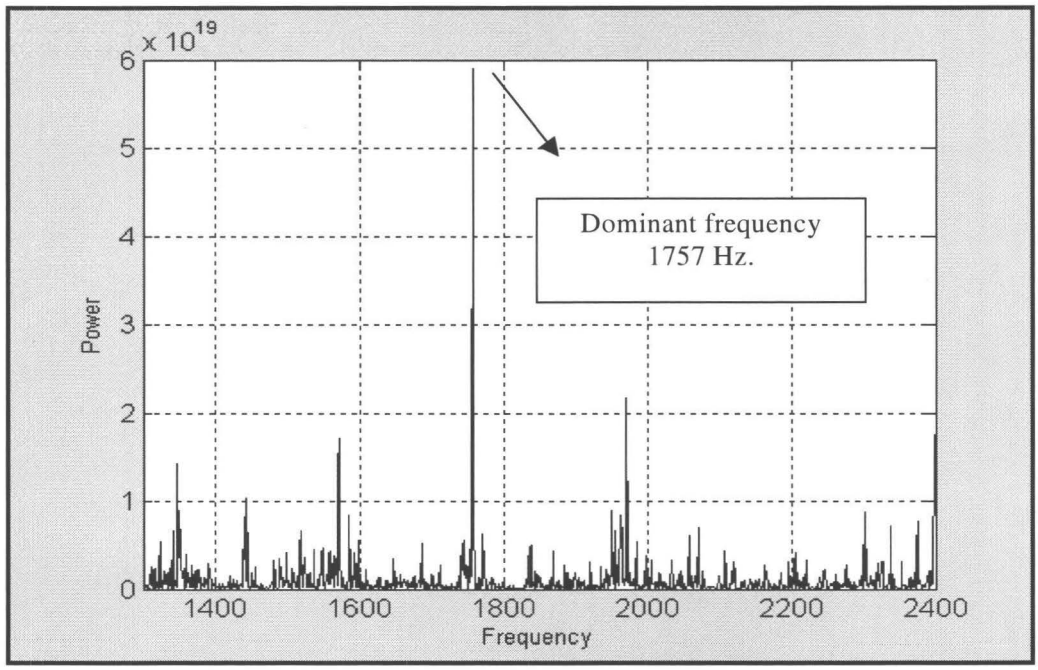

Figure A.21: Plot of the corresponding frequency vs. power for node # 300300 determined by FFT analysis

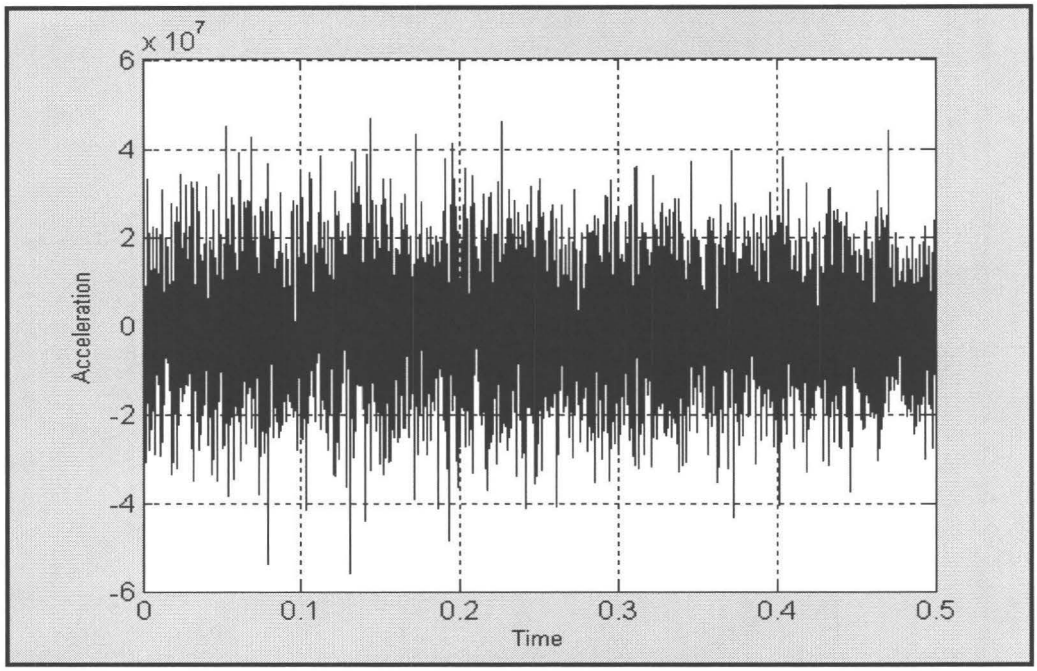

Figure A.22: Plot of the acceleration vs. time for node # 295485 determined by full model simulation

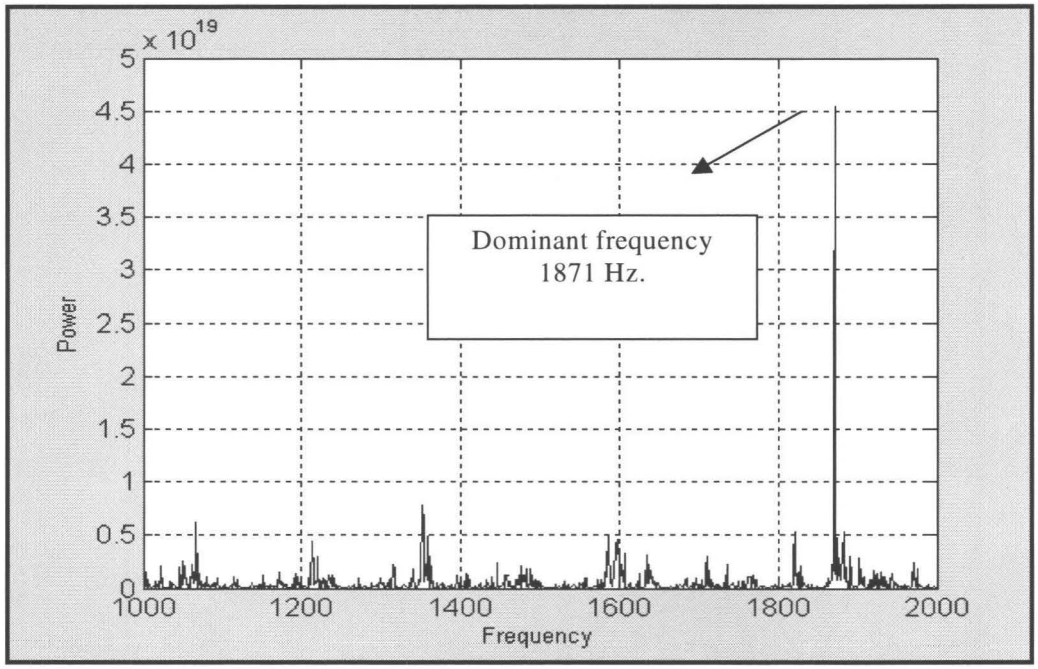

Figure A.23: Plot of the corresponding frequency vs. power for node # 295485 determined by FFT analysis

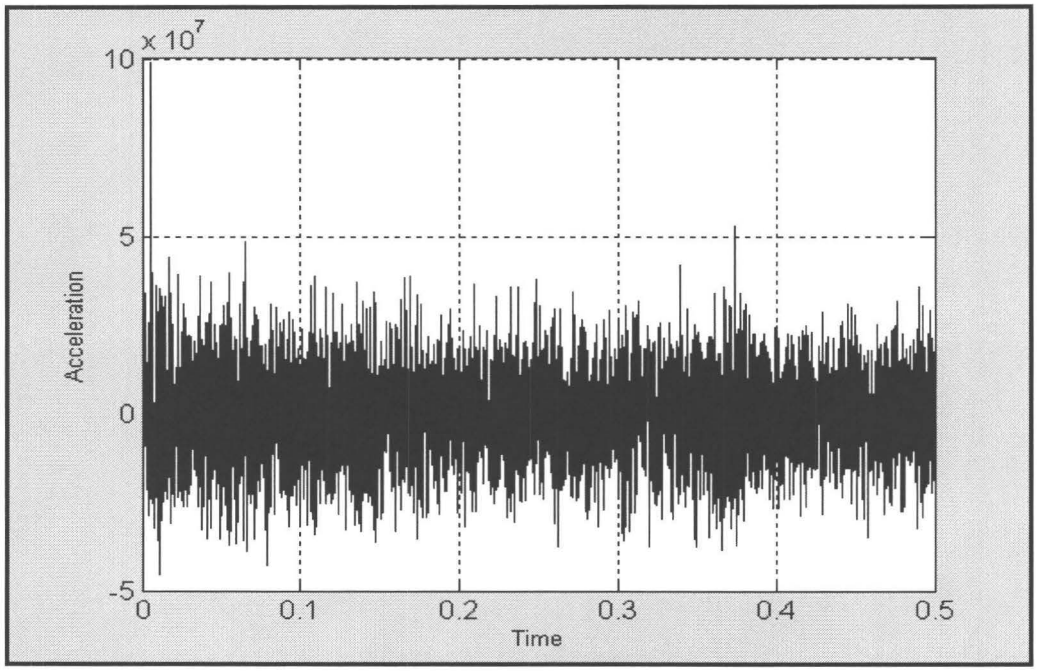

Figure A.24: Plot of the acceleration vs. time for node # 299661 determined by full model simulation

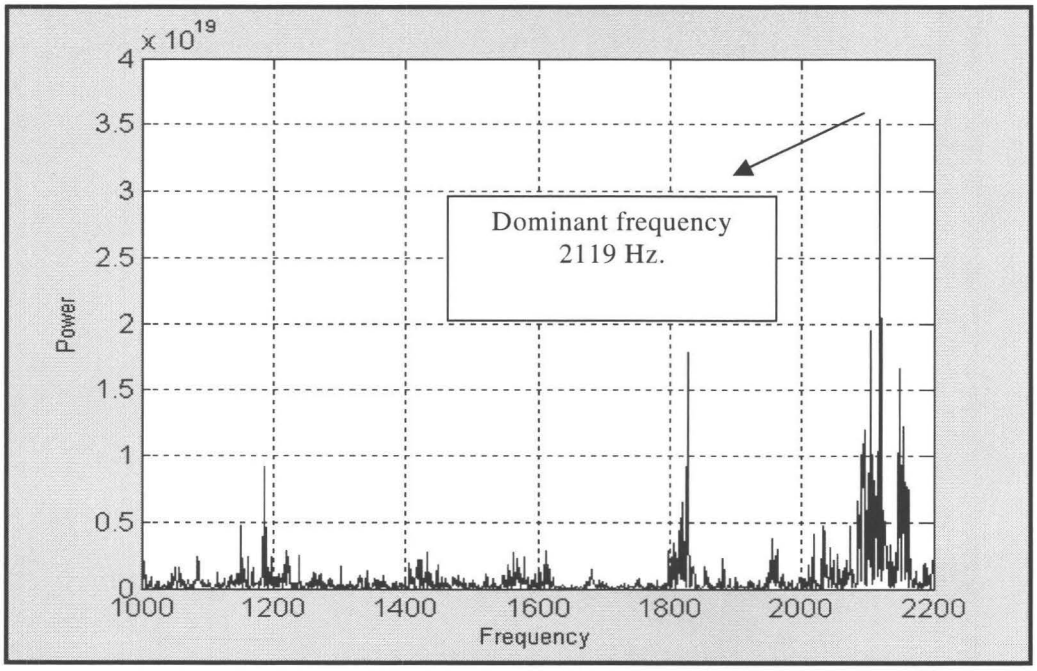

Figure A.25: Plot of the corresponding frequency vs. power for node # 299661 determined by FFT analysis

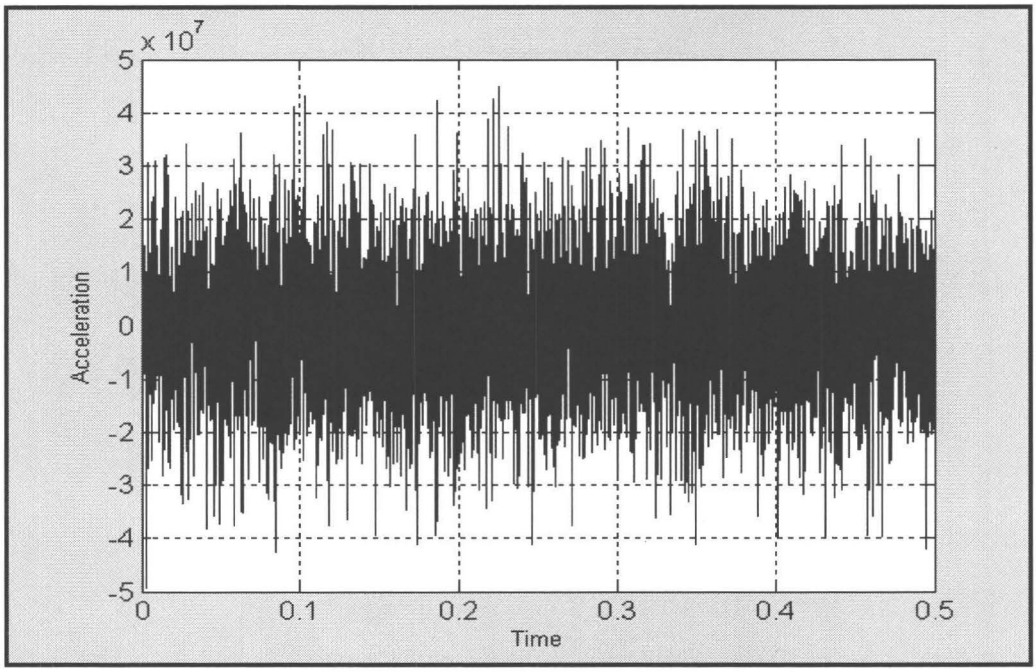

Figure A.26: Plot of the acceleration vs. time for node # 295548 determined by full model simulation

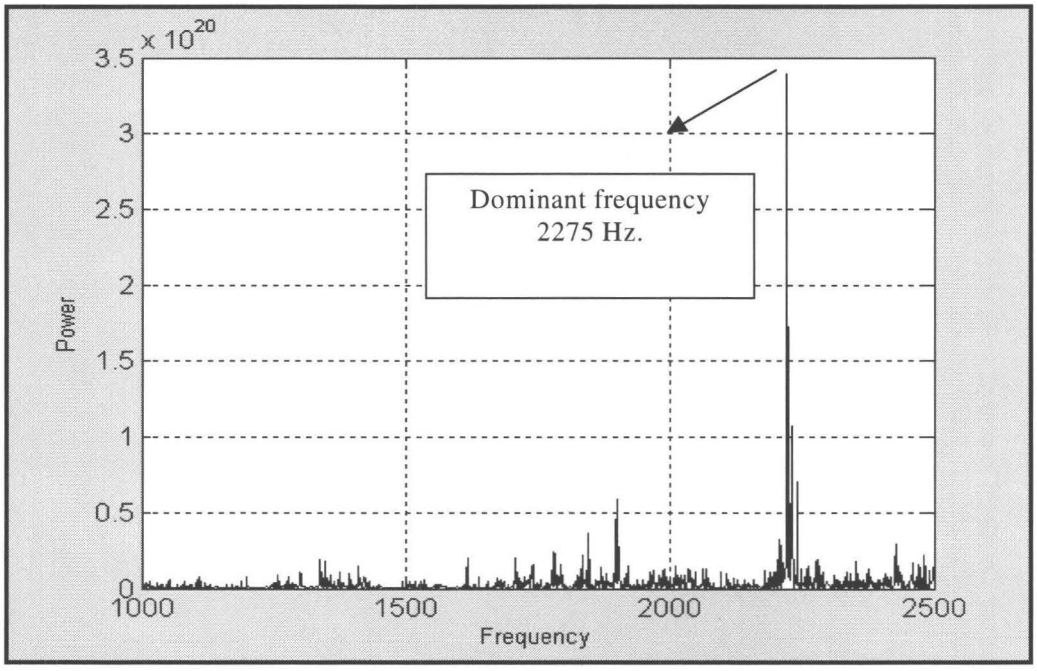

Figure A.27: Plot of the corresponding frequency vs. power for node # 295548 determined by FFT analysis

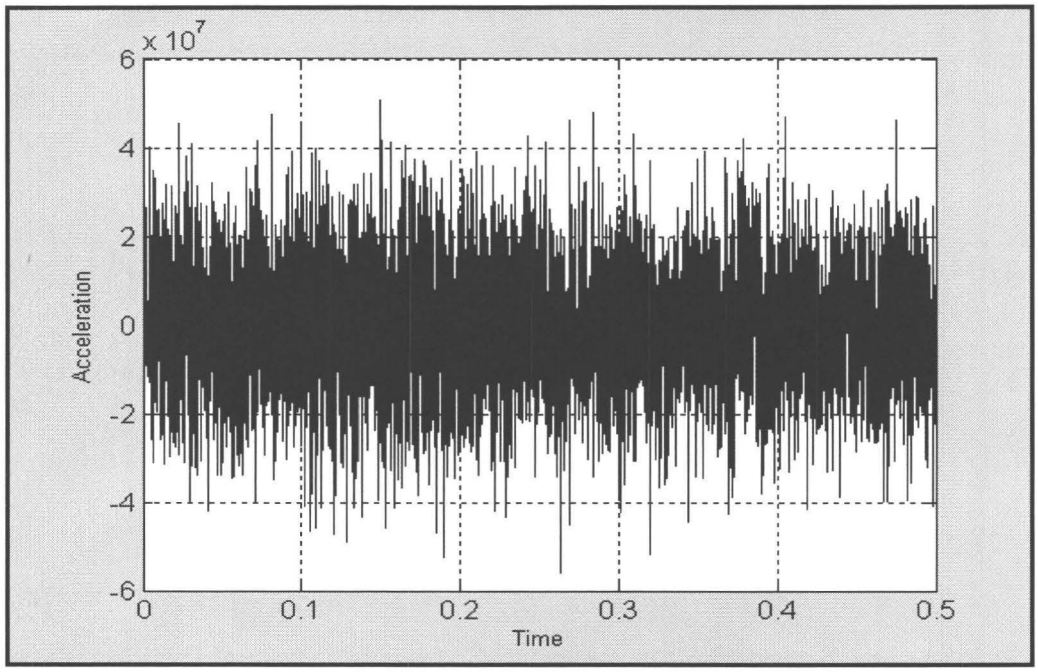

Figure A.28: Plot of the acceleration vs. time for node # 300271 determined by full model simulation

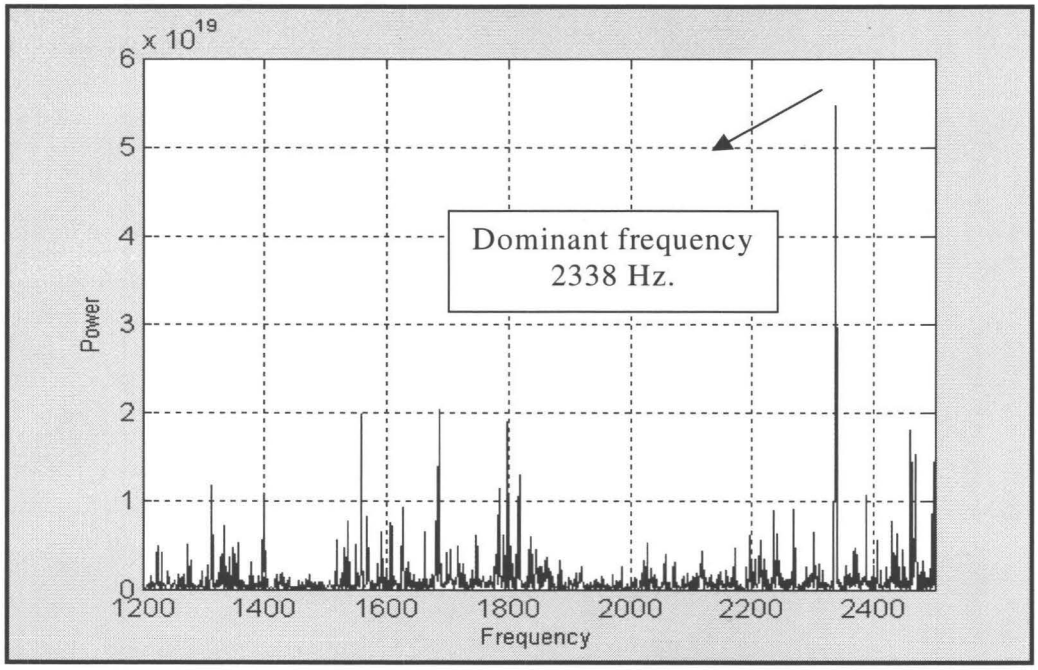

Figure A.29: Plot of the corresponding frequency vs. power for node # 300271 determined by FFT analysis

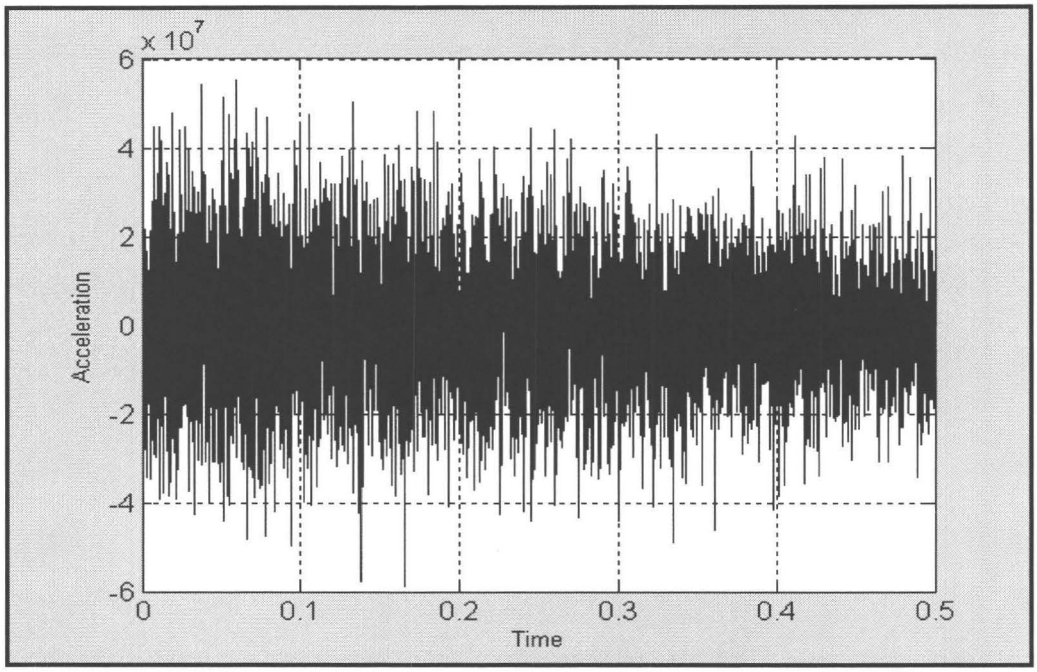

Figure A.30: Plot of the acceleration vs. time for node # 294360 determined by full model simulation

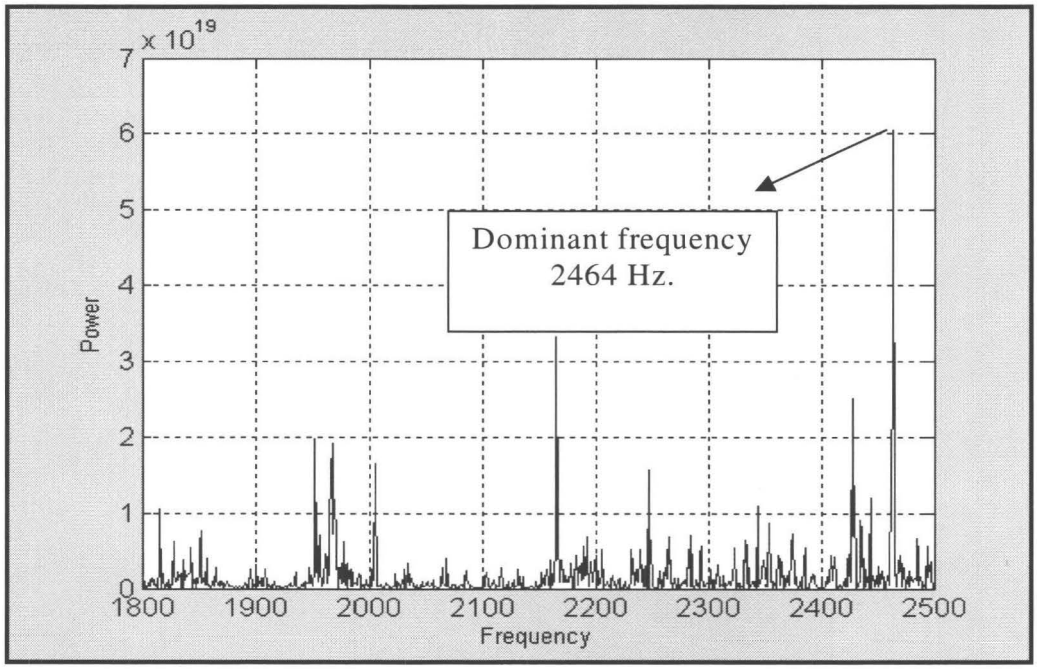

Figure A.31: Plot of the corresponding frequency vs. power for node # 294360 determined by FFT analysis

Appendix B

Frequencies Comparison of FE and Modal Analyses

Figure B.1 depicts nodal locations of the 15 preselected nodes around the boundary of the substructure (as shown earlier in Figure 4.15).

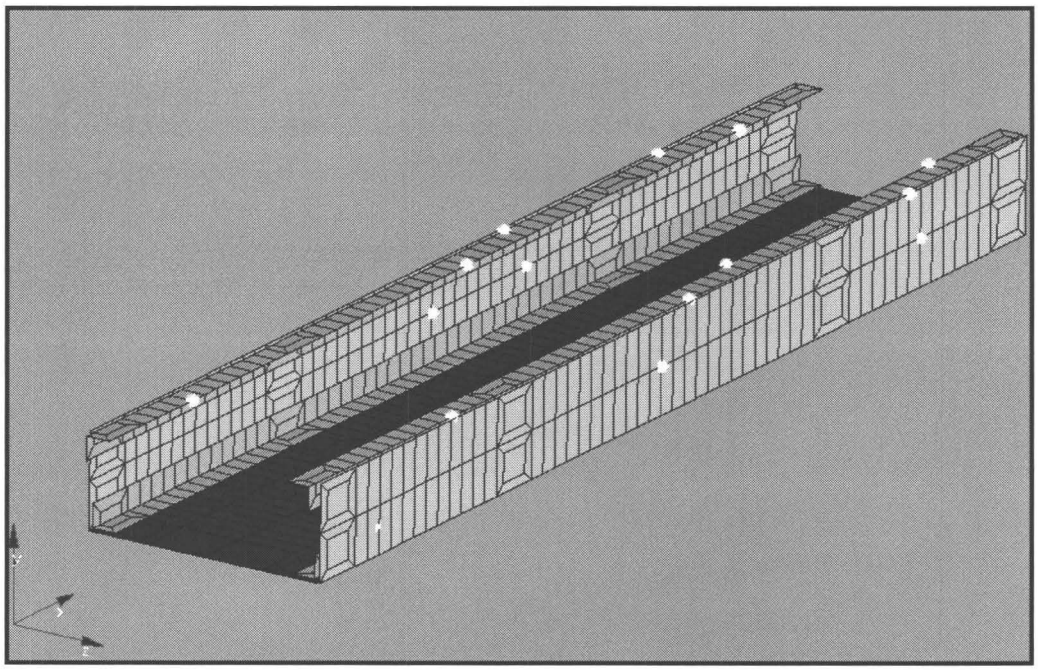

Figure B. 1: Locations of preselected nodes on the FE model

Table B.1 lists the nodal displacements and their resultant magnitudes determined from the full model modal analysis.

Table B.1: Nodal displacements and their resultant magnitudes determined from the full model analysis

Node number	X-displacement [mm]	Y-displacement [mm]	Z-displacement [mm]	Magnitude [mm]
300143	3.58	-0.87	0.38	3.70
300059	0.99	0.60	-0.71	1.36
299652	1.30	0.47	-0.62	1.51
299689	2.20	0.43	3.35	4.03
299915	0.02	-0.12	-0.20	0.23
300066	2.28	0.32	-0.03	2.31
294350	0.01	1.14	0.02	1.14
300125	3.03	1.55	-0.83	3.50
299760	0.02	0.35	0.02	0.35
300300	2.46	0.23	-0.21	2.48
295485	2.37	0.08	5.36	5.86
299661	0.66	0.08	0.69	0.95
295548	2.48	0.29	-6.39	6.86
300271	0.80	0.32	0.24	0.90
294360	0.02	1.53	0.01	1.53

Table B.2 shows the modal displacements determined by the sub model modal analysis.

Table B.2: Corresponding nodal displacements and their respective resultant magnitudes, determined by sub model analysis

Node number	X-displacement [mm]	Y-displacement [mm]	Z-displacement [mm]	Magnitude [mm]
300143	3.94	-0.97	0.42	4.08
300059	1.11	0.66	-0.78	1.51
299652	1.42	0.57	-0.70	1.68
299689	2.45	0.50	3.67	4.44
299915	0.02	-0.13	-0.22	0.26
300066	2.51	0.41	-0.04	2.55
294350	0.01	1.26	0.04	1.27
300125	3.39	1.70	-0.97	3.92
299760	0.02	0.39	0.02	0.39
300300	2.72	0.27	-0.30	2.75
295485	2.44	0.09	6.05	6.53
299661	0.73	0.09	0.75	1.06
295548	2.86	0.43	-6.98	7.55
300271	0.89	0.38	0.28	1.01
294360	0.04	1.69	0.01	1.69

Table B.3 lists the comparisons of the resultant displacement vectors, tabulated in Tables B.1 and B.2.

Table B.3: Comparison of the resultant displacements magnitudes determined by full model and sub model modal analyses

Node number	Modal analysis full model [mm]	Modal analysis sub model [mm]
300143	3.70	4.08
300059	1.36	1.51
299652	1.51	1.68
299689	4.03	4.44
299915	0.23	0.26
300066	2.31	2.55
294350	1.14	1.27
300125	3.50	3.92
299760	0.35	0.39
300300	2.48	2.75
295485	5.86	6.53
299661	0.95	1.06
295548	6.86	7.55
300271	0.90	1.01
294360	1.53	1.69

Table B.4 shows the participation factors, along with corresponding frequencies.

Table B.4: Normalized participation factors and corresponding frequencies determined from transient and modal analyses

Node number	Participation factors	Frequencies of system (Hz.)	Frequencies of subsystem (Hz.)
300143	0.0718	636	881
300059	0.0684	704	1084
299652	0.0930	851	1302
299689	0.0952	966	1462
299915	0.0536	1032	1588
300066	0.0685	1136	1706
294350	0.0496	1259	1935
300125	0.0836	1562	2238
299760	0.0480	1658	2589
300300	0.0836	1757	2627
295485	0.0543	1871	2835
299661	0.0493	2119	2974
295548	0.0552	2275	3202
300271	0.0707	2338	3308
294360	0.0552	2464	3676

Appendix C
Comparison of Measurements

The out-of-plane measurements were taken from the front section, middle section and rear section along the z-axis (as shown in Figure C.1). The measurements were taken from the front section, middle section and rear section along the z-axis, and compare the out-of-plane deformations between a substructure in a full model and a substructure in a sub model. At each section, namely, front, middle and rear, a total of 11 nodes were selected and the corresponding out-of-plane displacements were measured for both substructure.

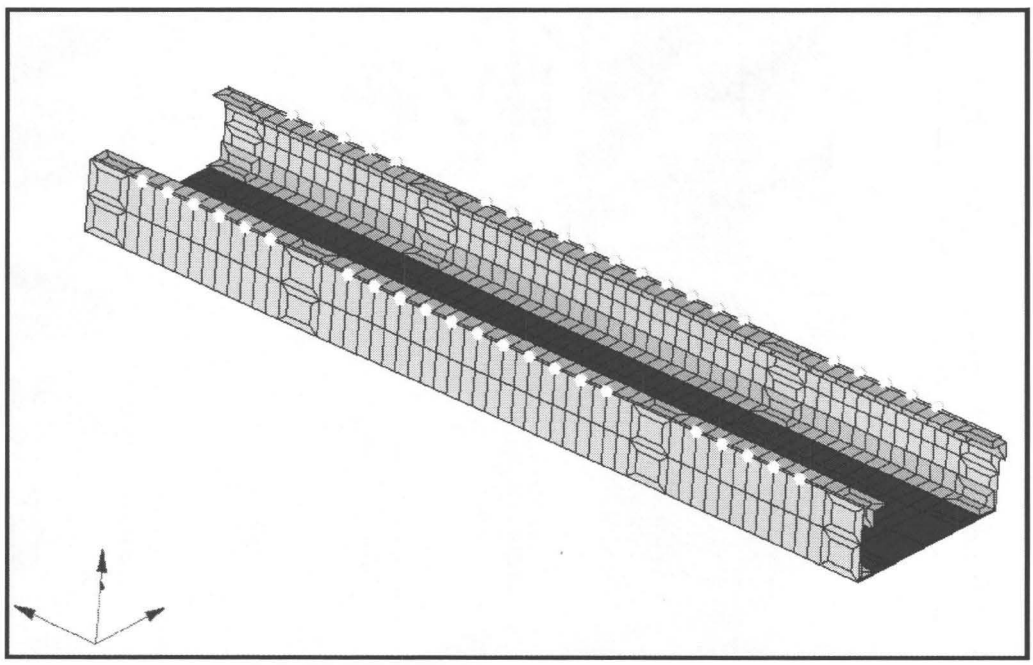

Figure C.1: Location of measurements along the z-axis corresponding to the out-of-plane measurements

Experimental measurements were obtained at various locations corresponding to the different sections, namely, front, middle and rear, for both isolated and *in situ* test articles. The same locations were used for obtaining out-of-plane deformations on both test articles and results were compared to each other. Figure C.2 depicts the locations corresponding to the out-of-plane measurements. These locations were identical in both the full and the isolated model. The measurements were obtained at five different locations along each section.

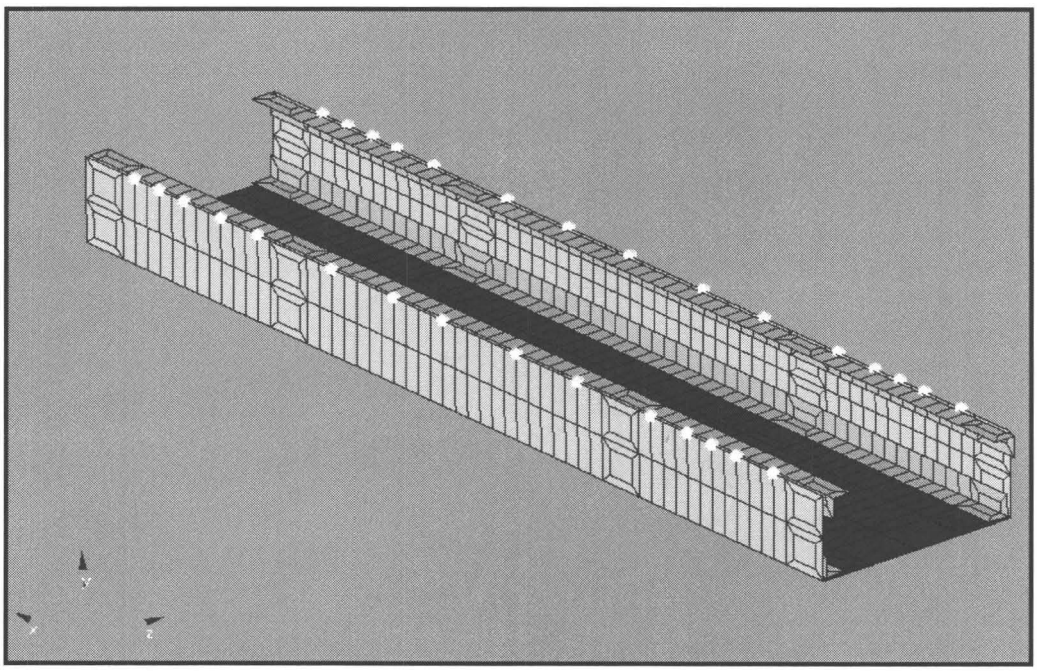

Figure C.2: Location of experimental measurements corresponding to the out-of-plane deformations for the substructure

A total of four measurements were performed on each section and the results were compared between the FE model and the test article. Figure C.3 depicts measurement locations. The error resulting from each measurement was calculated and averaged over a number of points for the front, middle and rear sections.

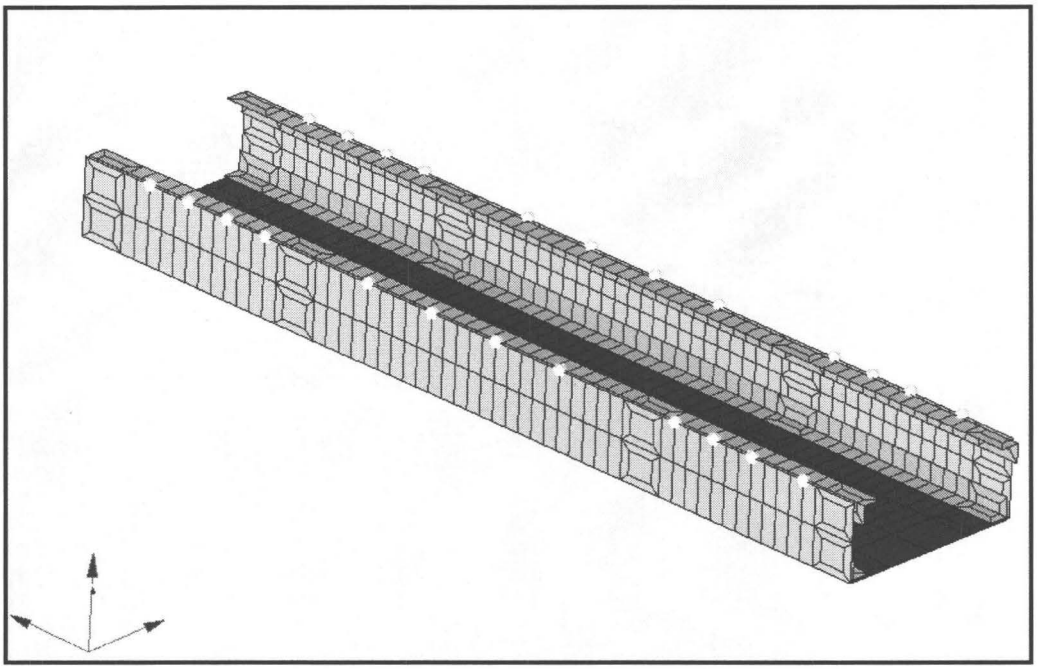

Figure C.3: Location of measurements corresponding to the out-of-plane deformations for the substructure between FE model and test article

Table C.1 tabulates the out-of-plane measurements corresponding to the full model and sub model simulations. The locations of these nodes are shown in Figure C.1.

Table C.1: Comparisons of the out-of-plane deformations determined by full model and sub model FE simulations

Substructure in full model, Numerical			Substructure in isolation, Numerical		
Front	Middle	Rear	Front	Middle	Rear
9.22 mm	6.49 mm	5.45 mm	9.96 mm	6.85 mm	5.19 mm
10.10 mm	6.10 mm	5.92 mm	10.88 mm	6.95 mm	5.42 mm
10.27 mm	6.23 mm	6.13 mm	11.24 mm	7.21 mm	5.66 mm
10.39 mm	5.94 mm	6.23 mm	11.84 mm	6.81 mm	5.77 mm
10.65 mm	6.91 mm	6.31 mm	12.33 mm	7.52 mm	5.90 mm
10.90 mm	8.16 mm	6.74 mm	12.25 mm	9.29 mm	6.25 mm
10.95 mm	9.24 mm	7.04 mm	12.33 mm	10.27 mm	6.47 mm
11.30 mm	8.74 mm	7.16 mm	12.24 mm	10.03 mm	6.53 mm
11.17 mm	8.96 mm	7.37 mm	11.94 mm	9.57 mm	6.77 mm
10.73 mm	8.69 mm	6.40 mm	11.78 mm	9.69 mm	5.87 mm
10.14 mm	8.94 mm	6.08 mm	10.85 mm	10.03 mm	5.52 mm

The out-of-plane measurements corresponding to the full scale, and sub scale experimental measurements are listed in Table C.2. The measurement locations are shown in Figure C.2. The measurements were obtained at five different locations along each section. These locations were identical in both the full and the isolated model.

Table C.2: Experimental measurements and comparisons determined by full scale and sub scale experimental testing

Substructure in full model			Substructure in isolation		
Front	Middle	Rear	Front	Middle	Rear
9.86 mm	9.83 mm	5.69 mm	10.84 mm	10.72 mm	5.27 mm
11.27 mm	11.36 mm	7.16 mm	12.37 mm	12.54 mm	6.66 mm
11.49 mm	10.87 mm	6.79 mm	12.47 mm	12.16 mm	6.29 mm
10.62 mm	10.22 mm	6.35 mm	11.68 mm	11.39 mm	5.87 mm
10.24 mm	9.38 mm	6.13 mm	11.22 mm	10.39 mm	5.59 mm

The out-of-plane measurements determined from numerical simulation and experimental measurements corresponding to the substructure are listed in Table C.3. A total of four measurements (as shown in Figure C.3) were taken on each section and the results were compared between the FE model and the test article.

Table C.3: Comparison of out-of-plane measurements corresponding to the substructure in full model determined from numerical simulation and experimental testing

Substructure in full-model, Numerical			Substructure in full-scale, Experimental		
Front	Middle	Rear	Front	Middle	Rear
9.55 mm	8.38 mm	5.42 mm	10.53 mm	9.23 mm	5.88 mm
10.28 mm	10.26 mm	6.25 mm	11.25 mm	11.32 mm	6.75 mm
11.53 mm	11.22 mm	7.24 mm	12.49 mm	12.24 mm	7.77 mm
9.77 mm	9.29 mm	5.95 mm	10.64 mm	10.27 mm	6.44 mm

The out-of-plane measurements determined from FE simulation and experimental measurements corresponding to the substructure are listed in Table C.4.

Table C.4: Corresponding out-of-plane measurements for isolated substructure determined from FE simulation and experimental testing

Substructure in sub-model, Numerical			Substructure in sub-scale, Experimental		
Front	Middle	Rear	Front	Middle	Rear
10.65 mm	9.32 mm	5.32 mm	11.57 mm	10.28 mm	5.75 mm
11.22 mm	10.53 mm	5.76 mm	12.25 mm	11.65 mm	6.22 mm
11.59 mm	11.28 mm	6.62 mm	12.69 mm	12.43 mm	7.21 mm
9.36 mm	8.38 mm	5.86 mm	10.34 mm	9.35 mm	6.34mm

Appendix D
Additional Comparison of FE Analyses

Figure D.1 depicts to the nodal locations corresponding to the 66 nodes around the boundary of the isolated substructure. These nodes were distanced between every 4 elements, and away from weld locations. The time history of the z-component of acceleration corresponding to these 66 nodes were extracted from the full-model FE analysis, and then converted to the frequency data using Fast Fourier Transform (FFT) analysis.

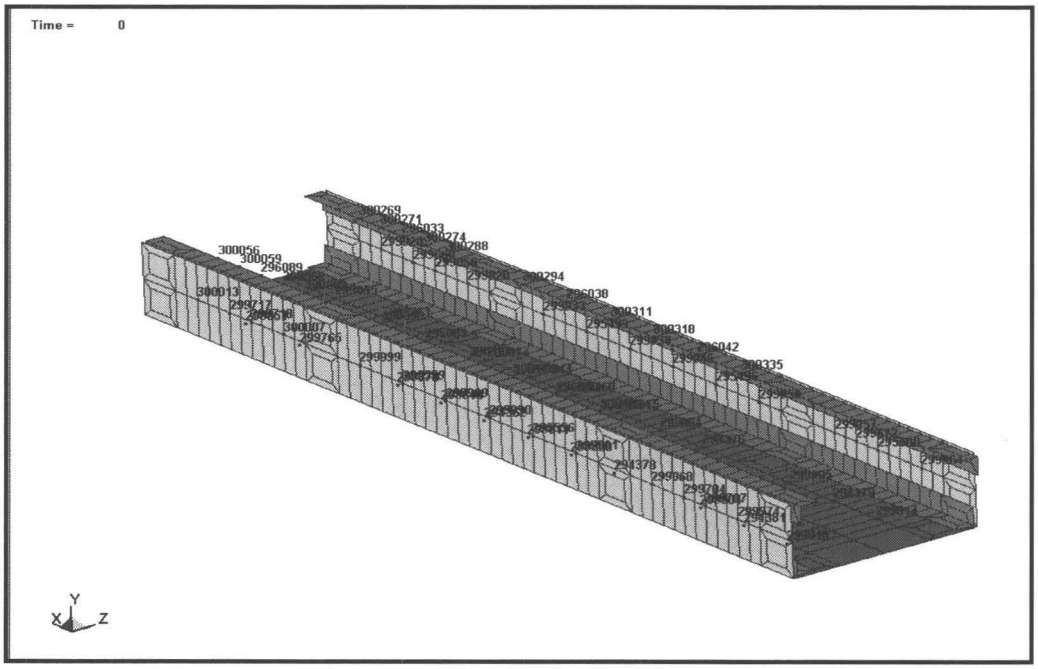

Figure D.1: Locations of 66 preselected nodes on the boundary of the FE model

Figure D.2 depicts the additional analyses performed on some randomly selected nodes and elements.

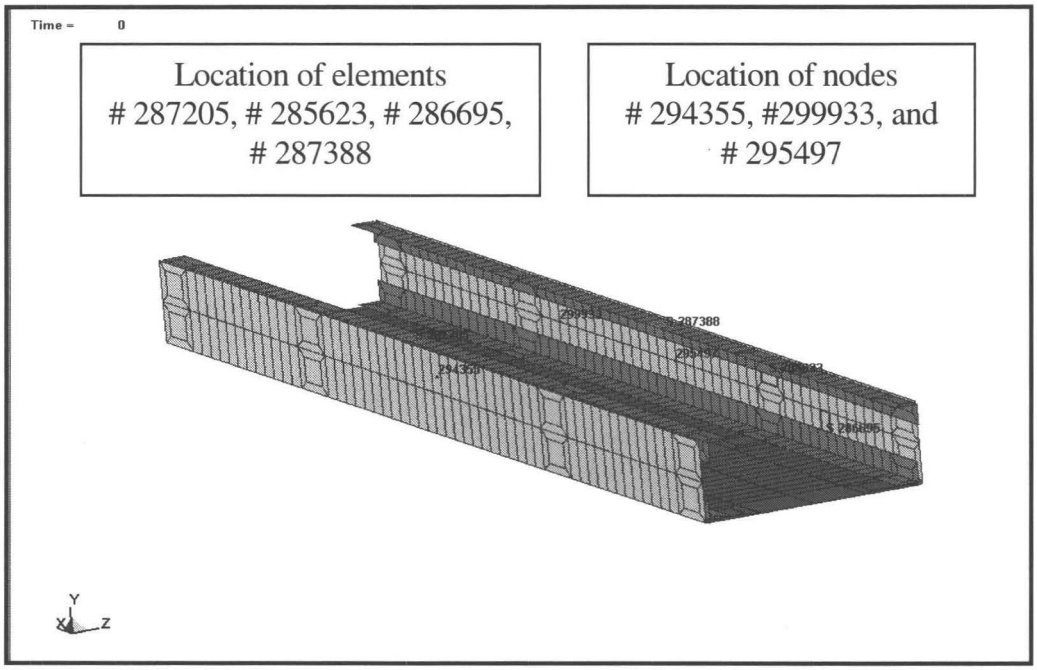

Figure D.2: Locations of additional nodes and elements for detailed analysis

These detailed analyses include the comparison of resultant displacements, resultant velocities, effective stresses (von-Mises), and effective plastic strains for preselected elements (as shown in Figure D.2) between the full model and the sub model FE simulations. Figures D.3 through D.16 depict these results. The results from these analyses were compared for the substructure in a full model and the substructure in isolation.

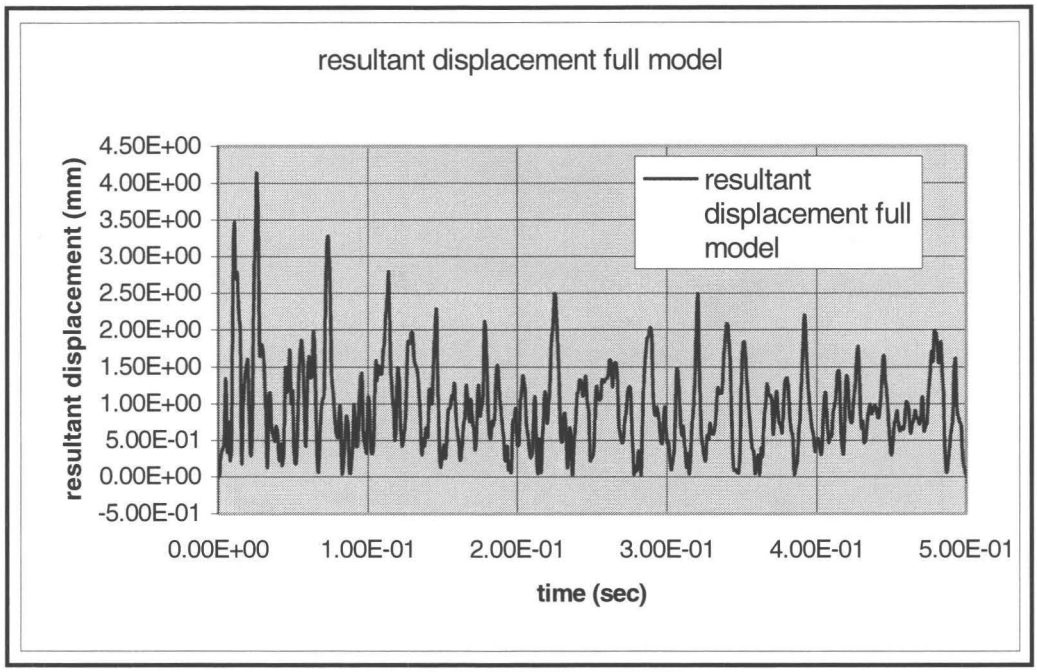

Figure D.3: Plot of resultant displacements for node # 294355 determined by the full model FE simulation

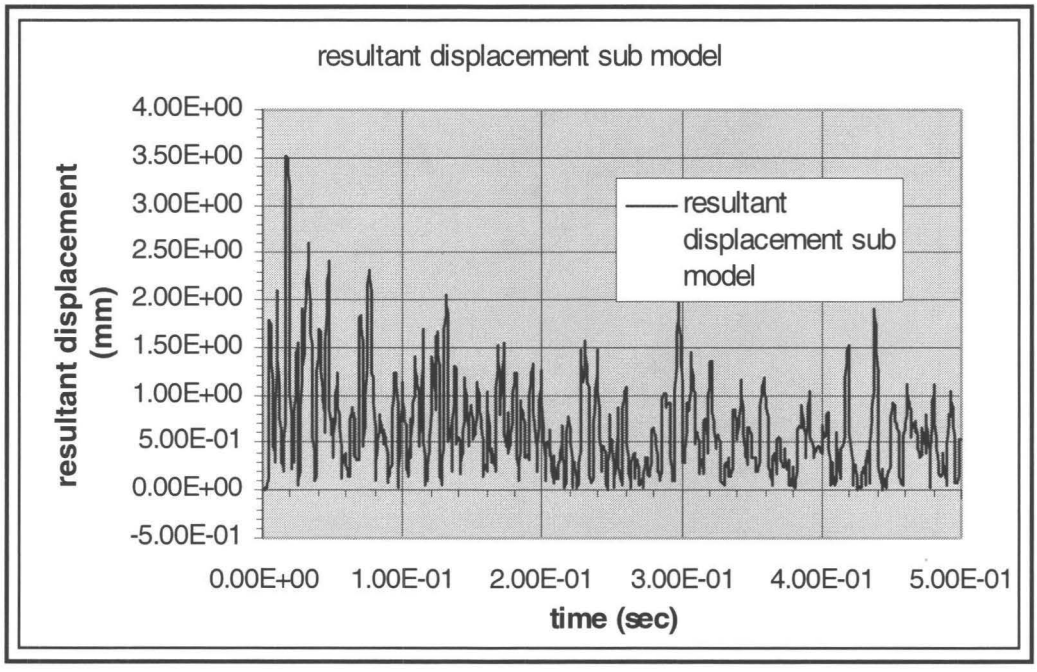

Figure D.4: Plot of resultant displacements for node # 294355 determined by the isolated model FE simulation

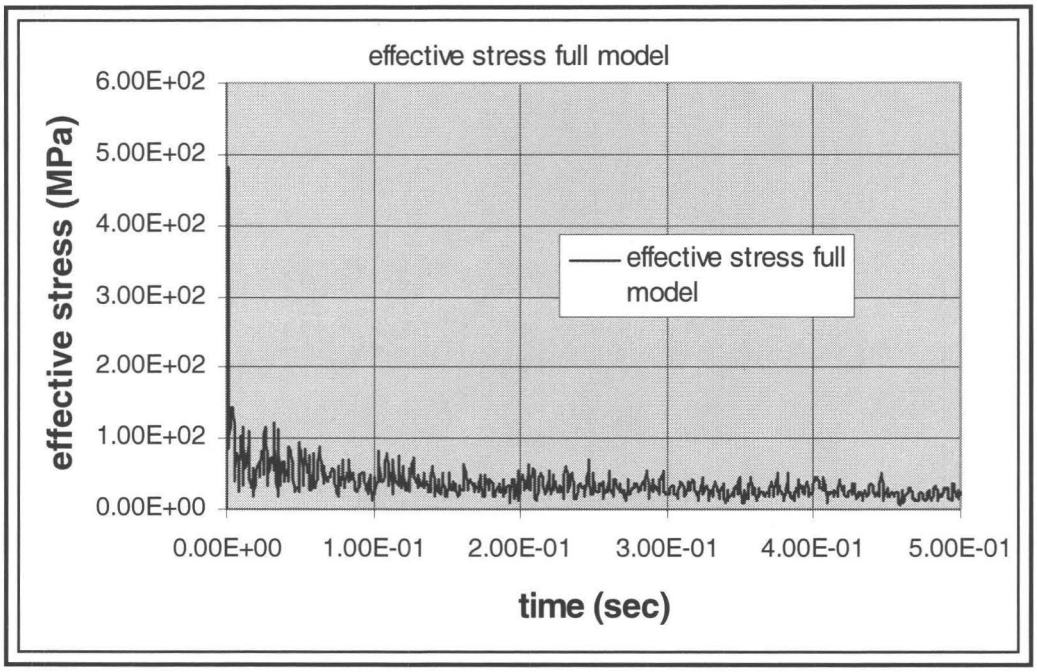

Figure D.5: Plot of effective stress for element # 287205 determined by the full model FE simulation

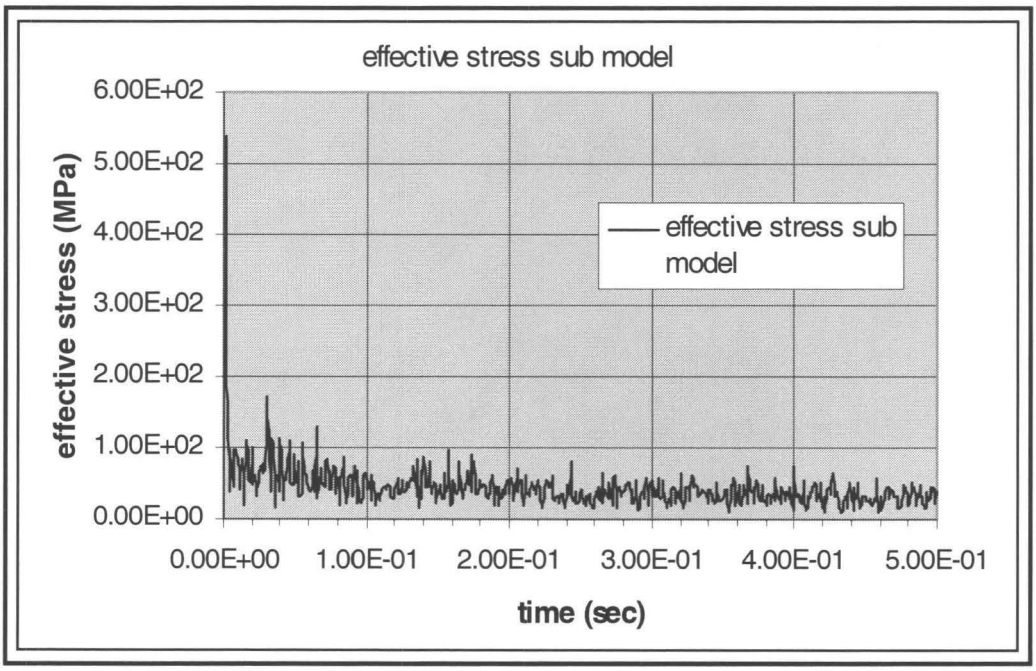

Figure D.6: Plot of effective stress for element # 287205 determined by the sub model FE simulation

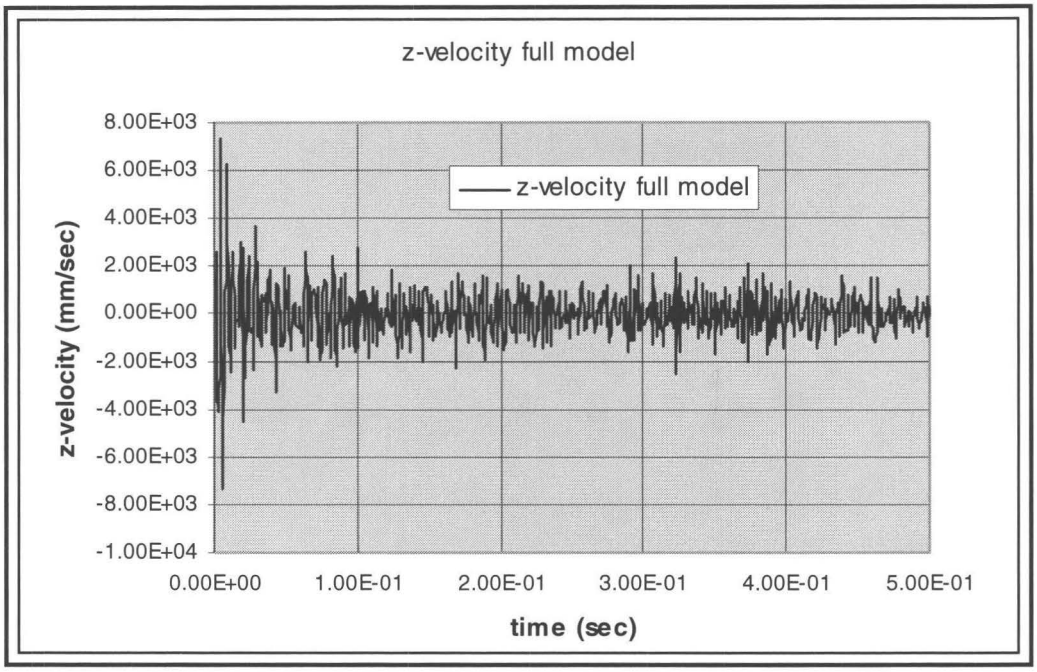

Figure D.7: Plot of z-velocity for node 299933 determined by the full model FE simulation

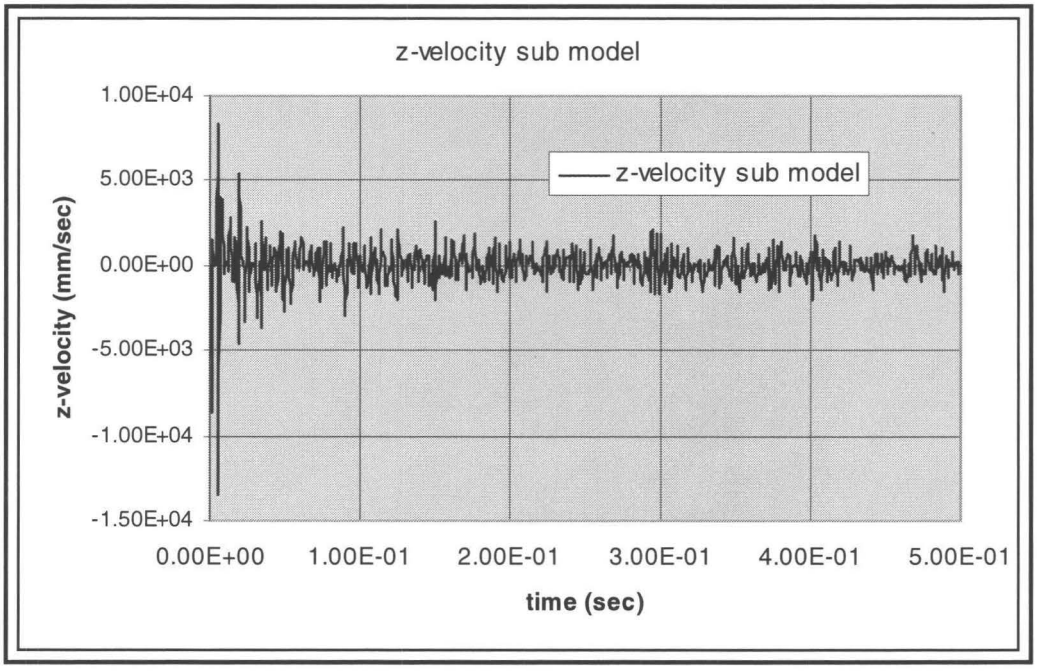

Figure D.8: Plot of z-velocity for node 299933 determined by the sub model FE simulation

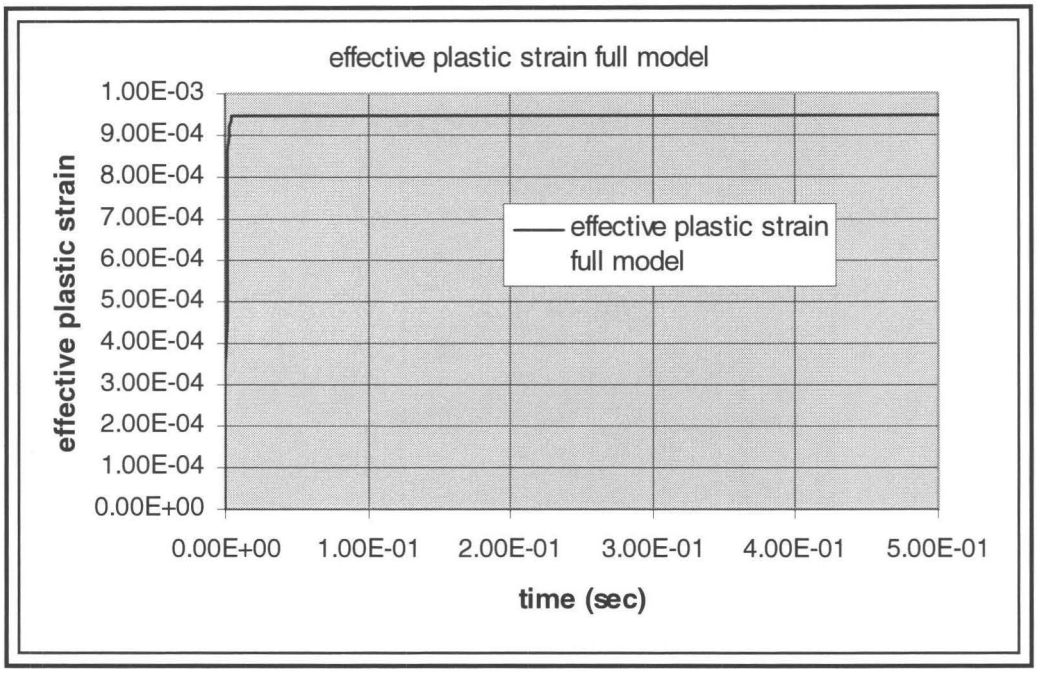

Figure D.9: Plot of effective plastic strain for element # 285623 determined by the full model FE simulation

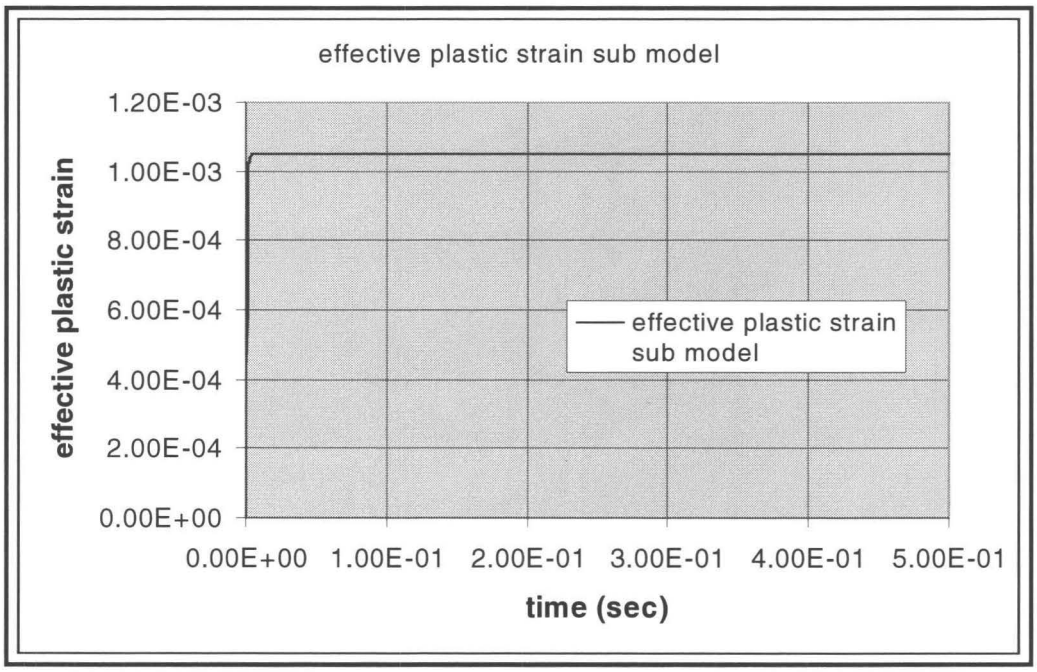

Figure D.10: Plot of effective plastic strain for element # 285623 determined by the sub model FE simulation

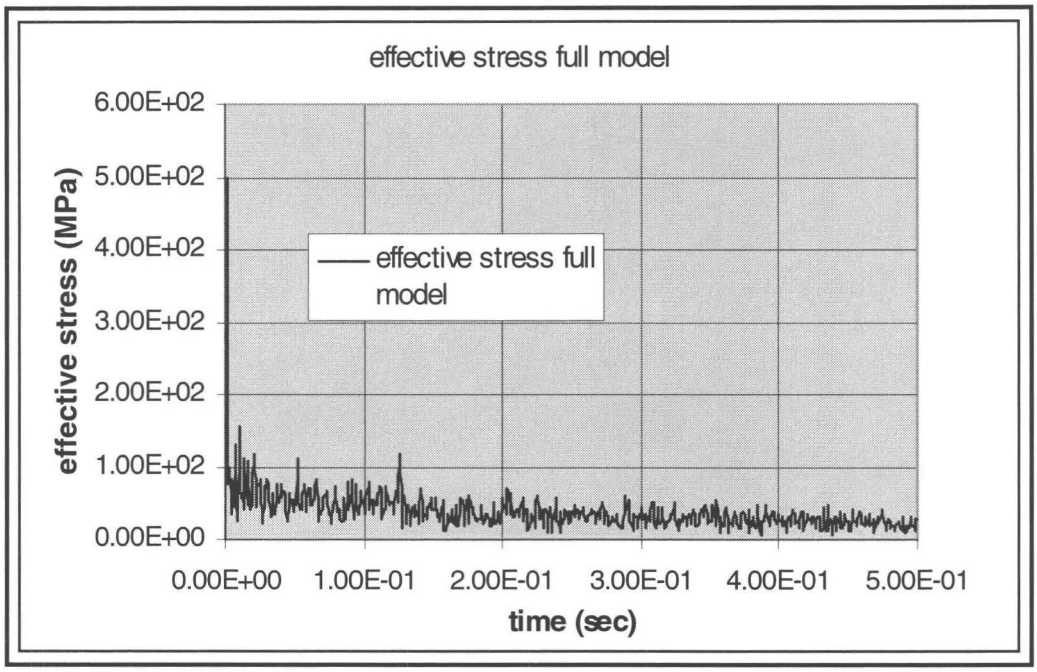

Figure D.11: Plot of effective stress for element # 287388 determined by the full model FE simulation

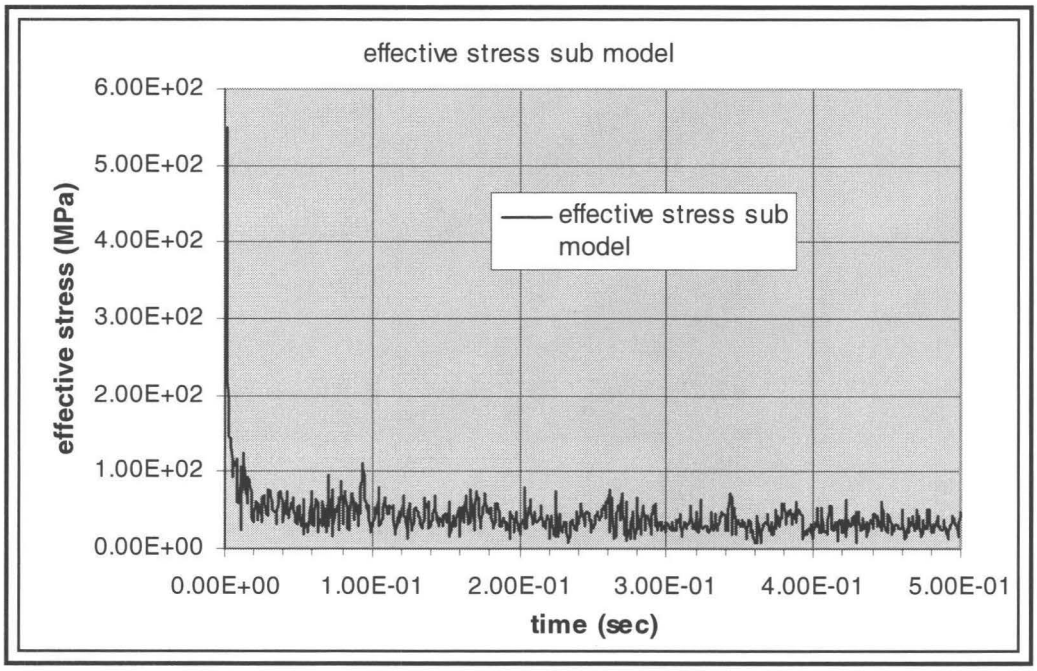

Figure D.12: Plot of effective stress for element # 287388 determined by the sub model FE simulation

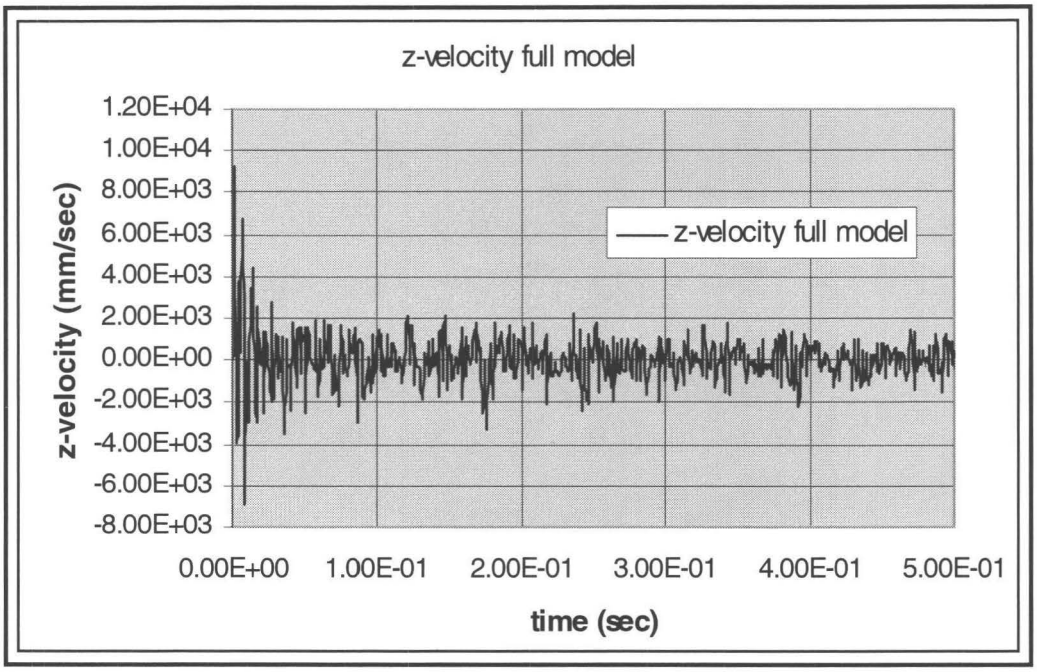

Figure D.13: Plot of z-velocity for node 295497 determined by the full model FE simulation

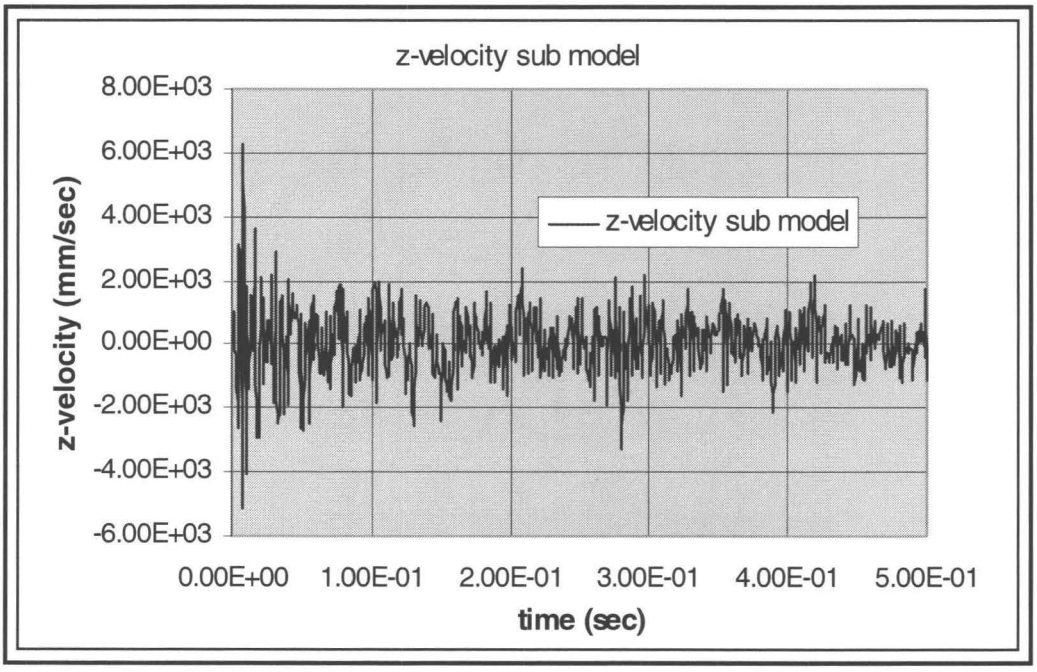

Figure D.14: Plot of z-velocity for node 295497 determined by the full model FE simulation

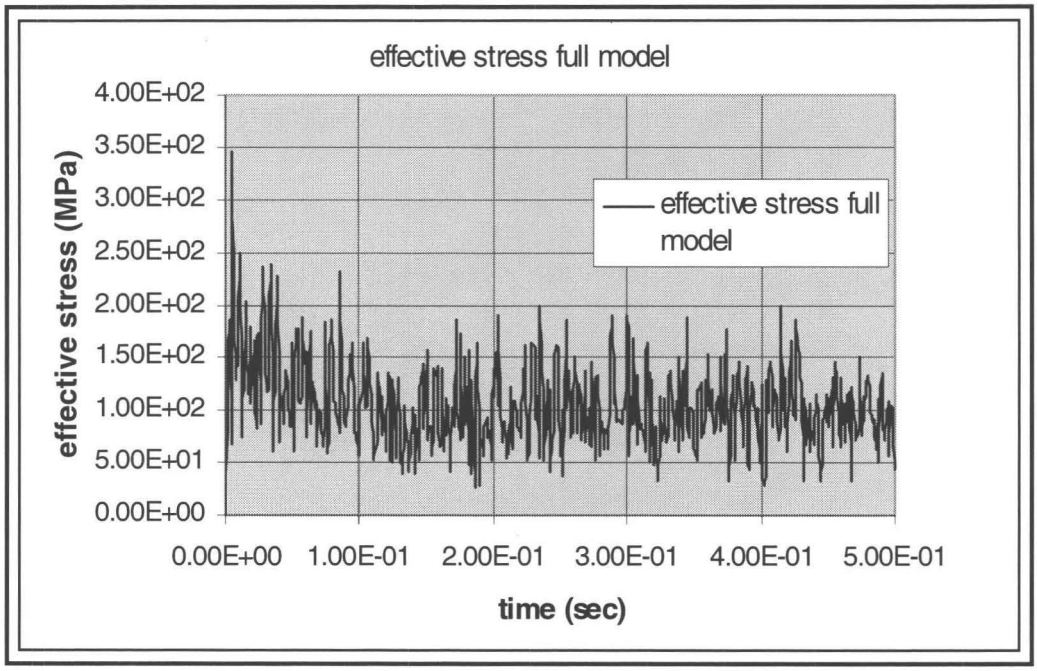

Figure D.15: Plot of effective stress for element # 286695 determined by the full model FE simulation

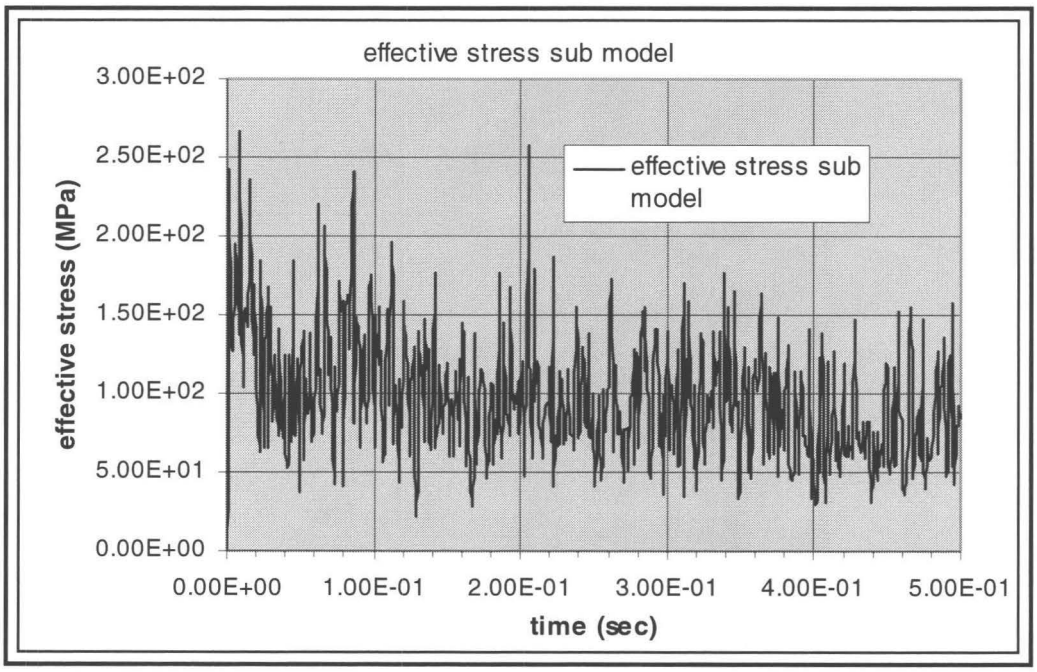

Figure D.16: Plot of effective stress for element # 286695 determined by the sub model FE simulation

These detailed analyses include the comparison of resultant displacements, resultant velocities, effective stresses (von-Mises), and effective plastic strains for additional elements and nodes (as shown in Figure D.17) between the full model and the sub model FE simulations. Figures D.18 through D.27 depict these results. The results from these analyses were compared for the subcomponent (right rail) in a full model and the substructure in isolation.

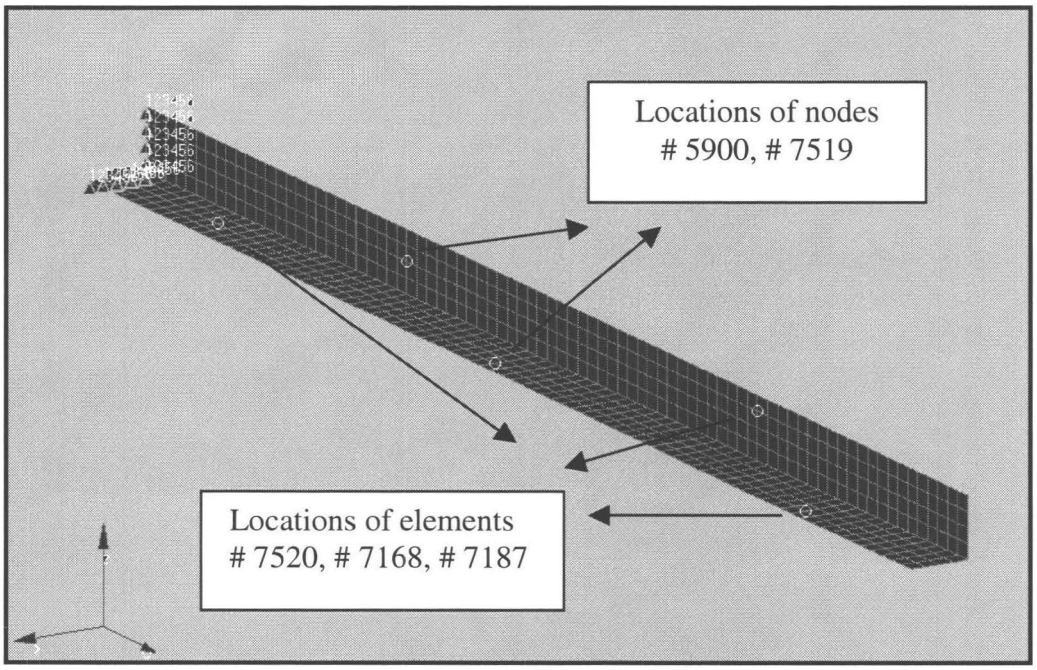

Figure D.17: Locations of preselected nodes, and elements on the FE model

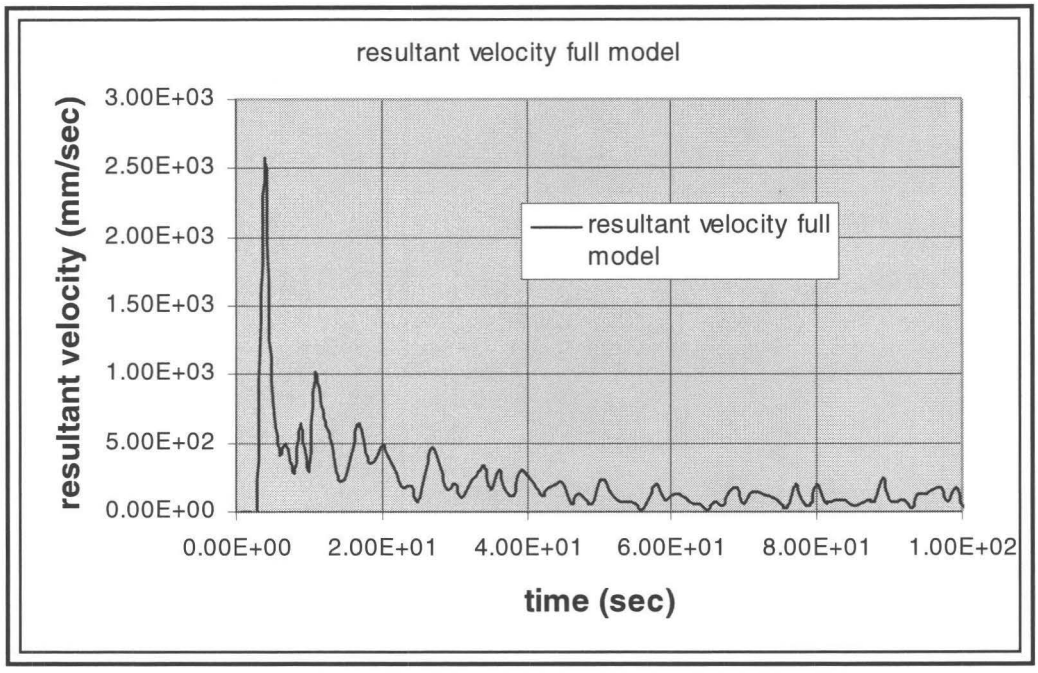

Figure D.18: Plot of resultant velocity for node # 7519 determined by the full model FE simulation

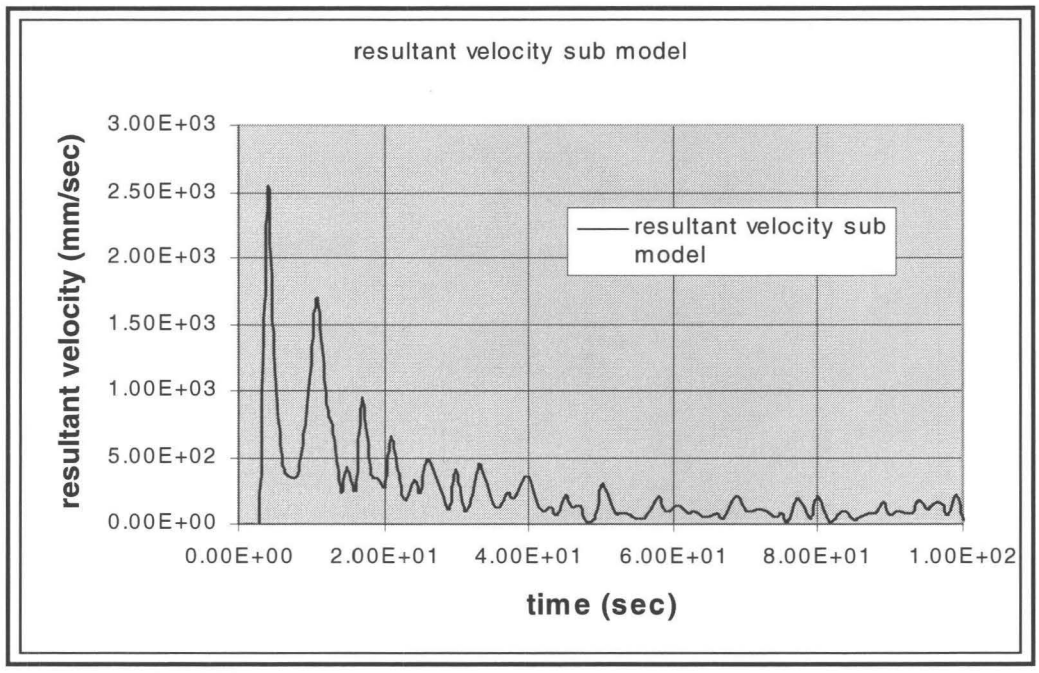

Figure D.19: Plot of resultant velocity for node # 7519 determined by the sub model FE simulation

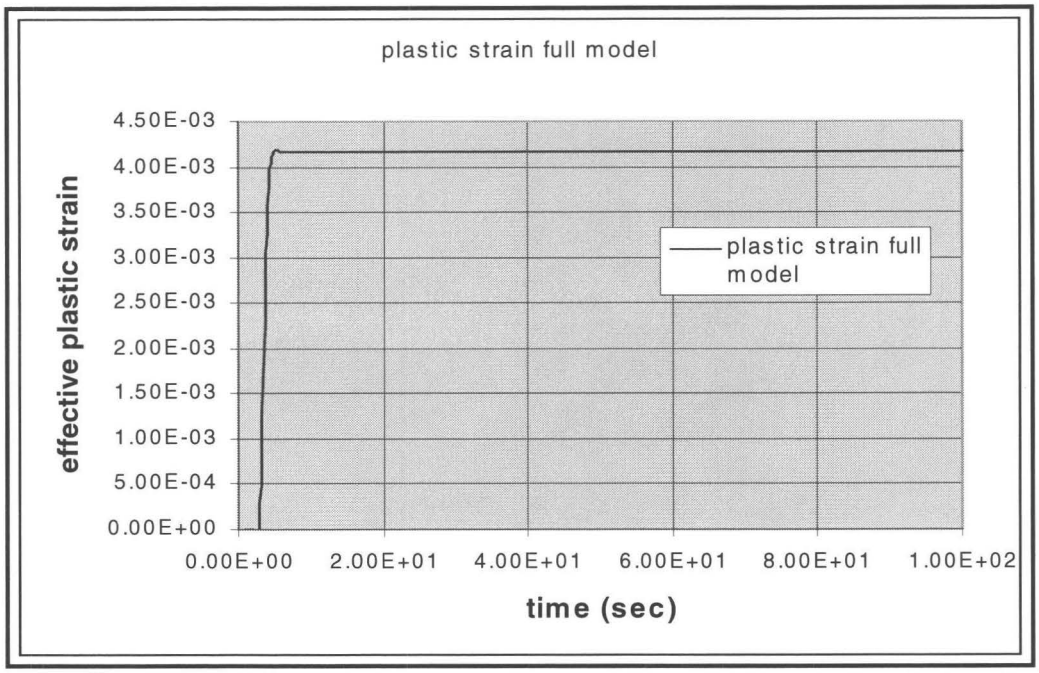

Figure D.20: Plot of effective plastic strain for element # 7520 determined by the full model FE simulation

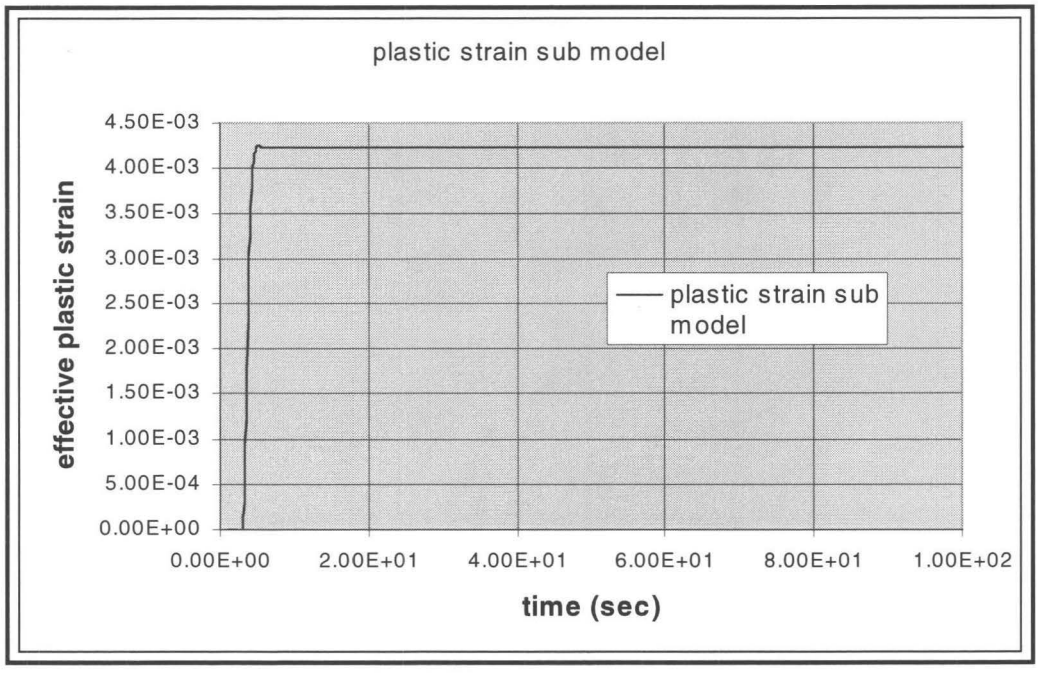

Figure D.21: Plot of effective plastic strain for element # 7520 determined by the sub model FE simulation

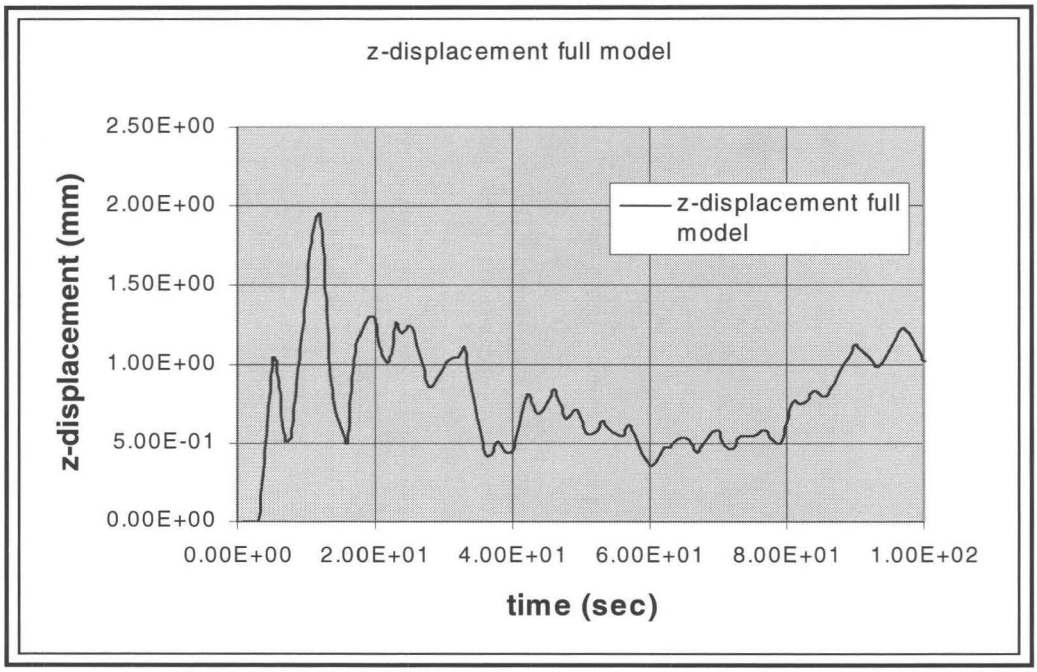

Figure D.22: Plot of z-displacement for element # 7168 determined by the full model FE simulation

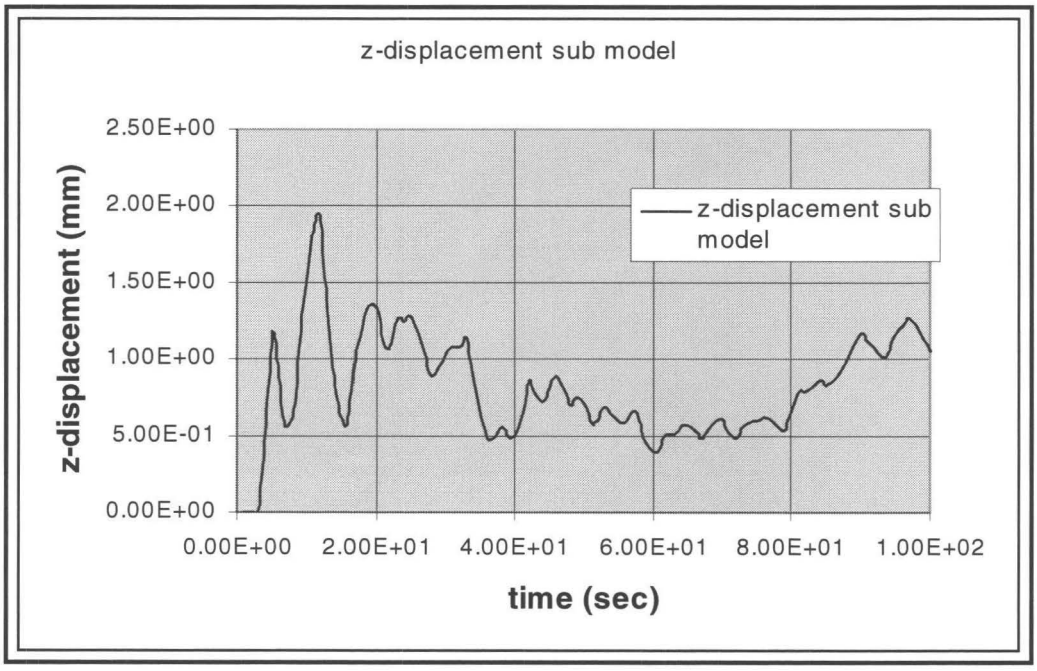

Figure D.23: Plot of z-displacement for element # 7168 determined by the sub model FE simulation

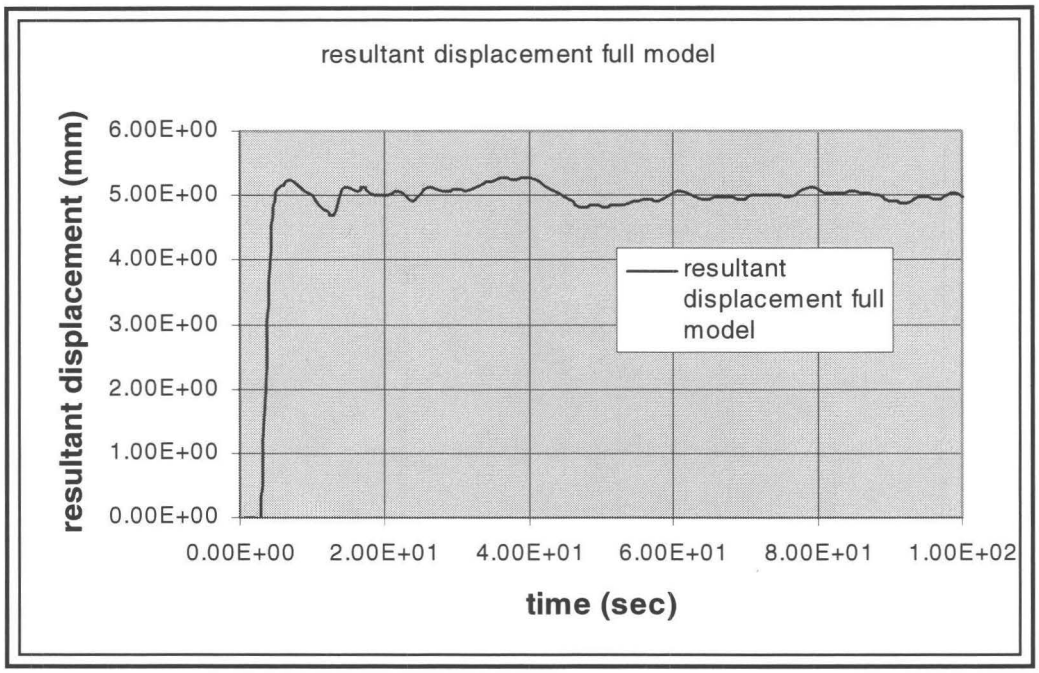

Figure D.24: Plot of resultant displacement for node # 5900 determined by the full model FE simulation

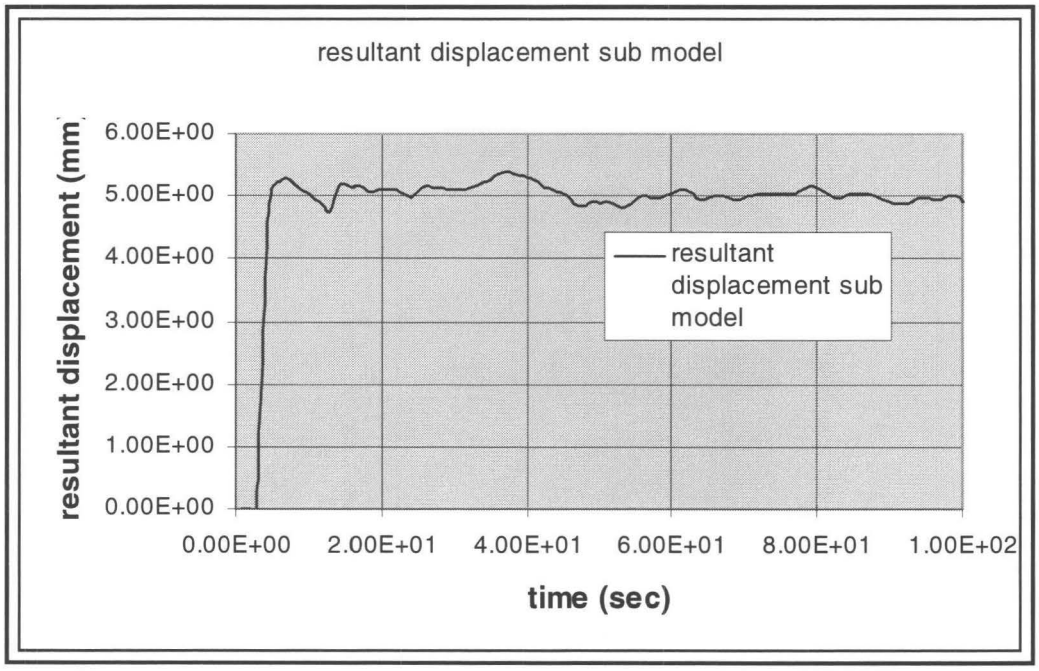

Figure D.25: Plot of resultant displacement for node # 5900 determined by the sub model FE simulation

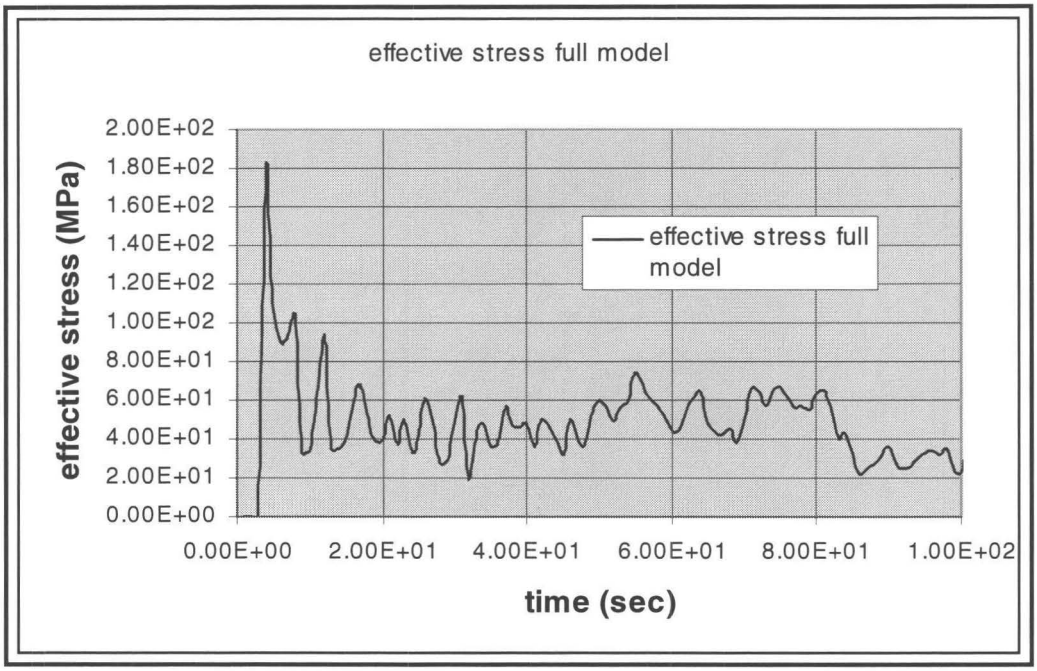

Figure D.26: Plot of effective stress (von-Mises) for element # 7187 determined by the full model FE simulation

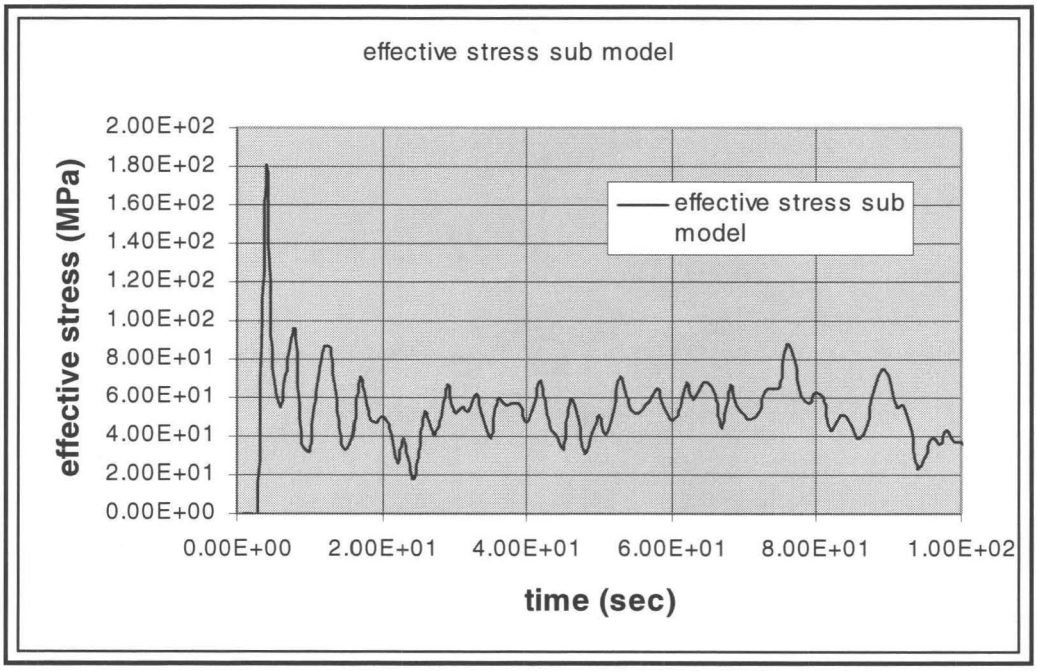

Figure D.27: Plot of effective stress (von-Mises) for element # 7187 determined by the sub model FE simulation

In addition, various comparisons were obtained during performing FE impact analyses, which, determined at various times for isolated subcomponent (right rail). These analyses include the comparisons of effective plastic strain, resultant displacement, and internal energy respectively. Figures D.28 through D. 30 depict comparisons at different time steps. In each figure the results were obtained for the subcomponent (right rail) in the full model and the sub model simulations.

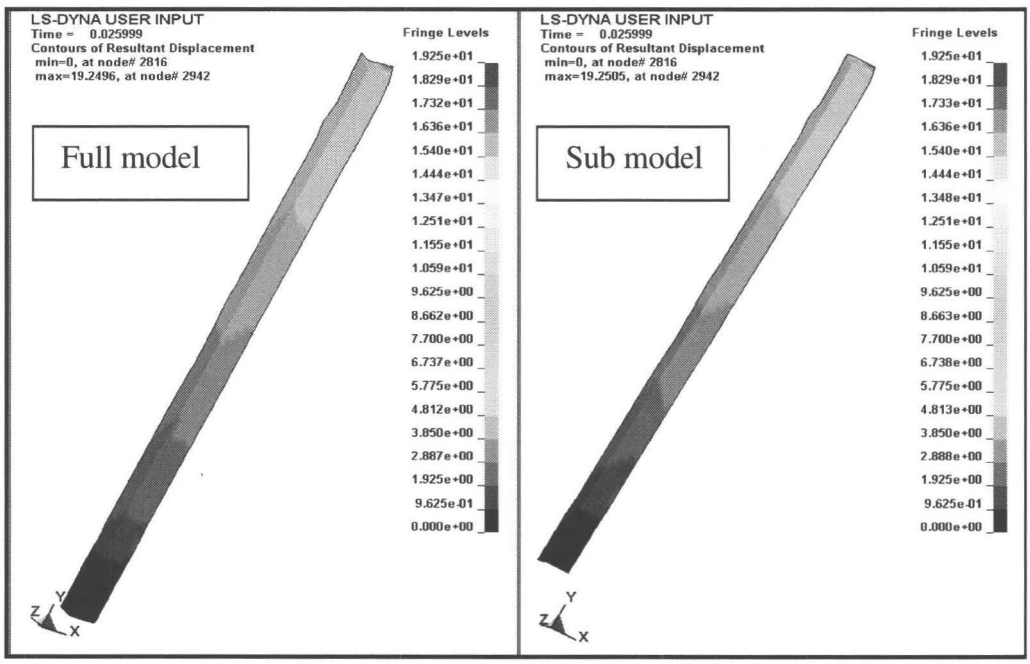

Figure D.28: Comparison of the resultant displacements obtained at time = 0.050999 (sec) for the right-rail determined by FE simulations

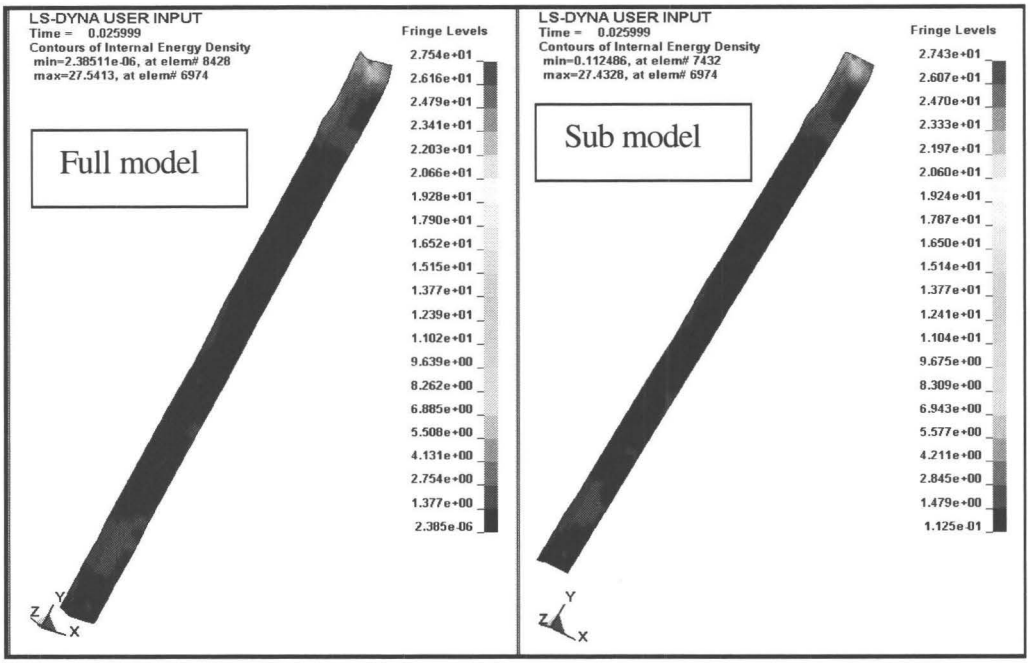

Figure D.29: Comparison of the internal energy obtained at time = 0.02599 (sec) for the right-rail determined by FE simulations

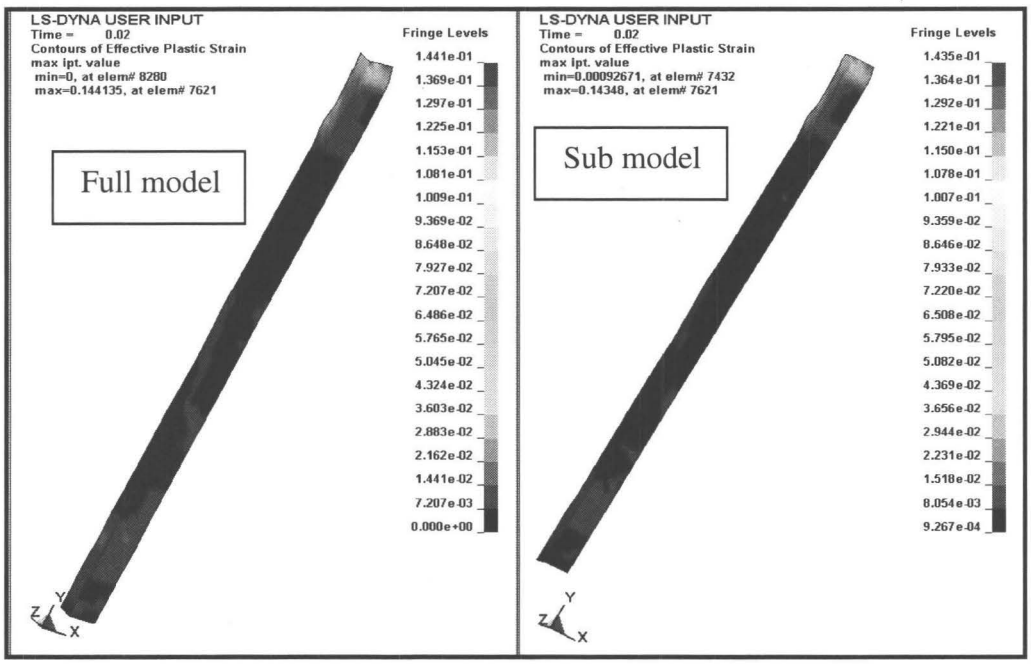

Figure D.30: Comparison of the effective plastic strain obtained at time = 0.02 (sec) for the right-rail determined by FE simulations

Appendix E
Experimental Apparatus

The component impact testing apparatus was designed and built to perform dynamic testing on small to medium size components. Since the experimental set up was designed for this study, a brief explanation of the set up is warranted.

Components of Impact Testing Apparatus

The experimental apparatus comprised of the following components.

Pressure Vessel

This apparatus used two pressure vessels: the primary and the secondary. The purpose of the primary pressure vessel (Manchester Tank Inc., Tennessee, USA) was to provide the pneumatic power needed to operate the impacting cylinder. The pressure vessel, shown in Figure E.1, is designed for a maximum pressure of 2.75 MPa and it has a storage capacity of 0.23 m^3 that discharged rapidly to the cylinder by operating the main ball valve. The ball valve opens from closed position to fully open position in 250 ms.

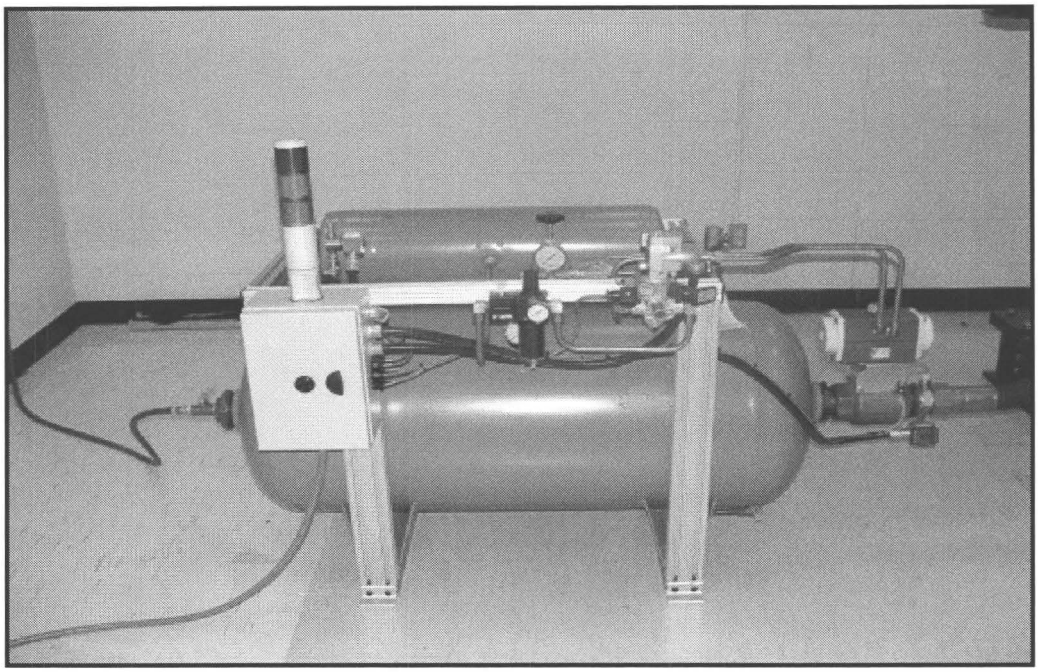

Figure E.1: Pressure vessel

A secondary vessel supplies the necessary pneumatic power for the main ball valve 63.5 mm diameter (see Figure E.2). The maximum operating pressure of the secondary tank is 1.2 MPa. The minimum pressure required to operate the ball valve is 345 kPa.

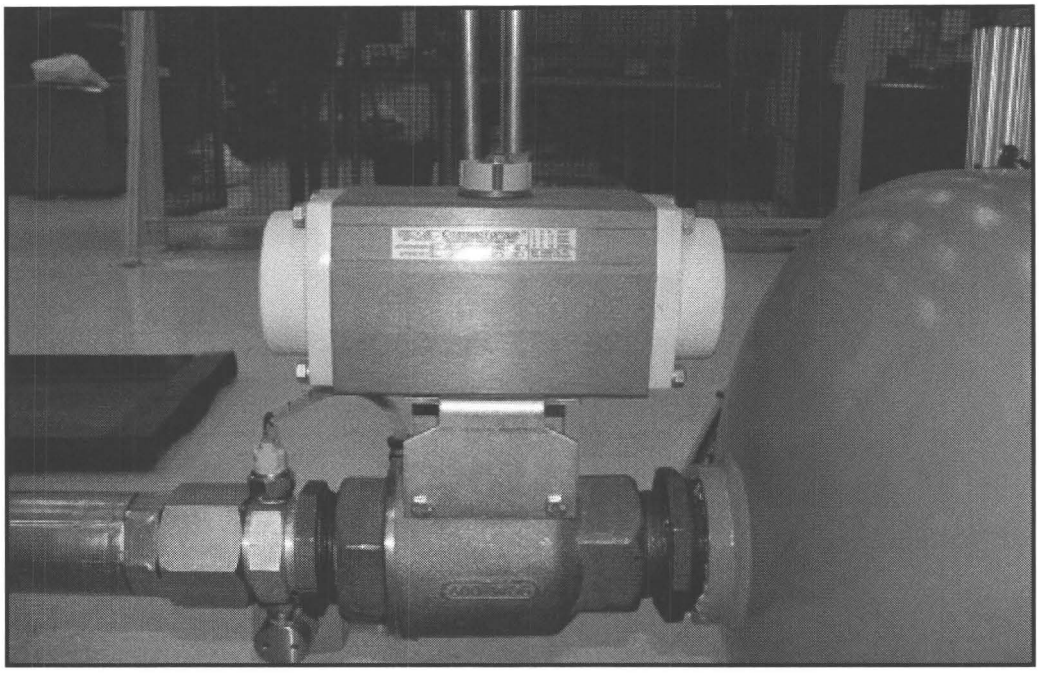

Figure E.2: Main ball valve

Pressure Gages and Limit Switches

In order to control the desired test protocol, a series of ball valves, pressure gauges and pressure switches were used in the apparatus. Each sensor or valve performs a specific task that is crucial to achieving the impacting speed. Once the desired pressure for a specific speed is reached, the limits switches and sensors signal the main ball valve to open and supply the pneumatic power to the cylinder. At this junction, the pneumatic cylinder accelerates the impacting head and the test is performed. Figure E.3 shows the pneumatic lay out and components.

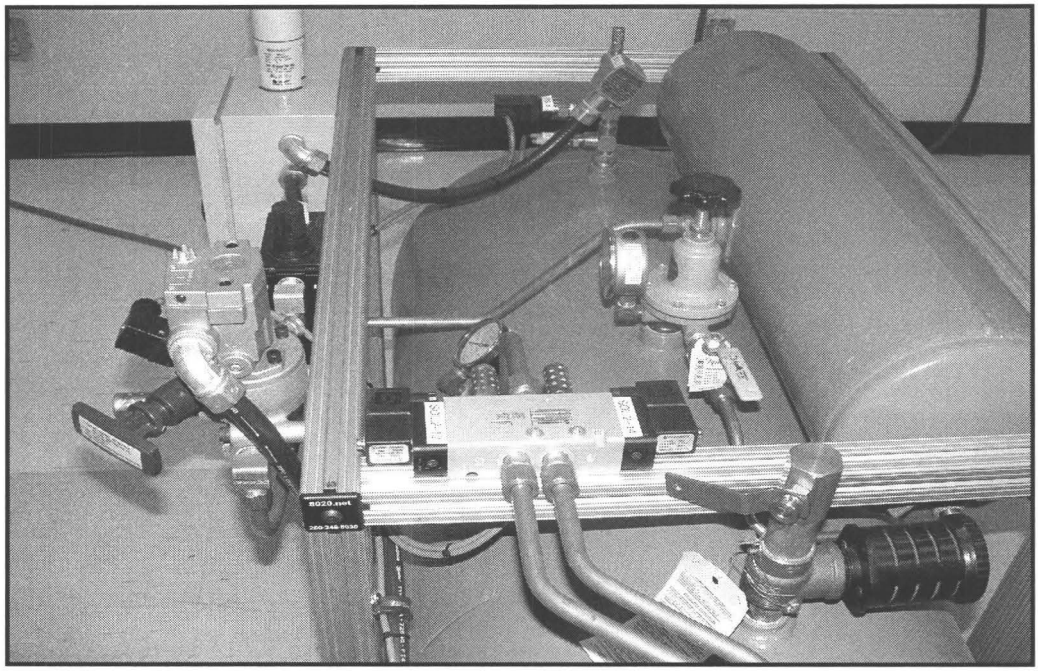

Figure E.3: Pneumatic lay out

Pneumatic Actuator

The actuator was custom designed to meet the functional requirements (see Figure E.4). The actuator was designed to provide the impacting energy indirectly to the test article by accelerating an impacting mass. This was a double-ended, single acting actuator with cast iron rings to ensure durability. The body of the actuator had a series of holes at the head end to provide a mechanical pressure relief mechanism just after the impactor had decoupled from the actuator. The actuator had a maximum operating pressure of 2.59 MPa.

Additionally, eight (8) mounting brackets were welded to the body of the cylinder to provide sufficient connection points. These connection brackets were 0.057 m (2.25 inches) long by 0.092 m wide by 0.0381 m high. The brackets had 0.035 m diameter

holes, cut at the center, that provided clearance for 1 5/6 -8 UNC bolts. The extension arm (ram) of the actuator was 1.67 m long. The head end of the actuator had an internal thread of 1 ¼-12 UNF and the tail end of the extension arm had 10 mm hole through. The purpose of this hole was to provide housing for a shear pin (see Figure E.5). The shear pin was only used if higher velocity needed to be achieved.

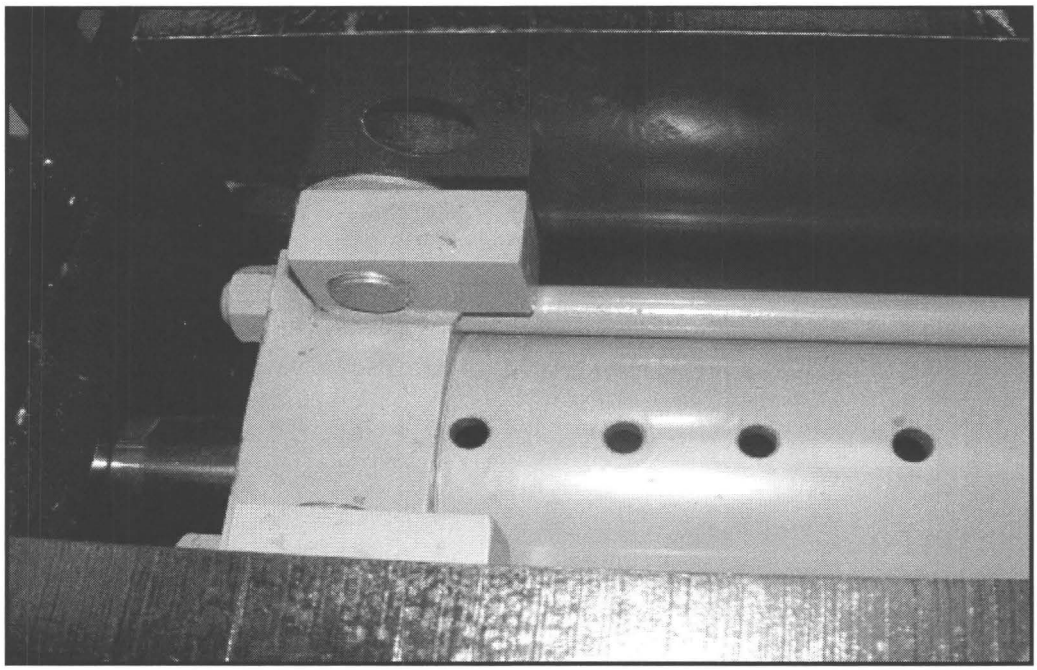

Figure E.4: Custom designed actuator

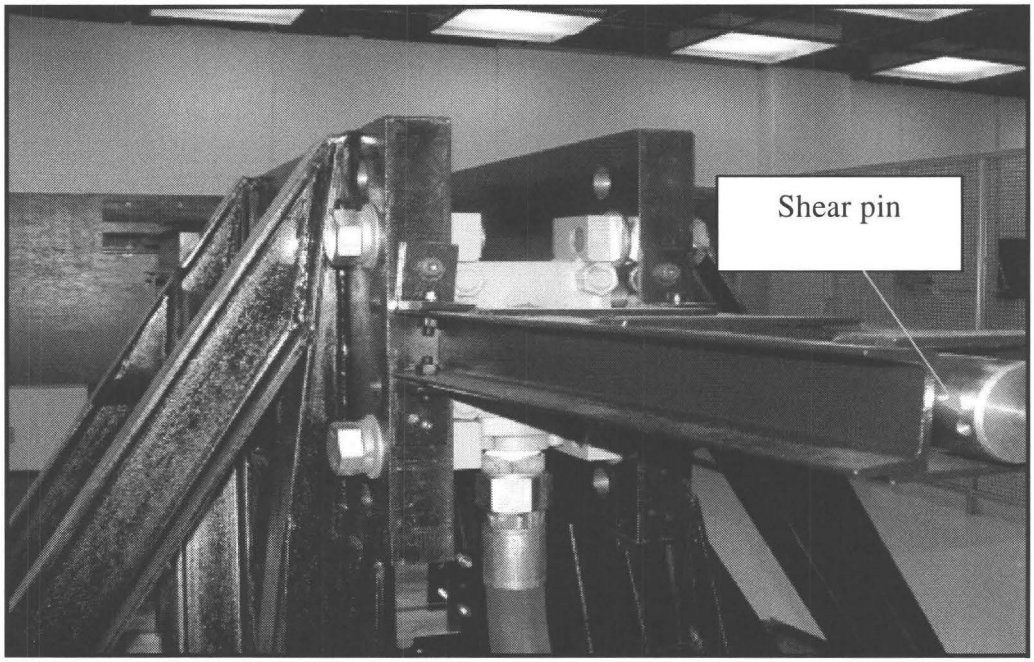

Figure E.5: The shear pin section of the actuator

Actuator Holding Frame

Actuator holding frame was designed such that the entire assembly could be moved to accommodate different test articles (see Figure E.6). It was comprised of two steel plates that held the cylinder between them with eight bolts. In addition, the cylinder could pivot at the centre so that if any repair was required the cylinder could be rotated and not taken apart completely. The frame was connected to the base of the apparatus with 3/4-10 UNC bolts and could be moved 0.46 m to accommodate the smaller test articles.

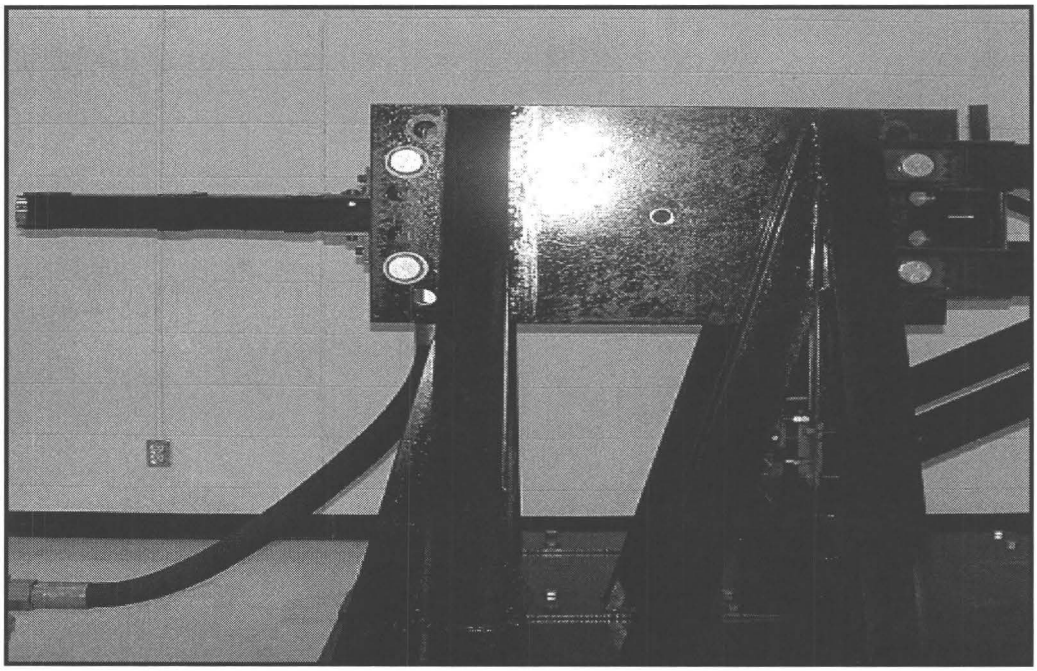

Figure E.6: Actuator holding frame

Component Holding Frame

The component-holding frame provided a mounting point to fasten the test article (see Figures E.7 and E.8). The holding frame was welded to a 0.91 m by 0.22 m plate. This provided a mounting point to the base bed assembly. In addition, the faceplate of the holding frame had a series of 0.019 m diameter hole in 0.2032 m square grid pattern. This provided a mounting point for test specimen.

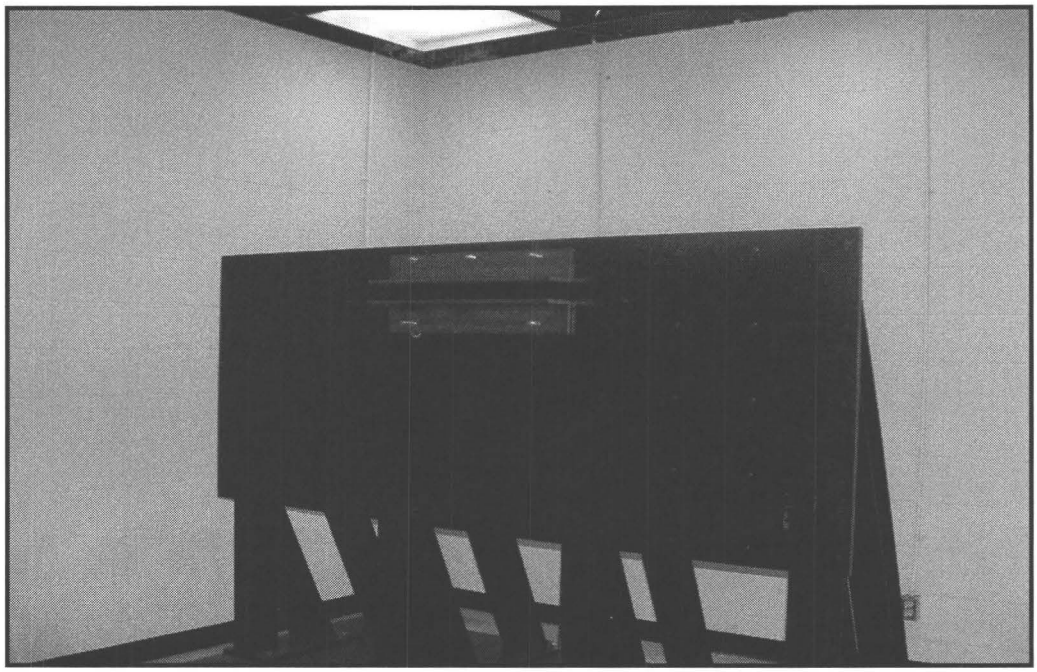

Figure E.7: Component holding frame # 1

Figure E.8: Component holding frame # 2

Base Assembly

The base assembly along with the actuator and components holding frame made up the entire impact-testing system. The base assembly made the impact-testing machine a self-reacting frame; thus, there was no need for the complete system to be restrained or bolted to the floor (see Figure E.9). This design was modular and both the cylinder holding frame and component holding frame could be moved closer to each other to accommodate the testing of smaller components.

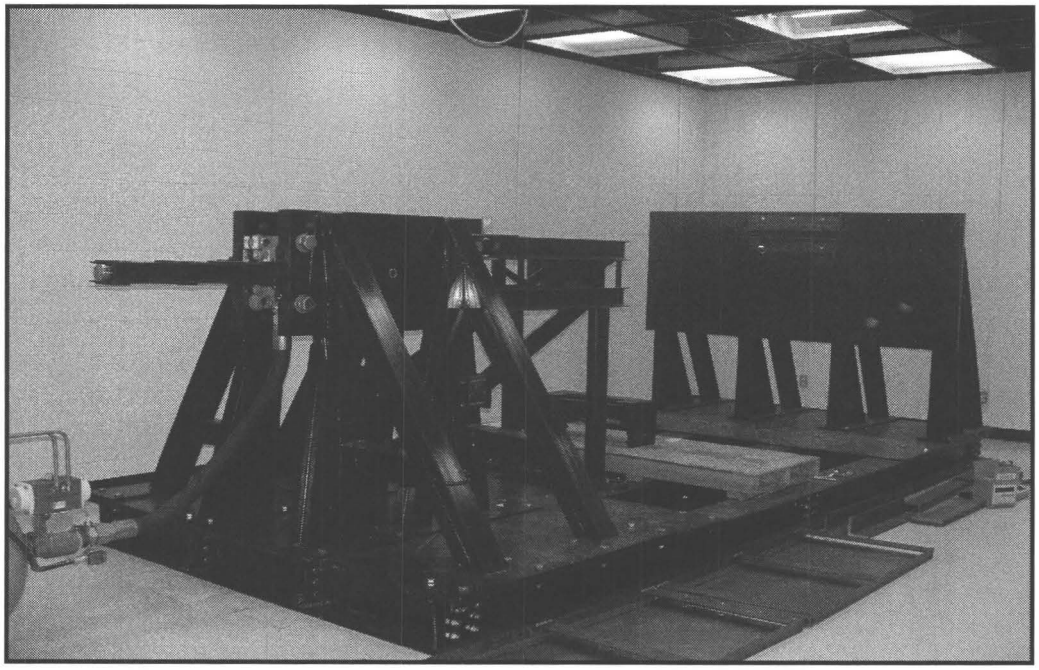

Figure E.9: Base assembly

Railing Assembly

A railing assembly was designed to provide a guide for the impactor and to provide a stopping mechanism (see Figure E.10). The accelerating mechanism came to a complete stop by impacting four rubber dampers. The rubber dampers had an impact capacity of 6.34 kJ at a maximum speed of 12 m/s. The four rubber dampers used in this apparatus provided a factor of safety of 2.25 based on the maximum impact energy capacity of the apparatus which is 11.25 kJ. The rubber dampers were mounted on to the railing frame with 19.05 mm bolts.

To briefly explain the function of the railing, the impactor was accelerated on the railing via cylinder and gained the desired speed on the track. Once the desired speed was achieved, it freely traveled on the rail until it reached the test specimen. The rail was designed such that there was only 0.15 m of free traveling distance before the impactor came into contact with the test specimen. This distance was chosen so that if the impactor bounced back, there would be sufficient room. Another reason was that the impactor might loose its velocity if it were to travel a longer distance due to friction between the track and rollers of the impactor. To ensure the impactor did not couple with the test article, the system was designed such that the impactor gained the intended speed on a rail and decoupled from the accelerating mechanism just prior to impact.

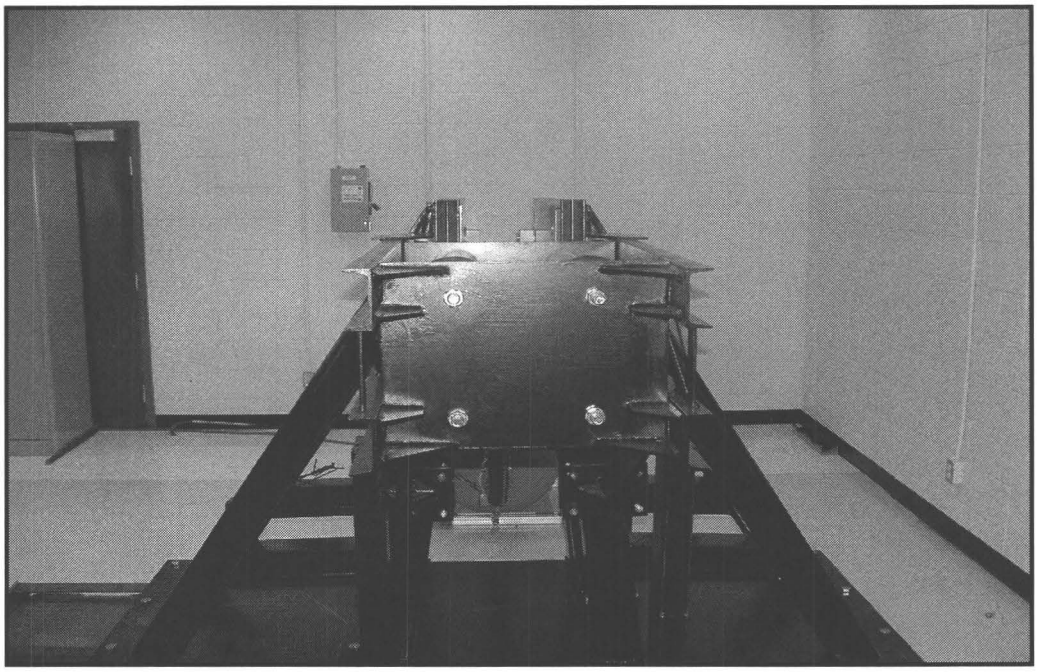

Figure E.10: Railing assembly

Based on the experimental data provided by the manufacturer of the damper, four dampers were used. Less number of dampers reduces the factor of safety and increases the bounce back force that, results in more stress to the actuator. Equally, a larger number of dampers lead to over stiffened stopping mechanism that also causes more stress on railing mechanism and reduced factor of safety of railing. It must be noted that the impacting head (impactor) should be designed and manufactured based on the design of the test article and the type and surface area of contact that is desired. Figure E.11 and E.12 depict the railing system.

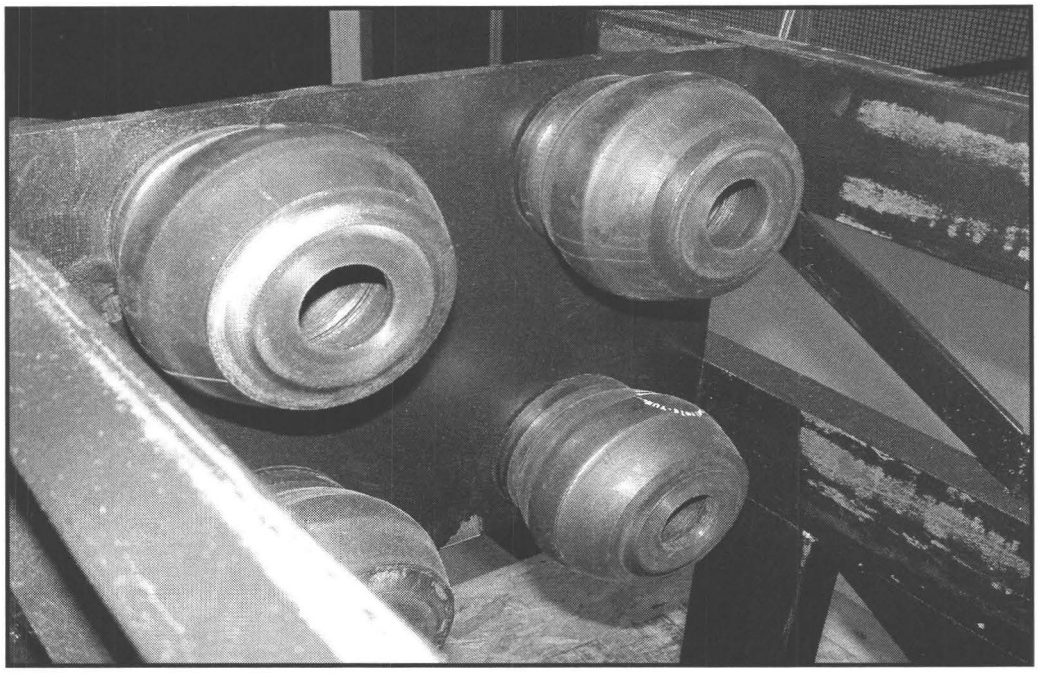

Figure E.11: Damper configuration of the railing assembly

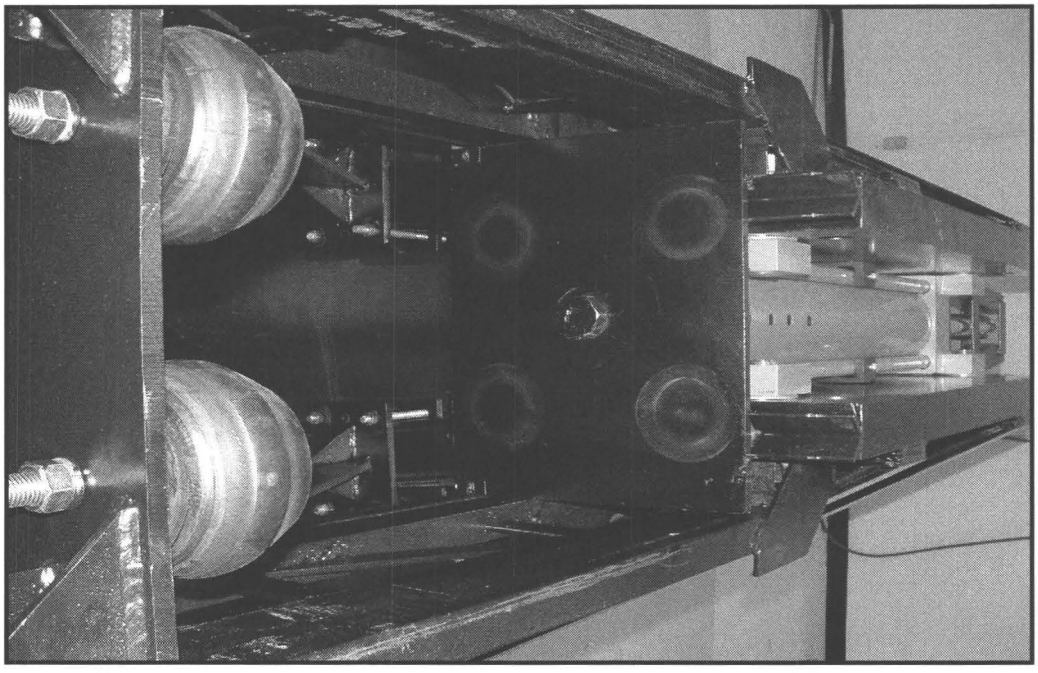

Figure E.12: Accelerating mechanism of the railing assembly

Safety Design

The system was designed primarily for automotive subcomponent dynamic testing. Therefore, there were limitations on the size of the test article, the velocity of impact, the energy absorption capability of the apparatus, and the impactor mass. The system was based on the rapid extension of the cylinder ram by a sudden discharge of pneumatic pressure to the cylinder. The pressure was released from the high capacity pressure vessel and discharged to the cylinder through a 0.0635 m electronically operated ball valve. The ball valve opened from a fully closed to a fully open position in 250 ms.

The pneumatic circuit had been designed such that there were multiple redundancies in the system. This ensured that if any one solenoid or switch failed the operation of the entire system stopped. Furthermore, to ensure the safety of the operator, a complete enclosure was designed and implemented to the apparatus. The physical enclosure stopped unauthorized personal from entering or operating the system. It also prevented any debris or broken off section from the test article to hit the operator and other personal and cause personnel injury. Figure E.13 depicts the control panel and gate. Since the impact speed is relatively high, the high frequency vibration resonates through the self-reacting frame to the floor. As such, the frame was mounted on vibration absorbers to damp the impact energy transfer to the floor. Furthermore, the frame was anchored to the floor via reinforced angle brackets and lag bolts.

Figure E.13: Control panel and physical enclosure

Data Acquisition System

The data acquisition system used was an IOtech Zonicbook 618E (Cleveland, USA). It is a portable vibration analysis and monitoring system with eight analog input channels at up to 100 KHz. The system connects to a computer via an Ethernet port.